UC Santa Barbara
UC Santa Barbara Electronic Theses and Dissertations

Title
Orbital design and electronic structure of topological metals

Permalink
https://escholarship.org/uc/item/6fc9f16k

Author
Teicher, Samuel Moses Langford

Publication Date
2022

Peer reviewed|Thesis/dissertation

eScholarship.org
Powered by the California Digital Library
University of California

University of California
Santa Barbara

Orbital design and electronic structure of topological metals

A dissertation submitted in partial satisfaction
of the requirements for the degree

Doctor of Philosophy
in
Materials

by

Samuel M. L. Teicher

Committee in charge:

Professor Ram Seshadri, Chair
Professor Stephen D. Wilson
Professor John W. Harter
Professor Vojtech Vlcek

March 2022

The Dissertation of Samuel M. L. Teicher is approved.

Professor Stephen D. Wilson

Professor John W. Harter

Professor Vojtech Vlcek

Professor Ram Seshadri, Committee Chair

March 2022

Orbital design and electronic structure of topological metals

Copyright © 2022

by

Samuel M. L. Teicher

To Celeste S. Kinginger and Jonathan L. Teicher,
exceptional parents and role models.

Acknowledgements

The development of a scientist is built on substantial support. While I can't possibly thank all of the teachers, mentors, co-workers, friends, and family members that have contributed to this work, I highlight here a few of the people who made this dissertation possible.

First and foremost, I would like to thank my advisor, Ram. Throughout my time at UCSB, Ram has developed a culture of mentorship both within our group and within the Materials Research Lab. He has been exceptionally generous in teaching me how to critique and present my work, helping me to arrange collaborations, and supporting me in sharing my work through presentations and conferences. In addition to setting a high scientific standard—emphasizing rigor, clarity and style—Ram has shared with me relentless optimism, which is an invaluable quality for a scientific researcher.

I have also benefitted immensely from the support of two unofficial co-advisors, Stephen Wilson and Leslie Schoop. Stephen has provided mentorship from the start of my time at UCSB, from his quantum mechanics lectures to detailed discussions of the history of high-temperature superconductivity at bagel hour. Stephen's feedback has consistently helped me to map my simulations onto the complexity of experimental reality. Leslie has helped me to describe my work in terms of simple chemistry concepts, readily offering detailed comments from my first to last publication, usually accompanied by upbeat emojis. I would also like to thank the Schoop group, especially Sebastian Klemenz, Shiming Lei, and Ratnadwip Singha, for a fun visit in Princeton and two subsequent years of fantastic collaboration.

I also thank other important scientific mentors involved in the work presented in this dissertation. First, my committee members, John Harter and Vojtech Vlcek. Through his group theory course and subsequent discussions, John introduced many of the symmetry concepts that are essential to this work. Vojtech has provided a helpful sounding board for a variety of simulation questions over the years. Also, instrumental to this work has been the collaboration and mentorship of Michelle Johannes at the Naval Research Laboratory and Jennifer Cano at Flatiron Institute, who contributed greatly to my recent work.

Prior to UCSB, I was supported by the teaching, mentorship and encouragement of many devoted STEM educators from ages 11 to 23, among them: Todd Dvorak, Bailey Kellermann, Fernando Alonso, Nancy Lang, Lisa Joseph, Fei Yao, Clyfe Beckwith, Chaya Nanavati, Peter Graham, Tim Wiser, Keith Schwarz, Mark Cappelli, Young Lee, Ian Fisher and Yuri Suzuki. I thank my previous research mentors, Song Tan, Craig Levin, David Reis and Zhirong Huang, and their research groups for introducing me to academic research in a number of fields.

The students of the Seshadri and Wilson groups at UCSB made this work possible. Emily Levin, Josh Bocarsly and Doug Fabini provided significant help welcoming me to the group, getting me started on research projects, and providing feedback on my early work. I thank Leo Lamontagne and Brian Barraza for levity and singular devotion to Burrito Friday and Molleigh Preefer for helpful advice. To Joya Cooley, Emily Schueller, and Julia Zuo—I thank you for copious experimental assistance. Zach Porter offered bottomless patience when teaching me how to perform transport measurements. Kartik Pilar formed running club with me and put up with my shtick for two years. I thank Brenden Ortiz for research partnership, commiseration and memes sent thoroughout our last two years of collaboration. I also thank my four research interns, Pernilla Tanner, Mitchell Koerner, Sam Pettus and Ida Svenningsson, for their hard work and curiosity—you never understand a topic as fully as when you teach.

Work at the Materials Research Laboratory is supported by an incredible staff. I would particularly like to thank Fuzzy Rogers, Amanda Strom, Youli Li, Miguel Zepeda-

Rosales, Jess Henry, Julie Standish, Mary McGuan, Dotti Pak, and Sara Sorenson, who have each spent hours navigating me through problems ranging from scientific software installation to troubleshooting a PPMS cryogenic measurement system to championing me through the labyrinthine maze of UC bureaucracy.

I would like to thank my friends and classmates in the Materials department and MRL for making UCSB such a fun place to go to grad school. In particular, I thank my roommates from the Calle Koral Crew, Caroline Reilly, Peter McWilliams, Julia Zuo, Jonas Kaufman and Flynn Walsh, for making the last four years a blast and keeping me sane during quarantine.

Finally, I thank Jonathan Teicher and Celeste Kinginger, the most supportive parents imaginable. I love you guys.

Curriculum Vitæ
Samuel M. L. Teicher

Education

2017–	Ph.D. candidate in Materials, University of California, Santa Barbara.
2015-2016	M.S. Applied and Engineering Physics—Materials science concentration, Stanford University.
2011-2016	B.S. Engineering Physics—Computational science concentration, Stanford University.

Publications

19. S. M. L. Teicher, J. Linnartz, R. Singha, D. Pizzirani, S. Klemenz, S. Wiedmann, R. Seshadri, J. Cano, and L. M. Schoop. 3D analogs of square-net nodal line semimetals: band topology of cubic $LaIn_3$. *In preparation*.

18. Y. Luo†, S. Peng†, S. M. L. Teicher†, L. Huai†, Y. Hu, B. R. Ortiz, Z. Wei, J. Shen, Z. Ou, B. Wang, M. Guo, M. Shi, S. D. Wilson, and J.-F. He, Distinct band reconstructions in kagome superconductor CsV_3Sb_5, *arXiv preprint* (2021). arXiv:2106.01248

17. Y. Hu†, S. M. L. Teicher†, B. R. Ortiz†, Y. Luo, S. Peng, L. Huai, J. Z. Ma, N. C. Plumb, S. D. Wilson, J.-F. He, and M. Shi, Charge-order-assisted topological surface states and flat bands in the kagome superconductor CsV_3Sb_5, *arXiv preprint* (2021). arxiv:2104.12725

16. Y. Wang, S. Yang, P. K. Sivakumar, B. R. Ortiz, S. M. L. Teicher, H. Wu, A. K. Srivastava, C. Garg, D. Liu, S. S. P. Parkin, E. S. Toberer, T. McQueen, S. D. Wilson, M. N. Ali, Proximity-induced spin-triplet superconductivity and edge supercurrent in the topological kagome metal $K_{1-x}V_3Sb_5$, *arXiv preprint* (2020). arxiv:2012.05898

15. F. Kaboudvand†, S. M. L. Teicher†, S. D. Wilson, R. Seshadri, and M. D. Johannes, Fermi surface nesting and the Lindhard response function in the kagome superconductor CsV_3Sb_5. *Accepted*, Feb. 2022, *Appl. Phys. Lett.*

14. G. Pokharel†, S. M. L. Teicher†, B. R. Ortiz, P. M. Sarte, G. Wu, S. Peng, J. He, R. Seshadri, and S. D. Wilson, Study of the electronic properties of topological kagome metals YV_6Sn_6 and GdV_6Sn_6, *Phys. Rev.* B **104**, 235139 (2021). [doi]

13. B. R. Ortiz†, S. M. L. Teicher†, L. Kautzsch, P. M. Sarte, J. P. C. Ruff, R. Seshadri, and S. D. Wilson, Fermi surface mapping and the nature of charge density wave order in the kagome superconductor CsV_3Sb_5, *Phys. Rev.* X **11**, 041030 (2021). [doi]

12. H. Zhao, H. Li, B. R. Ortiz, S. M. L. Teicher, T. Park, M. Ye, Z. Wang, L. Balents, S. D Wilson, and I. Zeljkovic, Cascade of correlated electron states in a kagome superconductor $\mathrm{CsV_3Sb_5}$, *Nature* **599**, 216 (2021). [doi]
11. R. Singha, T. H. Salters, S. M. L. Teicher, S. Lei, J. F. Khoury, N. P. Ong, and L. M. Schoop, Evolving Devil's staircase magnetization from tunable charge density waves in nonsymmorphic Dirac semimetals, *Adv. Mater.* **33**, 2103476 (2021). [doi]
10. S. Lei, S. M. L. Teicher, A. Topp, K. Cai, J. Lin, F. Rodolakis, J. L. McChesney, M. Krivenkov, D. Marchenko, A. Varykhalov, C. R. Ast, R. Car, J. Cano, M. G. Vergniory, N. P. Ong, L. M. Schoop, Band engineering of Dirac semimetals using charge density waves, *Adv. Mater.* **33**, 2101591 (2021). [doi]
9. B. R. Ortiz, P. M. Sarte, E. Kenney, M. J. Graf, S. M. L. Teicher, R. Seshadri, and S. D. Wilson, Superconductivity in the $\mathbb{Z}_2$ kagome metal $\mathrm{KV_3Sb_5}$, *Phys. Rev. Mater.* **5**, 034801 (2021). [doi]
8. B. R. Ortiz, S. M. L. Teicher, Y. Hu, J. L. Zuo, P. M. Sarte, E. C. Schueller, M. Krogstad, S. Rosenkranz, R. Osborn, R. Seshadri, L. Balents, J. He, and S. D. Wilson, $\mathrm{CsV_3Sb_5}$: a $\mathbb{Z}_2$ topological kagome metal with a superconducting ground state, *Phys. Rev. Lett.* **125**, 247002 (2020). [doi]
7. K. E. Wyckoff, D. D. Robertson, M. B. Preefer, S. M. L. Teicher, J. Bienz, L. Kautzsch, T. E. Mates, S. H. Tolbert, and R. Seshadri, High capacity $\mathrm{Li^+}$ storage through multielectron redox in the fast-charging Wadsley—Roth phase $\mathrm{(W_{0.2}V_{0.8})_3O_7}$, *Chem. Mater.* **32**, 9415 (2020). [doi]
6. S. Wang, E. E. Morgan, P. Vishnoi, L. Mao, S. M. L. Teicher, G. Wu, Q. Liu, A. K. Cheetham, and R. Seshadri, Tunable luminescence in hybrid Cu(I) and Ag(I) iodides, *Inorg. Chem.* **59**, 15487 (2020). [doi]
5. S. Klemenz, A. K. Hay, S. M. L. Teicher, A. Topp, J. Cano, and L. M. Schoop, The role of delocalized chemical bonding in square-net-based topological semimetals, *J. Am. Chem. Soc.* **142**, 6350 (2020). [doi]
4. E. E. Morgan, L. Mao, S. M. L. Teicher, G. Wu, and R. Seshadri, Tunable perovskite-derived bismuth halides $\mathrm{Cs_3Bi_2(Cl_{1-x}I_x)_9}$, *Inorg. Chem.* **59**, 3387 (2020). [doi]
3. S. M. L. Teicher, I. K. Svenningsson, L. M. Schoop, and R. Seshadri, Weyl nodes and magnetostructural instability in antiperovskite $\mathrm{Mn_3ZnC}$, *APL Mater.* **7**, 121104 (2019). [doi]
2. L. Mao, S. M. L. Teicher, C. Stoumpos, R. Kennard, R. DeCrescent, G. Wu, J. Schuller, M. L. Chabinyc, A.K. Cheetham, and R Seshadri, Chemical and structural diversity of hybrid layered double perovskite halides, *J. Am. Chem. Soc.* **141**, 19099 (2019). [doi]
1. S. M. L. Teicher, L. K. Lamontagne, L. M. Schoop, and R. Seshadri, Fermi level Dirac crossings in the 4d and 5d cubic metal oxides $\mathrm{NaPd_3O_4}$ and $\mathrm{NaPt_3O_4}$, *Phys. Rev.* B **99**, 195148(1–8) (2019). [doi]

[†] indicates equal contribution

Abstract

Orbital design and electronic structure of topological metals

by

Samuel M. L. Teicher

Topological materials are an exciting new area of inquiry. These materials exhibit fundamentally new and nonlocal phenomena including spin-polarized surface states. More tantalizing is the prediction that an intrinsic topological superconductor could exhibit quasi-particles called Majorana anyons and provide the materials platform for building a quantum computer robust to many of the decoherence effects that plague competing quantum computation technologies. A scalable quantum computer would be able to solve many problems that are fundamentally intractable with current computing technologies and is hoped to provide a path towards understanding some of the most difficult contemporary physics questions such as the interaction of electrons in correlated systems.

While new topological materials—especially topological superconductors—are desired, design rules for predicting new topological metals are far from understood. Electronic materials discovery, especially in the laboratory, is largely driven by chemical understanding of the atomic bonding motifs in the crystalline structure that generate relevant electronic structure features. By modifying these motifs via chemical substitution and comparing with carefully constructed simulations, new topological materials are discovered and understood. Here, we present computational studies on five families of topological metals with varying functional properties, ranging from catalytic activity to complex magnetic ordering and superconductivity. In each study, emphasis is placed on the orbital origins of the predicted topological electronic structure.

The first part of the dissertation explores bonding interactions and electronic structure in three cubic metals: Na(Pd,Pt)$_3$O$_4$, Mn$_3$ZnC, and LaIn$_3$. Chapter 2 describes the bonding of palladium and platinum d orbitals with square-planar coordinating O p orbitals in NaPd$_3$O$_4$ and NaPt$_3$O$_4$. This unusual geometry generates an inversion of d$_{x^2-y^2}$ and d_{z^2} bands, yielding an exotic nodal cube state that is a higher-degeneracy analog of a Dirac semimetal. Spin-orbit coupling effects partially fragment this cube, with stronger fragmentation in the Pt containing compound. Chapter 3 follows the electronic structure progression of antiperovskite Mn$_3$ZnC, which transitions from a ferromagnetic room temperature phase to a distorted non-collinear magnetic structure at low temperatures. The electronic structure of this material can largely be understood in terms of Mn d bonding and magnetism. The ferromagnetic phase is shown to host topological Weyl nodes and surface states. The Weyl nodes are largely gapped and eliminated in the low temperature phase. The removal of Weyl nodes via structural distortion and antiferromagnetic ordering is likely common to a wider variety of Weyl metals. In chapter 4, the Fermi surface of auricupride LaIn$_3$ is simulated and compared to experimental quantum oscillation measurements. The electronic structure is explained in terms of a simple tight-binding model involving only In p orbital interactions with close similarity to prior work on the ZrSiS family of square-net semimetals. While further experimental verification is needed, an initial survey suggests that LaIn$_3$ hosts a wide variety of topological surface states.

The second part of the dissertation examines the electronic structure of three compounds, CsV$_3$Sb$_5$, GdV$_6$Sn$_6$, and YV$_6$Sn$_6$, in which the relevant electronic properties derive largely from the bonding of d orbitals on 2D kagome planes of vanadium atoms. Chapter 5 offers a careful comparison of simulation results to experimental X-ray diffraction and quantum oscillation measurements that track the charge density wave and electronic structure transitions that occur upon cooling crystals of CsV$_3$Sb$_5$. The charge density wave is shown to derive primarily from breathing-mode distortions of the vanadium kagome net, which are energetically favored in the DFT and qualitatively agree with the experimental structural solution and low frequency quantum oscillation signals. The predicted band reconstruction, combined with an earlier prediction of $\mathbb{Z}_2$ topological surface states in CsV_3Sb_5, suggest that surface states may be active at the Fermi level at the superconducting transition temperature, indicating that CsV_3Sb_5 is a promising intrinsic topological superconductor candidate. Chapter 6 details the synthesis of GdV_6Sn_6 and YV_6Sn_6 crystals, electronic structure predictions and initial comparison of the simulated electronic structure to experimental ARPES measurements. Like CsV_3Sb_5, these kagome metals are predicted to host $\mathbb{Z}_2$ topological surface states. The relevant electronic structure of these materials derives from V-V, V-Sn, and Sn-Sn bonding interactions. Substitution on the Gd/Y site provides additional magnetic tunability.

Contents

List of Figures

List of Tables

Chapter 1

Introduction

The goal of this dissertation is to provide tools and chemical intuition for predicting and synthesizing topological semimetals based on *ab initio* calculations. While first-principles methods have progressed greatly in recent decades, making density functional theory calculations widely accessible and ubiquitous in the world of materials discovery, these advancements have not always translated to laboratory-relevant knowledge. Ambitious recent works have made significant impact in the field of topological materials by systematically calculating and categorizing topological invariants for large databases of materials at once, relying on mathematical rigor *sans* chemistry.[1, 2, 3] However, simplified bonding models, long known to solid-state chemists and physicists, still provide crucial insight in experimental work. Knowledge of the orbitals and bonding interactions at play in a given compound provide immediate impact for the experimentalist:

1. does the electronic structure feature of interest arise from d-orbital bonding on the M site? If so, I may be able to make an atomic substitution to replace M with a similar element that has larger or smaller d orbitals, thereby carefully tuning the properties.

2. is the electronic structure strongly affected by spin-orbit coupling (SOC)? If so,

I may be able to substitute an atom in the same column of the periodic table in order to increase the SOC strength. (see Chapter 2)

3. is the electronic structure feature of interest above or below the Fermi level? If so, I may be able to add or remove electrons through substitution of an element in a nearby column of the periodic table. (see Chapter 4)
4. do I want to make my material magnetic? If so, I may be able to substitute an atom with an additional d or f electron on one of the electron donating sites. (see Chapter 6)

Moreover, the intuition associated with naïve chemical bonding models often proves surprisingly prophetic in explaining instabilities—even in complex metals. A number of quasi-2D topological semimetals undergo charge density wave (CDW) distortions, and an increasing number of semimetals have been found to exhibit antiferromagnetic orderings at low temperature (discussion of a magnetic antiperovskite semimetal which undergoes both structural and antiferromagnetic ordering at low temperature is provided in Chapter 3, while in-depth computations and experimental collaborations untangling the breathing-mode distortion in a kagome superconductor are offered in Chapter 5). These findings are not unsurprising to solid-state chemists, however, since they align with intuition formed by the simple Peierls chain bonding model.

With this goal in mind, presented here are careful computational studies on five families of semimetals with varying functional properties, ranging from catalytic activity to complex magnetic ordering and superconductivity. In each study, emphasis is placed on the orbital origins of the predicted topological electronic structure.

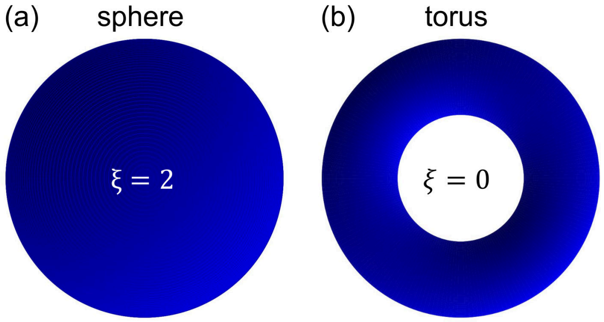

Figure 1.1: Real space topology. (a) a sphere has no holes and is categorized with an Euler characteristic, $\xi = 2$. (b) a torus or donut shape has a single hole and is categorized by a characteristic, $\xi = 0$.

1.1 Topology (in Real Space)

In mathematics, concepts of *topology* have long been used to describe the geometry of surfaces. One of the surprising findings in this field is that surfaces can be divided systematically into different classes based on their geometry. Fig. 1.1 displays two examples of 3D surfaces, (a) a sphere and (b) a torus. It isn't hard to see a practical difference between the two shapes—the torus has a hole in the middle. There is no way to continuously stretch the sphere into a torus or vice-versa, since conversion would require the formation or removal of a puncture hole. For real 3D surfaces, these findings are summarized through the Gauss-Bonnet theorem[4]:

$$\xi = \frac{1}{2\pi} \oint_S K dA \tag{1.1}$$

where K is the local Gaussian curvature, and $\int_S dA$ represents integration over the full surface area. ξ is known as the Euler characteristic and turns out to be a quantized property; ξ only adopts integer values. Integrating over the spherical surface of Fig. 1.1 (a), with a constant Gaussian curvature $K = 1/R^2$ we find $\xi = \frac{1}{2\pi}\frac{1}{R^2}\int_S dA = \frac{1}{2\pi R^2}(4\pi R^2) = 2$. It can be shown that a similar integration for the toroidal surface of Fig. 1.1 (b), yields $\xi = 0$.[5] Abbreviating further mathematical results, it turns out that these integrations are quite general: any surface without holes will have $\xi = 2$, any surface with one hole will have $\xi = 0$, any surface with two holes will have $\xi = -2$, etc. The Euler characteristic is a *topological invariant* characterizing the number of holes in a surface. Any two surfaces with the same ξ value can be continuously deformed into one another. A surface cannot be continuously deformed into another surface with a different Euler characteristic since this transformation would require puncturing the surface or removing holes.

This dissertation discusses topology in the context of the electronic properties of materials. While the dimensions may at first appear more abstract (energy-momentum space rather than real space), electronic structure topology is conceptually and mathematically similar, and categorizible in terms of topological invariants that are quantized to integer values.

1.2 Motivation

At its core, a chemical view of electronic structure topology is defined by an inversion of electronic states in a topological material with respect to an insulator. Air/vacuum are often the relevant insulator in experimental contexts, but inversion can also be defined across materials junctions, such as layered semiconductors or other heterostructures. Topological inversion is visualized schematically in Fig. 1.2. In an insulator (e.g., glass, semiconductors, air), (a), there is a gap in the energy spectrum. Electrons fill up and completely occupy a band of states called the *valence band*. A higher energy *conduction band* is unfilled, and separated from the valence band by the band gap (in reality, small numbers of electrons are thermally excited into the conduction band, but we are assuming very low temperatures for the moment). In order to conduct current, electrons must be excited from the valence band to a higher energy state in the conduc-

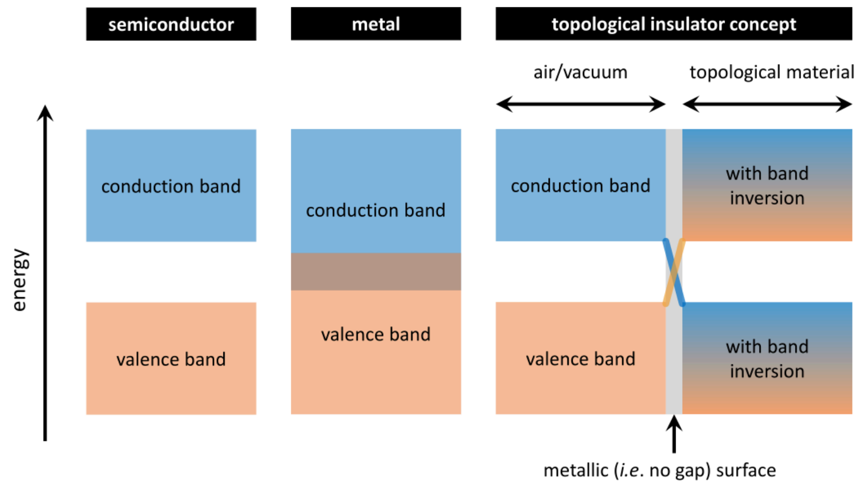

Figure 1.2: A chemical view of topology. **Semiconductor**: a semiconductor or insulator has a complete band gap in the energy spectrum. **Metal**: a metal has no band gap and no clear energy separation between conduction and valence bands. **Topological insulator concept**: in a topological insulator, valence states are 'inverted,' mixing into the conduction band and conduction states similarly mix into the valence band. This guarantees that surface bands will appear at the interface with air/vacuum—in which there is no band inversion.

tion band. In a metal, (b), by contrast, there is no gap and no well-defined separation between valence and conduction states. Instead, the electrons occupy the states up to a given energy level, referred to as the Fermi level, or Fermi energy, E_F. With even small energetic excitations, electrons can access a continuum of states immediately above E_F. For this reason, electrons tend to be more mobile in metals, yielding the high metallic electrical conductivity familiar in household wiring and electronics. Topological materials are distinct from either metals or insulators. Topological insulators (TIs), the first experimentally verified topological materials, share properties of both insulators and metals—they are insulators in the bulk, but exhibit metallic electronic conductivity on their surface. The topological insulator concept is demonstrated in (c). Here, there is mixing of the valence states (orange) into the conduction band (blue) and vice-versa. This band mixing is referred to as *inversion*, since the valence and conduction states on either side of the bandgap are inverted with respect to their usual positions. As a

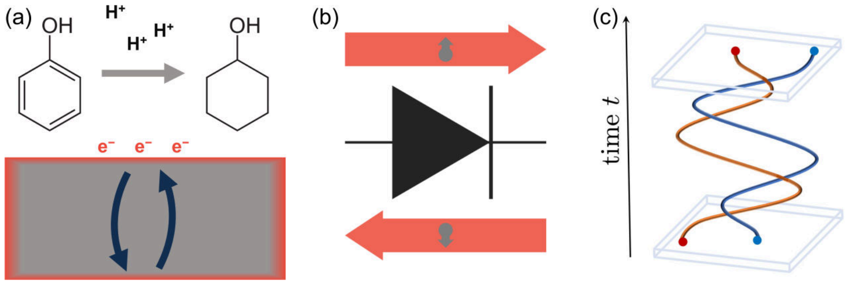

Figure 1.3: Schematics of potential applications for topological materials. (a) enhanced bulk transport and large surface state electron populations may generate good catalysts. (b) spin-momentum-locked surface states allow for selective spin transport—a necessity for spin diodes. (c) topological surface states may provide a path towards realizing majorana anyons, proposed quasi-particles that can store information in their relative position, which could be 'braided' by moving around each other.

result, continuity requires that the conduction and valence states cross at the interface between a TI and a normal insulator. The band crossing closes the band gap, but only on the surface of the material, guaranteeing metallic surface conductivity while preserving a bulk band gap. In a real material, the conduction and valence bands derive from different orbital states (e.g. s vs. p, or bonding/antibonding pairs like p_π,p_π^*), and band inversion can be described as an inversion of the orbital energies. In many cases, the surface states are potentially more interesting than conventional metallic bands: spin-orbit coupling (SOC) is often strong on the surface of a material, and can separate electrons into states with opposite magnetic spin. Electrons with a given spin (conventionally, 'up') move in the opposite direction from electrons with opposing spin ('down'), this phenomenon is known as *spin-momentum locking*.[6, 7]

These unusual properties enable a number of exciting applications for topological materials. Three applications are presented in schematic in Fig 1.3. A conventional property, perhaps overlooked in current literature, is that many of these materials are good electronic conductors, either on the surface, as in TIs, or in both the bulk and on the surface as in the topological semimetals to be discussed in depth in this dissertation. Good electronic conductivity is a key property for conventional electronic devices, such as computers and cellphones, and is also essential to newer renewable technologies for energy conversion, storage, and transport. Many known TI materials have been explored for thermoelectric energy conversion, owing largely to their high electrical conductivity with respect to other bandgap materials.[8, 9] Topological semimetals are proposed for catalysis applications due to their high bulk and surface conductivity and, often, surface state electron population.[10, 11] Semimetals have proven efficient catalysts for the hydrogen evolution reaction,[10, 12, 13, 14, 15] as well as oxygen evolution[16]. $NaPt_3O_4$, a semimetal which is discussed in Chapter 2, is known to be an effective catalyst for hydrogenation reactions. Fig. 1.3 (a) presents a cartoon of bulk and surface electron transport in a semimetal catalyst, depicting a hydrogenation reaction.

In addition to improving conventional technologies, topological materials provide tantalizing possibilities for new quantum technologies. Spin-momentum-locking provides the possibility of building a spin diode, in which electrons with opposite spin move in opposite directions and the relative conduction of the two spin populations could be controlled and switched (see schematic in Fig. 1.3 (b)).[17, 18, 19] Spin diodes are a key step in the field of spintronics, which aims to build computing devices in which spin currents are transported rather than electrical currents; a potentially low-power-use computing solution. Finally, a current holy grail is the use of topological materials to realize theoretically-predicted quasi-particles known as Majorana anyons. Theorists predict that by coupling spin-momentum locked surface states and superconductivity—either by producing layered devices with interfaces between topological materials and superconductors, or by discovering a single bulk material that is intrinsically both topological and superconducting—Majorana anyons can be realized on the surface of a real material.[20] While a rigorous theoretical discussion of anyons is beyond the scope of this introduction, a simple central concept is the question of what occurs when two particles exchange positions. Exchange is often summarized with a simple equation in introductory physics textbooks.[1] Suppose we have two particles with positions $\{x_1, x_2\}$. Quantum mechanics dictates that the system must be described by a wavefunction, $\psi(x_1, x_2)$ with a probability distribution $|\psi(x_1, x_2)|^2$. The particles we experience in everyday life are indistinguishable–all electrons are functionally identical. We therefore know that the probability distribution cannot change when the positions of the particles are swapped:

$$|\psi(x_1, x_2)|^2 = |\psi(x_2, x_1)|^2$$

meaning, in turn, that the exhange can be described with a simple phase factor, θ:

$$\psi(x_1, x_2) = e^{i\theta}\psi(x_2, x_1)$$

Assuming that swapping particles twice ($x_1 \to x_2 \to x_1$ and vice-versa) brings us back to the original state, we find that θ can only take on values $\{0, \pi\}$. These are the cases for bosons (e.g., photons) and fermions (e.g., electrons), respectively. All particles you experience in everyday life are either bosons or fermions. But this assumption about double swapping doesn't apply to anyons: anyons are theoretical particles that have *any phase factor,* $theta$*, other than* 0 *or* π. For this reason, it is proposed that anyons can store information in the phase factor associated with their relative positions, and that information can be stored and transferred by physically exchanging the positions of anyons over time, a process called *braiding*. Anyon braiding is visualized in Fig. 1.3 (c). Braiding presents an opportunity to store information nonlocally, providing protection against decoherence. A major challenge in current quantum computing de-

---

[1] See D. J. Griffiths, *Introduction to Quantum Mechanics, 2nd Ed.*, Prentice Hall (Upper Saddle River, N.J.): 1995, Chapter 5.

signs is that quantum states are often not robust; local perturbations, such as a lattice vibration in a crystal or incoming light (photons), can interact with and destroy the desired state. Due to the nonlocal storage of information in the braiding design, topological materials are proposed to provide a platform for quantum computers robust to local decoherence.[21] Heterostructure devices using a number of different superconductor/topological material/semiconductor combinations are under active investigation.[22][2]

Only a small number of intrinsic topological superconductor materials have been proposed thus far, among them iron-based superconductors,[23] doped variants of the topological insulator $\mathrm{Bi_2(Se_{1-x}Te_x)_3}$,[24] and doped topological crystalline insulators in the SnTe family[25]. Chapter 5 discusses initial calculations and accompanying experimental collaborations suggesting that the recently-discovered kagome metals $A\mathrm{V_3Sb_5}$ (A = K,Cs,Rb) may provide a new family of intrinsic topological superconductors. While these metals are not immediately relevant to devices since they must be cooled to a temperature on the order of 10 K before superconductivity manifests, these kagome metals present the possibility of new physics discoveries—the mechanism of the superconductivity and its relationship with proposed topological surface states, initially predicted in the work presented here, are far from fully explored. In chapter 4, new calculations are presented which suggest that the electronic structure of the $\mathrm{LaIn_3}$ family of metals, long known for superconductivity, feature bulk band inversion and likely host topological surface states at experimentally-relevant energies near E_F—these materials also show promise as intrinsic topological superconductor candidates.

---

[2] It is important to note here that topological protection resulting from bulk band inversion is not strictly necessary in heterostructure designs, since spin orbit coupling can induce spin-momentum locked surface states even in normal semiconductors with appropriate electron doping. A great deal of current effort pursues device stacks including conventional III-V semiconductors, such as InGaAs, layered with metallic superconductors. InGaAs is not a bulk topological insulator.

1.3 Berry curvature and the Chern invariant

The brief discussion of Majorana anyons in the previous section highlights the importance of the wavefunction phase in quantum systems. In many treatments of quantum mechanics, phase is largely neglected. After all, most observable quantities depend on the probability distribution of possible states, which is given by the modulus squared of the wavefunction:

$$|\psi|^2 = \psi^*\psi$$

as such, an arbitrary phase factor can always be added to the wavefunction, $\psi' = e^{i\theta}\psi$ without any change to the relevant modulus:

$$|\psi'|^2 = (\psi')^*(\psi') = e^{-i\theta}\psi^* e^{i\theta}\psi = \psi^*\psi$$

this phase choice is sometimes referred to as a reference gauge. While the wavefunction phase itself is arbitrary and gauge dependent, certain properties associated with the phase are *gauge invariant* and associated with real physical observables. One such quantity is the phase accumulated over a closed, circuitous path, a concept popularized by Sir Michael Berry now commonly referred to as the *Berry phase*.[26] We can quickly show that this quantity is gauge invariant. Any closed path can be decomposed into a set of states, $|u_1\rangle, |u_2\rangle, \ldots, |u_{N-1}\rangle$, such that the path evaluation around the loop is given by:

$$\langle u_1|u_2\rangle \langle u_2|u_3\rangle \cdots \langle u_{N-1}|u_1\rangle$$

since any wavefunction can be divided into an amplitude, A, and phase, θ, such that $\psi = Ae^{i\theta}$, the Berry phase, γ, can then be defined such that:

$$\gamma = -\mathrm{Im}\ln[\langle u_1|u_2\rangle \langle u_2|u_3\rangle \cdots \langle u_{N-1}|u_1\rangle]$$

suppose now that we change to an arbitrary gauge that adds phase factors to each state $|u_j\rangle$ such that $|u_{j,g}\rangle = e^{i\theta_j}|u_j\rangle$:

$$\gamma_g = -\text{Im}\ln[\langle u_{1,g}|u_{2,g}\rangle\langle u_{2,g}|u_{3,g}\rangle\cdots\langle u_{N-1,g}|u_{1,g}\rangle]$$

$$= -\text{Im}\ln[e^{-i\theta_1}\langle u_1|u_2\rangle e^{i\theta_2}e^{-i\theta_2}\langle u_2|u_3\rangle\cdots\langle u_{N-1}|u_1\rangle e^{i\theta_1}]$$

$$= -\text{Im}\ln[\langle u_1|u_2\rangle\langle u_2|u_3\rangle\cdots\langle u_{N-1}|u_1\rangle]$$

since the additional phase factors all cancel, the Berry phase is unchanged by the gauge transformation. The Berry phase can also be defined in an integral formulation for a path along a parameter, λ[27]:

$$\gamma = \oint_P A(\lambda)\cdot d\lambda$$

where $A(\delta) = \langle u_\lambda|i\partial_\lambda u_\lambda\rangle$ is a quantity known as the *Berry connection* or Berry potential. Via Stokes theorem, we can relate this path integral to an equivalent integral over the enclosed area of the loop: $\gamma = \oint_P A\cdot d\lambda = \int_S \nabla\times A\cdot dS = \int_S \Omega\cdot dS$ were dS is an infinitesimal element of the surface area, S, and $\Omega = \nabla\times A$ is known as the *Berry curvature*. It can be further shown that the Berry curvature of a fully enclosed surface is quantized according to the Chern theorem[27]:

$$2\pi C = \oint_S \Omega\cdot dS$$

where C is a topological invariant known as a Chern number. This formula is almost identical to the Gauss-Bonnet theorem described in equation 1.1 with the Berry curvature analogous to the Gaussian curvature and the Chern number in analog to the Euler characteristic. However, unlike the previous discussion of geometric invariants, the key consideration in evaluating the Chern number is usually the change of the wavefunction $\psi(\lambda)$ within the parameter space rather than the geometry of the space itself. In this discussion, the choice of parameter λ has been intentionally left vague. Berry phase has proven to be a useful general concept for describing wavefunction evolution in a number of subject areas including optics (conical diffraction), magnetic measurements (Aharonov-Bohm effect), and electronic structure (topological materials), with the λ parameter space of interest differing in each case.[28] A more complete derivation of the Chern theorem and other Berry phase quantities is given by Vanderbilt.[27]

While several different types of topological materials are described in this dissertation, in all cases topology arises from nontrivial Berry curvature and associated invariants. Here, the relevant parameter space is $\lambda = k$ where k is the crystal momentum. After motivating the origins of electronic band structure and the meaning of k in the next section, the electronic Chern invariant formula will be provided explicitly.

1.4 Orbital origins of band structure

An important first step in describing the orbital origins of topological electronic structure and band inversion is to provide some brief intuition as to the orbital origins of electronic states (bands) in extended solids, and the meaning of the momentum, k. A more complete treatment can be found in Refs. [29, 30]. We assume a periodic crystal in which atoms are evenly spaced in a chain. In individual atoms, electrons occupy individual spherical harmonics, including s-orbitals, which are perfectly spherically symmetric, p-orbitals, which have dumbbell-like shapes, and d and f orbitals, which have more complex structures with multiple lobes. Given any combination of orbitals χ_n on sites n, the wavefunction of the entire chain can be written as a linear

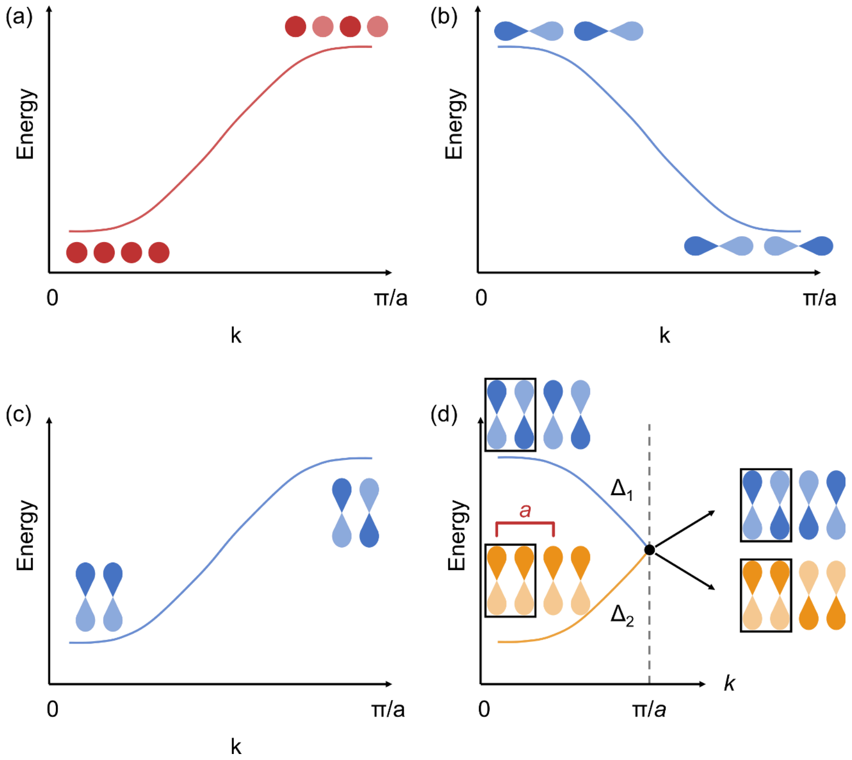

Figure 1.4: Orbital origins of electron bands. (a) an s-orbital band. (b) a p-orbital σ-bonding band. (c) a p-orbital π-bonding band. (d) when two orbitals are present in the unit cell, two bands are present, p_π and antibonding p_π^*. These bands have orthogonal wavefunctions and therefore cross without interacting. An alternative labeling for bands with orthogonal symmetry is to say that they have different irreducible representations, here denoted arbitrarily as Δ_1, Δ_2.

combination of the individual orbitals:

$$\psi_k = \sum_n e^{ikna}\chi_n \tag{1.2}$$

where a is the lattice constant separating the orbitals. Depending on the value of k, more or fewer of the orbitals have positive or negative wavefunction contributions. For $k = 0$, ψ_k is just the linear combination of the individual orbitals, yielding positive wavefunction contributions on every site. For $k = \pi/a$, the sign of the wavefunction switches between every adjacent site. The range of possible k values is infinite, but the range we must consider is quite limited. Similar to the real-space periodicity of the atoms, the wavefunction is periodic in k. We need only consider the range $-\pi/a \leq k \leq \pi/a$, since the states in this range can represent any possible value of k. This limited range is referred to as the Brillouin zone. Band structures are typically depicted as energy versus k plots within the Brillouin zone. With this knowledge, we can begin to plot simple bands. From the perspective of an introductory chemistry course we know that antibonding interactions tend to be less energetically favorable than bonds. Similarly, from introductory quantum mechanics examples such as the particle-in-a-box, we know that excited states of a system tend to have more nodes (sign-reversals) than the ground state. We therefore know that the $k = 0$ state for an s-orbital chain, which is purely bonding, will be more energetically favorable than the $k = \pi/a$ state at the edge of the Brillouin zone, which has purely antibonding interactions between all adjacent orbitals. We can draw a band like that in Fig. 1.4 (a). In (b), we see two p-orbitals aligned end to end in a σ bonding configuration. For this configuration, the band dispersion is opposite to s orbitals. For $k = 0$, all adjacent interactions are antibonding and for $k = \pi/a$ all interactions are bonding. Using similar arguments, we can show that p π-bonding bands, arranged as in (c), run upwards with k like s orbital bonding.

These simple models contain much of the intuition necessary to understand topological semimetals. Suppose now that we have two p π bonding atoms per unitcell, as depicted in Fig. 1.4 (d). We now find two possibilities for our unit cell: the p orbital pair can be either bonding (blue) or antibonding (orange). At $k = 0$, the bonding band is heavily energetically favored since all interactions are bonding, similarly, the antibonding band is much higher in energy since all interactions are antibonding. At $k = \pi/a$, both bands have the exact same energy; in both cases, half of the interactions are bonding and half antibonding. The bands cross at this point at the edge of the Brillouin zone. Two bands can only cross like this if they have orthogonal symmetry. In band structure literature, this is often abstracted with the comment that the two bands have different *irreducible representations* (irreps) with respect to the local point group (in this case, the point group at $k = \pi/a$). In this simple scenario, however, the rationale for band crossing is easily visualized: the antibonding band always has a node (sign reversal) at the center of each unit cell while the bonding band does not. The wavefunction overlap between the bonding and antibonding states will therefore be zero, and no interaction can occur between bands. In practice, irreps are a convenient and rigorous labelling scheme to determine which bands can cross and which bands will interact and form band gaps. Thanks to modern codes, irreps can be conveniently calculated and plotted as shown in schematic here.[31] Since the irreps are different (here, arbitrarily labeled Δ_1, Δ_2), the bands are guaranteed to cross with no interaction and band gapping. Even in larger crystals with more complex symmetry, the explanation for this irrep notation continues to be simple: bands with different irreps have orthogonal wavefunctions at a given k-point.

Simple bonding models also provide intuition as to the origins of symmetry-breaking distortions in crystalline solids. One of the simplest models is the Peierls distortion,[32]

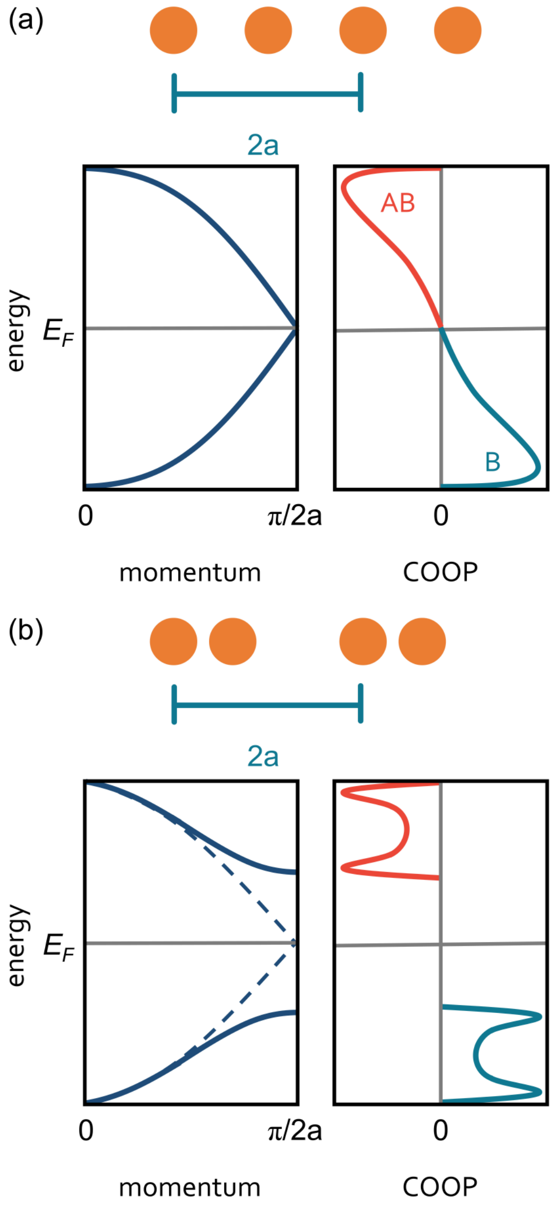

Figure 1.5: Peierls distortion schematic. (a) An undistorted chain of s-orbitals, with a crystal unit cell containing two orbitals, has a semimetal band structure in which the bonding states (teal) are fully-filled, the antibonding states (pink) are completely empty, and the bonding and antibonding bands meet at a single linear band crossing point. (b) a symmetry-breaking lattice distortion can create a band gap which separates the bonding and antibonding states, stabilizing the structure by lowering the energy of the occupied bonding states.

which alternates bond lengths in a 1D chain of s orbitals. The Peierls chain model is presented in Fig 1.5. In (a), we see a simple chain of s orbitals in which the unit cell contains two orbitals. The bonding arrangement is similar to the p π bonding of Fig. 1.4 (c), with separation between bonding and antibonding states and a band crossing at the end of the Brillouin zone. In (b), we see in schematic what can occur if the atoms break symmetry by alternating bond short and long bonds: bonding states move down in energy, antibonding states move up in energy, and the distortion is stabilized since the filled bonding states have lowered in energy below the original E_F. In addition to the band structure $E-k$ diagram, included are schematics of the crystal orbital overlap population (COOP), popularized by Roald Hoffmann and colleagues.[29, 33] COOP and related tools provide a semi-quantitative description of bond strength based on wavefunction overlap. Consider two crystal sites occupied by orbitals χ_1,χ_2. The total wavefunction of an electron in this material can be written: $\psi = c_1\chi_1 + c_2\chi_2$. The electron probability density is then given by[29]:

$$\begin{aligned}
1 &= \int |\psi|^2 d\tau \\
&= \int |c_1\chi_1 + c_2\chi_2|^2 d\tau \\
&= c_1^2 + c_2^2 + 2c_1c_2 \int (\chi_1^*\chi_2 + \chi_2^*\chi_1) d\tau
\end{aligned}$$

where $d\tau$ represents a volume integration over real space. The final integral represents a site wavefunction overlap which is positive for bonding and negative for antibonding interactions. Neglecting full formalism here in the name of brevity, COOP shares the intuitive property that negative values represent antibonding contributions and positive values represent bonding contributions. Significant work has pursued developing the Crystal Orbital Hamilton Population or COHP, an analog of COOP that

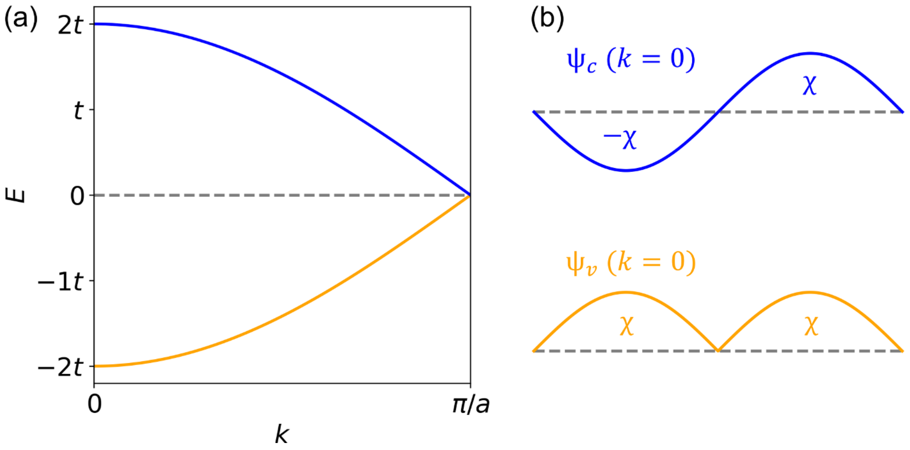

Figure 1.6: 1D diatomic tight-binding model. The band structure is shown in (a) for the ideal semimetal case, $\varepsilon_A = \varepsilon_B$. (b) presents a schematic visualizing the local wavefunction of a single unit-cell for $k = 0$. Here, it can be seen that the valence band (orange) and conduction band (blue) correspond to symmetric, bonding and antisymmetric, antibonding states, respectively.

can be determined from standard, plane-wave *ab-initio* calculations, which is leveraged significantly in the following chapters as a semi-quantitative estimate of bond strength.[33, 34, 35, 36] More rigorous discussion of the equations used to calculate COHP is offered in Appendix B.

1.5 Tight-binding formulation of the 1D diatomic chain

The linear combination of atomic orbitals (LCAO) method presented in the previous section is equivalent to a tight-binding formalism that may be more familiar to physicists. The simple Peierls chain model of Fig. 1.5 can be recreated with a linear chain tight binding model with two orbitals in the basis, and an alternating pattern of orbitals: $\cdots \phi_{n-1,A}$—$\phi_{n-1,B}$—$\phi_{n,A}$—$\phi_{n,B}$—$\phi_{n+1,A}$—$\phi_{n+1,B} \cdots$, etc. Letting $\varepsilon_A \equiv \langle \phi_{i,A} | \hat{H} | \phi_{i,A} \rangle$ and $\varepsilon_B \equiv \langle \phi_{i,B} | \hat{H} | \phi_{i,B} \rangle$ be the onsite energies of the orbitals $\phi_{i,A}$ and $\phi_{i,B}$, respectively, and $-t \equiv \langle \phi_{i,A} | \hat{H} | \phi_{i+1,B} \rangle$ be the hopping energy between sites, the Schrödinger equation can be written:

$$\hat{H}\psi = E\psi$$

and, expanding into matrix form:

$$\begin{bmatrix} \ddots & & & & \mathbf{0} \\ & \varepsilon_B & -t & & \\ & -t & \varepsilon_A & -t & \\ & & -t & \varepsilon_B & \\ \mathbf{0} & & & & \ddots \end{bmatrix} \begin{bmatrix} \vdots \\ \phi_{n,B} \\ \phi_{n,A} \\ \phi_{n-1,B} \\ \vdots \end{bmatrix} = E \begin{bmatrix} \vdots \\ \phi_{n,B} \\ \phi_{n,A} \\ \phi_{n-1,B} \\ \vdots \end{bmatrix}$$

which gives us the equations:

$$\varepsilon_A \phi_{n,A} - t(\phi_{n,B} + \phi_{n-1,B}) = E\phi_{n,A}$$

$$\varepsilon_B \phi_{n,B} - t(\phi_{n,A} + \phi_{n+1,A}) = E\phi_{n,B}$$

Following the LCAO notation previously provided in equation 1.2 we can write out the wavefunctions in the form $\phi_{n,A} = \chi_A e^{ikna}$ and substitute, yielding:

$$\varepsilon_A \chi_A - t\chi_B(1 + e^{-ika}) = E\chi_A$$

$$\varepsilon_B \chi_B - t\chi_A(1 + e^{ika}) = E\chi_B$$

We can then rewrite in the simpler matrix form:

$$\begin{bmatrix} \varepsilon_A & -t(1 + e^{-ika}) \\ -t(1 + e^{ika}) & \varepsilon_B \end{bmatrix} \begin{bmatrix} \chi_A \\ \chi_B \end{bmatrix} = E \begin{bmatrix} \chi_A \\ \chi_B \end{bmatrix}$$

Which can be solved to give the eigenenergies:

$$E_\pm = \frac{(\varepsilon_A + \varepsilon_B) \pm \sqrt{(\varepsilon_A - \varepsilon_B) + 8t^2(1 + \cos(ka))}}{2}$$

As previously motivated, the semimetal phase corresponds to the case of a uniform bonding chain. Here, this means the case in which $\varepsilon_A = \varepsilon_B$, with eigenvalues:

$$E_\pm = \pm t\sqrt{2(1 + \cos(ka))}$$

and corresponding eigenvectors:

$$v = \begin{bmatrix} \mp\frac{\sqrt{1+e^{-ika}}}{\sqrt{1+e^{ika}}}\chi_A \\ \chi_B \end{bmatrix}$$

where we have chosen to set $\varepsilon_A = \varepsilon_B = 0$ for convenience. This band dispersion is visualized in Fig. 1.6 (a). Analyzing the eigenvalues in the limit $k \to 0$, we find that the lower energy band corresponds to a symmetric bonding state with $v = [\chi_A, \chi_B]$ while the higher energy band corresponds to an antibonding state with $v = [-\chi_A, \chi_B]$. These state are visualized in schematic in Fig. 1.6 (b) assuming that χ_A and χ_B have a sinusoidal shape. These symmetric and antisymmetric wavefunctions are similar to the orbital model depicted in Fig. 1.4 (d). The band crossing is symmetrically allowed in this toy model due to the orthogonality of the bonding valence band and antibonding conduction band wavefunctions.

While simple, section 1.7 will demonstrate that this tight-binding model provides much of the intuition necessary to understand a model semimetal, graphene.

1.6 Topology in k space

In order to define topological invariants like those of section 1.3 for the electronic band structure of a material, we can define the Berry phase of a single band, n, integrated along a path in k space:

$$\gamma_n = \oint_C A_n(k) \cdot dk$$

and $A_n(k) = \langle u_{nk} | i\partial_k u_{nk} \rangle$. However, most systems have more than one filled band. It can be shown that the total Berry connection for a system can be given as the sum[27]:

$$A_{tot}(k) = \sum_{n=1}^{N} \langle u_{nk} | i\partial_k u_{nk} \rangle$$

with similar definitions of the total Berry phase and Berry connection:

$$\gamma_{tot} = \oint_C A_{tot}(k) \cdot dk = \int_S \Omega_{tot}(k) \cdot dS$$

We can therefore calculate the Berry phase and associated topological invariants for the electronic bands of a crystal calculated in k-space. Like the geometric topological invariants of section 1.1, these band structure topological invariants are unchanged by smooth, adiabatic changes of the system. A non-adiabatic change of the system that can change the topological invariant is the swapping of two bands near the Fermi level, i.e. a band inversion, which is analogous to the effect of puncturing a hole in a 3D surface on the Euler characteristic. When the electronic structure of a material is said to be topologically-protected, this means that a band inversion would be required to remove the topology.

1.7 Graphene as model semimetal

We now examine the simplified bonding models of the proceeding sections applied to a real material: graphene. Graphene is a good choice of focus for both pedagogical and historical reasons. The bonding in graphene is indeed fairly simple, and graphene, while not a topological semimetal itself, has had a major impact on the field of topological materials. Three dimensional semimetals are often thought of as 3D analogs of graphene.[37, 30] Considerable interest and subsequent research following both the Nobel prize work of Geim and Novoselov on graphene (2010)[38, 39] and Haldane, Kosterlitz and Thouless on topological invariants (2016),[40, 41] has contributed to the development of the current research field of topological semimetals.

Fig. 1.7 presents a summary of the bonding and electronic structure of graphene. In (a), we see that, due to the hexagonal lattice of carbon atoms, graphene has two atoms present in the unit cell. Since carbon only has occupied s and p orbitals, we need only consider orbitals that are linear combinations of s and p. The bonding in graphene is qualitatively well-described by sp^2 in-plane bonding, which is σ-like, and p_z out-of-plane bonds, which are π-like. Each carbon atom contributes 4 electrons, completely filling the sp^2 states and the p_z bonding band, but leaving the p_z antibonding band unoccupied. The result is very similar to the linear π-bonding chain of Fig 1.4 (d) and the 1D diatomic chain of section 1.5. Using simulation, we can visualize the charge density. In (b,c), we find that the charge density at the edge of the Brillouin zone indeed has a similar structure, separated into symmetric bonding and antisymmetric antibonding states. In (d), we find that this connection extends to the band structure: graphene also features a band crossing at the edge of the Brillouin zone (K) at the Fermi level. More formally than this analysis of the charge density, orthogonality of the bonding and antibonding band wavefunctions can also be shown in terms of the band

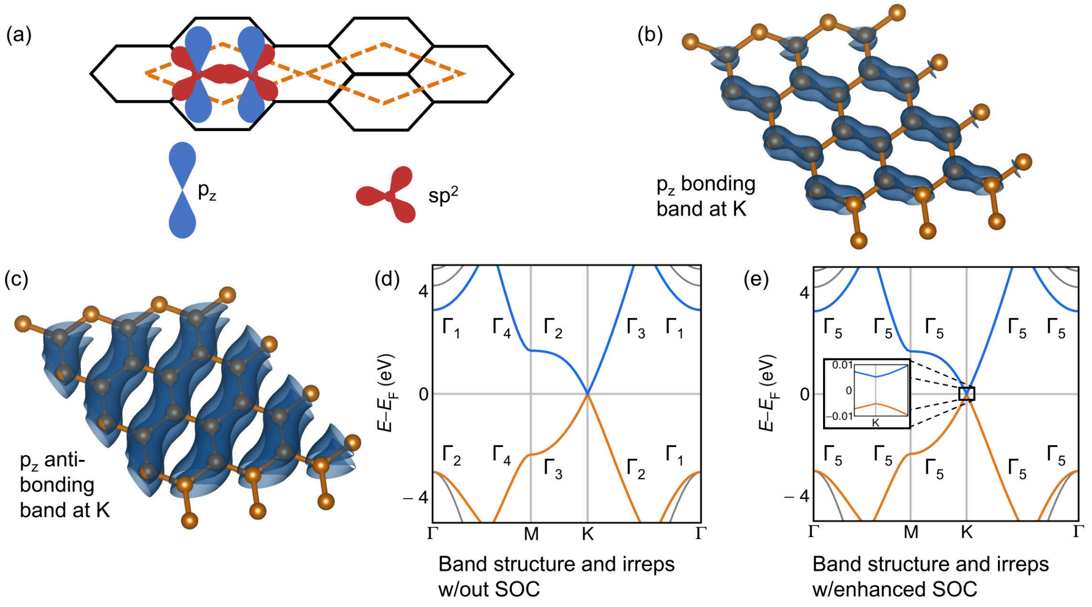

Band structure and irreps w/out SOC

Band structure and irreps w/enhanced SOC

Figure 1.7: Graphene bonding and band structure. (a) the graphene unit cell contains two carbon sites, which are occupied by sp^2 and p_z orbitals. (b,c) Using DFT simulations, we can visualize the p_z π bonding and antibonding states at the edge of the Brillouin zone, the K point. We find that the π bonding states (b) include local bonding pairs, and the antibonding states (c) have nodes in the center of these pairs. (d) band structure and irreps in the absence of spin-orbit coupling: there is a linear band crossing (Dirac node) at K. (e) band structure with artificially increased spin-orbit coupling (100×). When considering spin symmetry, both bands share the same irrep (Γ_5) and there is now mixing and a small band gap at K. Partial charge density contours are visualized at 0.027 $e/\text{Å}^3$.

C_{2v}	E	$\overline{E}$	C_2	σ_v	σ_v'
Γ_1	1	1	1	1	1
Γ_2	1	1	-1	1	-1
Γ_3	1	1	1	-1	-1
Γ_4	1	1	-1	-1	1
Γ_5	2	2	0	0	0

Table 1.1: Character table for the C_{2v} point group. This table employs the notation from [42]. There are 4 non-spinor irreps, Γ_1-Γ_4, and only one spinor irrep Γ_5.

irreps with respect to the point group along the M-K and K-Γ lines (C_{2v}): the bonding band has irrep Γ_2, while the antibonding band a different irrep, Γ_1.[42]

Linear bands crossings like these are special, and contribute to the relatively high electron mobility in many semimetals. In many materials, such as most semiconductors, the $E-k$ dispersion is well-described by a parabolic model: $E \propto k^2$. In semimetals like graphene, the dispersion is linear near the Fermi level: $E \propto k$. This has a corresponding result on the effective mass of the electron: theoretically, in materials with linear band dispersion, the electron is effectively massless. This is result is intimately related to the masslessness of photons, which also have a linear dispersion relationship ($\omega = ck$) due to the relativistically-defined constant speed of light, c.

This is not the full story, however, at least on the theory side. All electrons in extended solids experience relativistic effects, *spin-orbit coupling* (SOC), that scale with the atomic mass of the element they orbit. The carbon atoms of graphene are fairly light such that these effects are unimportant and invisible in the calculations shown so far. However, we can artificially increase the strength of SOC in the calculations by 100×, as shown in Fig. 1.7 (e), with the finding that a small band gap opens right at the Fermi level. We had previously shown that the band crossing at the K is avoided due to orthogonal wavefunctions and the correspondingly different irreps of the p_z π and π^* bands, so why is a band gap allowed to form when SOC is increased? SOC allows mixing between electron states with opposite spin, and spin symmetry becomes important when SOC is significant. Formally, we must consider only spinor irreps for large SOC systems. Table 1.1 presents the character table for the C_{2v} point group. Rather than focusing on the particulars of the symmetry operations embodied by each irrep (C_2 is a rotation around the z-axis, for example), what's important to notice is that there are four available non-spinor irreps, conventionally placed in the first block, Γ_1-Γ_4, whereas there is only one available spinor irrep in the second block, Γ_5. Because the Γ-M, M-K, and K-Γ lines all have C_{2v} symmetry in the hexagonal Brillouin zone, all bands must have the Γ_5 spinor irrep, meaning that no bands in Graphene-like materials can cross without gapping when SOC is strong. In general, the spin-mixing introduced by SOC tends to reduce the number of available irreps; therefore often resulting in the formation of local band gaps.

While the particulars of SOC gapping are unimportant for real graphene, SOC-gapped graphene-like lattices are model topological materials, with bulk band inversion resulting in surface bands crossing the SOC-gap. A good deal of early work on electronic structure topology focused on the Haldane model, which describes a 2D hexagonal system gapped by SOC.[43] SOC gapping and the irrep notation introduced here is essential to understanding the electronic structure of the materials discussed in the following chapters, since these materials feature elements with significantly greater atomic mass than carbon.

1.8 Recent progress in topological materials

This section provides brief coverage of recent developments in the field of topological materials and the progression from interest in topology in fully-gapped materials analogous to the topological insulator concept previously presented in Fig. 1.2 to more

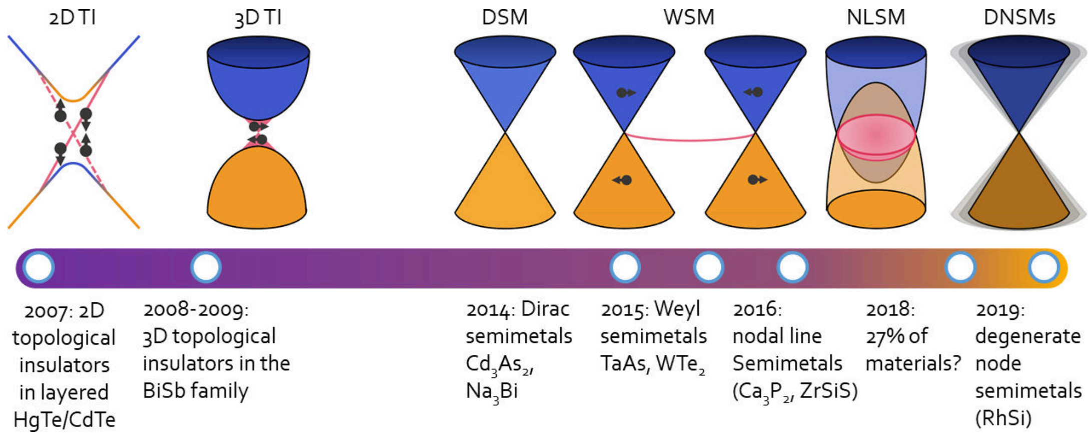

Figure 1.8: Timeline of recently discovered topological materials. Adapted from [30].

recent work on topological metals. All of the materials discussed in the body of this dissertation are bulk metals. A timeline is provided as a chronological guide in Fig. 1.8.

1.8.1 Topological insulators and the Z_2 invariant

The first experimentally verified topological materials were topological insulators with a bulk band gap. Aided by intuition from previous work on graphene,[44] Bernevig, Hughes and Zhang predicted a band-gapped topological phase in HgTe/CdTe quantum wells[45], which feature band gapping due to strong SOC. In 2D layered systems, surface states manifest along the edges of the layered device stack. This prediction was soon verified via transport measurements in 2007, with quantized Hall conductance indicating the presence of surface states.[46] The topological insulator concept was then extended to 3D crystals by Moore and Balents[47]. Fu and Kane predicted a 3D topological insulator phase in $Bi_{1-x}Sb_x$ alloys.[48] Single crystals of a 3D topological insulator exhibit surface states on *all the crystalline facets*, rather than just a 2D layer. The electronic structure of $Bi_{1-x}Sb_x$ was examined via angle-resolved photoemission spectroscopy in 2008, directly confirming the proposed band inversion and surface states.[49] Topological insulator phases were soon verified in a number of bis-

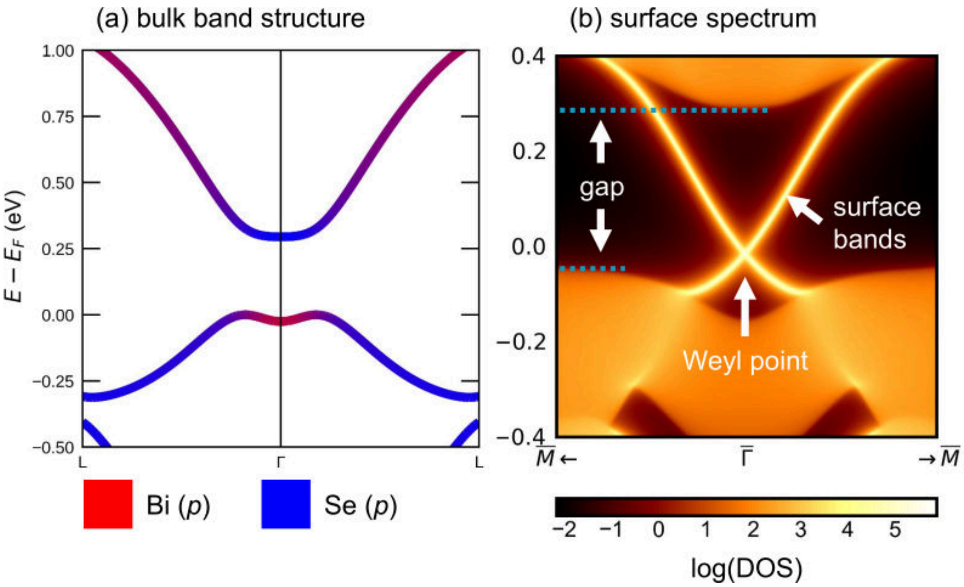

Figure 1.9: Simulated electronic structure of the topological insulator Bi_2Se_3. (a) presents the bulk band structure, which features an orbital inversion between Bi and Se p states. (b) surface spectrum with bright surface bands crossing the band gap. These surface states cross at $\overline{\Gamma}$, generating a Weyl node.

muth compounds, including $Bi_2(Se,Te)_3$.[50, 51, 52] Fig. 1.9 presents the simulated electronic structure of Bi_2Se_3, which is a prototypical example of how band inversion and topological surface states manifest in a real material. In (a), we find that the band gap of Bi_2Se_3 features a bulk band inversion between states with primary Bi p and Se p contributions. The result of this band inversion is demonstrated in (b): two spin-polarized surface bands with opposite E-k slope traverse the gap. The crossing of the surface states forms a characteristic conical shape, a Weyl cone.[3] In addition to predicting these new candidate materials, Fu and Kane also demonstrated that topological classification is particularly simple in inversion-symmetric, time-reversal invariant

---

[3] There are two conventions in the literature for naming the surface state band crossings. In earlier work, this crossing is usually referred to as a Dirac node. However, in later studies, especially after the advent of a significant body of work on Dirac and Weyl semimetals, authors often refer to the singly-degenerate band-crossings on the surface of crystals as Weyl nodes to distinguish them from bulk Dirac nodes, which are always doubly degenerate. I will use the latter convention. This discrepancy is somewhat silly; a topological insulator features mirrored copies of each surface band crossing on opposite faces of the crystal, meaning that the total band structure is effectively doubly degenerate.

(non-magnetic) materials. Under these conditions, topology can be conveniently computationally determined in terms of a $\mathbb{Z}_2$ invariant that can be determined as a product of the parity eigenvalues of the occupied bands in a system at several time reversal invariant momentum (TRIM) points in k space.[48] The parity product formula is:

$$(-1)^{\nu} = \prod_i \delta_i$$

where:

$$\delta_i = \prod_{m=1}^{N} P(\Gamma_i^m)$$

where N is number of occupied bands below the band gap (divided by two for spin-degeneracy), P is the parity operator, and Γ_i^m indicates the irrep of band m at TRIM point i. The 8 relevant TRIM points are $k = [n_1\frac{\pi}{a}, n_2\frac{\pi}{b}, n_3\frac{\pi}{c}]$ where (a,b,c) are the lattice parameters and (n_1,n_2,n_3) are equal to either 0 or 1. If the resulting product yields $\nu = 1$, and there is a complete gap between bands N and $N + 1$, the band gap is nontrivial and surface states are guaranteed. Note that this definition does not actually require that the material be a semiconductor. The $\mathbb{Z}_2$ invariant is also well-defined in metals under the condition that two consecutive bands do not cross.

1.8.2 Dirac and Weyl semimetals

In subsequent years, interest developed in extending the graphene band structure in 3D materials. The characteristic band dispersion around the K point in graphene forms a cone with linear dispersion (Fig. 1.7). This band dispersion can be described as a solution of the Dirac equation, originally developed by Paul Dirac.[53] The range of 3D materials with band structure similar to graphene have therefore been dubbed *Dirac semimetals*. Early experimental observations of Dirac semimetal phases were reported for Cd_3As_2[54, 55, 56] and Na_3Bi[57, 58] in 2014. While not explicitly topological materials in isolation, Dirac semimetals often exhibit unusually high bulk electronic mobility due to their linear band dispersion.

Transitions between Dirac semimetal and topological phases are common. Like early toy models of graphene, spin-orbit coupling can band gap Dirac phases in heavy-atom metals, yielding a $\mathbb{Z}_2$ topological insulator. However, another type of topological transition is available that can be experimentally simpler than chemical doping. The unusual predicted transport properties of singly-spin degenerate band crossings were discussed as early as 1983[59]. In the case that spin-symmetry is broken, the electronic structure is described by a Weyl Hamiltonian rather than a Dirac Hamiltonian. Early work by Weyl demonstrated a key difference: Weyl nodes are chiral, unlike Dirac nodes.[60] The net result is that Weyl nodes always form in pairs and that pairs of Weyl nodes with opposite chirality are connected by spin-polarized surface states, known as Fermi-arcs. Spin-symmetry breaking can be achieved by simply applying a magnetic field to a Dirac material. Alternatively, there are semimetal materials with intrinsic spin-symmetry breaking wherein Weyl physics always applies; these systems are known as *Weyl semimetals*. Among the first experimental studies on Weyl semimetals were studies performed on the TaAs[61, 62, 63, 64] and WTe_2[65, 66, 67] families in 2015.

In addition to high electron mobility,[55, 68] semimetal materials host a wide variety of interesting transport properties including large magnetoresistance and anomalous hall effect,[69, 18, 70], quantized circular photogalvanic effect,[71, 72, 73], and unusual quantum oscillations that appear to derive from surface states[74, 75]. An important note is that many known semimetal materials have imperfect Dirac or Weyl band structures: in addition to linearly dispersing Dirac and Weyl band crossings near the Fermi level, the electronic structures of these materials also contain conventional parabolic metal bands. For this reason the word semimetal is often a misnomer: rather than a being graphene-like, with a vanishingly-small density of states at E_F, most Weyl and Dirac candidate materials have a large number of states at the Fermi level, and are therefore better classified simply as metals. Practically speaking, semimetal transport properties and surface states can still be observed in many materials despite the presence of interfering metallic bands.

1.8.3 Nodal line semimetals

Although the Dirac bands in graphene cross at isolated points, forming cones in E vs. k space, extended band crossings are possible. Work in 2016 demonstrated that when additional symmetries such as mirror planes are present, extended nodal lines of Dirac or Weyl crossings can be stabilized. Materials exhibiting nodal lines are known as *nodal line semimetals*. One important early proposal was for a nearly ideal nodal circle in Ca_3P_2.[76] In such a mirror-protected system, shown in schematic in Fig. 1.8, surface states are predicted that connect between all the nodes on the loop. Surface states of this type are known as drumhead surface states. Unfortunately, Ca_3P_2 is fairly chemically unstable. In the years since, many additional promising nodal line materials have been discovered, among them the ZrSiS family of square-net semimetals[77, 78, 79].

While many nodal lines are predicted in high-symmetry metals, nodal lines are not usually robust to spin-orbit coupling. Few nodal materials with atoms as light as those of Ca_3P_2 have been predicted. For this reason spin-orbit coupling usually plays an important role in gapping nodal lines and most experimentally realized nodal lines are imperfect. A finding of the work presented in this dissertation is that nodal lines may be quite common in high-symmetry metals. All materials in the following chapters feature nodal lines in simulation when SOC is neglected.

1.8.4 High-throughput searches

How common are topological metals? While our understanding of topological metals is still expanding, high-throughput computational studies shed some light on this question. In 2018, three computational studies examined large databases of known materials and performed automated simulations attempting to classify all the materials with topological electronic structure features near the Fermi level.[1, 2, 3] While there is reason to doubt the accuracy of high-throughput calculations (the band gap problem and treatment of correlations, to be discussed, are key culprits), the result was stunning: up to 27% of known non-magnetic materials may be functionally topological. In future, topological electronic structure may be viewed not as a rarity, but a common feature of metals and small-bandgap semiconductors.

1.8.5 Degenerate Node Semimetals

In recent years, there has been increasing discussion of materials in which multiple band crossings are degenerate at the same point in k-space, including systematic theoretical predictions.[80, 81] In these materials multiple overlapping Dirac cones can appear at once. I will refer to these materials as degenerate node semimetals. In addition to stronger semimetal transport properties, it has been proposed that multiply-degenerate Weyl nodes can be detected via multiply-quantized circular photogalvanic effect. This effect was recently measured in candidate degenerate node semimetal RhSi.[73, 72, 82]

1.9 Brief discussion of computational techniques

1.9.1 *ab initio* computational methods

Our understanding of the electronic structure of materials has been immensely improved over the past 70 years by the development of computationally efficient, widely accessible and increasingly accurate simulations. Much of this success is built on density functional theory (DFT).

The history of quantum mechanical theory largely centers around success in shifting from classical models in which particles have definite positions and momenta to wavefunction models described by the Schrödinger equation,

$$\hat{H}\psi(\mathbf{r}) = E\psi(\mathbf{r}) \tag{1.3}$$

provided here in the time-independent form where $\hat{H}$ is the Hamiltonian, E is the system energy, and ψ is the wavefunction, which can depend on position, $\mathbf{r}$. While ψ itself is not a physical observable, Born demonstrated that the modulus squared of this quantity, $|\psi|^2$, can be interpreted as a probability density.[83] For example, the modulus square of a single electron wavefunction represents the probability of finding the electron in a given state. While complete, equation 1.3 does not provide immediate insight as to how one actually solves for the wavefunction in a real material. Assuming a system of electrons in a material, we can expand to write the Schrödinger equation as[84]:

$$\left[\frac{\hbar}{2m}\sum_{i=1}^{N}\nabla_i^2 + \sum_{i=1}^{N}\sum_{j<i}U(\mathbf{r}_i,\mathbf{r}_i) + \sum_{i=1}^{N}V_{ext}(\mathbf{r}_i)\right]\psi(\mathbf{r}) = E\psi(\mathbf{r}) \tag{1.4}$$

where m is the electron mass and there are N electrons in the system. The first bracketed term represents the kinetic energy of the electrons, the second bracketed term the energy associated with interaction between electrons and the final bracketed term the interaction of electrons with an external potential. In most materials, movement of atoms is many orders of magnitude slower than that of the electrons that surround them and form bonds between them. For this reason, quantum mechanical simulations of materials usually make the Born-Oppenheimer assumption[85]—that atomic nuclei have static, fixed positions—and focus on simulating the electrons and their response to the atomic potentials. Equation 1.4 makes use of the Born-Oppenheimer approximation by including the ionic potentials associated with atomic nuclei as part of the potentials, $V(\mathbf{r}_i)$, and neglecting explicit treatment of the nuclear wavefunctions. A practical concern with equation 1.4 is that computational limitations prevent a full treatment of electron interactions. Modeling even solitary atoms with three or more electrons is still an area of active development due to the difficulty in directly computing many-body interactions.

Hohenberg and Kohn proved two famous theorems that laid the groundwork for modern density functional theory approaches to solving the Schrödinger equation.[86] A functional is a function that takes another function as input. Hohenberg and Kohn proved important properties of the functional $E[n(\mathbf{r})]$, which takes an electron density, $n(\mathbf{r})$, as input in order to calculate an associated energy, E. The H-K theorems can be stated as the following[87]:

1. For any system of interacting particles in an external potential, $V_{ext}(\mathbf{r})$, the potential is determined uniquely[4] by the ground state electron density, $n_0(\mathbf{r})$.

2. There exists a universal functional for the energy, $E[n(\mathbf{r})]$, that is valid for any choice of external potential. For any given choice of $V_{ext}(\mathbf{r})$, the global minimum of this functional is the ground state energy and the electron density that mini-

---

[4] Up to a free constant determined by gauge choice.

mizes this functional, $n_0(\mathbf{r})$, is the ground state electron density.

As a result of the first theorem, we know that the Hamiltonian of a system is uniquely determined by $n_0(\mathbf{r})$. In principle then, all properties of a material (including ground **and** excited states) are determined given the ground state electron density. The second theorem tells us that knowledge of the functional $E[n]$ and external potential $V_{ext}(\mathbf{r})$ is sufficient to determine the ground state of a system (but not excited states). In the case of materials simulation, a primary contribution to the external potential is the periodic potential due to the atomic lattice of nuclei. Given a material with known crystalline structure and associated periodic potential, choice of the correct functional would allow precise determination of the ground state properties. Unfortunately, though the H-K theorems tell us that an exact energy functional must exist, we do not know the true functional.

While Hohenberg and Kohn provided a theoretical framework for density functional methods, the H-K theorems themselves do not provide immediate insight into how one can simplify the many-body problem of inter-electron interactions into a computationally tractable form. Kohn and Sham introduced the ansatz that a material can be modeled with completely independent electrons and that the effect of electron interaction and correlation can be accounted for by an exchange-correlation functional, $E_{xc}[n(r)]$.[88] The Kohn-Sham equation for the ground state energy functional can be written[87]:

$$E_{KS} = T_s[n] + \int d\mathbf{r} V_{ext}(\mathbf{r}) n(\mathbf{r}) + E_H[n] + E_{II} + E_{xc}[n] \tag{1.5}$$

where $T_s[n]$ represents the kinetic energy contribution, E_H is the so-called Hartree energy associated with coulomb interactions between the electron and surrounding charge density,

$$E_H[n] = \frac{1}{2}\int d^3r d^3r' \frac{n(\mathbf{r})n(\mathbf{r}')}{\mathbf{r}-\mathbf{r}'} \tag{1.6}$$

V_{ext} is the external potential experienced by the electrons due to the atomic nuclei as well as any applied fields and E_{II} represents the inter-ionic interaction. Given the correct choice of exchange-correlation functional, the ground state of a system can then be determined by minimizing the Kohn-Sham energy. While we don't know the exact exchange-correlation functional, one of the reasons that the Kohn-Sham ansatz works in practice is that electron correlations are screened in many materials: in compounds with large electron density, especially metals, the electron system is well described by the assumption that each electron mainly interacts with the total potential of the remaining electrons rather than with each other electron individually.[5] Significant research effort continues to pursue increasingly accurate choices of $E_{xc}[n]$.

Another important assumption made in order to reduce computational cost in most modern DFT codes is that core electrons are well-localized, not contributing significantly to chemical bonding, and can be approximated as part of the external potential, $V_{ext}(\mathbf{r})$. This assumption allows the simulation of only the valence electron wavefunctions, while approximating the contributions of core electrons as pseudopotentials[89] or PAW potentials[90] localized on the atomic sites.

Given the prior discussion, we can highlight both technical and fundamental challenges associated with the Kohn-Sham DFT calculations employed in this dissertation.

Two practical issues are limitations on the system size and accuracy of approximate choices of $E_{xc}[n]$. Despite incredible advancements in computing hardware and algorithmic efficiency, systems with hundreds or thousands of atoms are not currently

---

[5] The result of electron screening is that the effective coulomb potential can have an exponential attenuation: $V(r) = \frac{q}{r}\exp(-K_s r)$, where K_s is a screening constant. See Chapter 14 of Kittel, C., Introduction to Solid State Physics, 8th Ed. Wiley (New York): 2005, Chapter 14.

computationally tractable for most DFT users. DFT is usually most accurate in describing crystalline solids, which are well approximated by a small (periodic) unit cell with a small number of atoms. System size is an important constraint in topological materials because confinement effects usually mean that the surface electronic structure is only well converged with a large simulation cell, often 10s or even 100s of unit cells in length. As a result, current work on topological materials relies heavily on tight binding models. The work in this dissertation employs the popular strategy of fitting empirical tight binding models by post-processing DFT results with the WANNIER90[91] code. Tight binding models can be extended to large simulation cells at a fraction of the computational cost and can greatly speed up k-space interpolation of electronic properties. While the tight-binding strategy has achieved significant success in current topological materials literature and is successfully employed in the work contained in this dissertation, it is important to note that the atomic termination on the surface of a material—largely ignored herein—can be quite important to surface electronic properties.

Our inexact knowledge of $E_{xc}[n]$ can make it quite difficult to accurately simulate materials with strong electron correlations based on Kohn-Sham DFT. Standard 'workhorse' functionals such as the local density approximation (LDA)[92, 93] and generalized gradient approximation (GGA)[94] methods employed here often fail spectacularly when simulating strongly-correlated systems. This is a particular challenge for work on topological superconductors since the superconducting phase itself, which involves strong interactions such as Cooper-pairing of electrons, cannot be simulated with standard DFT methods. In practice, however, DFT can provide useful information about the electronic properties in the metallic phase of a material that has a low temperature superconducting transition. Extensive DFT calculations are employed in this dissertation in order to understand the metallic phases of superconducting metals

$LaIn_3$ and CsV_3Sb_5.

A fundamental issue is the treatment of thermal properties and excited states. Even with knowledge of the exact functional, $E_{xc}[n]$, the H-K theorems only guarantee an exact solution for the ground state properties of a material at 0 K. While progress has been made in modeling thermal transport via phonon calculations and adjusting for temperature effects via thermodynamic sampling, simulating excited states is a very present challenge.[6]

Both fundamental and technical issues both contribute to inaccuracy in the prediction of electronic band gaps using standard DFT methods, which is a particular challenge for the field of topological materials since accurate prediction of band inversion is necessary in order to correctly classify the topology in a material. The experimentally measured band gap of a material is the energy taken to excite an electron from an initial state in the highest occupied state of the valence band to the lowest unoccupied state in the conduction band. Thus, the DFT band gap is typically calculated by calculating the (Kohn-Sham approximated) ground state configuration and determining separation between the highest energy eigenvalue in the valence band and the lowest energy eigenvalue of the conduction band. However, it can be shown that even an exact Kohn-Sham density functional theory solution will not give an exact band gap using this method. In addition to the fundamental limitations on the treatment of excited states in general, the Kohn-Sham DFT band gap is known to be subject to error arising from *derivative discontinuity*.[96] This issue can be rationalized by examining the form

---

[6] While excited states are out of the scope of Hohenberg-Kohn DFT, an analogous time-dependent formulation (TDDFT) has been developed on the Runge-Gross theorem,[95] that can, in principle, determine excited states as a unique functional of the density assuming the exact functional is known. TDDFT methods are not employed here.

of the potential, V_{xc} associated with the exchange correlation functional[87]:

$$V_{xc}(\mathbf{r}) = \varepsilon_{xc}([n],\mathbf{r}) + n(\mathbf{r})\frac{\delta\varepsilon_{xc}([n],\mathbf{r})}{\delta n(\mathbf{r})} \tag{1.7}$$

where $\varepsilon_{xc}([n],\mathbf{r})$ is defined such that $E_{xc}[n] = \int d\mathbf{r} n(\mathbf{r})\varepsilon_{xc}([n],\mathbf{r})$. The final derivative term is discontinuous in an insulator, meaning that adding or exciting a single electron should change the Kohn Sham potential for the entire system. Despite this fundamental error, an engineering rationale for estimating band structure and band gaps with Kohn-Sham eigenstates nonetheless is that many approximate choices of $E_{xc}[n]$ have been optimized to achieve accurate band gaps, with reasonable quantitative success. However, a practical limitation is that many of the known functionals with good band gap performance are very computationally costly.

Band gap and correlation errors result in frequent DFT-based predictions of band topology in materials that are in reality insulators with no band inversion. This issue is particularly present in high throughput searches, wherein computationally inexpensive Kohn-Sham functional choices are favored. Correlation error is at play in the incorrect classification of the classic Mott insulator material NiO in the Topological Quantum Chemistry Database, where it is predicted to be a metal based on a paramagnetic calculation.[97, 1, 98, 99, 100] In the following, I present an archetypical example of band gap underestimation in PdO.

Band gap underestimation in electron-precise PdO

Palladium oxide adopts the crystal structure shown in Fig. 1.10 (a). The palladium atoms form square-planar units with coordinating oxygen atoms on the corners. The full structure is formed out of corner-connected square planes. The electronic structure is well described by a ML_4 square planar crystal field splitting model (b) in which

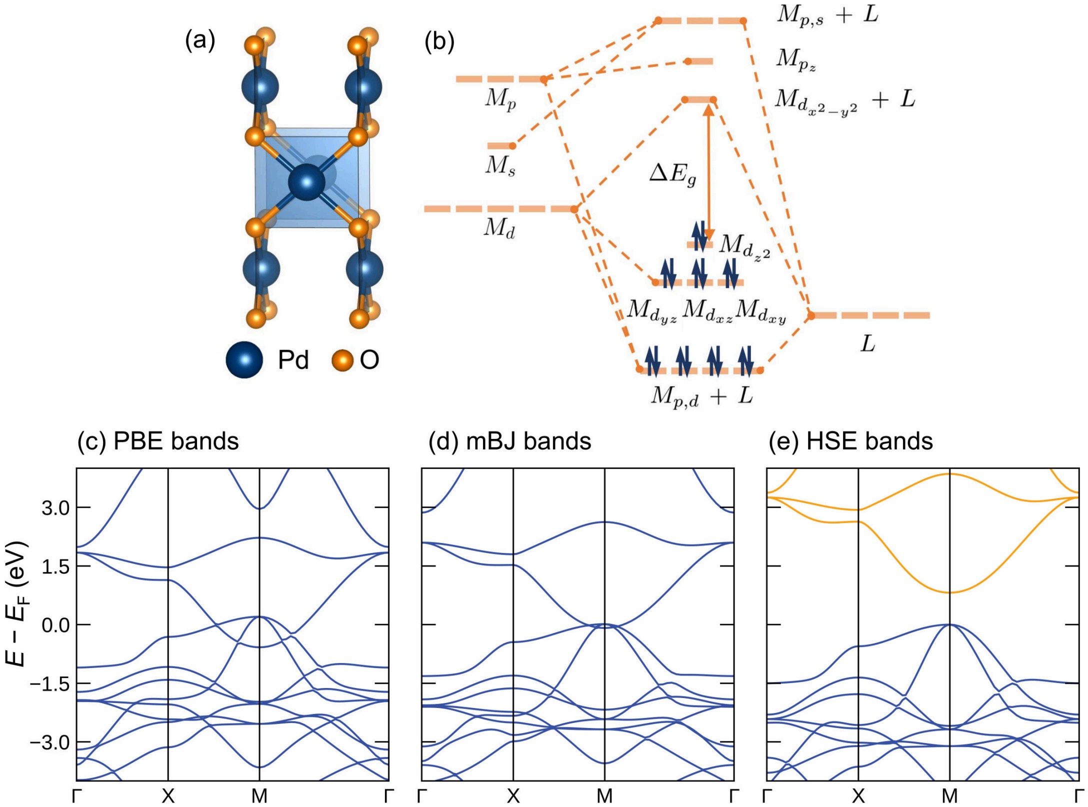

Figure 1.10: Crystalline and electronic structure of PdO. (a) The crystal structure of PdO is composed of Pd-O square planar bonding units connected at the corners. (b) The main features of the electronic structure can be explained via square-planar ligand field splitting. Electrons fill up to the top of the d_{z^2} band, leaving an insulator with band gap ΔE_g. (c,d,e) simulations with increasingly computationally intensive functional choices (PBE $<$ mBJ $<$ HSE), see increasing separation between the d_{z^2} and $d_{x^2+y^2}$ bands. Only the HSE functional correctly predicts an insulator.

palladium metal (M) donates two elections to ligand oxygen (L), which has a strongly favored oxidation state of O^{2-}. The $Pd^{2+}O^{2-}$ system has a total of 16 valence electrons. The first eight electrons bond with oxygen in $M_{p,d} + L$ states, leaving eight electrons in palladium d states. Of these d states, the in-plane $M_{d_{x^2-y^2}}$ states are highest in energy due to strong antibonding interaction with oxygen. The electrons therefore fill up to the top of the $M_{d_{z^2}}$ band, leaving a semiconductor with band gap ΔE_g.

While the electronic structure of PdO may be intuitive to a chemist, DFT calculations regularly predict this semiconductor to be a metal. Palladium oxide is representative of a general issue with contemporary density functional theory simulations: DFT tends to underestimate band gaps. Fig. 1.10 (c,d,e) present calculations completed with increasingly computationally-intensive functional choices, the Perdew-Burke-Ernzerhof (PBE),[94] modified Becke-Johnson (mBJ),[101] and Heyd-Scuseria-Ernzerhof (HSE)[102] functionals. The PBE functional greatly underestimates the band gap, predicting a metal with significant overlap between the $d_{x^2+y^2}$ conduction band and the d_{z^2} valence band. There is some improvement with the mBJ functional, but PdO is still incorrectly predicted to be a metal. The HSE functional correctly predicts that PdO is a semiconductor, and has been previously shown to yield results approximately consistent with experiment.[103] In operation, the mBJ and HSE functionals combat band gap error by incorporating the wavefunction, in addition to the electron density, as input (differing from the pure density functional formulation provided in the previous section). mBJ incorporates the wavefunction to make a kinetic energy correction while HSE mixes standard DFT (which tends to underestimate band gaps) and more intensive Hartree-Fock calculations (which tend to overestimate band gaps).

The semiconductivity of palladium oxide has been well-documented since at least the 1970s when Rogers and coworkers demonstrated single crystal vapor transport and transport measurements[7].[104] Despite this, all three of the major 2018 high-throughput topological materials classification efforts mentioned previously incorrectly classify PdO. Based on PBE calculations, Ref [3] and (at time of writing) the Topological Quantum Chemistry Database[1, 98, 99, 105] classify PdO as a 'high symmetry point semimetal' and nodal line semimetal, respectively. Ref. [2] employs the mBJ functional in an attempt to avoid band gap underestimation, producing a band structure similar to Fig. 1.10 (d). Based on this flawed calculation, Tang *et al.* highlight PdO as a particularly promising semimetal candidate for applications.

Palladium oxide serves as a cautionary tale about the limitations of high-throughput DFT studies. Any system like PdO that is electron-precise, with easily-assignable whole number oxidation states that can lead to a band gap between states associated with different electron shells, warrants further examination. Additional details on similar crystal field models and their comparison to electronic structure simulations can be found in Ref. [29]. Chapter 2 discusses the electronic structure of $NaPd_3O_4$ and $NaPt_3O_4$, which have a close structural relationship with PdO, but are metals due to the fact that they are not electron-precise.

1.10 Brief discussion of experimental methods

As described in the previous section, despite the success of first principles methods, computational predictions of electronic structure fail to accurately recreate experimental reality in a wide variety of materials. Theoreticians studying new electronic materials therefore devote significant time and effort comparing electronic structure models to experimental results in order to improve simulations and determine which *ab initio*

---

[7] I have independently repeated the $PdCl_2$ growth technique reported by Rogers *et al.* As discussed in their work, PdO crystals have a noticeable green patina, which is also consistent with the existence of a band gap.

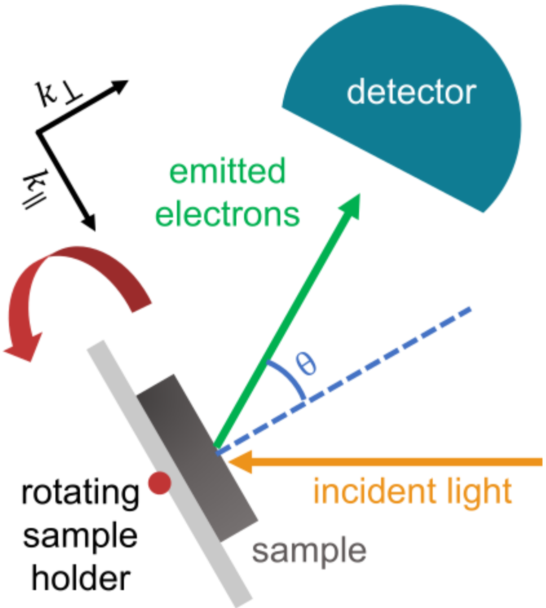

Figure 1.11: ARPES schematic. Angle resolved photoemission spectroscopy (ARPES) involves photoemission of electrons that are excited by incident light. These electrons are then sensed by a detector, which records energy information. By rotating the angle of the detector with respect to the sample normal, information about the in-plane momentum, $k_\parallel$ can be gained. Extracting full momentum information, including the sample-normal momentum $k_\perp$, is more complex and often involves careful variation of the incident photon energy.

predictions are trustworthy. Careful comparison to experimental results is particularly crucial in the field of topological semimetals since topology can depend on subtle band inversion. This section briefly discusses the experimental methods used to study the band structure and Fermi surfaces in the following chapters. Details involved in comparing these experimental data to electronic structure calculations are emphasized.

1.10.1 Experimentally determining band structure *via* angle-resolved photoemission spectroscopy

In order to experimentally reconstruct the band structure of a material, a technique is needed that collects data about both the energy, E, and momentum, k, of the electrons. Angle resolved photoemission spectroscopy (ARPES) fulfills these requirements. An ARPES experiment is depicted in schematic in Fig. 1.11. Electrons are excited by incident light and ejected from the material. Photoemitted electrons are sensed by a detector that records their energies. From this recorded kinetic energy, the band energy of the electron in the material relative to the Fermi level can be extracted:

$$E_{band} = h\nu - E_{kin} + \Phi$$

where $h\nu$ is the incident photon energy and Φ is the work function. ARPES analysis typically assumes the *sudden approximation*—that the electron escapes the region in which it was excited fast enough that it does not have time to interact with the local charge density (photo-hole). Under this assumption, the band energies detected by ARPES can be interpreted as peaks of the single particle spectral function. Under the further assumption of weak electron correlation, the energy of peaks in the ARPES spectrum, E_{band}, can be interpreted as the energy of an individual electron band and profitably compared to a calculated density functional theory band structure.[8]

By varying the angle of the detector with respect to the surface normal and examining the variation of the detected electron energies, the momentum of electrons on the plane parallel to the surface of the material, $k_{\|}$, can be extracted. Since kinetic energy is defined to be $\frac{p^2}{2m}$, where p is the total momentum, and the crystal momentum, k, is defined such that $p = \hbar k$, the total crystal momentum is $k = \frac{1}{\hbar}\sqrt{2mE_k}$. Because the in-plane symmetry is unbroken on the surface of a crystalline material, the momentum component parallel to the surface is preserved and can be determined from the detector

---

[8] In practice, observed spectral peaks often have a tail related to correlated quasi-particle excitations even in ‘normal’ metals without particularly strong correlation. These tails are not recreated by DFT eigenvalue band structures like those calculated in this thesis.

angle, θ, and the kinetic energy, E_{kin}[106]:

$$k_{\parallel} = \frac{1}{\hbar}\sqrt{2mE_{kin}}\sin\theta$$

Combining these two elements, the E vs. $k_{\parallel}$ band structure of the material can be reconstructed. An element is still missing, however. The band structure also varies with the momentum perpendicular to the sample surface, $k_{\perp}$. While the momentum perpendicular to the surface is not preserved, an analytical expression can still be derived with additional assumptions. Often, it is assumed that the final state of the photoexcited electrons during detection is an ideal free electron state (a better assumption for higher photon energies). In this case, the perpendicular momentum component can be shown to be[106]:

$$k_{\perp} = \frac{1}{\hbar}\sqrt{2m(E_{kin}\cos^2\theta + V_0)}$$

Here, V_0 is an unknown energy known as the inner potential. A convenient experimental tuning knob for determining $k_{\perp}$ is the incident photon energy, which changes E_{kin} and allows a fitting of the periodic change of $k_{\perp}$ and assignment of V_0.

The experimental reality is more complex than the cartoon of Fig. 1.11. A few salient details warrant discussion. First, multiple light sources are available for photoemission experiments including lasers and X-ray synchrotrons. Incident light is often polarized. Higher energy light sources have longer attenuation length of photons into the sample and can offer better $k_{\perp}$ resolution. In general, attentuation lengths are short and ARPES usually probes the surface electronic structure, which may be different than the bulk electronic bands. ARPES requires high-quality crystalline samples with clean surfaces. In order to generate a pristine surface, crystals are often exfoliated under vacuum. While many materials can be computationally predicted to be topological semimetals, only a select few candidates can be conveniently grown as high-quality, exfoliable single crystals. The requirement of exfoliability favors 2D materials, which often form in layers that can be easily separated by peeling. 2D materials can also be easier to compare to theory since the $k_\perp$ dependence of the electronic structure is usually weak.

The band structure visualized in ARPES is often treated as a picture, like a photograph, of the electronic bands and placed next to DFT band structures in publications as a verification of the theory. Agreement is often sufficiently good to make this treatment reasonable. However, even in materials with weak correlations for which first principles single-electron band structures are valid, the intensity visualized in ARPES depends on a number of intrinsic factors not present in standard band structure calculations. Assuming a free-electron-like final state, the full intensity is given by[107]:

$$I \propto \int dk_\perp |T^f|^2 |M_{if}(k_\perp)|^2 \cdot \frac{\delta k_\perp}{(k_\perp - k_\perp^0)^2 + (\delta k_\perp/2)^2} \cdot \frac{\delta E}{(E^i - E^i(k_\perp))^2 + (\delta E/2)^2}$$

where $k_\perp^0$,E^i are the momentum and energy of the initial band state and $\delta k_\perp$, δE are Lorentzian variances. The first term, $|T^f|^2$ is a transmission matrix element representing the probability of an electron escaping the material. $|M_{if}|^2$ is a photoexcitation matrix element depending on the overlap of the initial and final wavefunctions and polarization of incident light. The final two fractions represent intrinsic Lorentzian broadening in the surface normal momentum $k_\perp$ and the energy. Intrinsic Lorentzian spread in $k_\perp$ can mean that peaks in the ARPES intensity do not have one-to-one correspondence with simulated bands. For example, the highest intensity of a free-electron like parabolic band will appear slightly above the true band bottom.

In addition to these intrinsic factors, real experimental equipment has limited resolution. Resolution spread in $k_\parallel$ and E is often treated as Gaussian.

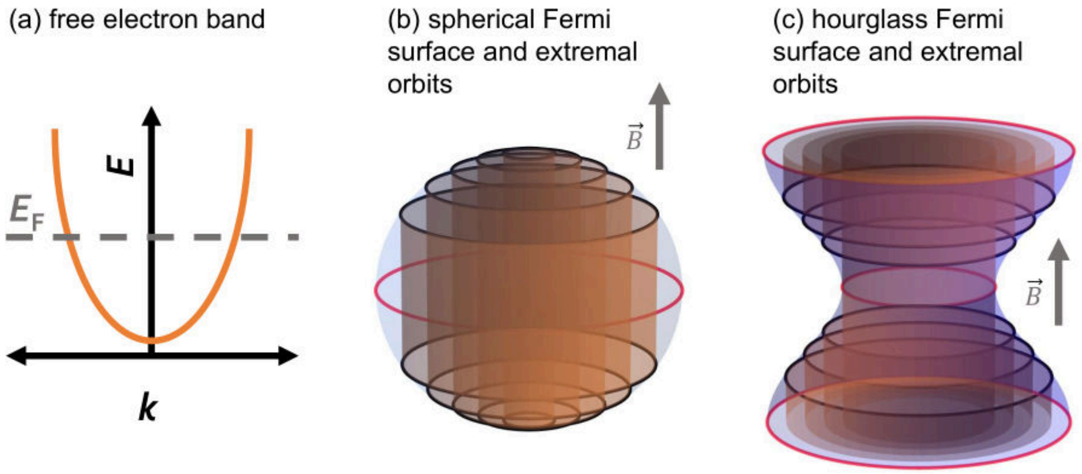

Figure 1.12: Schematic of free-electron Fermi surfaces and extremal orbits. (a) a free-electron-like band has a parabolic dispersion in E vs. k with electrons filling up to the Fermi level, E_F. (b) the Fermi surface is a 3D contour in k space corresponding to the isosurface at E_F. For a free-electron-like band, the Fermi surface is a sphere. When a magnetic field, $\overrightarrow{B}$, is applied, electrons can be considered to be confined to finite quantum states, visualized by the orange cylinders and lines. The single extremal orbit with largest cross-sectional area is highlighted in red. For an hourglass Fermi surface, (c), there are two extremal orbits corresponding to the largest and smallest cross-sectional areas.

1.10.2 Experimentally determining Fermi surfaces *via* quantum oscillations

As previously described, metals are characterized by a continuous spectrum of bands that are partially filled up to an energy level called the Fermi level, E_F. While thermal effects smear out the electron population, the most chemically and electronically active electrons in metals have energies close to E_F. A good deal of relevant electronic properties of metals can therefore be understood purely in terms of the Fermi surface, which is the isosurface in k-space occupied by electrons with energy E_F. Assuming a partially-filled free-electron band with parabolic dispersion, like that of Fig. 1.12 (a), setting $E = \mathbf{k}^2 = E_F = \text{const}$ yields a perfectly spherical Fermi surface, visualized in Fig. 1.12 (b).

At very low temperatures and under large applied magnetic fields, metals exhibit oscillations in their electronic properties corresponding to their Fermi surface geometry. In 1930 Lev Landau[108] demonstrated that when applying a magnetic field to confined electrons, a spectrum of states is created with quantized energies, now commonly referred to as *Landau levels*. Rather than occupying the continuous Fermi surface, electrons are confined to states known as *Landau tubes* with quantized orbits in the plane perpendicular to the applied magnetic field. In the case of a free electron, these Landau tubes are cylinders like the orange cylinders visualized in Fig. 1.12 (b). As the magnetic field, $\overrightarrow{B}$, is increased, the radii of the the cylinders increases until they reach the edge of the Fermi surface. Periodically, the area of one of these cylinders reaches the edge of the Fermi surface, which results in a divergence in the density of occupied states at the Fermi level. Since many experimentally observable properties of a metal depend strongly on the density of states, these properties exhibit periodic and measureable oscillations. The oscillation frequnecy is given by the Onsager relation[109]:

$$F = \left(\frac{\hbar}{2\pi e}\right) A$$

The frequency, F, measured in Tesla, is directly proportional to the area, A, of an extremal orbit, which is a local minimum or maximum of the Fermi surface cross-sectional area in a plane perpendicular to the applied magnetic field. For a sphere, there is only one extremal orbit, which is the maximal cross-section, drawn with a red line in Fig. 1.12 (b). Another simple Fermi surface example is an hourglass, which can occur in quasi-2D materials with free-electron-like conduction in-plane. In this case, presented in Fig. 1.12 (c), there are two extremal orbits corresponding to the largest and smallest circular cross-sections. Precisely these two extremal orbits are observed for an hourglass Fermi surface in the compound CsV_3Sb_5 in Chapter 5. Additional discussion of the origin of Landau levels and a more detailed explanation of the Onsager relation is provided in Appendix C.

Quantum oscillations are commonly measured in the resistivity (Shubnikov de Haas effect) and magnetization (de Haas van Alphen effect). While the prefactors are different for each measurement type, in both cases the full quantum oscillation amplitude from the Lifshitz-Kosevich (L-K) formulas is proportional to[109]:

$$\text{amplitude} \propto \frac{X}{\sinh(X)} \exp\left(-\frac{\pi mc}{eH\tau}\right)$$

where:

$$X = \frac{2\pi^2 kTmc}{e\hbar H}$$

T is the temperature, H is the applied field, m is the cyclotron mass of the electrons, and τ is the scattering time. From this expression, it can be seen that quantum oscillation amplitude is maximized when temperature is low, applied field strength is high, and electrons have high mobilities with low effective mass and long scattering time. In experiments where the temperature and applied field are known, the cyclotron mass is commonly extracted by measuring quantum oscillations under varying temperature and then fitting the resulting data to the functional form $X/\sinh(X)$.

Since the frequency of oscillations is proportional to the extremal orbits of the Fermi surface, quantum oscillations in materials with very small Fermi surfaces can have very large and easily-observable periods. For this reason, the first experimental observation of quantum oscillations was achieved in bismuth metal.[110] Bismuth quantum oscillation data similar to the original observations of de Haas and van Alphen are presented in in Fig. 1.13 (a). The sample used for this measurement is shown in the inset. The sample was a chunk of co-aligned bismuth grains oriented with the easy cleavage plane

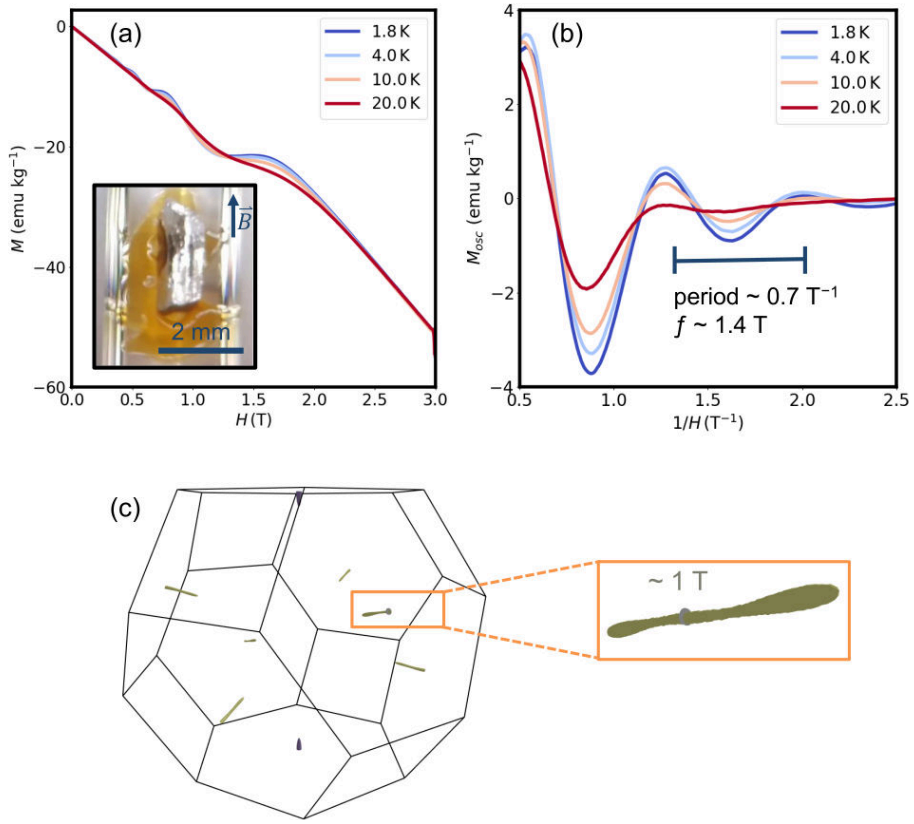

Figure 1.13: Large-period quantum oscillations in bismuth. (a) Raw experimental measurement of quantum oscillations in the magnetization of Bi. Inset shows the sample of co-aligned crystalline Bi grains with the the easy cleavage plane perpendicular to the applied field. (b) oscillation data after subtracting the background signal and re-plotting against inverse field. The period of oscillations is approximately $0.7\,\mathrm{T}^{-1}$, corresponding to a frequency of about 1.4 T. (c) The bismuth Fermi surface consists of electron (long, green) and hole (wider, purple) pockets with exceptionally small size. The observed oscillations derive from the electron pockets which have predicted smallest extremal cross-sections of about 1 T. An electron pocket and extremal orbit (gray line) are shown in close-up. Measurements were conducted on a Quantum Design PPMS operating in VSM mode. The Fermi surface was visualized using SERENDIPITY.

perpendicular to the applied field. Similar to sample requirements for ARPES, aligned crystals are needed to get coherent quantum oscillation signal, however, as shown here, it is sometimes possible to use aligned crystalline grains from flux rather than a single solid crystal. While the magnetization shows an overall negative slope with increasing field due to diamagnetism, at low temperatures between 1.8 K and 20 K clear oscillations can be seen in the signal. (b) shows the quantum oscillation data after typical processing. The diamagnetic background slope has been subtracted in order to extract the oscillatory signal, M_{osc}, and the x-axis has been re-plotted as inverse field. Using this second plot, we can see that the oscillatory signal has frequency of approximately 1.4 T. While this frequency is easy to visually extract in Bi, when the signal is more complicated with multiple frequency components a Fourier transform is commonly used to rigorously determine the component frequencies. The incredibly low frequency signal corresponds to exceptionally small extremal orbits. The Fermi surface of Bi is presented in Fig. 1.13 (c). The full Fermi surface is comprised of multiple distinct, disconnected 3D surfaces, called pockets. There are six thin green electron pockets and two wider purple hole pockets. All of the pockets are quasi-ellipsoidal. The measured frequency derives from the electron pockets, which have smallest cross-section of approximately 1 T, as shown in the close-up. While more precise crystal in-plane orientation is necessary to more rigorously compare to the calculated extremal orbits, this measured frequency is in almost perfect agreement with early experimental work by Shoenberg which found a quantum oscillation frequency of 1.4 T for the electron pockets when field is applied along the in-plane binary axis of the crystal[109].

Quantum oscillations can provide a nice complement to ARPES for materials with 3D electronic structures and Fermi surfaces. In practice, 3D crystals are often harder to exfoliate due to isotropically-strong bonding. 3D materials also have band structures that vary strongly with $k_{\perp}$, which can make ARPES comparison to calculated bands

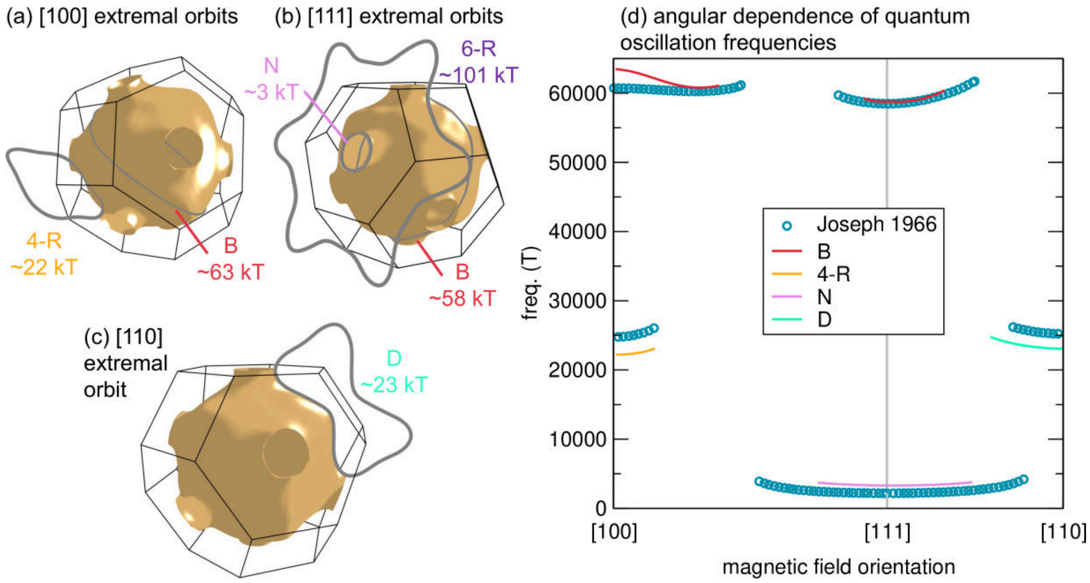

Figure 1.14: Angle-dependent quantum oscillations in copper. The Fermi surface of copper supports a wide variety of extremal orbits under changing magnetic field orientation. (a,b,c) present extremal orbits for magnetic field oriented along the high--symmetry [100],[111], and [110] directions, respectively. These orbits are known as the "belly" (B), "neck" (N), four and six-fold "rosettes" (4-R,6-R), and the "dogbone" (D). (d) presents a numerical comparison for select orbits between early angle-dependent data from Joseph and coworkers[111], shown as blue circles, and numerical calculations completed using the SERENDIPITY code, presented as solid lines.

more complex. By contrast, while indirect, quantum oscillations provide a covenient method for determining the 3D Fermi surface of a metal. By rotating the crystal and applying magnetic fields along multiple directions, the sizes of all the extremal orbits of a Fermi surface can be determined and carefully compared to simulated predictions. While ellipsoidal Fermi surfaces like the pockets of bismuth have relatively simple extremal orbits, even a mild increase in geometric complexity can yield more complicated orbits.

Fig. 1.14 depicts the angle-dependent extremal orbits of copper metal. As opposed to the exceptionally small Fermi surface in bismuth, copper has a free-electron-like Fermi surface that is exceptionally large. This Fermi surface extends outward so far that it intercepts the edges of the Brillouin zone. The copper geometry results in a variety of more complex extremal orbits depending the applied field direction. Orbits corresponding to the large cross-sections of the main quasi-spherical Fermi surface and the small circular Brillouin zone edge are usually referred to as “bellies” (B) and “necks” (N), respectively. Orbits passing through multiple Brillouin zones form the “dog bone” (D) and 4- and 6-fold “rosettes” (4-R,6-R). Fig. 1.14 (d) provides a direct comparison between experimentally measured de Haas van Alphen quantum oscillation frequencies and quantum oscillation frequencies calculated from the displayed first-principles Fermi surface, demonstrating relatively good agreement. By carefully and iteratively comparing results to electronic structure models with controlled tuning parameters, increasingly accurate 3D models of Fermi surfaces and metallic electronic properties can be achieved.

I am currently developing a code, SERENDIPITY, that automates extraction of quantum oscillation frequencies from first-principles calculations and provides tools for 3D plotting of extremal orbits. SERENDIPITY is leveraged significantly in Chapters 4 and 5 to determine the origins of experimentally-observed quantum oscillations in the compounds $LaIn_3$ and CsV_3Sb_5.

1.11 Electronic structure and predicted $\mathbb{Z}_2$ surface states: CsV_3Sb_5

[9]Here, I provide an explicit example of electronic structure calculations and topological classification informed via experimental ARPES.

Figure 1.15 presents the structure of CsV_3Sb_5. This layered material has a hexagonal

---

[9] The contents of this section are adapted from Ref. [112]: B. R. Ortiz, S. M. L. Teicher, Y. Hu, J. L. Zuo, P. M. Sarte, E. C. Schueller, A. M. M. Abeykoon, M. J. Krogstad, S. Rosenkranz, R. Osborn, R. Seshadri, L. Balents, J. He, and S. D. Wilson, CsV_3Sb_5: a $\mathbb{Z}_2$ topological kagome metal with a superconducting ground state, *Phys. Rev. Lett.* **125**, 247002. ©APS publishing, 2020, reprinted with permission.

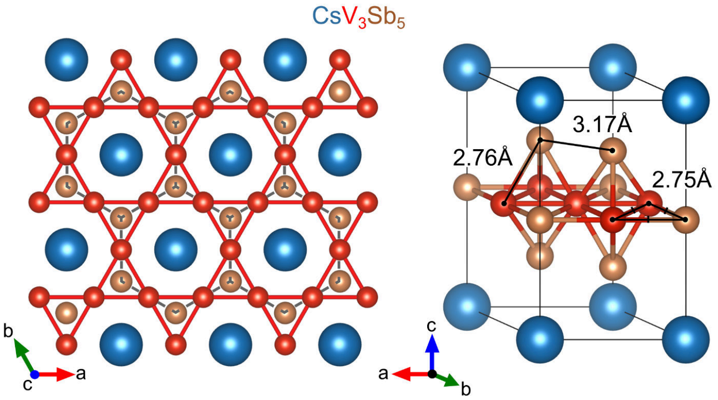

Figure 1.15: Ambient temperature crystal structure of CsV_3Sb_5. The structure of CsV_3Sb_5 is shown from above (left) and in a 3D view (right.)

lattice with quasi-2D connectivity in the a-b plane. The vanadium atoms form a kagome network of interconnecting triangles and hexagons with bond length 2.75 Å. In the planes just above and below the kagome layer along the c axis, antimony atoms form hexagonally-connected antimonene layers analogous to graphene with bond length 3.17 Å. The antimonene bonding connectivity is indicated by the gray dashed lines in the overhead view. Transport measurements on CsV_3Sb_5 exhibit anomalies at 94 K and 2.5 K. The 2.5 K anomaly is well-characterized as a superconducting transition.[112] New results, including the work discussed in depth in Chap. 5, strongly suggest that the 94 K transition is a charge density wave.

Due to the 2D layered structure and weak van der Waals bonding along the c-axis, crystals of CsV_3Sb_5 can be conveniently exfoliated for ARPES measurements. ARPES results are compared to the *ab initio* simulated electronic structure in Fig. 1.16. The measured and simulated E vs. $k_\parallel$ band structures are displayed in (a). While overall agreement is remarkably good, there are several key differences. First, the experimental measurement appears fuzzier due to finite resolution. Second, there are no bands above E_F in the experiment: since no electrons occupy these states at low temperature, they cannot be detected in ARPES. The simulated band structure density is somewhat

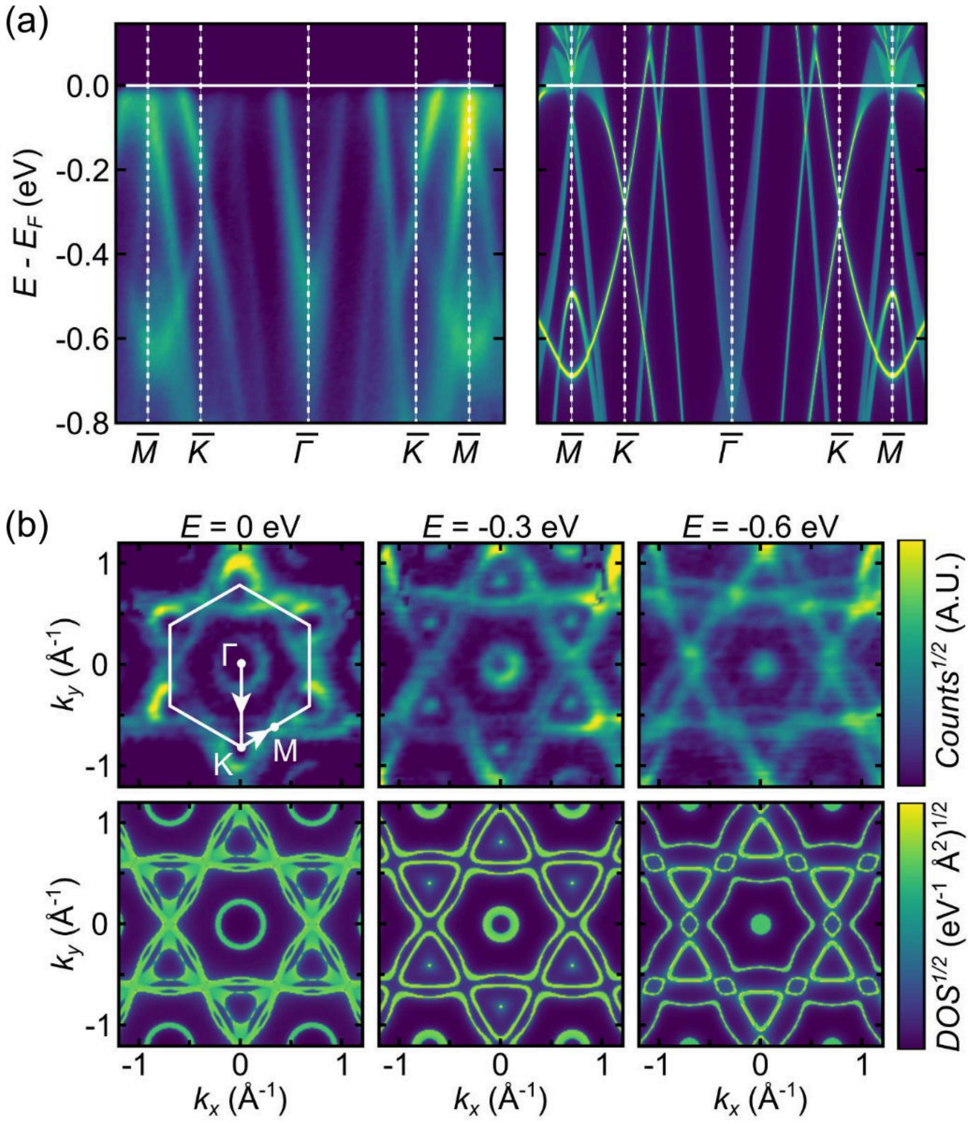

Figure 1.16: Comparison of ARPES data and simulated band structure in ambient structure CsV_3Sb_5. (a) ARPES band E vs. k band structure data (left) is compared to simulated bands (right). (b) constant energy k-space maps visualize the Fermi surface at 3 constant energy contours ($E = 0\,\text{eV}$, $-0.3\,\text{eV}$, and $-0.6\,\text{eV}$). The upper three panels display measured ARPES intensity while the lower three panels are simulation results. Intensity values represent counts and density of states in the ARPES and simulation, respectively. Intensity values are normalized by a square root.

different than the band structures that have been presented so far in this introduction. There is almost no experimental $k_\perp$ resolution, so the ARPES measurement effectively samples all values of $k_\perp$ at once. The band structure has therefore been simulated using the surface Green's function method,[113] which produces a band density that is effectively an average of the band structure over $k_\perp$. Fig. 1.16 (b) presents constant energy maps of the band density in the $k_\|$ plane, again comparing measurements and simulation. These constant energy cuts again show remarkable agreement from $E = E_F$ down to $E = E_F - 0.6$ eV. Small asymmetries in the experimental energy maps are present that are not seen in the simulation. These weak asymmetries are likely due to matrix element effects, as discussed in Ref. [114].

These ARPES results validate the CsV_3Sb_5 model. While some correlation effects are present that are not accounted for in the DFT (after all, this material is a low-temperature superconductor), these data strongly suggest that the DFT model accurately recreates the electronic band structure of CsV_3Sb_5 in the ambient temperature metallic phase. With confidence in the simulated band structure, we can examine the relevant physics in greater detail. Due to the hexagonal symmetry, we will be able to define a topological invariant in this system using similar techniques to previously discussed work on graphene.

Fig. 1.17 (a) presents the calculated band structure of CsV_3Sb_5. A 3D schematic of the hexagonal Brillouin zone is provided for reference. While this compound is metallic because there are partially-filled bands at E_F, we can define two band gaps that cross the Fermi level, highlighted in light purple and light blue. As discussed in section 1.8.1, the topological invariant across a band gap can be calculated via a parity product formula. The relevant parity products have been calculated at the TRIM points and are shown in a table. The parity products for the filled states up to bands 131 and 133 yield nontrivial $\mathbb{Z}_2$ invariants for the light purple and light blue gaps, respectively.

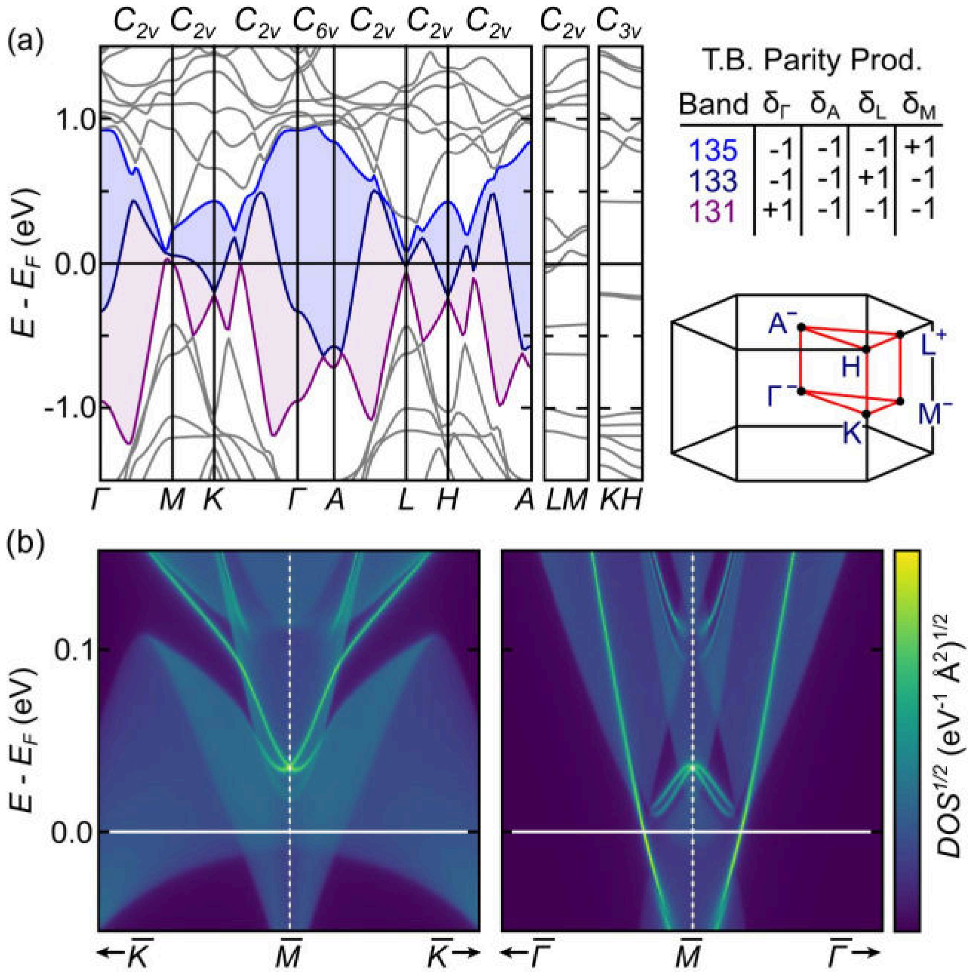

T.B. Parity Prod.

Band	δ_Γ	δ_A	δ_L	δ_M
135	-1	-1	-1	+1
133	-1	-1	+1	-1
131	+1	-1	-1	-1

Figure 1.17: $\mathbb{Z}_2$ topological invariant and surface states in CsV_3Sb_5. (a) the band structure of CsV_3Sb_5 includes two band gaps that cross the Fermi level that lie between bands 131 and 133 (light purple) and between bands 133 and 135 (light blue). Point groups for each segment are annotated above the band structure (C_{2v},C_{6v},etc.). By calculating the parity products at the TRIM points (Γ,A,L,M), shown in the hexagonal Brillouin zone, the corresponding $\mathbb{Z}_2$ invariants can be determined. The nontrivial invariants for occupied states up to bands 131 and 133, presented in the table for the current tight-binding model, indicate nontrivial topology for both the light purple and light blue band gaps. Corresponding to this prediction, nontrivial surface states can be found in the simulation just above the experimentally-observed Fermi level at the $\overline{M}$ point, as displayed in (b).

For example, in the case of band 133, the total product is:

$$(-1)^{\nu} = (\delta_{\Gamma})(\delta_A)(\delta_L)^3(\delta_M)^3 = (-1)(-1)(+1)^3(-1)^3 = -1$$

(The M and L points are 3-fold degenerate) Since $\nu = 1$, the gap is nontrivial. This $\mathbb{Z}_2$ invariant formula only guarantees topological surface states when there is a complete gap between the the two bands. Although this material is a metal, such a complete gap exists in the light blue region between bands 133 and 135. This can be shown with relative ease by examining the point groups. Similar to graphene, the point group for most segments of the band structure is C_{2v}. Referring to Table 1.1, we know that no band crossings along any of these segments will be robust to spin orbit coupling. Along the remaining segments (Γ-A and K-H) where symmetry protected band crossings could occur, there is a relatively large gap between bands 133 and 135 that is visible by eye (greater than 0.5 eV in both cases). We can therefore quickly conclude that there is a complete band gap in the light blue region. The nontrivial $\mathbb{Z}_2$ invariant and complete band gap guarantee that CsV_3Sb_5 will exhibit surface states similar to a topological insulator.

The most obvious surface states in CsV_3Sb_5 are located at the $\overline{M}$ point. Fig. 1.17 (b) displays these surface states along the high symmetry $\overline{K} - \overline{M} - \overline{K}$ and $\overline{\Gamma} - \overline{M} - \overline{\Gamma}$ lines. Comparing to Fig. 1.9, the surface state dispersion along $\overline{K} - \overline{M} - \overline{K}$ can be seen to be quite similar to that of Bi_2Se_3.

The surface states in CsV_3Sb_5 remain unverified because they lie slightly above E_F at ambient temperature, and were undetectable in this original ARPES study. Chapter 5 presents work modeling the 94 K structural distortion in CsV_3Sb_5, which is predicted to be a breathing mode distortion based on DFT results carefully compared to single crystal X-ray diffraction data and Shubnikov de Haas quantum oscillations. These results suggest that the charge density wave distortion reconstructs the band structure, lowering states near the M point. Newer ARPES studies also confirm a lowering of the M bands in the low temperature CDW phase and increased intensity signal is found right at the Fermi level at low temperatures—a possible indication of the predicted surface states.[115] This validated band structure calculation has also provided a basis for recent phenomenological models, such as that in Ref. [116], that aim to explain correlated phenomena and superconductivity in CsV_3Sb_5.

$\mathbb{Z}_2$ band topology may be common in nonmagnetic kagome metals. Chapter 6 includes predictions of similar $\mathbb{Z}_2$ surface states in kagome metals GdV_6Sn_6 and YV_6Sn_6.

1.12 Examples of instabilities in semimetals

Given the prior qualitative discussion of Peierls model instability, we expect that symmetry-breaking distortions may play an important role in materials with Dirac or Weyl band crossings near the Fermi level. This section presents two established examples of such symmetry-breaking distortions: structural distortions in square-net semimetals and antiferromagnetic ordering in chromium metal.[10]

1.12.1 Square net semimetals: stability of Peierls-like bonding motifs

Square-net semimetals in the ZrSiS family have attracted significant recent research attention due to their large-dispersion Dirac bands and chemical variety. The crystal

---

[10] In this section, I reference the chemical description of the Peierls chemical bonding model from Fig. 1.5. In the physics community, the denomination 'Peierls-like' is often used to refer to charge density wave transitions driven by Fermi surface nesting. Johannes and Mazin have provided evidence that this Fermi surface nesting mechanism is fairly rare in systems with 2D and 3D bonding.[117] The instability of half-filled bands with nonbonding character described here is more general and not specific to a Fermi surface nesting mechanism.

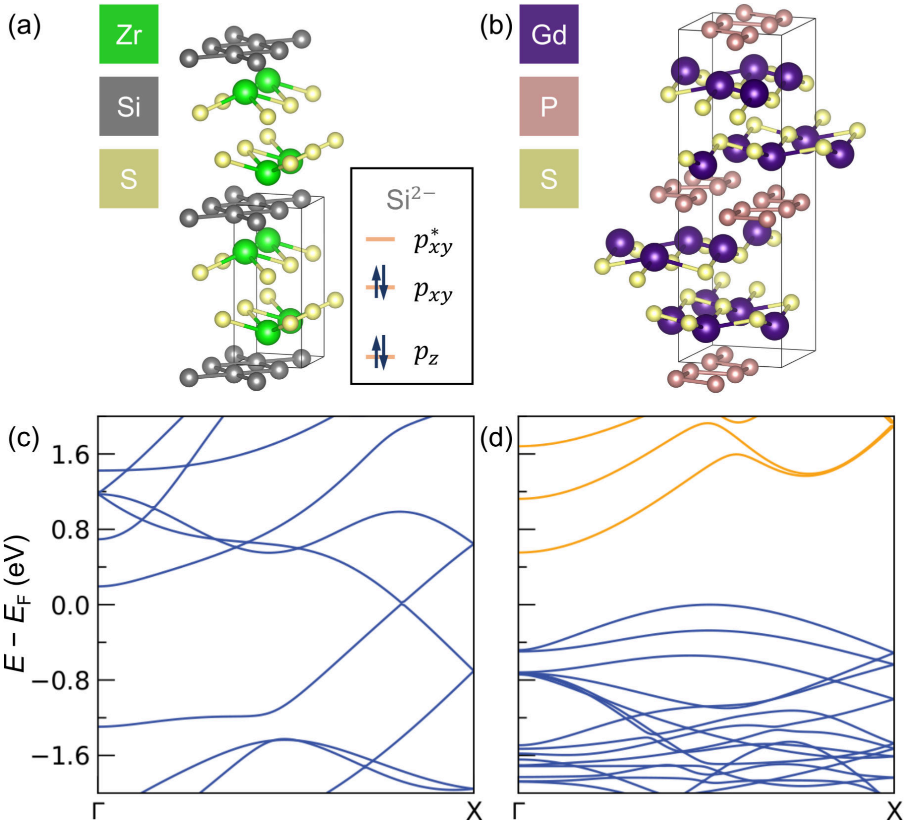

Figure 1.18: Crystalline and electronic structure of square-net semimetals. (a,b) display the crystal structures of ZrSiS and GdPS. An approximate electron filling model is shown in the inset of (a) for the p orbitals of Si. (c,d) show the corresponding band structures of ZrSiS and GdPS, respectively. ZrSiS has an undistorted square-net, leaving a Dirac cone at the Fermi level whereas distorted GdPS is a band-gapped insulator.

structure of ZrSiS is shown in Fig. 1.18 (a). Zr and S form bonding layers with a distorted rock salt configuration. Si forms flat interspersing planes with square planar bonding coordination. The approximate oxidation states of Zr and S are Zr^{4+} and S^{2-}, which leaves Si in an unusual Si^{2-} state. The relevant band structure near the Fermi level can largely be understood in terms of a tight-binding model in which only Si p orbitals are present.[118] Close bonding in the square planes raises the energy of in-plane Si p_{xy} orbitals with respect to out-of plane Si p_z orbitals. With four p electrons localized on the Si site, this model can be described by the cartoon in the inset of Fig. 1.18 (a): the p_z band is filled and the remaining two electrons half-fill the p_{xy} bands, leaving the p_{xy} bonding states filled while the antibonding p^*_{xy} states are empty. In analog to the Peierls model, the half-filled p_{xy} band in ZrSiS yields Dirac cones at the Fermi level, as shown in the band structure of Fig. 1.18 (c).

As discussed in detail by Tremel and Hoffmann,[119] the ZrSiS structure can become unstable with slight chemical substitution or doping. They compared ZrSiS to the related compound GdPS, which is insulating. In GdPS, the nominal oxidation states are $(Gd^{3+})(P^{1-})(S^{2-})$, yielding an identical orbital electron filling and an electronic structure which is dominated by P^{1-} states near the Fermi level. In the case of GdPS, however, the P square net is not the most stable configuration; rather than evenly-spaced squares, the P atoms form distorted long-short chains in analog to the 1D Peierls model, as shown in Fig. 1.18 (b). This symmetry-breaking distortion allows mixing of the $p_{x,y}$ states and formation of a band gap, which is simulated in Fig. 1.18 (d).

The dissertation author collaborated on a recent study demonstrating that this simple p-orbital model is quite general for a wide range of square-net materials. The stability of the Dirac crossings in hundreds of square-net materials can be accurately predicted based on a simple bond length ratio between the in-net bonds and the distance between the square-net and rock salt layers.[121] Additional new work on the

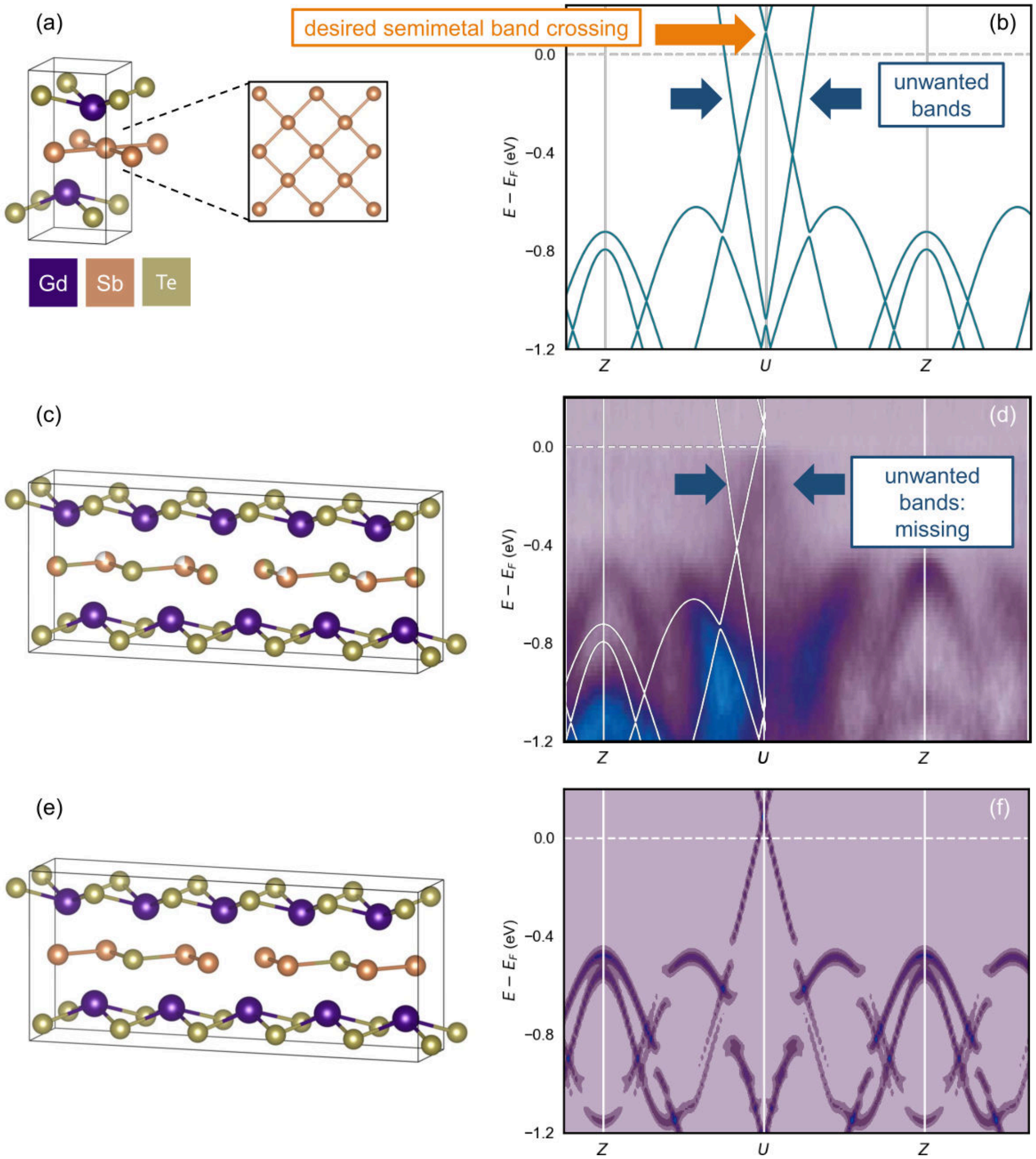

Figure 1.19: Band engineering in $\mathrm{GdSb}_x\mathrm{Te}_{2-x-\delta}$. (a) unit cell of stoichiometric GdSbTe with perfect Sb square-net, shown in inset. (b) simulated unit cell band structure. In addition to a Dirac crossing close to E_F, there are two undesirable metallic bands. (c) experimental structure of doped $\mathrm{GdSb}_{0.46}\mathrm{Te}_{1.48}$. In analog to the Peierls chain, the doped Sb nets have formed bonding chains with uneven spacing. The unwanted bands are absent in ARPES measurements of this doped structure, (d). Unit cell bands are overlaid in white as a guide for the eye. DFT simulations performed on the approximated structure shown in (e) confirm this band gapping, with unfolded band intensity (f) in remarkable agreement to the ARPES. Despite the massive band gapping of the unwanted metallic bands, the desired semimetal band crossing is preserved, demonstrating that Peierls-like band gapping can be used to 'clean' semimetal band structures. Adapted from Ref. [120].

square-net metal GdSb$_x$Te$_{2-x-\delta}$[120] suggests that Peierls-like distortions aren't necessarily a liability. Rather than impeding topological band structure, controlling Peierls-like distortion can be used to 'clean' square-net semimetal band structures, removing unwanted metallic bands while preserving Dirac cones as shown in the experimental and simulation results of Fig. 1.19. A similar band cleaning effect is also predicted in the doping series CeSb$_x$Te$_{2-x-\delta}$.[122]

Chapter 4 draws on this understanding of 2D square-net materials, demonstrating that the electronic structure of 3D cubic auricupride metals can largely be understood using an analogous half-filled $p_{x,y}$ model that similarly stabilizes Dirac crossings near the Fermi level.

1.12.2 Chromium metal: antiferromagnetism as symmetry breaking

Rather than distortions of the crystal structure, many materials display magnetic ordering transitions that share some qualitative similarities to the Peierls instability. In 2002, Decker and coworkers proposed a mechanism that they dubbed an *electronic Peierls distortion* for the antiferromagnetic transition in chromium metal.[123] The simulation results plotted in Fig. 1.20 recreate the original findings of Decker *et al.* The top row displays simulation results for a non-spin-polarized calculation of the electronic structure of chromium metal performed on the bcc structure conventional cell, (a). The band structure in (b) displays two large dispersion band crossings, Dirac nodes, at the Fermi level, highlighted in orange. There is an incomplete pseudogap in the density of states in (c). (d) shows the crystal orbital Hamilton population. The filled states below the Fermi level are largely bonding (positive), while the unfilled states above the Fermi level are antibonding (negative), which promotes stability. However, there is

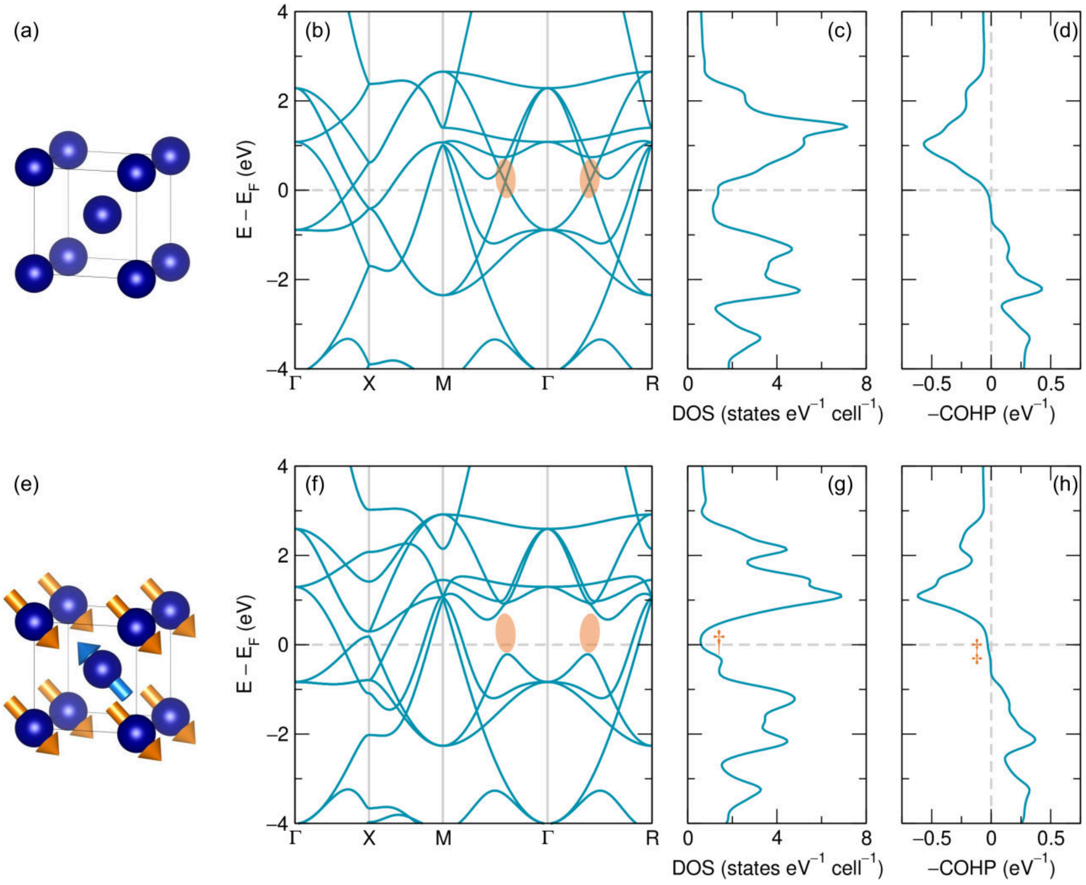

Figure 1.20: Electronic instability and antiferromagnetic ordering in chromium. The electronic band structure, density of states, and total Cr-Cr crystal orbital Hamilton population are plotted for non-spin polarized (a) and antiferromagnetic (e) configurations in (b,c,d) and (f,g,h), respectively. All simulations are performed on the conventional cubic cell. Upon transitioning to the the energetically-favored antiferromagnetic state, Fermi level Dirac cones are gapped out (orange highlights in (b),(f)), a deeper pseudogap opens up in the DOS (†), and the flat non-bonding region of the COHP is extended (‡). Figure adapted from Ref. [123].

a large non-bonding region with a COHP value of 0 at and just below the Fermi level. Decker and co-workers argue that instability of these Fermi-level non-bonding states to band gapping drives the antiferromagnetic ordering transition, in analog to the Peierls model and COHP previously presented in Fig. 1.5. The intuition here is simple. Rather than making the two crystal sites in the lattice distinct and breaking symmetry by altering the bonding in a long-short-long pattern like the 1D Peierls chain, two atomic sites can also be made distinct by placing oppositely-directed antiferromagnetically-ordering spins.

An antiferromagnetic magnetic ordering is stabilized in the simulation, consistent with the true ground state of chromium (by about 25 meV/atom in my simulation). While the true low temperature phase of chromium includes long range magnetic order, the antiferromagnetic phase is well-approximated by the bcc antiferromagnetic ordering of Fig. 1.20 (e). Upon magnetic ordering, the electronic structure undergoes a number of subtle, but notable, transitions. The large Fermi level Dirac bands are shown to gap in (f). This corresponds with the opening of a new and deeper pseudogap in the density of states in (g) and a stretching of the crystal orbital Hamilton population curve in (h) that widens the non-bonding region near E_F. These results are consistent with a picture in which certain bands in the electronic structure undergo a Peierls-like bonding transition, while the rest of the electronic structure is unaffected by the magnetic ordering. While the density of states near the Fermi level is decreased, chromium remains a metal in the antiferromagnetic phase.

Qualitatively speaking, many compounds that have antiferromagnetic ordering have similar non-bonding COHPs to chromium. Based on the examples discussed in this section, we would expect that materials with Dirac and Weyl band crossings near the Fermi level might exhibit low temperature transitions to structurally-distorted and antiferromagnetically-ordering phases. In chapter 3, this bonding intuition will be used to rationalize a transition to a distorted and antiferromagnetically-ordering low temperature phase in Mn_3ZnC.

1.13 Permissions and Attributions

1. The contents and figures of section 1.11 are adapted from Ref. [112]: B. R. Ortiz, S. M. L. Teicher, Y. Hu, J. L. Zuo, P. M. Sarte, E. C. Schueller, A. M. M. Abeykoon, M. J. Krogstad, S. Rosenkranz, R. Osborn, R. Seshadri, L. Balents, J. He, and S. D. Wilson, CsV_3Sb_5: a $\mathbb{Z}_2$ topological kagome metal with a superconducting ground state, *Phys. Rev. Lett.* **125**, 247002. ©APS publishing, 2020, reprinted with permission.

2. Figure 1.19 includes content previously published in Ref. [120]: S. Lei, S. M. L. Teicher, A. Topp, K. Cai, J. Lin, G. Cheng, T. H. Salters, F. Rodolakis, J. L. McChesney, S. Lapidus, N. Yao, M. Krivenkov, D. Marchenko, A. Varykhalov, C. R. Ast, R. Car, J. Cano, M. G. Vergniory, N. P. Ong, and L. M. Schoop, Band engineering of Dirac semimetals using charge density waves, *Adv. Mater.* **33**, 2101591 (2021). ©Wiley, 2021, reprinted with permission.

3. The content of chapter 2 has previously appeared in Ref. [124]: S. M. L. Teicher and L. K. Lamontagne, L. M. Schoop, and Ram Seshadri, Fermi-level Dirac crossings in $4d$ and $5d$ cubic metal oxides: $\mathrm{NaPd_3O_4}$ and $\mathrm{NaPt_3O_4}$, *Phys. Rev.* B **99**, 195148. ©APS publishing, 2019, reprinted with permission. We thank Claudia Felser for encouraging this work, and Douglas Fabini and Xie Zhang for helpful discussions.

4. The content of chapter 3 has previously appeared in Ref. [125]. Reproduced from S. M. L. Teicher and I. K. Svenningsson, L. M. Schoop, and Ram Seshadri, Weyl

nodes and magnetostructural instability in antiperovskite Mn_3ZnC, *APL Mater.* **7**, 121104 (2019), with the permission of AIP Publishing.

5. The content of chapter 4 is the result of a current collaboration. S. M. L. Teicher, J. Linnartz, R. Singha, D. Pizzirani, S. Klemenz, S. Wiedmann, J. Cano and L. M. Schoop, 3D analogs of square-net nodal line semimetals: band topology of cubic $LaIn_3$. *Submitted*. Reproduced here with permission from the authors.

6. The content of chapter 5 has previously appeared in Ref. [126]. Reproduced from B. R. Ortiz, S. M. L. Teicher, L. Kautzsch, P. M. Sarte, J. P. C. Ruff, R. Seshadri, and S. D. Wilson, Fermi surface mapping and the nature of charge density wave order in the kagome superconductor CsV_3Sb_5, *Phys. Rev.* X **11**, 041030 (2021). ©APS publishing, 2021, reprinted with permission. S. W. gratefully acknowledges discussions with Leon Balents, Binghai Yan, and Ziqiang Wang. We gratefully thank Matthew Benning and Michael Ruf of Bruker Corporation for their assistance in the integration of synchrotron data with Apex3 and their crystallography discussions.

7. The content of chapter 6 has previously appeared in Ref. [127]. Reproduced from G. Pokharel, S. M. L. Teicher, B. R. Ortiz, P. M. Sarte, G. Wu, S. Peng, J. He, R. Seshadri, and Stephen D. Wilson, Study of the electronic properties of topological kagome metals YV_6Sn_6 and GdV_6Sn_6, *Phys. Rev.* B **104**, 235139 (2021). ©APS publishing, 2021, reprinted with permission.

Part I

Electronic structure of cubic metals

Chapter 2

Dirac crossings in cubic metal oxides $NaPd_3O_4$ and $NaPt_3O_4$

[1]The cubic oxide metals NaM_3O_4 (M = Pd or Pt) crystallize in the non-symmorphic $Pm\bar{3}n$ space group. First-principles calculations are employed here to understand the role of the MO_4 square planes and M–M interactions in the development of the electronic structure. The compounds host numerous Dirac crossings near the Fermi level which, in the absence of spin-orbit coupling, appear to form a cubic nodal state. Spin-orbit coupling fragments this nodal state into smaller regions with Dirac-like character, with the fragmenting being more pronounced in the the M = Pt compound.

2.1 Introduction

Dirac semimetals (DSMs) have become an active area of research due to their exceptional transport properties, arising as a consequence of a linear band crossing, or Dirac point, which results in massless charge carriers known as Dirac fermions. In order for the transport to be dominated by Dirac fermions, Dirac points in the electronic structure should be proximal to the Fermi level with few or no other bands at the same

---

[1] The contents of this chapter previously appeared in Ref. [124]: S. M. L. Teicher and L. K. Lamontagne, L. M. Schoop, and Ram Seshadri, Fermi-level Dirac crossings in $4d$ and $5d$ cubic metal oxides: $NaPd_3O_4$ and $NaPt_3O_4$, *Phys. Rev.* B **99**, 195148. ©APS publishing, 2019, reprinted with permission.

energy. DSMs could be considered 3D analogs of graphene, which is a 2D material with purely linear band crossings at the Fermi level.[37] There is an additional constraint on DSMs, however, that graphene does not satisfy, that the crossing must be symmetry-protected such that it does not gap out due to spin-orbit coupling (SOC) and or an applied magnetic field.[128] In recent years, a push to develop design principles for 3D DSMs that possess these protected linear band crossings near the Fermi level has yielded the experimental verification compounds Na_3Bi and Cd_3As_2.[129, 130, 58, 56] A closely related class of materials to DSMs have degenerate Dirac crossings along a line in the Brillouin zone, rather than points and these are called nodal-line semimetals.[131, 76, 132] SOC is often unfavorable for the formation of these features in the electronic structure since symmetry protections tend to only exist along high-symmetry lines in k-space, and thus do not usually fully stabilize the nodal lines, which are frequently circular or oval.[30] Nodal-line semimetals with certain symmetry protections exhibit drumhead-shaped surface states that are proposed to host novel correlated electron physics.[132] Recently, it has been proposed that rather than displaying nodal lines, there could exist compounds in which the degenerate band crossings trace a connected 3D surface — a spherical shell — in the Brillouin zone,[133] these nodal-sphere semimetals could exhibit similar correlated surface states.

Analyzing and understanding crystallographic and compositional motifs that lead to linear band crossings proximal to the Fermi level is important in identifying new compounds and advancing potential technological applications. It is also of particular interest to examine oxide compounds which are somewhat underrepresented in the space of Dirac and related materials. To this end, we present electronic structure calculations on the complex platinum group metal oxides, NaM_3O_4 (M = Pd, Pt). Since the strength of SOC scales approximately as Z^4/n^3, (Z is the atomic number and n is the principal quantum number) comparing the Pd and Pt compounds allows the role of SOC in the development of the electronic structure to be scrutinized.

From the perspective of current applications, these complex Pd and Pt oxides are known for their their ability to be p-doped. Unlike most oxides which have valence bands dominated by localized O p orbitals and are most conveniently electron doped, these Pd and Pt compounds can be easily hole-doped using alkali metals.[134, 135] The semiconducting d^8 oxides (Ca/Sr)(Pd/Pt)$_3$O$_4$ can be hole doped by Na substitution for Ca/Sr. Substitution on this site does not significantly change the crystal structure or the qualitative nature of bands, allowing fine tuning of the Fermi level. Sodium doping of $\mathrm{Ca}M_3\mathrm{O}_4$ and $\mathrm{Sr}M_3\mathrm{O}_4$ has been shown to convert these semiconductors into metals.[136, 137, 138, 139] $\mathrm{Na}M_3\mathrm{O}_4$ can be viewed as the 100%-doped end-member in which Ca or Sr has been completely replaced by Na. Lamontagne *et al.* recently proposed that Na doping in $CaPd_3O_4$ and $SrPd_3O_4$ may proceed *via* a non-uniform percolative transition, with significantly increased local disorder in $SrPd_3O_4$ impeding percolation relative to $CaPd_3O_4$.[140]

Platinum metal has also long been ubiquitous as a chemical catalyst, and Pd oxides are well-known for their use in automotive catalytic converters. In the 1970s, $Na_xPt_3O_4$ was proposed to be one of the main active components of the Adams catalyst, a compound useful for catalyzing organic hydrogenation reactions that was first described by Adams and Voorhees in 1922, whose properties proved difficult to reproduce over a half-century of subsequent syntheses.[141, 142] In recent years, there has been significant general interest in the enhanced catalytic action of ionic noble metal species and noble metal oxides.[143, 144, 145, 146] It is interesting to ask whether topological surface states and/or potentially enhanced charge transport due to linear dispersion at Dirac and Weyl band crossings could play a role in the catalytic activity of these compounds. Indeed, a growing number of catalysts including the pure noble metals Pd and Pt, have been suggested as hosting non-trivial topological states and linear band

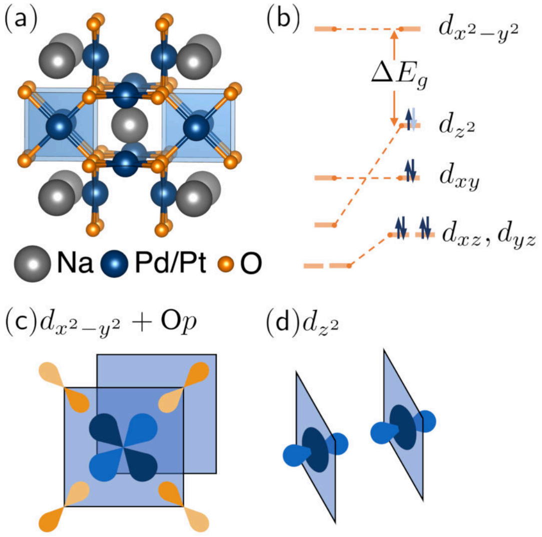

Figure 2.1: NaM_3O_4 structure and bonding. (a) Crystal structure of $Na(Pd/Pt)_3O_4$ in the non-symmorphic space group $Pm\bar{3}n$ (#223).(b) Crystal field splitting for the general square planar case, modified here through the interaction between the partially filled d_{z^2} levels across the faces of the square planes. The energy gap for the corresponding d^8 compounds would be between the d_{z^2} and $d_{x^2-y^2}$ levels. For (Ca/Sr)M_3O_4, the d_{z^2} states are filled, resulting in a band insulator. For NaM_3O_4, however, the d_{z^2} states are partially filled, resulting in a metal. (c) The $d_{x^2-y^2}$ + O p interaction for a single square plane. (d) The stacked MO_4 square planes in the unit cell yield a network of inter-planar $M_{d_z^2}$ bonding.

crossings in their electronic structure.[10, 11]

$NaPd_3O_4$ and $NaPt_3O_4$ crystallize in the cubic $Pm\bar{3}n$ space group (#223) shown in Fig. 2.1(a). The structure consists of corner-connected MO_4 square planes. Closely-spaced, infinite parallel stacks of MO_4 square planes also run along all three cubic axes. The space group has an n glide that results in nonsymmorphic symmetry. Recently, there has been significant interest in 3D nonsymmorphic crystals, especially due to the fact that these compounds can host protected multiply-degenerate band crossings in which more than 4 bands overlap at high-symmetry points in the Brillouin zone. At these overlap points, even more exotic analogs of Dirac fermions could potentially be realized.[147, 77, 80] Group #223 can host band crossings that are up to eight-fold degenerate.[80]

The crystal-field splitting of square planar M as presented in Fig. 2.1(b), has been described using tight binding models as popularized by Hoffmann[29] and an important feature is that interaction of the d_{z^2} orbitals raises this level over the d_{xy} level as shown in the right. The $d_{x^2-y^2}$ orbitals form a 3D-connected bonding network with the O p orbitals at the corner of each square planar group [Fig. 2.1(c)]. The d_{z^2} orbitals form independent bonding chains with two square planar groups *per* unit cell along the cubic axes [Fig. 2.1(d)]. 3D bonding increases the energy dispersion of the $d_{x^2-y^2}$ bands (which would not be expected to have particularly significant dispersion in the isolated chain model), allowing them to cross the d_{z^2} bands near the center of the Brillouin zone, and, as will be shown, resulting in symmetry-protected Dirac crossings. Doublet, Canadell, and Whangbo have developed a semi-empirical tight-binding model for NaM_3O$_4$ and provided band-folding explanations for the electronic structure of the $d_{x^2-y^2}$ and d_z^2 states near the Fermi-level.[148] The Pd/Pt ions in NaM_3O$_4$ have a nominal 2.33+ charge, making these compounds metallic with partially-filled d_z^2 orbitals. This is in contrast to the isostructural, band semiconducting compounds with Ca or Sr which have d^8 Pd^{2+} or Pt^{2+} and a fully-filled d_z^2 level. The compounds (Ca/Sr)M_3O$_4$ have previously been suggested to be topological semimetals, but these compounds are actually insulating both at appropriate levels of electronic structure theory as well as in experimental studies.[149, 140]

We present here a detailed electronic structure description of the two compounds $NaPd_3O_4$ and $NaPt_3O_4$ using a combination of plane-wave pseudopotential and plane-wave local orbital density functional theory calculations in tandem with tight-binding models to identify Dirac crossings near the Fermi level that appear to form a nodal cube, not unlike the nodal-sphere semimetallic state proposed previously by Wang *et al.* [133] Spin-orbit coupling fragments this nodal cubic state into 14 protected Dirac crossings in both the Pd and Pt compounds. This work points to the potential of complex oxides to enrich the domain of Dirac and related quantum materials and supports the view that there may be a role for previously ignored features in the electronic structure playing a role in the catalytic properties of compounds of the platinum group metals.

2.2 Methods

First principles electronic structure calculations were performed using Vienna ab initio Simulation Package VASP [150, 151, 152] and WIEN2k codes,[153] with and without SOC. Computation performed using VASP utilized PAW[90, 154] potentials, while computations involving WIEN2k employed linear augmented plane waves and local orbitals.[155] The Perdew, Burke, Ernzerhof (PBE) generalized gradient approximation [94] was used for the exchange energy while Vosko, Wilk, and Nusair interpolation was used for the correlation energy.[156] While computationally expensive hybrid functionals such as HSE06,[157] are known to improve band gap estimations in a wide range of semiconductors, including in simple and complex Pd oxides,[103] previous empirical comparisons of transition metal and metallic transition metal oxide systems suggest that the additional electron screening in hybrid functionals provides little improvement over PBE and can reduce accuracy in estimations of key material parameters.[158, 159] We employed a $10 \times 10 \times 10$ Monkhorst-Pack [160] k-point grid. Structural relaxations and static self-consistent calculations used the default smearing algorithms for VASP and WIEN2k, first-order Methfessel-Paxton [161] and tetrahedral smearing with Blöchl corrections,[162] respectively. The plane wave energy cutoff for VASP was set to 520 eV and the plane-wave expansion parameter, RKMAX, for WIEN2k was set to 8.5. The density of states calculations provided in the supplemental material utilized tetrahedral smearing and band structures were calculated using Gaussian smearing.[163] Structures were initially relaxed in VASP (to lattice parameters of

5.728 Å and 5.765 Å for the the Pd and Pt compounds, respectively, within expected error from experimental values of 5.650 Å[164] and 5.689 Å[165]) using the conjugate gradient descent algorithm with a force cutoff of 0.01 eV/Å. Self-consistent static calculations and electronic structure calculations were subsequently performed using VASP and WIEN2k with energy convergence better than 10^{-5} eV.

Brillouin zone energy gap calculations on the $k_z = 0$ plane were calculated in VASP using a $30 \times 30 \times 1$ k-mesh and Gaussian smearing. Orbital-projected band structures were calculated using WIEN2k without SOC but were checked against results from VASP and a spin-polarized WIEN2k calculation with SOC. The charge density of valence electrons contributing to energy states within 0.1 eV of the Fermi level was computed using WIEN2k. Irreducible representations of electronic bands were determined using the IRREP subprogram in WIEN2k. The Brillouin zone Dirac crossing calculations were performed by projecting our VASP calculations onto maximally localized Wannier functions using Wannier90,[91] starting from initial projectors corresponding to valence orbitals (Na s and p; Pd/Pt s,p, and d; O s and p), constructing a tight-binding model from these localized Wannier functions, and subsequently using the GapPlane and GapCube functions in the Wannier Tools package [166] with 400×400 and $200 \times 200 \times 200$ sampling meshes, respectively. The tight-binding models are very slightly asymmetrical with respect to the cubic crystalline structure; this is a result of Wannier90's Wannier function localization algorithm rather than inherent asymmetry in the original DFT simulation. Structures were visualized with VESTA.[167]

2.3 Results

The electronic band structures of $NaPt_3O_4$ and $NaPd_3O_4$ with and without the inclusion of SOC are given in Fig. 2.2. We focus our attention on the bands near the Fermi

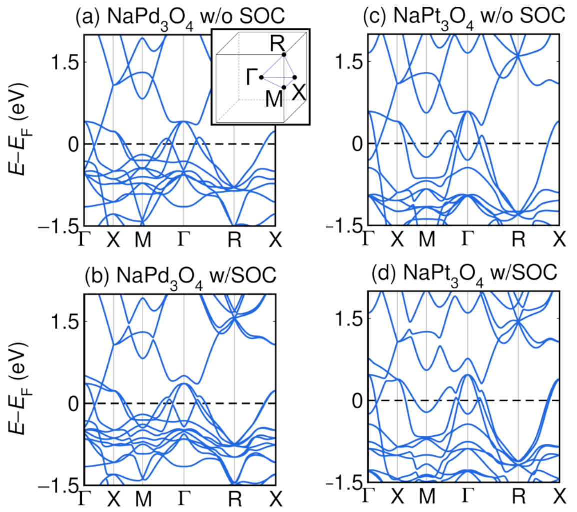

Figure 2.2: NaM_3O$_4$ band structure. Band structures of NaPd$_3$O$_4$ (a) without and (b) with SOC and NaPt$_3$O$_4$ (c) without and (d) with SOC calculated using the PBE functional in VASP. A linear band crossing near the Fermi level is evident in the $\Gamma - X$ direction with large energy dispersion (≈ 0.5 eV). Smaller linear band crossings occur along $M - \Gamma$ and $\Gamma - R$.

level from the Γ to X high symmetry points. These bands cross just below the Fermi level with a large linear energy dispersion that is as great as 0.5 eV in NaPt$_3$O$_4$. Viewing along the $M - \Gamma$ and $\Gamma - R$ branches, additional, smaller linear band crossings can be seen. A close-up view of the band crossings is provided in Fig. 2.3. The Dirac crossings along $\Gamma - X$ and $\Gamma - R$ are symmetry-protected, while the $M - \Gamma$ crossing is gapped out when SOC is included. Calculations in VASP and WIEN2k show good agreement for states above the Fermi level and in the Fermi level region where the Dirac crossings lie. Predicted energies for states below the Fermi level differ slightly for the two methods. This is unsurprising given the local orbital approach in WIEN2k. Although WIEN2k calculations are not shown in Fig. 2.2 for the sake of visual clarity, a direct comparison of the band structures calculated in both codes is available in the supplementary information.[163]

Nonsymmorphic symmetry protects multiply-degenerate band crossings in both ma-

(a) NaPt$_3$O$_4$ w/o SOC

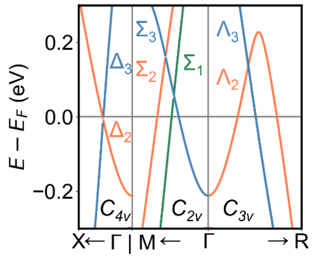

(b) NaPt$_3$O$_4$ w/SOC

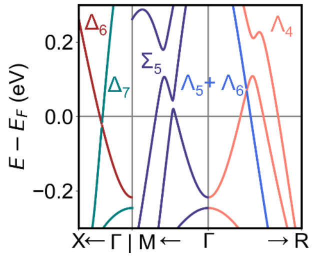

Figure 2.3: Close-up views of NaM_3O$_4$ Dirac cones. Dirac cones lie along the $\Gamma - X$, $M - \Gamma$, and $\Gamma - R$ paths of the band structures of NaPt$_3$O$_4$ (a) without and (b) with SOC calculated in WIEN2k. The Dirac cones along $M - \Gamma$ are gapped by SOC whereas the other Dirac cones are protected in both compounds. Colors of the plotted bands represent calculated irreducible representations (irreps).

terials. Eight-fold crossings can be seen at energies near 1.5 eV and between -0.6 eV and -1.5 eV at the R point, the energy of the latter, sub-Fermi level degeneracy varying significantly with M site species and simulation program. While the eight-fold crossings are very far from the Fermi level in these compounds, they are relevant to electronic structure of closely-related compounds. It has been shown that the Fermi level of the isostructural compound LaPd$_3$S$_4$ lies near the upper eight-fold degeneracy at R and Pt$_3$O$_4$ appears to have a Fermi level near the lower eight-fold degeneracy.[80]

In order to explore the origins of the Fermi level Dirac crossings, we consider symmetry and orbital character. Formally, symmetry protects band crossings from gapping if the two crossing bands have different irreducible representations (irreps) with respect to the point group of the k-vector.[30] When SOC is significant, the two band irreps must be different with respect to the double group, which accounts for spin.

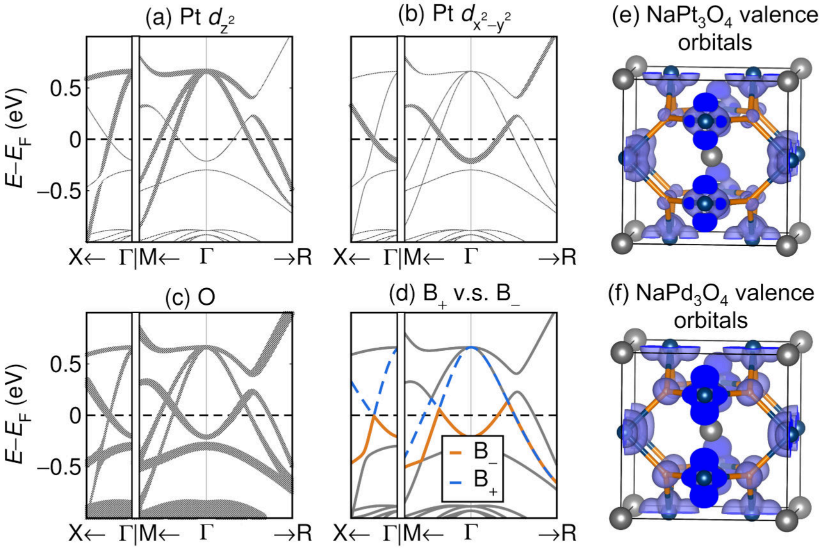

Figure 2.4: Determination of NaM_3O_4 band orbital character. (a)-(c): orbital projected band structures of $NaPt_3O_4$ calculated in WIEN2k. Dirac cones are generated by the crossing of M d_{z^2} and M $d_{x^2-y^2}$ bands. (d): the same plot with an overlay of the simulation-defined bands B_+ and B_- that form the tops and bottoms of the Dirac crossings, respectively. These bands will be further visualized in Fig. 2.5 and Fig. 2.6. (e,f): Charge density of valence states contributing to bands within 0.1 eV of the Fermi level in $NaPt_3O_4$ and $NaPd_3O_4$, respectively, suggesting primary contributions from Pt $d_{x^2-y^2}$ and d_{z^2} orbitals in combination with O p orbitals. The charge density is visualized at a constant contour of 0.0021 e^- Å^{-3}.

The gapping of the Dirac crossing along $M - \Gamma$ when SOC is introduced can be explained as a consequence of the cubic space group. The $\Gamma - X$, $M - \Gamma$ and $\Gamma - R$ lines in k-space obey C_{4v}, C_{2v}, and C_{3v} point group symmetries, respectively. Without SOC, the crossing bands have different irreps in each of these point groups and all three crossings are allowed (See the irrep-colored bands of Fig. 2.3). When SOC is introduced, there is only one spinor irrep available in the double group of C_{2v} and the Dirac crossing along $M - \Gamma$ therefore gaps out. Explicitly, we calculate the irreps of the crossing bands along the three high-symmetry Brillouin zone lines in the system with SOC: $\Gamma - X : \{\Delta_6, \Delta_7\} \rightarrow \{\Delta_7, \Delta_6\}$; $M - \Gamma : \{\Sigma_5, \Sigma_5\} \rightarrow \{\Sigma_5, \Sigma_5\}$; $\Gamma - R : \{\Lambda_4, \Lambda_5 + \Lambda_6\} \rightarrow \{\Lambda_5 + \Lambda_6, \Lambda_4\}$.[42] The irreps are identical for both the Pd and Pt compounds. There is an exchange of irreps at the $\Gamma - X$ and $\Gamma - R$ crossings, and these crossings are therefore protected, while no such exchange can occur along $M - \Gamma$. More specifically, the Dirac crossings along $\Gamma - X$ and $\Gamma - R$ are protected by C_4 and C_3 rotational symmetry, respectively, as the irreps of the crossing bands at these points are distinguished by their character with respect to these symmetry operations. Overall, we can state that the symmetry protections in the system are completely general properties of the cubic Brillouin zone and can be extended to cubic compounds in other space groups.

Figure 2.4 presents orbital-projected band structures and a visualization of the valence electron charge distribution contributing to energy states near the Fermi level in NaM_3O_4. The difference in symmetry between the bands crossing at the Dirac cones can be seen to reflect a difference in orbital origin. The dominant contributions are from M $d_{x^2-y^2}$ and d_{z^2} orbitals in tandem with O (mainly p) states. Density of states calculations supporting this conclusion are also offered in the supplement.[163] The Dirac crossings are created by the overlap of partially-filled d_{z^2} bands with large-dispersion $d_{x^2-y^2}$ bands that dip down in energy at Γ. Oxygen states overlap significantly with

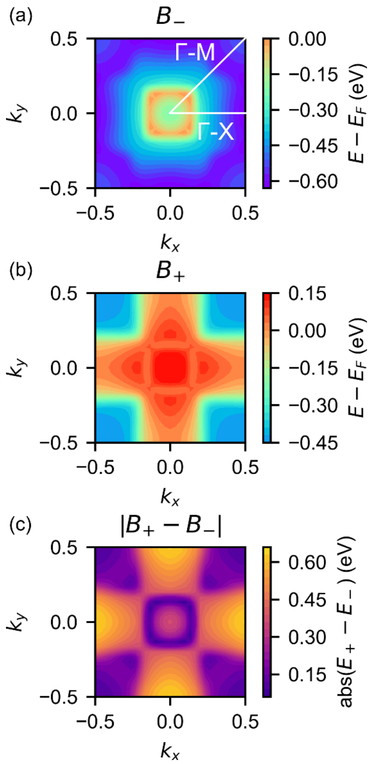

Figure 2.5: Heatmaps of NaM_3O_4 band energies on the $k_z = 0$ plane. Energies of the B_- and B_+ bands are shown for $NaPt_3O_4$ with SOC. The absolute value of the energy separation between the B_- and B_+ bands is shown in (c). The Fermi-level Dirac crossings between the B_- and B_+ comprise an approximately square energy degeneracy loop in the region $\{-0.2 \leq k_x \leq 0.2; -0.2 \leq k_y \leq 0.2\}$.

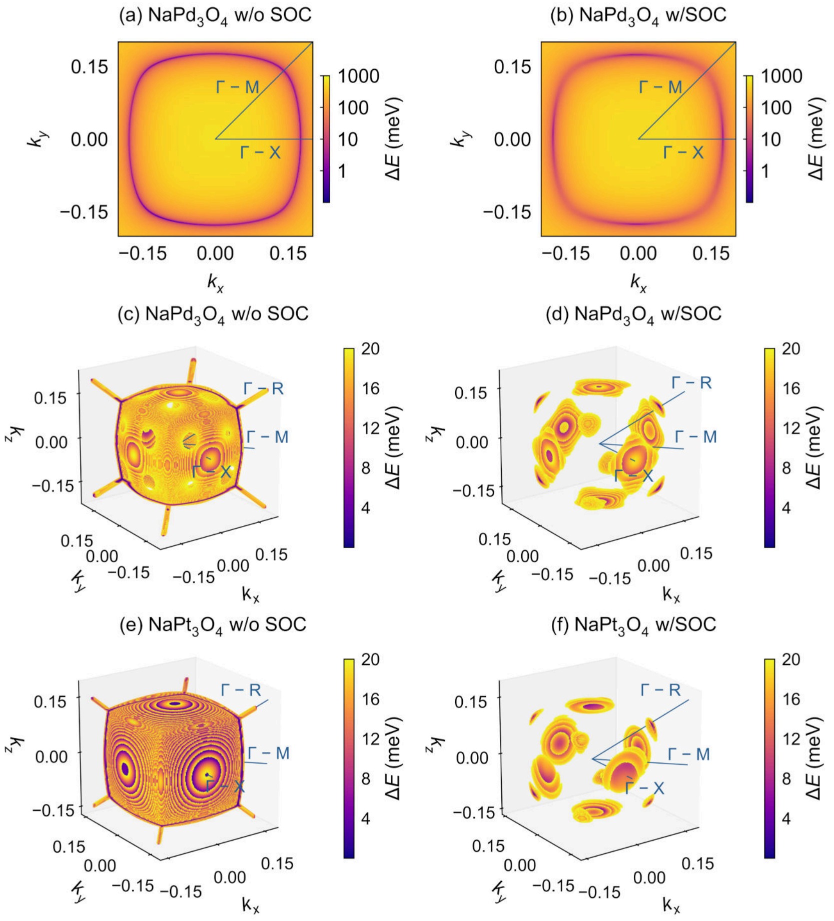

Figure 2.6: Visualization of NaM_3O_4 nodal surfaces. High-resolution calculations of energy-splitting between NaM_3O_4 B_+/B_- bands in k-space, performed with tight-binding model: 2D plots in (a) and (b) show all energies on a logarithmic scale, while for 3D plots in (c-f) the maximum energy cutoff was 20 meV.

both orbitals, but interact more strongly with the $d_{x^2-y^2}$ band. It is important to note here that we are using a local bonding basis to describe the the states, rather than the crystal coordinates, such that $d_{x^2-y^2}$ refers to an M orbital with lobes pointing along the square planar coordinated bonds towards oxygen. Although the orbital decomposition generally follows the energy level diagram of Fig. 2.1(c), the non-negligible interaction of oxygen states with the d_{z^2} might be somewhat unexpected. Figure 2.4 (e,f) show that the O p orbitals are oriented along $[111]$ axes, facing out of the square coordination plane defined by M-O bonding such that they can interact with additional orbitals along the z-axis. The Pd compound has more disperse orbitals than the Pt compound and has less directional d orbital preference along the Pd-O bonds (the Pd d orbitals have more d_{xy} character in addition to the primary $d_{x^2-y^2}$, d_{z^2} character).

From the perspective of simulation, all three Dirac crossings of interest occur between the same two bands. Since the system is metallic, there is no good division between "valence" and "conduction" bands, we refer to the band with greater energy at the Γ point, which descends in energy towards the Dirac crossings along Γ-X, Γ-M, and Γ-R, as the "B_+" band, while the band with lower energy at Γ will be referred to as "B_-." These simulation-defined bands are visualized in Fig. 2.4(d). While this scheme is sufficient for our purposes, note that the Γ-R Dirac cone is actually 6-fold degenerate (composed of 3 separate sets of spin-degenerate bands) in the non-SOC calculations, though this degeneracy is gapped by SOC.

Figure 2.5 shows the energy landscape of the B_- and B_+ bands along a constant $k_z = 0$ slice in the (cubic) Brillouin zone for $NaPt_3O_4$. As discussed by Doublet *et al.*, the roughly square shape of the Fermi surface of the d_{z^2} band can be viewed as a consequence of the relative independence of the MO_4 bonding chains along x and y.[148] Despite the 3D connectivity of the M $d_{x^2-y^2}$+ O p bonding network, the corresponding Fermi surface is roughly square as well. The net result is that both the B_- and

B_+ bands have cubic symmetry. There are two regions where these bands come close together: along a square loop at the center of the Brillouin zone, corresponding to the Dirac crossings, and, far below the Fermi level, along the $\Gamma - M$ line from the center of the diagram to the corners.

In order to achieve a higher k-space sampling resolution to more precisely visualize the locations of the Dirac crossings, we implemented Wannier-interpolated tight-binding models as discussed in section 2.2. Figure 2.6 shows calculations of the energy gaps in the area of the Brillouin zone near the central square intersection region of Fig. 2.5. (a) and (b) demonstrate that there is a full square nodal line in the $k_z = 0$ plane that is interrupted by gapping along $\Gamma - M$ when SOC is introduced. (c) and (d) show that the nodal square in the Pd compound without SOC is part of a larger small energy-splitting region with roughly cubic shape, but small holes in the nodal cube, which SOC gaps into eight protected degeneracies along $\Gamma - R$ and six protected degeneracies along $\Gamma - X$ for a total of 14 Dirac points. The $\Gamma - R$ crossings have sharp dispersion whereas the $\Gamma - X$ Dirac crossings have very small dispersion along the faces of the cube and appear flat and plate-like even after SOC is included. The nodal cube in $NaPt_3O_4$ in the absence of SOC is found to be a complete cube, (e), similar to a nodal sphere semimetal. More generally, the cubic degeneracy region in the Pt compound is noticeably more square than the similar region in the Pd compound and the stronger SOC in this compound more fully removes the nodal cube degeneracy, although small, plate-like dispersion along $\Gamma - X$ remains (see supplement for $k_z = 0$ plane nodal lines in $NaPt_3O_4$).[163] At the smallest energy splittings available in our tight-binding models, the intersection region in the Pd compound is reduced to a number of nodal lines. The Pt compound, by contrast, has a full, nodal-cubic Dirac degeneracy in the absence of SOC down to the lowest reasonable simulation energies (see supplement).[163] These qualitative findings were found to be robust to re-parameterization of the tight-binding model using a number of alternative orbital projections, including a model including only the M $d_{x^2-y^2}$, d_{z^2} and O p orbitals previously discussed.

2.4 Conclusions

We have shown that the high symmetry structures of NaM_3O$_4$ result in the formation of 14 Fermi level Dirac crossings that are protected against spin-orbit coupling, with a particularly large linear energy dispersion region about $\Gamma - X$. These compounds can potentially be doped between interesting electronic states including the nonsymmorphic-symmetry-enabled degenerate R point bands of M_3O$_4$, the Dirac cones of NaM_3O$_4$ discussed, and the insulating compounds (Ca/Sr)M_3O$_4$.

The $Pm\bar{3}n$ cubic space group appears promising for the generation of a stable nodal cube state with surface states that could host exciting correlated electron physics.[133] While the compounds discussed here have significant SOC that prevents the realization of a true nodal cube, this state might be achieved in related systems by lowering SOC using lighter elements. The presence of a full nodal cube in the Pt compound without SOC also gives us some hints as to how we might go about creating such a state in a real material. The cubic Dirac degeneracy of these compounds is a direct consequence of the quasi-independence of the MO$_4$ square-planar bonding chains in the unit cell. The d_{z^2} bonding network is nearly independent along the cubic axes resulting in a B_+ band that creates the nodal cubic state [Fig 2.5(a)]. Dirac character along the $\Gamma - X$ direction is directed towards the cubic faces of the (001) single crystal surface with metallic or mixed Dirac-metallic character along other high-symmetry directions. Interaction with the ligand oxygens increases the 3D connectivity of the $d_{x^2-y^2}$ bonding network and reduces the how cubic the Dirac crossings are. In the absence of SOC, increased Pd-O bonding in the Pd compound compared to the Pt-O bonding of the Pt compound results in a less perfect nodal cube degeneracy. A possible way to reduce the M-O bonding would be to increase the lattice parameter though chemical strain, for example though substituting K^+ or Rb^+ for Na^+.

Effects of these predicted Fermi level Dirac crossings and large k-space regions of linear dispersion may be detectable in magnetotransport measurements. A number of compounds in this family, including $Na_xPt_3O_4$, have been previously synthesized as single crystals suitable for transport studies.[168, 169, 170, 171] Nodal-line semimetals frequently show signs of anomalous transport such as large magnetoresistance and low-field quantum oscillations.[172, 173]

The band inversion in this system results from bonding chains, rather than the relativistic contraction of s orbitals on a single atomic site (as in the now-canonical DSM examples Na_3Bi and Cd_3As_2), so this compound can be classified with other new "molecular" semimetals such as ZrSiS that feature large linear energy dispersion.[118]

The significance of the transport contribution from linear bands to catalysis has not yet been fully deciphered. Nonetheless, Dirac transport in NaM_3O_4 may further our understanding of the Adams catalyst on the centennial of its discovery. While topological semimetals have been previously examined as catalysts for the hydrogen evolution reaction, hydrogenation catalysts may also prove a fruitful avenue of inquiry.

Chapter 3

Weyl nodes and magnetostructural instability in antiperovskite $\mathrm{Mn_3ZnC}$

[1]The room temperature ferromagnetic phase of the cubic antiperovskite $\mathrm{Mn_3ZnC}$ is suggested from first-principles calculation to be a nodal line Weyl semimetal. Features in the electronic structure that are the hallmark of a nodal line Weyl state—a large density of linear band crossings near the Fermi level—can also be interpreted as signatures of a structural and/or magnetic instability. Indeed, it is known that $\mathrm{Mn_3ZnC}$ undergoes transitions upon cooling from a paramagnetic to a cubic ferromagnetic state under ambient conditions and then further into a non-collinear ferrimagnetic tetragonal phase at a temperature between 250 K and 200 K. The existence of Weyl nodes and their destruction via structural and magnetic ordering is likely to be relevant to a range of magnetostructurally coupled materials.

3.1 Introduction

Antiperovskite carbides are a family of materials with the cubic perovskite structure and formula $X_3B\mathrm{C}$ where X is the least electronegative element in the formula and C

---

[1] The contents of this chapter have previously appeared in Ref. [125]. Reproduced from S. M. L. Teicher and I. K. Svenningsson, L. M. Schoop, and Ram Seshadri, Weyl nodes and magnetostructural instability in antiperovskite $\mathrm{Mn_3ZnC}$, *APL Mater.* **7**, 121104 (2019), with the permission of AIP Publishing.

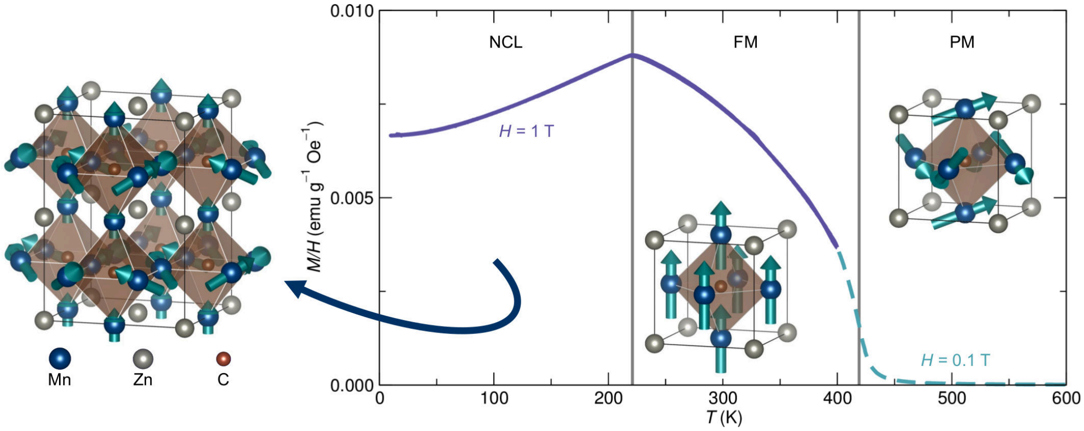

Figure 3.1: Reported crystal and magnetic structures of Mn_3ZnC. Mn_3ZnC undergoes transitions from paramagnetic (PM) to ferromagnetic (FM) states in the cubic antiperovskite structure with a $T_C \approx$420 K. A lower temperature antiferromagnetic transition with $T_N \approx$219 K is associated with noncollinear ferrimagnetic ordering in a tetragonal structure.

is carbon (see Fig. 3.1). Related carbides have a long history in metallurgical research, associated with the larger family of so-called MAX phases.[174] Several members of the family such as Co_3AlC[175] have been explored for applications in structural alloys and Mn_3SnC[176] and carbon-doped Mn_3ZnN[177] exhibit negative thermal expansion effects. Some antiperovskite carbides are also of interest for their functionality. Mn_3GaC is known to display giant magnetoresistance[178] and Ni_3MgC is an 8 K superconductor, the latter rationalized by first principles calculations as being associated with a flat band with large density of states near the Fermi level.[179, 180]

More recently, the larger class of antiperovskites has been explored due to the prediction of topological electronic states. The Ca_3PbO and Ca_3BiN families include Dirac semimetals[181, 182]—materials with a graphene-like linear-band crossing, or Dirac cone, near the Fermi level[37, 130]—as well as topological insulators[183] and topological crystalline insulators[184] with a bulk band gap and metallic surface states. Magnetization and resistivity data in two recent studies on Sr_3PbO and Sr_3SnO provide preliminary evidence for Dirac transport[185] and low-temperature superconductivity,[186] respectively. The Cu_3PdN family is predicted to include nodal line semimetals, in which Dirac crossings persist over an extended region, a line, rather than a single point in the Brillouin zone.[187] Nodal line semimetals can host a unique class of drum-head topological surface states with k-vectors connecting all the Dirac nodes on the nodal ring in the Brillouin zone.[132] However, as is common in predicted nodal line compounds, the relatively large spin-orbit coupling due to the heavy Pd atom in Cu_3PdN partially gaps the nodal line, preventing the realization of a true nodal line semimetal.[187]

The topic of this chapter is Mn_3ZnC, a material that has been explored since the 1950s due to its interesting magnetic transitions. In a series of studies, Butters and Myers,[188] Brockhouse and Myers,[189] and Swanson and Friedberg[190] provided early characterization of these transitions, which include a paramagnetic to ferromagnetic transition with reported Curie temperatures 350 K$< T_C <$500 K[188, 191, 192] and antiferromagnetic ordering with reported Néel temperatures 215 K $< T_N <$ 233 K.[188, 191, 192] In the 1970s, Fruchart and colleagues solved the magnetic structures via neutron diffraction, determining the [001] ferromagnetic room temperature structure and more complex non-collinear low temperature structure shown in Fig 3.1.[193, 191] The magnetic moments, localized on the Mn site, are approximately 1.3 μ_B in the ferromagnetic state and 2.7μ_B and 1.6 μ_B in the noncollinear, antiferromagnetically-coupled and collinear, ferromagnetically-aligned layers of the low temperature structure, respectively. The low magnetic moments suggest that the magnetism is fairly itinerant in this system relative to most Mn magnetic materials. In the 1980s, the transition shifts in Mn_3ZnC were studied under large applied magnetic fields and pressures.[192, 194]

Theoretical attempts to explain the magnetic transitions in Mn_3ZnC have focused on the presence of a large Fermi level flat band. In 1975, Jardin and Labbé proposed that the main bonding interactions in this system originate from Mn d_{xz}, d_{yz} and C p orbitals and generated a tight-bonding model with sharp peaks in the density of states.[195] Should the Fermi level lie at one of these peaks, the ferromagnetic to paramagnetic transition could be explained by Stoner exchange and the low temperature structural distortion by a Jahn-Teller-like energetic benefit accrued through further reducing the density of states near the Fermi level. Non-spin polarized density of states calculations reported later indeed found a large spike in the density of states just above the calculated Fermi level.[196] This work was extended with density of states calculations on both the spin-polarized, ferromagnetic and non-collinear, ferrimagnetic structures, demonstrating that spin polarization opens up a pseudo gap at the Fermi-level in the ferromagnetic phase, consistent with a Stoner exchange mechanism, and that a wider gap opens just below E_F in the ferrimagnetic state.[197]

Here, we use first principles calculations to show that the cubic ferromagnetic phase of Mn_3ZnC that is stable at room temperature is a nodal line Weyl semimetal. Although Weyl nodes are common in ferromagnetic metals, including bcc Fe,[198] to-date studies on Weyl nodal lines are more of a rarity: the first experimental work towards verification of a Weyl nodal line has recently been completed for the Heusler compound $MnCo_2Ga$.[199] In Mn_3ZnC, we present a computational bonding analysis that provides qualitative explanations for the magnetic transitions that create and destroy this delicate Weyl ferromagnet phase. Motivated by interest in the Weyl nodes and their potential role in magnetostructural instabilities, we experimentally revisit the transitions in this material via magnetoentropic mapping, which is a sensitive probe for low energy and metamagnetic reordering.

3.2 Methods

3.2.1 Computational

Density functional theory simulations were completed in VASP [150, 151, 152] and WIEN2k[153] using the Perdew, Burke, Ernzerhof functional [94] with projector augmented waves,[90, 154] and linear augmented plane waves + local orbitals[155], respectively. PAW potentials for VASP were selected based on the version 5.2 recommendations. All calculations described in the text were performed in VASP other than the band irrep assignments of Fig. 3.3 (c), which were completed using the IRREP subprogram of WIEN2k. A $17 \times 17 \times 17$ Γ-centered k-mesh was employed for electronic structure simulations of the ferromagnetic phase. These calculations are well-converged for much lower density k-meshes, but high k-mesh density is desirable for accurate Wannier function fitting; an $8 \times 8 \times 8$ mesh was used for relaxation steps. Calculations for the expanded low temperature tetragonal cell were performed using a $5 \times 5 \times 4$ Γ-centered k-mesh for relaxation and self-consistent steps and a $7 \times 7 \times 5$ mesh for the density of states. The plane wave energy cutoff for VASP and the plane-wave expansion parameter, RKMAX, for WIEN2k were set to values better than 500 eV and 8.0, respectively. Tetrahedral smearing with Blöchl corrections[162] was used for relaxations and self-consistent calculations. Structures were relaxed in VASP via the conjugate gradient descent algorithm with an energy convergence cutoff of 10^{-4} eV. Subsequent self-consistent static calculations and non self-consistent electronic structure calculations were performed using VASP and WIEN2k with energy convergence better than 10^{-5} eV. The surface states of Mn_3ZnC were determined by projecting our VASP calculations onto maximally localized Wannier functions using Wannier90,[91] starting from initial projectors corresponding to valence orbitals (Mn d; Zn s, p, d; C p; with a frozen fitting window $E_F \pm 2\,\mathrm{eV}$), constructing a tight-binding model from these localized Wannier functions, and finally using the Wannier Tools package [166] to calculate the Green's function spectrum.[113] The VASP simulations input into Wannier90 were simulated with noncollinear spins on a non-symmetrized k-mesh with and without SOC. The Mn magnetic moments in these simulations were constrained to point along [001]. Fine k-mesh mapping of the Weyl node locations in the 3D Brillouin zone was also performed on this tight-binding model. Berry curvature was determined using the Wannier90 KSLICE module. The band structure of Fig. 3.5 was unfolded using BandUP.[200, 201] Orbital projections, density of states, and crystal orbital Hamiltonian populations for the high temperature phase were determined using LOBSTER.[33, 34, 35, 36] The density of states and orbital projections for the low temperature structure are reported using default VASP projections as LOBSTER does not support noncollinear magnetism. A post-process Gaussian smoothing with standard deviation 0.2 eV was applied to all calculated density of states and COHPs. Structures are visualized with VESTA.[167]

3.2.2 Experimental

Samples of Mn_3ZnC were produced by a two-step solid-state synthesis, following a previous report,[192] starting from stoichiometric quantities of Mn (Fisher Scientific, 99.95%), Zn (Strem Chemicals, 99.9%), and C (Alfa Aesar, 99%) and adding 7 mass % Zn during the second mixing step. Additional Zn was included to decrease the Mn:Zn ratio of the final material towards 3. Wavelength-dispersive X-ray fluorescence measurements performed on a Rigaku ZSX Primus IV suggest that the composition is close to $Mn_{3.16}Zn_{0.84}C$. Magnetic measurements were performed on a Quantum Design MPMS3 operating under vibrating sample magnetometer mode. High temperature measurements (T >400 K) including the PM-FM transition utilized the oven heater stick attachment option while lower temperature measurements used a standard brass sample holder. The magnetization curve in Fig. 3.1 was generated by measuring magnetization at fields of 1 T, 0.1 T; below and above 300 K, respectively, and normalizing the high temperature magnetization curve such that there was no discontinuity at 300 K. $\partial M/\partial T$ and ΔS_M curves are calculated using methods reported previously.[202] Additional experimental details, including our attempts to develop an original microwave synthesis route for this and related antiperovskite carbides, are provided in the supplementary material.[203]

3.3 Results

We first consider the density of states (DOS) for the cubic, ferromagnetic phase of Mn_3ZnC, as shown in Fig. 3.2. We consider only Mn d states because other orbital contributions are small near the Fermi level (see supplementary material[203]). From Fig. 3.2 (a), we can see that the DOS is relatively large at the Fermi level and that there is a large DOS peak just above this level. This is consistent with the hypothesized Stoner exchange mechanism for the ferromagnetism in this material. Indeed, in the spin-polarized calculation, Fig. 3.2 (b), we find that the onset of ferromagnetism eliminates this DOS peak, reducing the Fermi-level DOS. The mechanism appears to be somewhat distinct from that originally proposed by Jardin and Labbé, however, as the near-Fermi level DOS peak in the non spin-polarized calculation originates from Mn d_{xy} states, rather than d_{xz}/d_{yz} states. Here, we consider the local symmetry of the Mn d orbitals in terms of the cell coordinates (this is the preference in prior literature). From this perspective, we find that the d_{xz}/d_{yz} orbitals are equivalent and point from one Mn towards its Mn neighbors and are involved in strong Mn-Mn bonding and some Mn-C bonding. d_{z^2} and d_{xy} orbitals have lobes pointing from Mn towards C and Zn atoms and

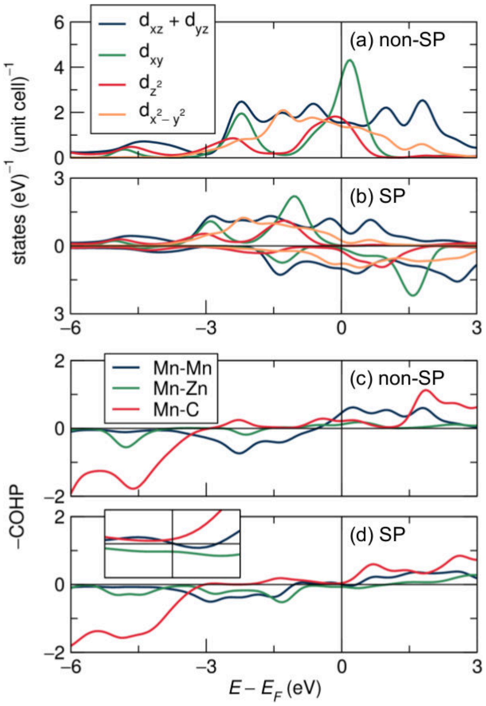

Figure 3.2: Density of states and crystal orbital Hamiltonian population for the Mn_3ZnC ferromagnetic phase. Partial density of states of the dominant Mn d-orbital contributions are compared (a) without and (b) with spin polarization. The crystal orbital Hamiltonian populations for Mn-Mn, Mn-Zn, and Mn-C bonding are presented (c) without and (d) with spin polarization. Inset of (d) shows close-up of COHP in the region just about the Fermi level ($E_F \pm 0.5$ eV).

are expected to be important in Mn-C and Mn-Zn bonding, respectively. Finally, $d_{x^2-y^2}$ orbitals point directly towards no other atom and are expected to be more weakly involved in bonding.

The proposed picture of a simple ferromagnetic distortion is further complicated when we consider these bonding interactions via the crystal orbital Hamiltonian population (COHP), a quantity derived from wavefunction overlap that is negative for bonding and positive for antibonding interactions. In a normal ferromagnet, such as iron, the COHP shows significant antibonding at the Fermi level.[204] By splitting the spin populations, the normal ferromagnet is able to stabilize and fill a greater number of bonding states near the Fermi level, and relatively few antibonding states. The d_{xy} orbitals, however, are not expected to be strongly (anti-)bonding; the COHP, Fig. 3.2 (c), confirms the relatively weak strength of Mn-Zn interactions in this energy region. Rather than elimination of a sharp antibonding peak due to the d_{xy} states, the spin-polarization appears to be stabilized by two effects: first, the reduction of the antibonding states just below the Fermi level and, second, the development of Mn-Zn bonding states originating from the originally weakly-bonding d_{xy} band, Fig. 3.2 (d). In the end, rather than a magnetic metal with a large number of bonding states at the Fermi level, we are left with a semimetal that has non-bonding character near E_F. Examining the COHP immediately about the Fermi level (Fig. 3.2 (d), inset), we find that the Mn-Zn interactions are bonding and the Mn-C interactions are anti-bonding. The Mn-Mn COHP displays a subtle cross-over from antibonding to bonding at the Fermi level. Such a Fermi level COHP cross-over is typical of antiferromagnetic metals, although it usually involves bonding states below the Fermi level and antibonding states immediately above. In analog to the simple tight-binding chain model of $1s$ orbitals, which forms a metal with a completely filled bonding band that can support a symmetry breaking lattice displacement of the atoms with a resulting bandgap, the Peierls

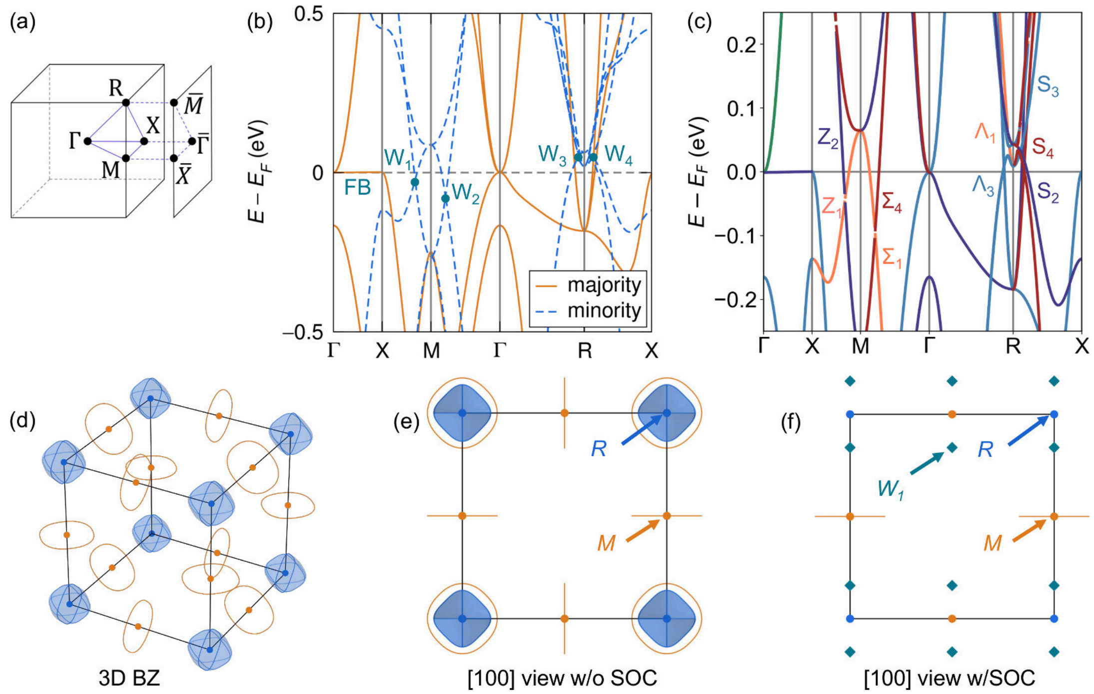

Figure 3.3: Mn_3ZnC bulk band structure and Weyl crossings. (a) high-symmetry points in the bulk Brillouin zone and (100)/(001) surface-projected Brillouin zone. (b) spin-polarized band structure showing a flat-band in the majority states and four types of near-Fermi level Weyl crossing. (c) close-up band structure with bands colored by irreducible representation. (d-f): schematics of Weyl surfaces in the 3D Brillouin zone. (d) 3D view without SOC. (e) (100) view without SOC. (f) (100) view with SOC. In the absence of SOC, Nodal loops are displayed around M (orange) and 3D nodal surfaces around R (blue). With magnetization along [001], SOC gaps the nodal surfaces and many of the nodal loops, leaving behind $k_z = 0$ nodal loops and isolated W_1 nodes.

distortion,[29] the bonding in Mn_3ZnC appears susceptible to symmetry breaking via both physical lattice distortion and antiferromagnetic ordering, either of which could distinguish the Mn sites and generate an electronic gap.

This ferromagnetic semimetal phase becomes much more interesting when we consider the electronic band structure in Fig. 3.3, which reveals several Weyl nodes. Fig. 3.3 (a) depicts the bulk cubic Brillouin zone. Fig. 3.3 (b) presents the spin-polarized band structure with orange majority bands and blue minority bands. Five features of interest are labeled. First, despite the gapping of the density of states at the Fermi level, a flat band, FB, persists along Γ-X right at the Fermi level. Along X-M and M-Γ, we find linear band crossings, Weyl nodes, in the minority bands, labeled W_1 and W_2. On either side of the R point, we also find linear band crossings just above the Fermi level involving both the majority and minority bands. The Weyl nodes on either side of R are labeled W_3 and W_4. Note, however, that there are actually several Weyl nodes on either side of R and this labeling is a reduction for the sake of simplicity.

The colors of the bands in Fig. 3.3 (c) depict the irreducible representations (irreps) of bands involved in the Weyl crossings. A band crossing is protected against gapping if the irreps of the two crossing bands are different; this represents orthogonality of the electronic states generating these bands. In the absence of spin-orbit coupling (SOC), we can consider this system in the paramagnetic space group ($Pm\overline{3}m$, #221). The point group of the k-vectors along X-M, M-Γ and R-X is C_{2v} and along Γ-R the point group is C_{3v}. The Z_1 and Z_2 irreps differ in their symmetry with respect to C_2 rotation and the mirror operation σ_v', indicating that the W_1 node is protected by these operations. The Σ_1 and Σ_4 irreps differ with respect to C_2 rotation and the mirror operation σ_v. The W_4 nodes involve crossings of S_2, S_3, S_4 bands. The nearest Weyl crossings to the Fermi level along Γ-R and R-X actually involve bands with the same irrep, Λ_3 and S_4, respectively. However, these crossings have bands of orthogonal spinor character, as can be seen when comparing with Fig. 3.3 (b). When SOC is incorporated in the simulation, we must consider the coupling of the magnetic moment to the lattice as well as majority / minority spin mixing interactions. Spin mixing gaps the lowest energy W_3, W_4 crossings and the breaking of C_2 and mirror symmetries along R-X gaps the W_4 Weyl nodes. The W_3 Weyl crossings due to Λ_1, Λ_3 crossings, meanwhile, are left untouched by SOC. When considering the $k_x = 0$ Brillouin zone plane, which in the non-SOC calculation had been equivalent, however, both nodes are not preserved. Viewing the W_1 and W_2 nodes, on the $k_x = 0$ plane, we find that two of the four W_1

nodes and all four of the W_2 nodes gap out (see supplement for additional details on the effect of SOC). In all cases, the magnitude of the SOC gaps in this material are relatively small due to its low-mass $3d$ electrons.

Mapping the Weyl nodes in the 3D Brillouin zone, we find that the Weyl nodes in this system are not isolated points, but instead nodal lines and surfaces as depicted in Fig. 3.3 (d,e). The W_1 and W_2 nodes are part of a nodal line about the M point whereas the lowest energy W_3 and W_4 nodes form a 3D connected surface about the R point. Because of the large number of $W_{3,4}$ Weyl crossings, additional $W_{3,4}$ nodal surfaces may exist which have not been considered. In general, although individual band crossings and nodal lines can be protected, there are no symmetries that can fully protect a 3D nodal surface in the presence of SOC.[133, 124] The nodal surfaces depicted in Fig. 3.3(d,e) about R are no exception. Because these surfaces result from the crossing of bands of opposite spinor character, and SOC allows spin-channel mixing, these nodal surfaces gap out and the nodal surface is no longer realized in the final electronic structure after SOC has been incorporated. We find that some of the M nodal lines, however, are protected. The nodal loops on the $k_z = 0$ plane are protected against gapping, while the nodal loops on the $k_x, k_y = 0$ planes gap, leaving only isolated Weyl crossings on the X-M lines. This results in the spin-orbit-gapped configuration shown in Fig. 3.3 (f).

The protection of the M nodal lines is a direct result of the mirror symmetry in the cubic antiperovskite structure. While we have already shown that a combination of C_2 and mirror symmetries protects the band crossings along the Γ-M and M-X high symmetry lines, recomputing the irreps along a generic path through the loop with point group C_s shows the band crossings to be protected by $\overline{C_2}$, which is equivalent to a mirror. The M nodal lines on the $k_z = 0$ plane are preserved under SOC because the [001]-oriented collinear magnetic moment does not break mirror symmetry on this

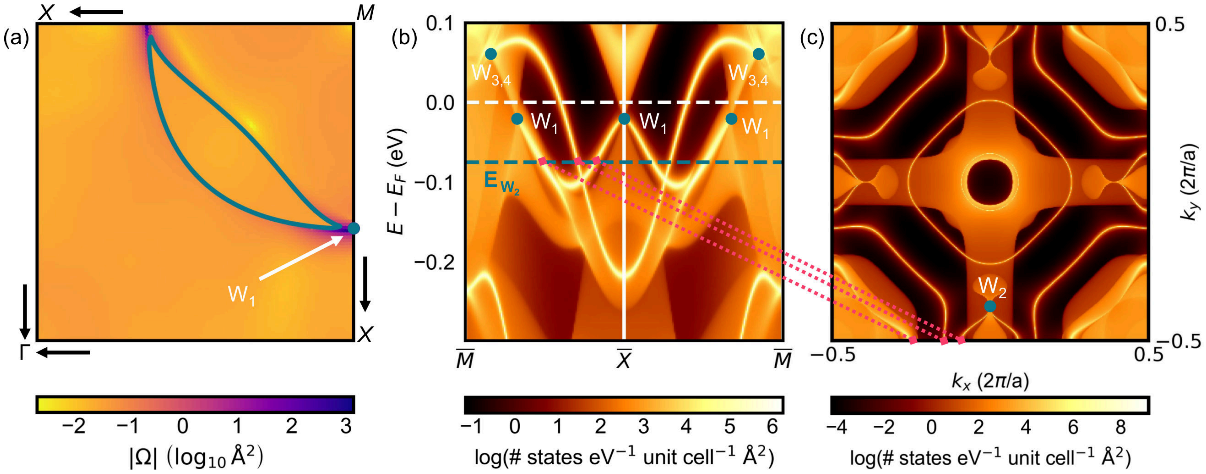

Figure 3.4: Characterization of Weyl behavior in Mn$_3$ZnC. (a) $k_z = 0$ cut through the bulk BZ showing large Berry curvature near the W_1 Weyl crossings. A constant energy band-cross-section is overlaid in teal. (b) surface density of states calculation showing brightly-colored surface states connecting between $W_{3,4}$ and between W_1 Weyl points. The energy level of the W_2 Weyl points is also shown. (c) constant energy Fermi arc calculation for the (001) surface at the energy level of the W_2 nodes. Dotted pink lines connect between surface states at the W_2 level in (b) and the locations of these states in (c) to guide the eye.

plane. Likewise, the M nodal lines on the $k_x, k_y = 0$ planes gap because the magnetic moment does break the mirror symmetry on these planes—except at the W_1 nodes where the nodal line is tangent to the $k_z = 0$ plane and perpendicular to the [001]-magnetic moment.

These nodal lines are similar to those described in a theoretical tight-binding model of Ca$_3$P$_2$ with imposed spin and previously predicted in alloys of the real material ZrCo$_2$Sn (also under [001] magnetization).[132, 205] Due to the soft ferromagnetism and readily-reorientable magnetization in ZrCo$_2$Sn, it was proposed that the effective number of Weyl nodes can be tuned by changing the applied field direction. Mn$_3$ZnC also appears to be a soft ferromagnet and could exhibit similar tunability.

Now that the existence of a protected $k_z = 0$ nodal loop has been established, we might expect to see drumhead surface states connecting between the nodes of this loop on the (001) surface of the material. Fig. 3.4 characterizes the Weyl nodes and their surface states. Weyl nodes can be described as sources and sinks of a quantity called the Berry curvature or Berry flux, defined as:

$$\nabla_{\mathbf{k}} \times \langle u_{\mathbf{k}} | i\partial_{\mathbf{k}} u_{\mathbf{k}} \rangle$$

where $u_{\mathbf{k}}$ represents the Bloch wavefunction.[27] Low energy electronic excitations analogous to quantum Hall surface states, Fermi arcs, are topologically protected between Weyl nodes emitting and collecting Berry flux.[128] Fig. 3.4 (a) shows the magnitude of the Berry flux in the $k_z = 0$ plane at an energy level near the W_1 nodes, highlighting large Berry flux concentration at the nodes. Fig. 3.4 (b) and (c) present the Weyl surface states projected on a (001) surface. We can see bright surface bands connecting between two W_1 nodes and between two $W_{3,4}$ nodes (Note, following Fig 3.3 (a), that the R-M and X-M lines are projected onto the $\overline{M}$ and $\overline{X}$ points when flattening the cubic Brillouin zone along k_z). The energy level of the W_2 nodes is overlaid in teal. In Fig. 3.4 (c), we can see a Fermi surface cut taken at the W_2 energy level with W_2 nodes clearly visible along $\overline{\Gamma}$-$\overline{X}$. Fermi arcs emitting from the W_2 points can be seen to connect to W_2 nodes in the neighboring Brillouin zone due to the periodic boundary conditions. The $\overline{M}$-$\overline{X}$-$\overline{M}$ line in Fig. 3.4 (b) corresponds to the edges of the plot in Fig. 3.4 (c). Comparing between Fig. 3.4 (b) and (c), we see that the surface states connecting the W_1 nodes are identical to the surface states connecting the W_2 nodes; there is indeed a drumhead surface state connecting W_1, W_2 and the other nodes on the nodal line about the M point.

In general, materials with electronic structure features like those in Fig. 3.3 (b)—degenerate flat bands and near-Fermi level band crossings—and especially semimetals with a large concentration of Weyl crossings like this nodal-loop compound, often distort at low temperatures. The energy-lowering transitions that tend to break such nodes

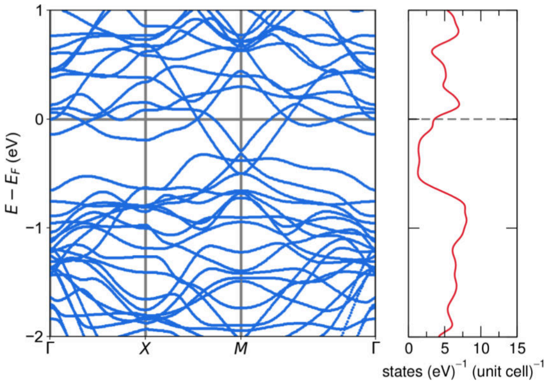

Figure 3.5: Electronic structure of the low temperature phase of Mn$_3$ZnC. (Total) DOS values have been normalized to the high-temperature unit cell to provide fair comparison to Fig. 3.2. A large gap is seen that can be accessed by decreasing the electron count through slight electron deficiency. This unfolded band structure allows a direct comparison of the ferrimagnetic tetragonal cell bands to the band structure of the ferromagnetic cubic unit cell. Although there is significant gapping and removal of Weyl nodes just below the Fermi level, a small number of Weyl nodes persist at E_F.

are frequently referenced to the idealized models of Peierls or Jahn-Teller distortions. The well-established experimental fact is that a symmetry-breaking low-temperature distortion does activate in this material, involving both a tetragonal stretch of the atomic positions and a magnetic reorientation of the spins with partial antiferromagnetic coupling (Fig. 3.1).

The density of states of the low temperature structure provide valuable insight for the origin of the low temperature phase. Fig. 3.5 shows the DOS and band structure of the tetragonal low temperature structure with fully non-collinear spins and associated antiferromagnetic coupling. A large pseudogap is seen to open up in this case, as would be expected from the description of the antiferromagnetic ordering as a Peierls-like symmetry breaking. We also considered simulations with the tetragonal low temperature structure with no spin polarization and collinear, ferromagnetic polarization. However, because the tetragonal distortion is fairly small, the density of states for these phases exhibit only minor changes with respect to those of Fig. 3.2. Further, when allowed to relax, the non-spin polarized and collinear spin polarized structures relax into the cubic structure. This analysis suggests that though both are coupled, it is probably the new magnetic ordering, rather than tetragonal distortion alone, which drives the transition.

The relationship between the new magnetic ordering and potential electronic instabilities, flat bands and Weyl nodes, can be examined via the band structure of the low temperature phase in Fig. 3.5. In order to provide a direct comparison to the band structure and Weyl nodes of the ferromagnetic phase in Fig. 3.3, we have unfolded the bands of the low temperature cell into a Brillouin zone corresponding to that of the low temperature cubic primitive cell. We see that, in the low temperature structure, the flat band and several of the Weyl nodes have disappeared. The DOS pseudogap can be seen in the relatively empty region of the band structure about 0.2 eV below the Fermi level. Despite the formation of the pseudogap, a few Weyl nodes remain at the calculated Fermi level. Part of the discrepancy between our simulation and the expectation for the stabilization of a pseudogap *at the Fermi level* likely results from electron deficiency in the real material. As early as Butters and Myers' first study, Mn_3ZnC was found to have varying composition and magnetic properties with nominal Mn:Zn ratios greater than 3.[188] The Mn:Zn ratio of our best sample, measured by wavelength-dispersive X-ray fluorescence, was close to 3.76, which, in a rigid band approximation, would result in a deficiency of 0.8 electrons per primitive cubic cell and a Fermi level near the exact center of the pseudogap. We expect that the true Mn:Zn ratio in our samples lies somewhere between the idealized value of 3.00 and the measured value of 3.76; while samples of this material appear pure in laboratory X-ray diffraction, synchrotron X-ray diffraction suggests that small nonmagnetic impurities of carbides Mn_5C_2 and Mn_7C_3 as well as MnO (which orders antiferromagnetically, but far lower in temperature than the transitions discussed here) may be present in addition to the majority Mn_3ZnC phase.[206]

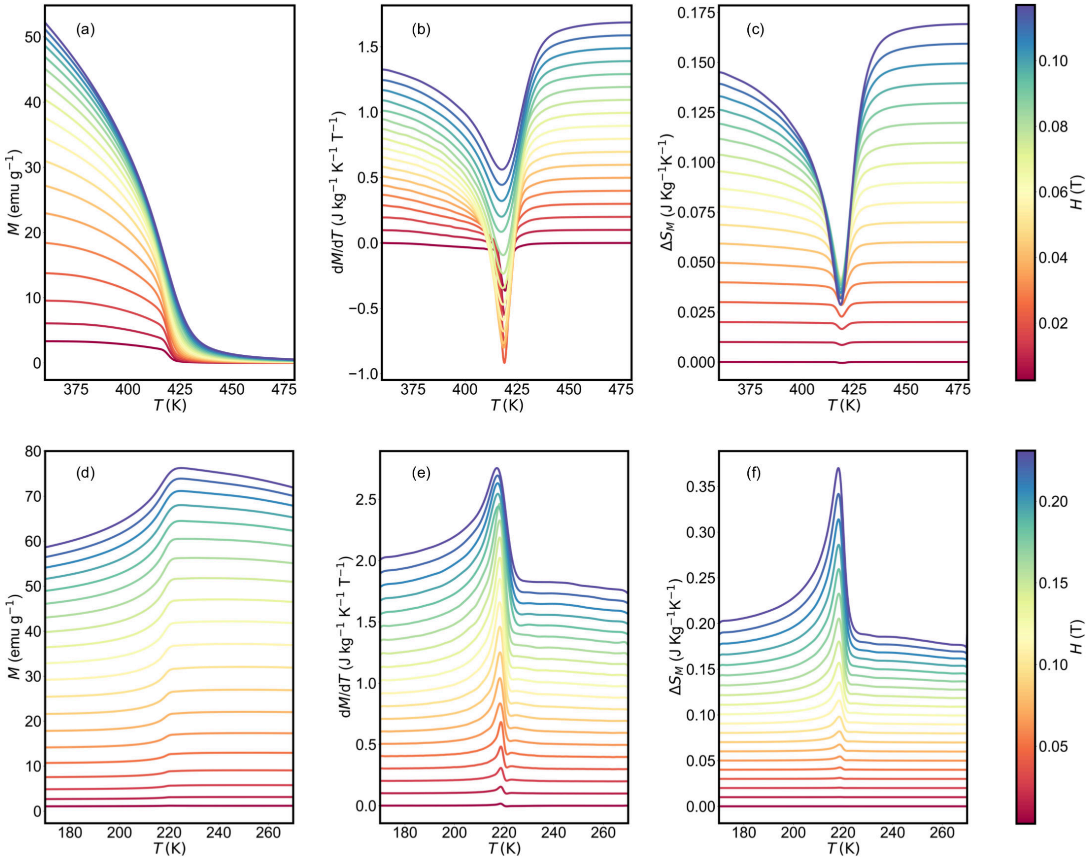

Figure 3.6: Magnetoentropic mapping of the Mn_3ZnC PM-FM and FM-NCL transitions. (a) line plots of the magnetization, (b) magnetization derivative ($\partial M/\partial T$), and (c) magnetic entropy change (ΔS_M) taken under varying magnetic field are shown across the paramagnetic to ferromagnetic transition that occurs at approximately $420\,\mathrm{K}$ in our sample. (d-f) provide similar plots for the FM-NCL transition ($\approx 219\,\mathrm{K}$). Lines in (b,e) and (c,f) are offset by 0.1 and 0.01 units, respectively, for visual clarity.

Motivated by interest in these electronic structure changes associated with magnetostructurally coupled transitions, we performed experimental magnetoentropic characterization of both the high and low temperature transitions. Fig. 3.6 (a) presents magnetization data measured across the paramagnetic to ferromagnetic transition, which takes place near $420\,\mathrm{K}$ in our sample. While magnetization has been measured in older studies, to the best of our knowledge no studies of the the sharp, low field magnetization curves for either of the two magnetic transitions have been previously reported. Fig. 3.6 (b) shows the partial derivative, $\partial M/\partial T$, of these magnetization curves, displaying a large transition peak at low fields that reduces in magnitude and broadens as the field is increased. Fig. 3.6 (c) shows the magnetic entropy change, ΔS_M across the transition. The magnitude of ΔS_M is a direct probe of the magnetostructural coupling strength in this compound.[207] The peak ΔS_M value is significant but not anomalous, suggesting medium magnetostructural coupling strength in this compound. Negative ΔS_M transitions are typical of the magnetocaloric effect seen in paramagnetic to ferromagnetic transitions in many magnetic materials. Characterization of the antiferromagnetic ordering transition in (d-f) is consistent with this finding. This transition is qualitatively similar in that it is sharp for low applied field, broad at high field and has ΔS_M values with approximately the same magnitude of ≈ 0.1 J Kg^{-1} K^{-1}. The positive sign of ΔS_M is typical of the inverse magnetocaloric effect seen at many antiferromagnetic ordering transitions.

3.4 Conclusions

We have shown electronic structure simulations predicting that the room temperature phase of Mn_3ZnC is an exotic Weyl nodal line semimetal with nodal loops, isolated Weyl nodes, and drumhead surface states. The magnetic and electronic characterizations of the two transitions in this material that create and destroy this phase, meanwhile, appear relatively conventional. The upper transition can be explained by the reduction of near-Fermi level antibonding states and strengthening of Mn-Zn bonding, while the lower transition can be explained by the need to break symmetry and open a gap by expanding the unit cell to allow for antiferromagnetic ordering. An electronic Peierls distortion through antiferromagnetic ordering can allow for spin population energy shifts and the formation of a pseudogap that remove flatbands and Weyl nodes near the Fermi level. Despite the significant pseudogap, we found that a limited number of Weyl nodes still persist near the Fermi level in the low-temperature structure. However, even a small electron deficiency, expected based on the tendency towards Zn deficiency in experimental work, moves the Fermi level into the pseudogap of the low temperature structure.

There is interest at present in the Peierls-like structural distortions and phonon resonances associated with Weyl nodes.[208] The finding of Weyl nodal lines in Mn_3ZnC, a classic magnetic transition material, suggests that Weyl instability may play a role in a much wider range of magnetostructurally-coupled materials. Many other magnetic materials that have a low temperature antiferromagnetic ordering likely transition through a semimetal state with near-Fermi level Weyl nodes. In fact, prototypical itinerant antiferromagnet chromium itself, the material for which the electronic Peierls instability concept was coined, hosts Fermi level Dirac crossings in non-spin polarized calculations, some of which are preserved in its transition to a low temperature antiferromagnetic ordering.[123] One major distinction between Mn_3ZnC and conventional antiferromagnetic materials is the reversed Peierls-like bonding structure with antibonding states below the Fermi level, non-bonding states at E_F, and bonding states just above. This reversed bonding structure is indicative of band inversion and could prove a useful hallmark in the search for topologically-interesting magnets.

In addition to the bonding analysis we have presented to explain the structural transitions, important future work will focus on rigorously disentangling the relationship between Weyl nodes, flat bands, and phonon-mediated instabilities in Mn_3ZnC and related semimetals. There is incredible potential for nesting in the Fermi surface of Mn_3ZnC; the flat-bands alone, which perfectly bisect the Brillouin zone in k_x, k_y, k_z directions, provide maximal nesting at the calculated Fermi level in any supercell scheme as well as the tantalizing prospect of coupling flat-band-related correlation effects to Weyl physics. We urge caution. Just as flat band degeneracies in DFT are not a guarantee of interesting correlation effects in experiment, substantial evidence suggests that calculations of Fermi surface nesting are insufficient to prescriptively predict charge density waves, spin density waves and other lattice incommensurate instabilities.[117] An important first step has been provided by a recent study on $(TaSe_4)_2I$, which relates the characteristic q-spacings of the Weyl nodes, peaks in the electronic susceptibility, and CDW-modulation vectors observed in experimental X-ray measurements.[209]

Overall, our results suggest that compounds which display Weyl-like features in idealized high-symmetry structures may actually undergo transitions to more complex ground states than initially supposed.

Chapter 4

3D analogs of square-net nodal line semimetals: band topology of cubic $LaIn_3$

[1]In 2D systems, the origins of topological band structure have been linked to simple chemical bonding models. Here, we investigate the 3D metal $LaIn_3$ and show that its electronic structure and band topology is well-modeled using a tight-binding model consisting of only In p-orbitals. We predict this material to be a nodal line semimetal with Dirac crossings and topological surface states at the experimental Fermi level. This compound can be considered a 3D chemical analog of 2D square-net semimetals in the ZrSiS family, with primary $p_{x,y}$ orbital contributions and cubic connectivity. $LaIn_3$ and related auricupride metals are established superconductors and may provide a valuable platform for exploring the interplay between topological electronic structure and superconductivity.

---

[1] The contents of this chapter are the result of a current collaboration. S. M. L. Teicher, J. Linnartz, R. Singha, D. Pizzirani, S. Klemenz, S. Wiedmann, J. Cano and L. M. Schoop, 3D analogs of square-net nodal line semimetals: band topology of cubic $LaIn_3$. *Submitted*. Reproduced here with permission from the authors.

4.1 Introduction

In recent years, topological materials have been realized in which a band inversion in the bulk electronic structure generates a new and exciting phenomenon—spin-polarized metallic surface states.[6, 128, 30] Topological materials can exhibit a number of interesting transport properties deriving from their electronic structure, including high mobility,[55, 68, 210] quantized circular photogalvanic effect,[71, 72, 73] and large anomalous Hall effect[69, 18, 70]. A new frontier is the combination of topology and correlation effects, especially superconductivity. Theoretical models predict that an intrinsic topological superconductor could host Majorana anyons, quasi-particles that may provide a technological path towards developing a topological quantum computer that is robust to local decoherence effects that plague other proposed quantum computing technologies.[211, 20, 21] Here, we explore the electronic structure of superconducting $\mathrm{LaIn_3}$, ultimately concluding that this material hosts nontrivial bulk band topology.

Topological materials of recent research interest are square-net semimetals in the ZrSiS family.[118, 212] The relevant electronic structure of these materials derives from partially-filled p_x and p_y orbitals that form a 2D square planar bonding lattice. Despite a wealth of strongly-correlated and magnetic phases in these materials,[213, 214, 215, 120, 122, 216, 217, 218] tight-binding models have demonstrated remarkable success in predicting the relevant electronic structure in square-nets—in fact, it appears that the topological classification across the entire family can be largely predicted *via* a simple ratio of bond lengths inside and outside the square-net.[121] We will demonstrate that the electronic structure of the 3D cubic metal $\mathrm{LaIn_3}$ can be understood in terms of a chemically-analogous tight binding model with primary $p_{x,y}$ contributions.

LaIn$_3$ forms in the AuCu$_3$ structure, with La atoms at the corners of the unit cell and In atoms at the centers of the faces, as visualized in Fig. 4.1 (a). The auricupride structure of these materials was explored as early as 1934.[219] Gambino and coworkers discovered low temperature superconductivity in the isostructural compounds LaTl$_3$ (T_c=1.57 K), LaSn$_3$ (T_c=6.45 K), and LaPb$_3$ (T_c=4.05 K) in 1968 while searching for superconducting compounds that could be doped with rare earth elements.[220] Superconductivity and transport properties were further examined during the 1970s, with detection of an extremely low temperature superconducting transition in LaIn$_3$, suggested to activate close to 0.7 K.[221, 222, 223, 224]

Detailed quantum oscillation studies of LaIn$_3$[225, 226] and LaSn$_3$[227, 228] were performed by Umehara and coworkers in the 1990s in order to understand the band structure and Fermi surface; at this point, interest was also driven by a desire to understand related rare earth compounds,[229, 230, 231] which have more complex and correlated electronic structures due to f orbital contributions and magnetic ordering. Antiferromagnetic CeIn$_3$, which has a theoretical band structure similar to LaIn$_3$ when Ce f-orbitals are localized, was a material of particular research focus.[232, 233, 234, 235, 236, 237] Quantum oscillation studies show that two of the Fermi surface pockets in this material, labeled d and a in the notation of Umehara, are identical to those in LaIn$_3$[238]. Taken together, the body of the previous work is quite promising; many features of the Fermi surface of these materials revealed from quantum oscillations experiments were well-described by simple *ab initio* calculations employing the local density approximation. For this reason, LaIn$_3$ has been considered a reference for understanding related heavy fermion systems such as CeIn$_3$. Nonetheless, discrepancies between simulation and experiment persist. To date, the low frequency quantum oscillation components in LaIn$_3$ as well as the origin of an experimental frequency branch previously detected for [111] magnetic field orientation (just below

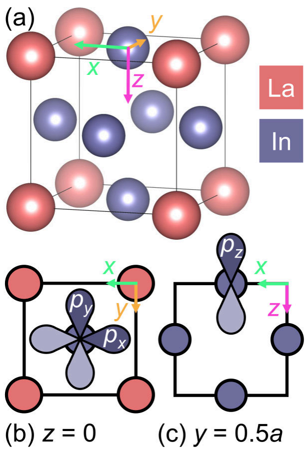

Figure 4.1: Crystal structure of LaIn$_3$. (a) LaIn$_3$ forms in the cubic L1$_2$/AuCu$_3$ structure type with space group $Pm\bar{3}m$ (#221). The electronic structure of this material can largely be understood in terms of In p bonding interactions. These p orbitals can be separated into two symmetry-distinct sets: (b) p_x and p_y orbitals, which point between neighboring La atoms on the faces of the unit cell, and (c) p_z orbitals, which point between neighboring In atoms towards the center of the unit cell. Orbitals are depicted for local coordinate axes set on the In atom at the top of the unit cell.

branch **k** in Umehara *et al.*[225] and Fig. 4.3 (e)) are not understood.

Herein, we revisit the electronic structure of LaIn$_3$, demonstrating that the Fermi surface can be recreated by a tight-binding model with only In p orbital contributions and offer an improvement over previous results, showing that the [111] frequency branch detected in previous experiment can be accounted for by a small onsite energy adjustment related to La d state localization. We also provide new experimental quantum oscillation data that confirms the prior findings of Umehara and co-workers and clarifies the low-frequency spectrum. With confidence in our Fermi surface model, we further characterize the electronic structure, demonstrating that this material is a topological nodal line semimetal. Ultimately, we conclude that LaIn$_3$ and related cubic superconductors may provide an exciting materials platform for exploring the interplay of topological surface states and superconductivity.

4.2 Methods

4.2.1 Experimental

Single crystals of $\mathrm{LaIn_3}$ were grown in self-flux method using excess indium as the metal flux. High-purity elemental lanthanum (Sigma Aldrich 99.9%) and indium (Sigma Aldrich 99.999%) were mixed in the molar ratio 1:14 under argon atmosphere. The mixture was taken in an alumina crucible, which was then sealed inside an evacuated quartz tube. The tube was heated to 1000 °C in 12 hrs in a box furnace, kept at this temperature for 6 hrs followed by a slow cooling (3 °C/h) to 400 °C. At this temperature, the tube was centrifuged to separate the single crystals from the excess indium flux. The stoichiometry of the obtained crystals was checked using energy dispersive x-ray spectroscopy (EDS) in a Verios 460 scanning electron microscope operating at 15 kV and equipped with an Oxford EDS detector. EDS was performed on several samples from the same batch and at different randomly selected regions of the crystals to confirm the homogeneity of the chemical composition.

The single crystals were shipped to HFML (Radboud University, Nijmegen, Netherlands) under argon atmosphere in order to measure de Haas-van Alphen (dHvA) effect by the cantilever torque magnetometry technique. The sample was glued onto a BeCu cantilever (thickness $50\,\mu$m, leg length 4.5 mm and leg width 0.4 mm) using GE-7031 low temperature varnish. The change in magnetization of the sample was measured as a changing capacitance of a parallel plate capacitor set-up between the movable cantilever and the fixed bottom plate. The base capacitance of 1.5 pF was compensated by an analog capacitance bridge to decouple any electrical noise. The sample was first characterized in an Oxford superconducting magnet up to 16 T and down to ^{3}He temperatures, and then the magnetization was investigated up to 30 T in a Bitter magnet down to 0.3 K. Both cantilever torque magnetometry measurements are in good agreement with susceptibility measurements performed by Umehara *et al.*[225, 229] The quantum oscillations in magnetization, namely de Haas-van Alphen (dHvA) oscillations, start from 3 T onwards and evolve in a rich and complex quantum oscillation pattern. According to the Lifshitz-Kosevich formalism,[239] dHvA oscillations are periodic with respect to the inverse of the applied magnetic field ($1/B$); their amplitude exponentially increases with reduction of $1/B$ and the frequency corresponds to the extremal cross-sectional area, namely the cyclotron orbit, of the Fermi surface (FS) in the momentum space, perpendicular to the magnetic field, B. By tilting the angle between the sample and the applied magnetic field, making use of a rotating stage allowing for *in situ* rotation, and tracing the evolution of the frequencies as function of angle, the full FS topography can be probed and mapped.

4.2.2 Computational

The electronic structure of LaIn_3 was simulated in VASP[150, 151, 152] *v*5.4.4 using a $11 \times 11 \times 11$ Γ-centered k-mesh, a plane-wave energy cutoff of 500 eV, and the recommended PAW potentials[90, 154] for *v*5.4. The local density approximation (LDA)[92, 93] functional was found to predict the extremal orbits in closest agreement with experimental quantum oscillation data, consistent with the earlier findings of Umehara and coworkers[225] (other functional choices tested: PBE,[94] LDA+U,[240] and SCAN[241]). The structure was relaxed to an ionic energy step convergence of 10^{-6} eV, with a final lattice parameter $a = 4.657\,\text{Å}$, in reasonable agreement with prior experimental measurements of $a \approx 4.735\,\text{Å}$[242]. All calculations were converged with energy cutoff criterion of 10^{-8} eV. For the calculations with spin-orbit coupling (SOC), SOC corrections were activated for all steps after structural relaxation. Orbital projections and crystal orbital Hamilton populations were computed in LOBSTER.[33, 34, 35, 36] A 0.1 eV Gaussian smoothing was applied to the density of states and crystal orbital Hamilton population curves. Spin orbit coupling was neglected in LOBSTER calculations due to the limitations of that code.

Tight-binding models were constructed by post-processing in WANNIER90[91] using a spherical harmonic basis-set of p orbitals located on the In atomic sites with fitting to the p-majority bands near E_F. Both SOC and non-SOC tight binding models were constructed. Models were reduced in PYTHTB[243] such that only hopping terms larger than 10^{-3} eV were preserved and then re-symmetrized using WANNHR_SYMM[244]. The reduced version of the tight-binding model was generated by limiting the full model to hopping terms larger than 10^{-1} eV and hopping distances less than 7 Å. The p_{xy} reduced model in Fig. 4.4 is shown with further reduction to terms larger than $2{\times}10^{-1}$ eV in order to visually highlight the Dirac crossings. Fermi surface interpolation and surface state Green's function calculations were performed in WANNIERTOOLS[166, 113]. Surface states are calculated for an In terminated surface with no La atoms. Extremal orbit calculations were performed in SERENDIPITY,[2] a new code in development that leverages previous algorithmic developments by Rourke and Julian[245] as well as the open source python packages SPGLIB,[246] TRIMESH,[247] and PLOTLY[248].

Previous experimental quantum oscillation data[225] were extracted using WEBPLOTDIGITIZER[249].

Crystal structures were visualized in VESTA[167].

---

[2] SERENDIPITY is in development. Interested parties can contact Samuel Teicher: smlteicher@gmail.com

4.3 Results

4.3.1 Crystal and Electronic Structure of $\mathrm{LaIn_3}$

We begin by examining the orbital origins of the $\mathrm{LaIn_3}$ electronic structure. Fig. 4.2 (a) presents the density of states. In the electronically-relevant range $-10\,\mathrm{eV} < E_F < 4\,\mathrm{eV}$, In s, In p, La d, and La f states all make significant contributions. Unlike related rare earth family members such as $\mathrm{CeIn_3}$, the f band is far above the Fermi level and can largely be neglected in discussing the electronic structure. Similarly, the In s states are largely filled, forming a band from about -3 eV to -8 eV, and do not contribute strongly near the Fermi level. In Fig. 4.2 (b), the crystal orbital Hamilton population (COHP) is provided. COHP is a semi-quantitative evaluation of relative bond strength based on wavefunction overlap that is negative for bonding and positive for antibonding interactions. While In s/In p, In s/La d, In p/In p, and In p/La d, bonding interactions all contribute significantly to the filled states and the bands just above the Fermi level, we find that the electronic structure near the Fermi level is largely driven by In p / In p and In p / La d bonding, consistent with the results of previous studies.[250, 228] COHP results align with the expectation that the filled states are largely negative stabilizing bonding interactions, while the higher energy spectrum largely consists of positive antibonding states. The antibonding In s/In p interaction near E_F may play a mild destabilizing role, though no lone-pair driven structural distortions are known or expected in these materials (similar antibonding lone-pair interactions are quite important in other main-group cubic materials such as SnTe[251] and perovskites[252]). We now focus in on the electronic structure closest to the Fermi level.

Fig. 4.2 (c) provides a close-up of the main In p and La d bonding interactions near

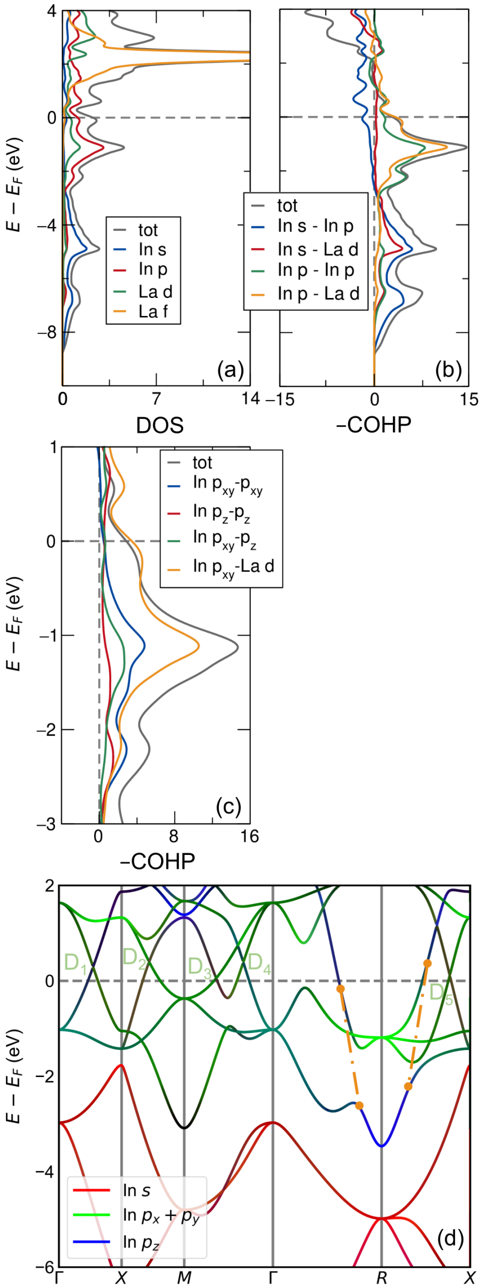

Figure 4.2: Orbital origins of LaIn_3 electronic structure. (a) orbital-projected density of states calculation. (b) crystal orbital Hamilton population, showing dominant interorbital bonding interactions. (c) close up of COHP showing the main In p and La d interactions near E_F. (d) orbital-projected band structure. The relative projection magnitude is represented by RGB color value. Dirac nodes are labeled $D_1, \ldots, D_5$. Dashed guidelines for the p_z band dispersion are overlaid in orange.

E_F. In p orbitals can be separated into a basis with two symmetry-distinct sets. Indium p_x and p_y orbitals point between neighboring La atoms on the faces of the cubic unit cell (Fig. 4.1 (b)). Indium p_z orbitals point towards the center of the unit cell, between the neighboring In atoms (Fig. 4.1 (c)). Note that we use x, y, z here to refer to the local symmetry at the In site rather than the crystal axes; e.g., the p_z orbital points along a different x, y, z direction depending on which In atom you examine. The COHP curves in Fig. 4.2 (c) are broken down into separate contributions from In p_{xy}, In p_z, and La d orbitals. The strongest bonding contributions near the Fermi level derive from In p_{xy} / La d and In p_{xy} / In p_{xy} interactions. Significant interaction with La d states is unsurprising given the local orientation of the In p_{xy} orbitals. The In p_z states have relatively little overlap with La d, forming a band with much wider energy dispersion than the In p_{xy} states. In p_{xy} / In p_z interactions also play a small but non-negligible role.

In Fig. 4.2 (d), a band structure with In s, In p_{xy} and In p_z projections is provided, offering further specificity. In s states form a series of bands (red) below the Fermi level that reach a maximum energy of about -2 eV. In p_{xy} orbitals (green) are the main contributors in the region of interest within $-2\,\mathrm{eV} < E_F < 2\,\mathrm{eV}$, with one major exception. A parabolic band of In p_z states (blue) with wide dispersion runs down along the Γ-R and X-R lines, crossing the p_{xy} region, and reaching a minimum at the R point with an energy close to -3 eV. This band is partially gapped by interaction with the p_{xy} states, and dashed orange guidelines are provided to mark the band path across the gaps. Aside from the bands closest to R, In p_{xy} states are the main contributor to all bands at the Fermi level. A second plot comparing In p, La d and La f projections is provided in the supplementary material.

The band dispersion also provides important information about potential properties of the related compounds. Returning to the DOS, we see that the Fermi level in LaIn_3

lies just below a low density pseudogap region. By slightly increasing the electron count, for example by doping along the $\mathrm{La(In_{1-x}Sn_x)_3}$ series, one could likely reach a semimetal regime. Examining the band structure, we find that the semimetal region of the density of states corresponds to an energy region with many linear band crossings, or Dirac nodes, just above E_F. Relevant Dirac nodes are labeled $D_1, \ldots, D_5$. Tuning the Fermi level to a Dirac node can result in high mobility metals with interesting transport properties. Dirac materials can also exhibit topological surface states; subsequent sections will demonstrate that such surface states are present in $\mathrm{LaIn_3}$.

4.3.2 Fermi surface and comparison to experimental quantum oscillation frequencies

The simulated Fermi surface of $\mathrm{LaIn_3}$ from DFT is shown in Fig. 4.3 (a). The 3D isosurface can be divided into three distinct pockets. Pocket 1, Fig. 4.3 (b), is comprised of an inner closed spheroidal region connected to an outer enclosing region by thin offshoots along the cube diagonal (Γ-R line). Pocket 2, Fig. 4.3 (c), is an octahedral lattice of thinner arms connecting wider sections at each of the cube faces (X points). Pocket 3 encloses the cube corners (R points).

In order to understand how our simulated electronic structure compares to experimental reality, we turn to de Haas-van Alphen quantum oscillation (QO) data, which is an ultrasensitive probe of Fermi surface topography.

Previous work by Umehara and coworkers[225] demonstrated that DFT simulations with the LDA functional generated a Fermi surface that recreated much of the quantum oscillation frequency spectrum seen in experiment. The quantum oscillation frequency is given by the simple Onsager relation[109]:

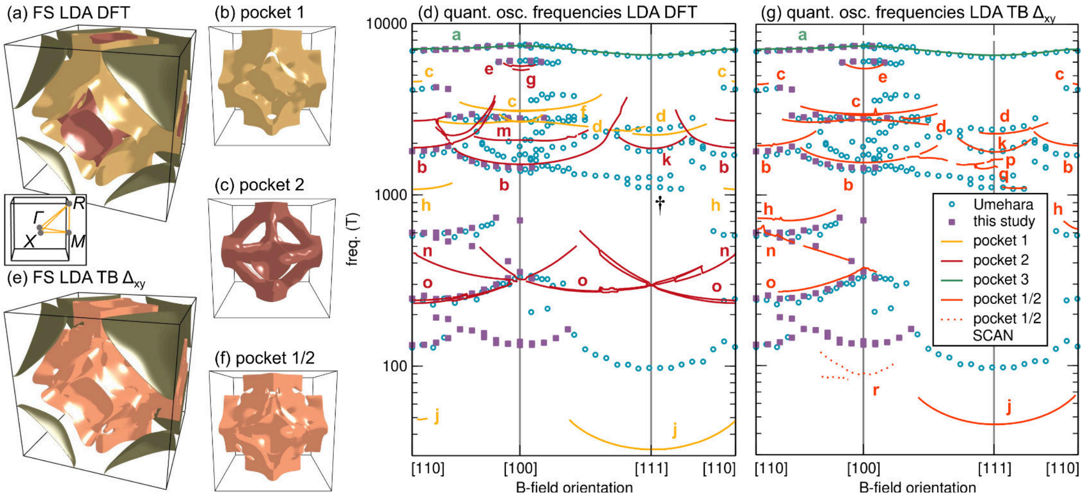

Figure 4.3: LaIn$_3$ Fermi surface and quantum oscillation frequencies. (a) the DFT model of the Fermi surface consists of 3 distinct pockets, color-coded in yellow, red, and green, respectively. Conventional labeling of high symmetry points (Γ,X,M,R) for the cubic Brillouin zone is provided in the inset. Pockets 1 and 2 are displayed in (b,c), respectively. Calculated quantum oscillation frequencies, (d), show remarkable agreement with experiment, though there are significant discrepancies in the low frequency spectrum (f <1000 T) and there is no explanation for the [111] frequency branches marked with †. (e) a 'correlation corrected' Fermi surface from a tight-binding model with slightly lowered In $p_{x,y}$ on-site energy. Pockets 1 and 2 have connected together into a combined pocket, labeled '1/2', and holes have opened up in their joint isosurface, (f). (g) correlation adjustment improves the frequency fit and explains the † frequency branch. While the LDA Δ_{xy} model alone cannot explain the lowest measured frequencies along [110] and [100], a similar Δ_{xy} model built from DFT calculations with the SCAN functional provides the **r** orbit.

$$F = \left(\frac{\hbar}{2\pi e}\right) A$$

where F is the QO frequency, in Tesla, e is the electron charge, and A is the area of an 'extremal orbit', a local extremum in the 2D cross-section of the 3D Fermi surface perpendicular to the applied magnetic field direction. In this way, QO measurements are able to identify specific 2D orbit paths undertaken by electrons in k-space: experimentally detected quantum oscillations are directly proportional to extremal areas enclosed by Fermi surface pockets. The SERENDIPITY code automates extraction of extremal orbits; identified orbits that overlap with the experimental signal are presented in Fig. 4.3 (d). Experimental data from the original work by Umehara, as well as new original experimental data collected along the [110]-[100] path are displayed as scatter points. Connected lines indicate calculated extremal orbits. A nice feature of SERENDIPITY is the ability to order orbits by pocket of origin, and orbit lines are color-coded appropriately. In general, our results align with the prior work of Umehara *et al.* with orbits **a**-**k** identical to those identified in their prior work. Orbits **m**,**n**,**o** are newly identified here. While the discovery of orbit **o** improves on the previous Umehara fit by explaining the presence of the second-lowest frequency branch, the lowest frequency signal for [110] and [100] field orientations is still unexplained. Comparing between the Umehara data and our new signal, there is overlap in almost all locations, reconfirming the previous experimental results and demonstrating that there is neglible variation of the quantum oscillation signal between samples. Improved low-field signal demonstrates that the lowest frequency branch is connected across the [100] field orientation, meaning that this signal cannot arise purely from orbit **j**. While small orbits can be difficult to fit from DFT due to rapid area change with Fermi level, the much larger ≈1000 T frequency branch at [111], marked by †, suggests that the current Fermi surface model must be incomplete. Neither the model presented by Umehara *et al.* nor the initial DFT Fermi surface model presented here provide any explanation for this signal. Full visualization of relevant extremal orbit paths is provided in the supplementary material.

4.3.3 In p based tight-binding approach and correlation correction

Based on the orbital character assignments of Fig. 4.2, which demonstrated that In p states contribute most to the electronic structure near the Fermi level, we might wonder whether a simpler orbital-based electronic structure model is possible. Using WANNIER90 we fit a tight-binding model composed of only In p orbitals to the near-Fermi level electronic structure from DFT. The full model includes many smaller-energy Hamiltonian terms in order to almost perfectly recreate the DFT bands. However, reducing the model to only the most significant interactions (minimum energy 0.1 eV, maximum hop distance 7Å), we can gain useful qualitative understanding of the $\mathrm{LaIn_3}$ electronic structure.

In Fig. 4.4 (a), we present a version of this reduced model in which interactions between p_{xy} and p_z orbitals have been switched off. Despite an upward energy shift, this electronic structure has many similarities to the full $\mathrm{LaIn_3}$ band structure. To first order, the band structure can be seen to result mainly from a p_{xy} manifold at the Fermi level that is crossed by a broad dispersion p_z band only at R. This aligns with structural intuition from Fig. 4.1: it is more favorable to fill the p_{xy} states, which point between the La sites, than to fill the p_z states, which interact with neighboring In atoms. Most of the Dirac band crossings previously presented in the full electronic structure, $D_2, \ldots, D_5$, derive from p_{xy} interactions and can be reproduced in this pure p_{xy} model (D_1 results from p_{xy}-p_z bonding and is not reproduced here).

Our results suggest that an In p based tight binding model can accurately describe

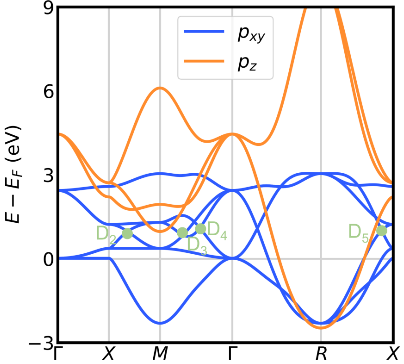
(a) reduced TB no p_{xy}-p_z interaction

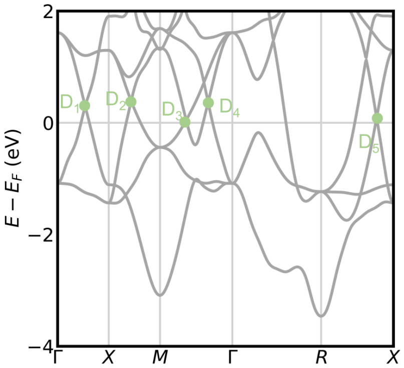
(b) full TB no SOC

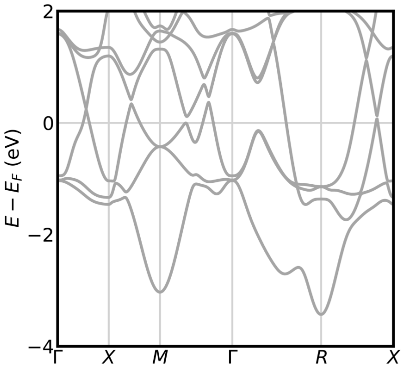
(c) full TB SOC

Figure 4.4: Electronic structure of the LaIn$_3$ In p tight-binding model. (a) reduced tight binding models confirm the orbital origins of electronic structure. Removing $p_{x,y}$ and p_z interactions, the near-Fermi level electronic structure and Dirac nodes in LaIn$_3$ can largely be described in terms of a $p_{x,y}$ lattice with a large-dispersion p_z band crossing E_F only at R. (b) full tight-binding model without spin-orbit coupling. (c) final tight-binding model with spin-orbit coupling. All models include the on-site correction $\Delta_{xy} = -0.025\,\text{eV}$.

the band structure, Fermi surface and pertinent electronic structure features (Dirac nodes) in LaIn$_3$. This simple parametrization also provides a clue as to how to improve our electronic structure model. *Ab initio* models, particularly when using the local density approximation, often over-delocalize charge density due to inexact treatment of correlation effects. Delocalization error is generally much greater for d-orbitals than p-orbitals. Assuming that correlation plays an important role in the current DFT error, we would expect the DFT model to reproduce the p_z Fermi pockets surface well, while having errors in the p_{xy} pockets due to the strong interaction of the p_{xy} orbitals and La d charge density. This is indeed the case, as can be seen when re-examining Figs. 4.3 (a)-(d). p_z orbitals contribute most significantly to the 3rd pocket centered at the R point and the predicted extremal orbit for this pocket (**a**) is in almost exact quantitative agreement with the experimentally measured frequency band. The rest of Fermi surface derives primarily from p_{xy} states where we would expect some error.

Since we expect the La d orbitals to be over-delocalized, the simplest correlation correction that can be performed on the tight-binding model is a reduction of the p_{xy} on-site energy since the interaction of the p_{xy} and La d orbitals should be reduced in the real material. We performed such an on-site energy correction, determining that a value $\Delta_{xy} = -0.025$ eV generated a Fermi surface that addresses many of the discrepancies between the pure DFT Fermi surface and experimental quantum oscillation signal. The 'correlation corrected' Fermi surface is presented in Fig. 4.3 (e). As a result of lowering the p_{xy} energy, a gap forms that connects the first and second pockets, generating a combined pocket, labeled "1/2." Pocket 1/2 is visualized in Fig. 4.3 (f). Distinct from the previous DFT model, this combined pocket is pierced by several small holes near the Γ-M line. The predicted extremal orbits are provided in Fig. 4.3 (g). Overall, there is some improvement in quantitative agreement of the **h**, **n**, **o**, and **j** orbits. The gap along Γ-M removes the **g** orbit, leaving only the **e** [110] high frequency extremal orbit below **a**, which agrees better with the single frequency branch seen in experiment. An explanation for the missing [111] orbits at † also falls naturally out of this model: the **p** and **q** signals derive from subtle orbits entangling the new holes in the pocket 1/2 isosurface, as detailed in the supporting material. While this tight-binding model from DFT calculations with the LDA functional cannot explain the lowest frequency signal for [100] field orientation, performing a similar tight-binding model parametrization and correlation correction ($\Delta_{xy} = -0.025\,\mathrm{eV}$) based on SCAN functional calculations provides the **r** orbit, which may explain this signal. While the LDA model offers an overall better fit, geometric differences between the two Fermi surfaces are only slight. The **r** orbit in the SCAN calculations also derives from the new holes in the pocket 1/2 isosurface, suggesting that almost all the discrepancy between previous calculations and experiment may be explained purely by mild correlation error. The SCAN model quantum oscillation fit is provided in the supplement.

All further results were determined using our full correlation corrected tight-binding model rather than pure DFT. In aid of further theoretical work, full and reduced 18-term versions of our LDA tight-binding model are provided in the supporting material.

Overall, the final correlation-corrected band structure of Fig. 4.4 (b,c) is only subtly different from the original DFT bands due to the minor correlation correction shift. The quantum oscillation comparison suggests that the experimental Fermi level lies just within the spin-orbit gap of the D_3 node, as shown here, with important ramifications for predicted topological surface states, discussed in the following.

4.3.4 Nodal lines, topological classification and surface states

We now examine the Dirac crossings in greater detail, initially excluding spin-orbit effects from the discussion. In Fig. 4.5, we identify the 3D nodal regions for which

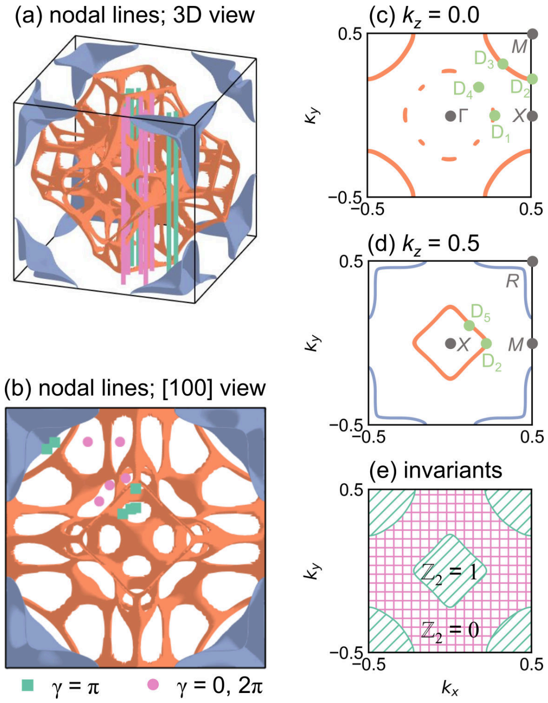

Figure 4.5: Topological classification of LaIn$_3$. LaIn$_3$ hosts a wide variety of nodal lines near the Fermi level, shown in (a,b) for an isosurface contour $\Delta_{\text{band}} = 0.13\,\text{eV}$. Nodes can be separated into two contributions, a main region of interconnected nodal lines, centered at Γ (orange), and a low gap region near the R point at the corners of the cube (purple). The topological invariant classification for relevant [100] surfaces is relatively simple, depending only on nodal lines about the M and X points on the $k_z = 0.0$ and $k_z = 0.5$ high-symmetry planes depicted in (c) and (d), respectively. Integrating along any line that passes through these nodal lines gives a nontrivial Berry phase $\gamma = \pi$. Paths that do not pass through these loops yield a trivial Berry phase $\gamma = 0, 2\pi$. The integration paths are shown in 3D in (a) and from above in (b), with nontrivial and trivial integrations in green and pink, respectively. The resulting surface Brillouin classification is given in (e). We expect to find nontrivial drumhead surface states in the non-trivial regions (green, diagonal hatch) corresponding to the nodal loops with $\mathbb{Z}_2 = 1$.

the band separation Δ_{band} is small (for this TB model the gap of interest near E_F is between bands 3 and 4). In Figs. 4.5 (a,b) this nodal isosurface, displaying intersections between bands 3 and 4, is plotted in 3D and from above along the [100] direction. The nodal isosurface consists of two distinct regions: a central connected array of nodal lines (orange) and a low Δ_{band} region near the R points at the corners of the cube (purple). The latter is less relevant since the R band crossing region lies much lower in energy (about -1 eV when examining the band structure of Fig. 4.2 (d)). The orange nodal lines correspond to the Dirac nodes near the Fermi level. The nodal surface is quite complex owing to the high symmetry and large number of mirror planes in this cubic material. Orange nodal lines in Fig. 4.5 (a) can be identified on planes perpendicular to all high symmetry directions ([100],[110],[111]). Any of these nodal lines could potentially host topological surface states. In lieu of a full classification, we discuss the topological classification of the [100] surface, which is most relevant due to the cubic habit of experimentally-grown $\mathrm{LaIn_3}$ crystals, and greatly simplifies the discussion. There are only two symmetry-distinct nodal lines lying in [100] planes, a loop enclosing the M point on the $k_z = 0.0$ plane (Fig. 4.5 (c)) and a loop enclosing the X point on the $k_z = 0.5$ plane (Fig. 4.5 (d)). Dirac nodes D_2, D_3 are part of the M nodal loop and Dirac nodes D_2, D_5 part of the X loop.

Materials with mirror symmetry-protected nodal lines carry a $\mathbb{Z}_2$ invariant that can be determined via a Wilson loop calculation integrating the Berry curvature over a closed loop in k-space. The determined Berry phase, γ, is defined modulo 2π such that values of $0, 2\pi$ indicate a topologically trivial band gap and a value of π indicates a nontrivial band gap. Topological surface states are expected in nontrivial gaps. Due to periodicity of the Brillouin zone, the Berry phase within these nodal loops can be determined by integration from $k_z = -0.5$ to 0.5 through any complete gaps in the nodal surface. Such a Berry phase evaluation has previously been performed in other nodal line materials, including ZrSiTe[253]. Unlike ZrSiTe, the nodal surface here is quite complex and the evaluation cannot be completed along high-symmetry lines in k space. We have evaluated the Berry phase in each of the symmetry-distinct gaps though the nodal surface (white spaces in Fig. 4.5 (b)). Integration lines can be seen in 3D in Fig. 4.5 (a) and from above in Fig. 4.5 (b). We find non-trivial regions with $\gamma = \pi$ (green lines and squares) at the center of the Brillouin zone and near the corners. We also find $\gamma = \pi$ when integrating in a loop around either the X or M nodal lines, as expected. These results for the [100] surface can be simply summarized in Fig. 4.5 (e): both the X and M nodal lines result in regions with a nontrivial $\mathbb{Z}_2$ invariant (green, diagonal hatch). While all of the symmetry-protected nodal lines in $\mathrm{LaIn_3}$ can host surface states, these surface states can hybridize and gap out on surface projections with an even number of overlapping nodal lines. On the [100] surface Brillouin zone, every point is enclosed by at least one nodal loop, but only the regions in the X and M loop projections, shown in Fig. 4.5 (e), feature an odd number of surface states and are topologically protected.

The surface spectrum of $\mathrm{LaIn_3}$ is quite rich. Fig. 4.6 presents topological surface states associated with the nodal loops. In Fig. 4.6 (a), the surface spectrum is presented along a path intersecting the M nodal loop and the k_z-integrated Berry phase along the path is shown in Fig. 4.6 (b). A pair of bright surface states in Fig. 4.6 (a) near the $\overline{Z}'$ point can be seen to coincide with the nontrivial Berry phase $\gamma = \pi$ within the M loop; these bands form a protected drumhead surface state interconnecting all the Dirac nodes on the loop. Nodal loop surface states are also present at $\overline{\Delta}'$. Though these surface bands are clearly visible in the current simulation, they result from the projection of an even number of nodal loops and are not topologically protected. Fig. 4.6 (c) presents the calculation in the presence of spin-orbit coupling. While mirror-protected drumhead surface states are not guaranteed to be robust to spin-orbit effects,

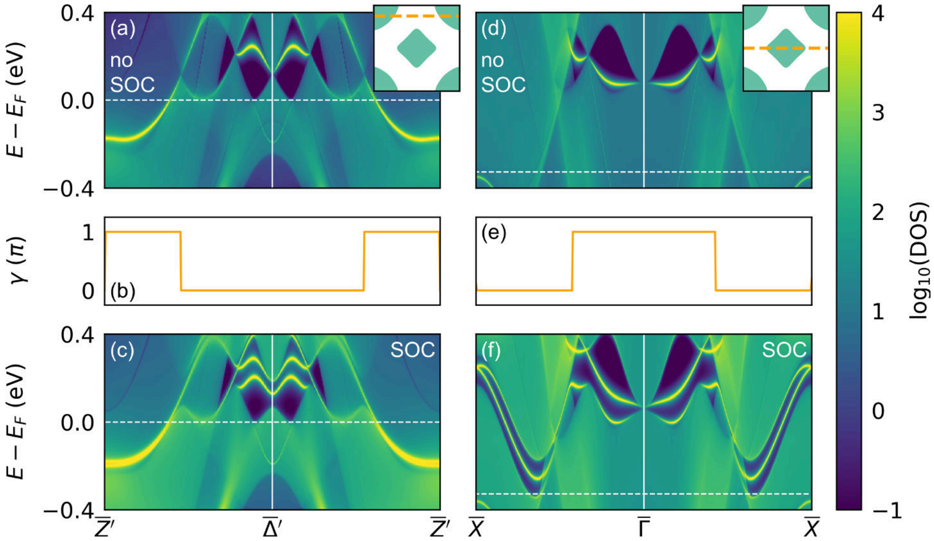

Figure 4.6: Topological surface states in LaIn$_3$. (a) presents the surface spectrum along the $\overline{Z}'$ ($k_x, k_y = -0.5$,0.375) - $\overline{\Delta}'$ (0.0,0.375) - $\overline{Z}'$ (0.5,0.375) path that intersects the M nodal loop. Bright surface bands can be seen near $\overline{Z}'$ and $\overline{\Delta}'$. (b) provides the topological invariant calculation with a nontrivial Berry phase $\gamma = \pi$ within the nodal loop. (c) demonstrates that the surface states are robust to the opening of small band gaps associated with spin-orbit coupling. (d-f) show similar results for the $\overline{X}$-$\overline{\Gamma}$-$\overline{X}$ line that intersects the X nodal loop. Insets of (a,d) show the k-paths with respect to the topological invariant classification of Fig. 4.5 (e). The Berry phase calculation in (e) is taken along a slightly offset adjacent path with $k_y \mathrel{+}= 0.02$ to avoid interecting the Dirac nodes.

here the band structure change is relatively minor with only small band gapping effects. The Fermi-level topological surface states can still be seen even after spin-orbit coupling is incorporated. Fig. 4.6 (d-f) demonstrate similar results for a path intersecting the X loop. The X loop surface states near $\overline{\Gamma}$ are shown to be robust to spin-orbit coupling as well. Discussion of the full surface state spectrum and additional surface states is offered in the supplement.

4.4 Discussion

We have demonstrated that the electronic structure of LaIn_3 can be described using only In p orbitals. This yields a tight-binding model in which the lower energy In $p_{x,y}$ manifold is partially filled and the In p_z manifold is largely unoccupied. While the electron valence in this intermetallic is not precise, the resulting electronic structure aligns with intuition for $\mathrm{La}^{3+}(\mathrm{In}^{1-})_3$: the In $p_{x,y}$ bands are approximately half-filled, yielding a band structure with multiple Dirac nodes in close proximity to E_F. This half-filled $p_{x,y}$ model is a close analog of the semimetal band structure of ZrSiS in which Si^{2-} valence yields filled Si p_z and half-filled Si $p_{x,y}$ manifolds.

We performed original quantum oscillation measurements reconfirming the prior results of Umehara *et al.* and clarifying the low-frequency spectrum. Detailed comparison of the experimental oscillation frequencies and calculated extremal orbits suggests that the Fermi surface is relatively well-understood with only naïve correlation correction necessary to account for the main discrepancies between *ab initio* simulation and experiment. The good fitting achieved with the local density approximation hints that the In p states in this compound may be relatively delocalized—again, potentially in analog to bonding in the ZrSiS family metals.[121]

Using our tight-binding models we explored the electronic band topology and predicted surface state spectrum of LaIn$_3$, identifying symmetry-protected nodal lines and drumhead surface states close to the Fermi level. Following from our analysis of the Fermi surface extremal orbits, we find that previously unexplained frequency branches can be explained by a small onsite energy adjustment ($\Delta_{xy} = -0.025\,\mathrm{eV}$) that places the Fermi level in the spin-orbit gap of the D_3 Dirac node, generating holes in the Fermi surface which result in new **p** and **q** orbits. This Fermi level placement guarantees that the M drumhead surface states will be active at E_F.

Nodal line surface states have been proposed to promote surface superconductivity[254] and idealized models suggest that nodal line electronic structure may promote low-temperature transitions to a number of intriguing correlated phases;[255] although drumhead surface states may be unstable to the opening of an s-wave superconducting gap, the experimental nature of this interaction is largely unknown and experimentally unexamined.

Given established superconductivity and the rich spectrum of nodal line surface states predicted here, which persist over a large energy range, the LaIn$_3$ family may provide an exciting platform for further exploring the interaction between topological surface states and superconductivity. Compounds in the doping series LaIn$_{3-x}$Sn$_x$ are readily prepared as high quality single crystals via either flux or melting techniques[220] and offer both high electronic mobility and experimentally-accessible superconducting transitions. In addition to electronic doping, the stability of the compounds LaPb$_3$ and LaTl$_3$ also present an opportunity for carefully tuning the effective spin-orbit coupling.

4.5 Supplementary Material

4.5.1 SCAN TB model

SCAN calculations were performed in VASP using identical parameters to the LDA model described in the text. The relaxed lattice parameter was 4.753 Å. Tight binding model construction was performed using the same method, including the final onsite energy adjustment $\Delta_{xy} = -0.025$ eV. Extremal orbits and calculated quantum oscillation frequencies extracted using the SCAN TB model are detailed in Fig. 4.8.

4.5.2 Symmetry and Irreducible Representations

Fig. 4.12 (a) provides the band structure of our final tight-binding model in the absence of spin-orbit coupling (SOC). Bands are colored based on irreducible representation (irrep) and the point group for each segment of the band path is given. By examining the irreps of each pair of bands forming each Dirac band crossing, we can gain understanding of the symmetries protecting each Dirac node. Two bands can cross without interaction and form a Dirac node if and only if they belong to two separate irreps. Symmetry operations differing between these irreps are the symmetries that protect the node. We use the irrep numbering convention of Koster.[42] TB-model irreps were calculated with IR2TB[31]. In the calculation without SOC all Dirac band crossings consist of bands with differing irreps and are therefore symmetry-protected. After SOC is included in (b), small band gaps form in the $D_2, \ldots, D_5$ Dirac nodes. All of these crossings lie along lines with C_{2v} point group symmetry. There is only one spinor irrep (#5) in this point group, meaning that all bands may interact in the presence of SOC. The D_1 node remains ungapped as its two bands derive from separate spinor irreps.

Further than demonstrating the symmetry protection of all five near-Fermi level Dirac nodes in the absence of spin-orbit coupling and the protection of the D_1 node even with spin-orbit effects activated, we can also use the irreps to show that the M and X nodal loops are protected by mirror symmetry; a necessary condition for the validity of the topological invariant classification and nodal line surface state discussion of Figures 4.5 and 4.6 in the chapter body. Using the irrep notation of Fig. 4.12 (a): D_2 is protected by the crossing of Z_2 and Z_4 irreps, which differ by the mirror operations IC_2' and IC_2'', meaning that D_2 is protected by two mirror operations. D_3 (D_5) arises from the intersection of $\sum_1$ (S_1) and $\sum_3$ (S_3) which is protected by the same two mirrors. Since all of the high-symmetry Dirac nodes on the M and X loops are protected by mirror symmetry, we may conclude that these are both mirror-protected nodal loops. This can be similarly shown by calculating along a low symmetry path in the point group C_s across either loop, in which case a single mirror operation can be seen to protect the band crossing.

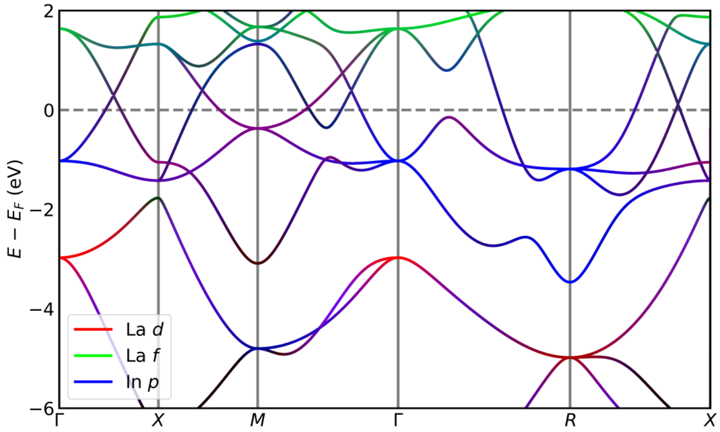

Figure 4.7: Additional LaIn$_3$ orbital-projected bands. Here we, provide an additional orbital-projected band structure in complement to Fig. 4.2 in the chapter body. The relative magnitude of orbital projections is represented by RGB color value. The near-Fermi level electronic structure can be seen to derive from In p / La d contributions, with the La f states un-filled. The pocket around R derives from In p_z states with little La d contribution. Other regions of the band structure that derive mainly from In $p_{x,y}$ states, such as the region around M, have strong interaction with La d.

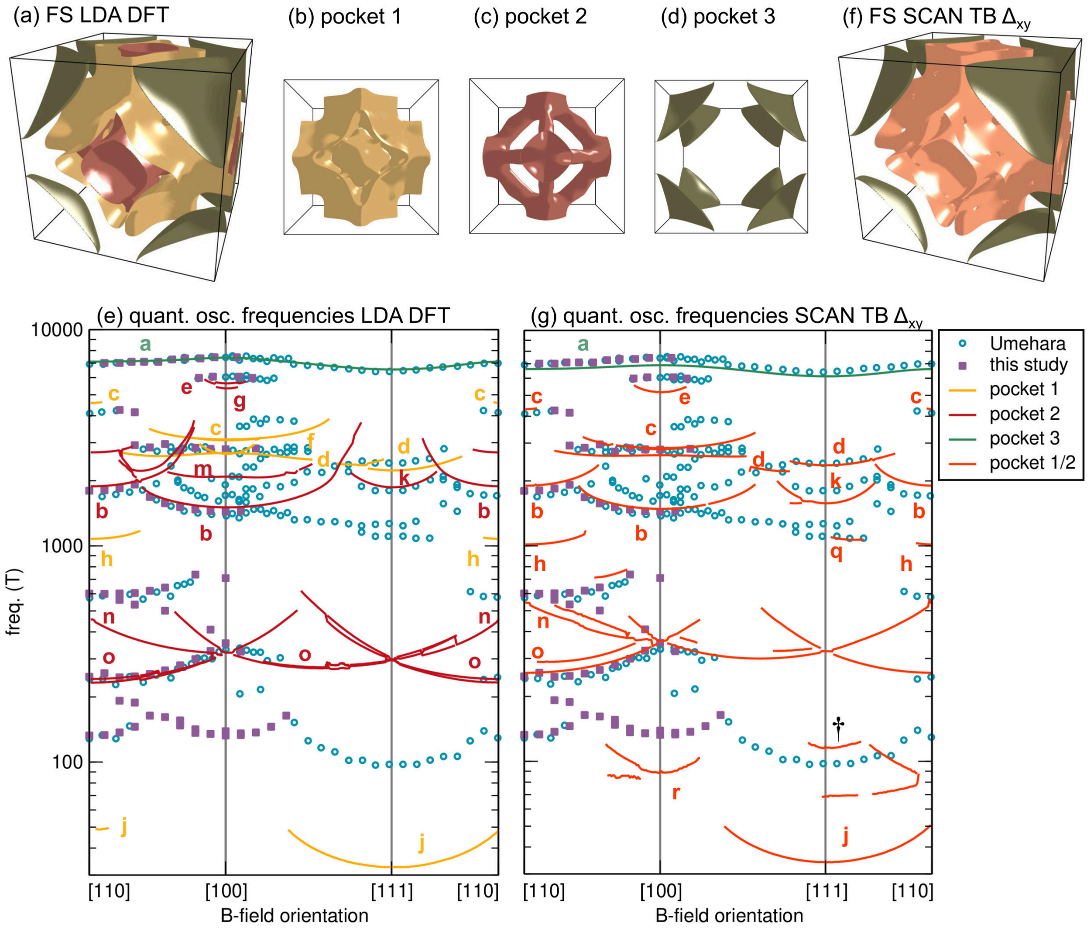

Figure 4.8: LaIn$_3$ SCAN TB model Fermi surface and predicted quantum oscillation frequencies. Here, we provide a quantum oscillation comparison similar to that of Fig. 4.3 in the chapter body, but with a TB model derived from a SCAN rather than LDA DFT calculation and similar onsite energy correction $\Delta_{xy} = -0.025\,\mathrm{eV}$. The SCAN results are generally intermediary between the LDA DFT and the corrected LDA TB model results, with slightly worse quantitative fitting of the **h** orbit and a weaker version of the frequency splitoff that leads to the **p** and **q** orbits in the LDA TB model. However, the SCAN TB model provides the **r** orbit, which appears to explain the lowest frequency signal for [100]-oriented field. As marked with †, the SCAN model also provides possible alternative explanations for the lowest [111] frequency; suggesting that this signal may not actually derive from the **j** orbit.

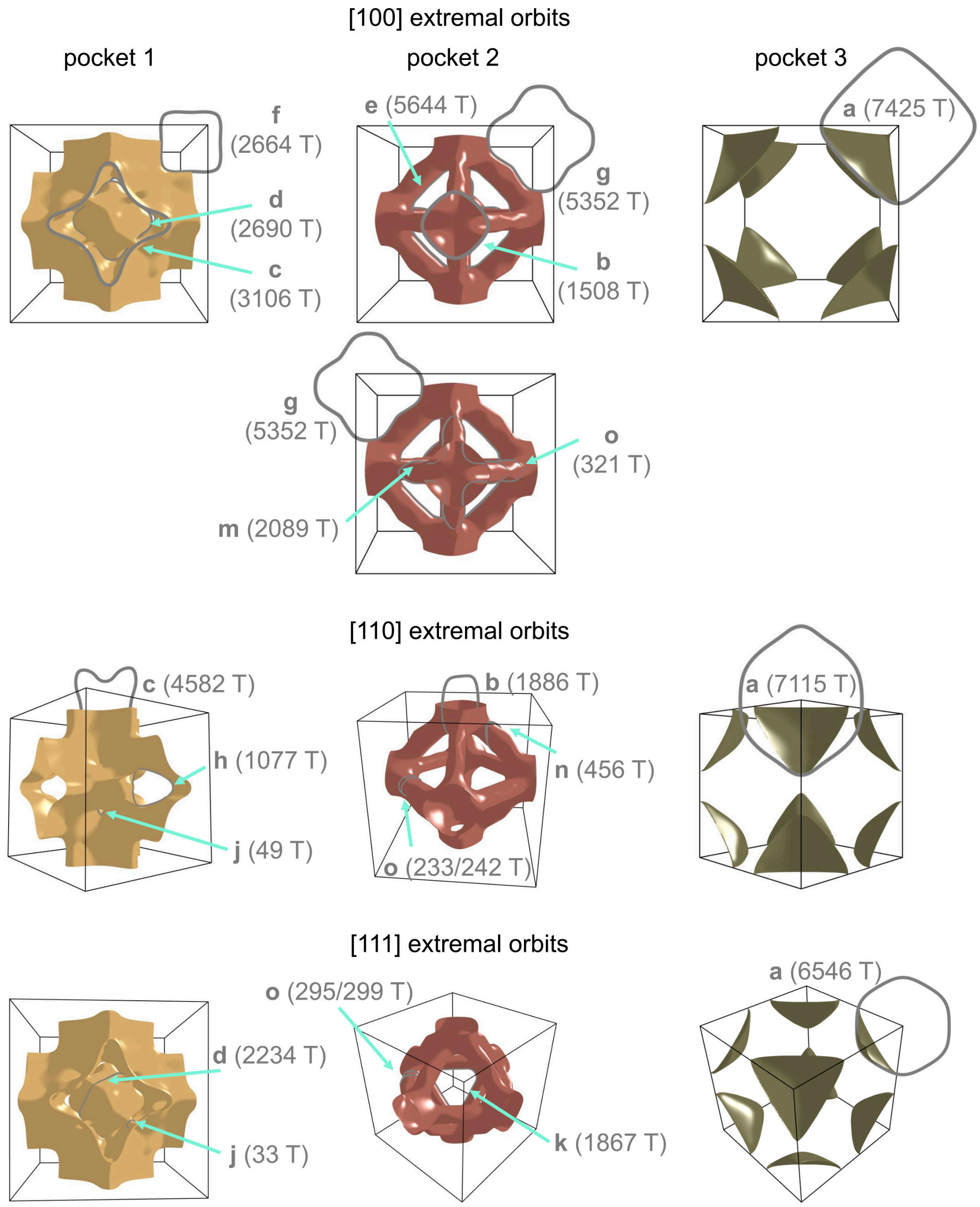

Figure 4.9: Visualization of LaIn$_3$ extremal orbits. 2D extremal orbit paths associated with the frequencies in Fig. 4.3 (e) of the chapter body are provided here for the high symmetry field orientations ([100],[110],[111]). Orbit paths are plotted as gray lines and explicit predicted frequencies are provided in Tesla.

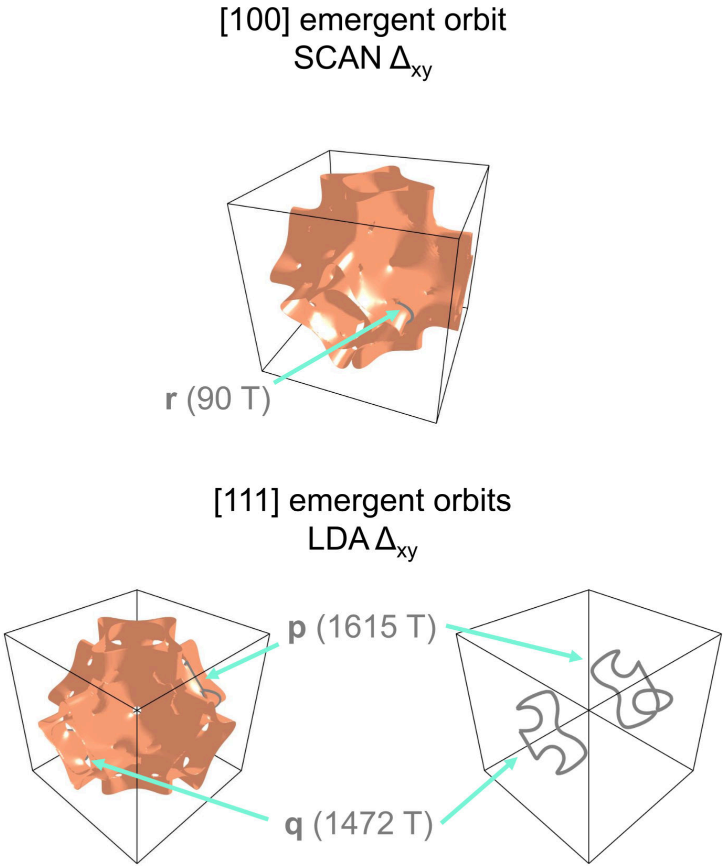
[100] emergent orbit
SCAN Δ_{xy}

[111] emergent orbits
LDA Δ_{xy}

Figure 4.10: Visualization of the LaIn$_3$ emergent extremal orbits extracted from correlation corrected tight binding models. Orbit paths are plotted as gray lines. All emergent orbits derive from the small holes interpenetrating the pocket 1/2 Fermi surface. Compare to Fig. 4.3 (f) in the chapter body.

(a) DFT-TB comparison

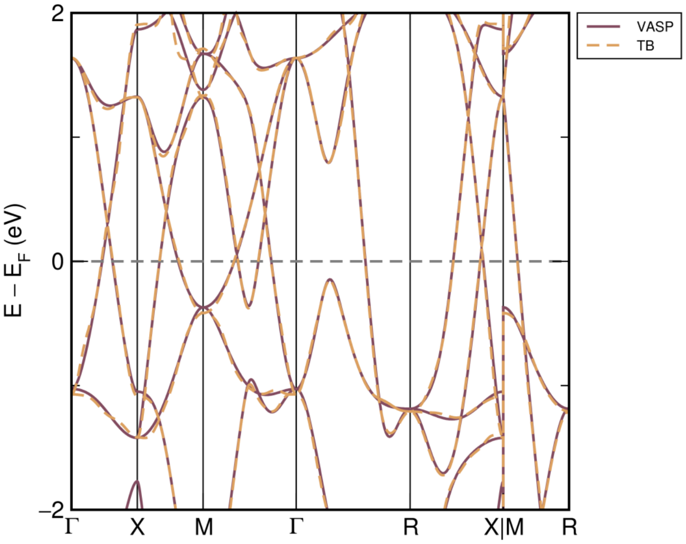

(b) TB model comparison

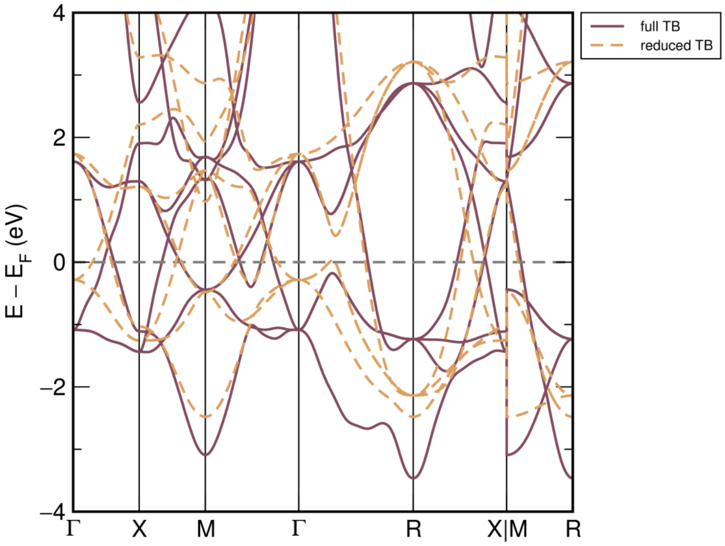

Figure 4.11: LaIn$_3$ TB model comparison. (a) comparison between LDA DFT and our full TB model without correction ($\Delta_{xy} = 0$). The band structures are virtually-identical near E_F. (b) comparison between our full final TB model with correction ($\Delta_{xy} = -0.025\,\text{eV}$) and the reduced version of the model described in the text. While the reduced version of the model does not quantitatively recreate the band structure, it achieves similar band structure and topology with only 18 unique Hamiltonian terms. Spin orbit coupling is neglected for the calculations in this figure.

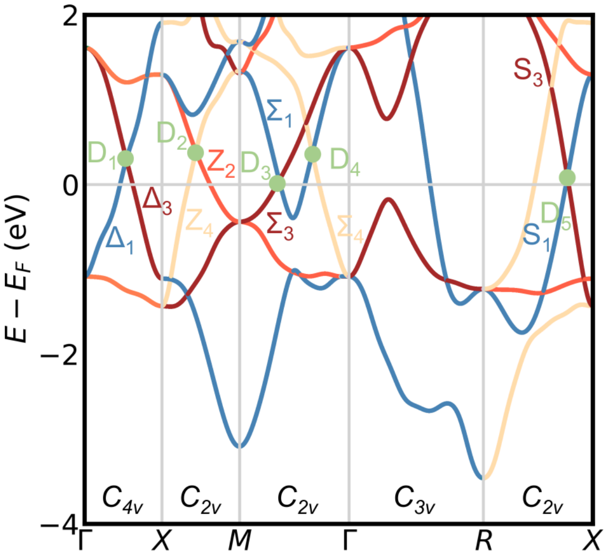
(a) full TB no SOC

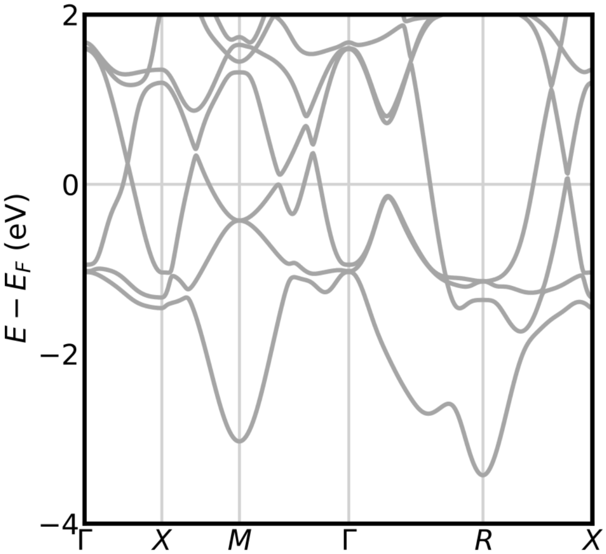
(b) full TB SOC

Figure 4.12: LaIn$_3$ TB model symmetry and irreps. This is a version of Fig. 4.4 in the chapter body providing additional symmetry information for our full final tight-binding model. In (a) the point groups (C_{4v}, C_{2v},etc.) are provided for each branch of the non-SOC band structure and each band is colored based on its irreducible representation (irrep). Irreps contributing to the Dirac nodes, $D_1, \ldots, D_5$ are explicitly labeled. (b) presents the SOC band structure, in which several of the Dirac cones have been gapped.

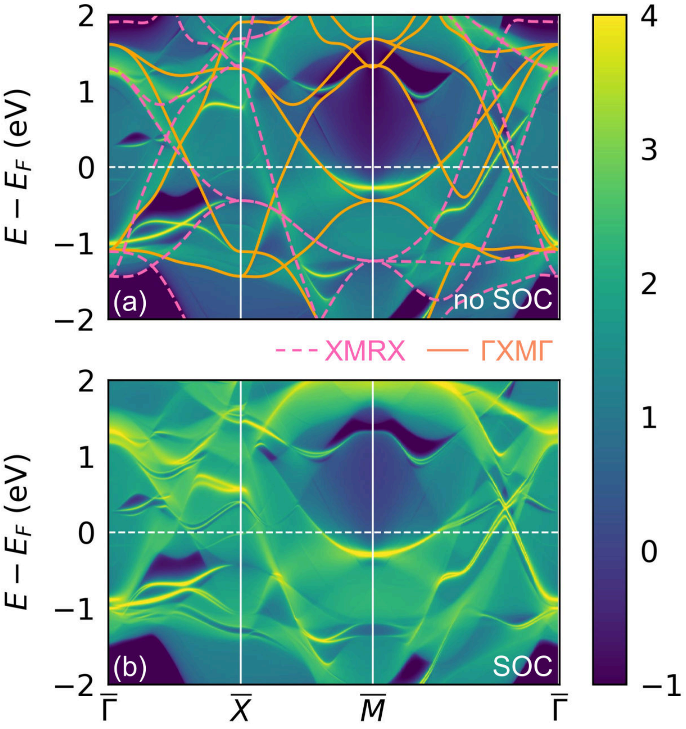

Figure 4.13: Full LaIn$_3$ surface state spectrum. Full [100] surface state spectrum of LaIn$_3$ calculated with the final version of the TB model ($\Delta_{xy} = -0.025\,\text{eV}$). (a) surface states in the absence of spin-orbit coupling. The bulk band structures along the corresponding Γ-X-M-Γ and X-M-R-X paths are provided as orange (solid) and pink (dashed) lines for reference. (b) surface states in the presence of spin-orbit coupling. LaIn$_3$ hosts a rich variety of additional surface states not discussed in the main chapter text.

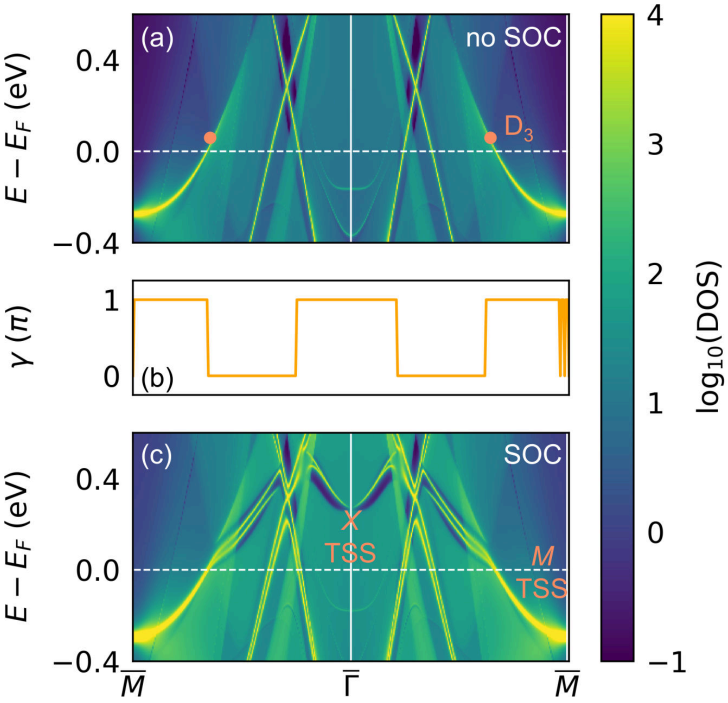

Figure 4.14: LaIn$_3$ $\overline{M}$-$\overline{\Gamma}$-$\overline{M}$ surface spectrum. Surface state spectrum along the $\overline{M}$-$\overline{\Gamma}$-$\overline{M}$ line (a) without and (c) with SOC. (b) provides the Berry phase evaluation for the gap between bands 3 and 4 in the absence of SOC. Non trivial invariants $\gamma = \pi$ are found for the regions near $\overline{M}$ enclosed by the M nodal loop and near $\overline{\Gamma}$ enclosed by the X nodal loop. After SOC is activated in (c), bulk gaps form near $\overline{\Gamma}$ and at the D_3 Dirac node. The X loop and M loop topological surface states (TSS) are explicitly identified. The result of the quantum oscillation fitting and correlation adjustment is that the Fermi level likely lies within the spin-orbit gap of the D_3 node (this Fermi level placement is what creates the Fermi surface holes that generate orbits **p**, **q**, and **r**), which, in turn appears to guarantee that M loop surface states are active at the Fermi level. In addition to the X and M loop surface states, other high-energy-dispersion surface states can be seen. These states may also be relevant depending on the surface reconstruction/potential realized in experiment. Since the Berry phase evaluation is undefined at Dirac nodes, the Berry phase calculation has been performed along a slightly shifted adjacent k-path with $k_y \mathrel{+}= 0.02$ where no nodes are present.

Part II

Electronic structure of Vanadium kagome metals

Chapter 5

Fermi surface mapping and the nature of charge density wave order in the kagome superconductor $\mathrm{CsV_3Sb_5}$

[1] The recently discovered family of $A\mathrm{V_3Sb_5}$ (A: K, Rb Cs) kagome metals possess a unique combination of nontrivial band topology, superconducting ground states, and signatures of electron correlations manifest via competing charge density wave order. Little is understood regarding the nature of the charge density wave (CDW) instability inherent to these compounds and the potential correlation with the onset of a large anomalous Hall response. To understand the impact of the CDW order on the electronic structure in these systems, we present quantum oscillation measurements on single crystals of $\mathrm{CsV_3Sb_5}$. Our data provide direct evidence that the CDW invokes a substantial reconstruction of the Fermi surface pockets associated with the vanadium orbitals and the kagome lattice framework. In conjunction with density functional theory modeling, we are able to identify split oscillation frequencies originating from reconstructed pockets built from vanadium orbitals and Dirac-like bands. Complementary diffraction measurements are further able to demonstrate that the CDW instability

---

[1] The contents of this chapter previously appeared in Ref. [126]: B. R. Ortiz, S. M. L. Teicher, L. Kautzsch, P. M. Sarte, J. P. C. Ruff, R. Seshadri, and S. D. Wilson, Fermi surface mapping and the nature of charge density wave order in the kagome superconductor $\mathrm{CsV_3Sb_5}$, *Phys. Rev.* X **11**, 041030. ©APS publishing, 2021

has a correlated phasing of distortions between neighboring V_3Sb_5 planes, and the average structure in the CDW state is proposed. These results provide critical insights into the underlying CDW instability in AV_3Sb_5 kagome metals and support minimal models of CDW order arising from within the vanadium-based kagome lattice.

5.1 Introduction

While kagome insulators are traditionally sought as potential hosts of quantum spin liquid states and laboratories for highly frustrated magnetism [256, 257, 258, 259, 260], kagome metals are equally interesting due to their potential to host topologically nontrivial electronic states interwoven with local electronic symmetry breaking. At a single-orbital tight binding level, the kagome structural motif naturally gives rise to an electronic structure with Dirac points and a flat band that together provide the potential for an interplay between topologically nontrivial surface states and substantial electron correlation effects. A wide array of instabilities have been predicted, ranging from bond density wave order [261, 262], charge fractionalization [263, 264], spin liquid states [265], charge density waves (CDW) [266] and superconductivity [261, 267].

The electron filling within the kagome framework controls the formation of a wide variety of predicted electronic instabilities. For band fillings near $5/4$ electrons per band [261, 268, 269, 270, 271], a Van Hove singularity is formed at the Fermi level due to the presence of saddle points along the zone edge. Excitations between these saddle points can lead to CDW order, and, in some limits, unconventional superconductivity. The recently discovered class of AV_3Sb_5 (A: K, Rb Cs) kagome metals [272] are potential realizations of this physical mechanism with each member exhibiting thermodynamic anomalies associated with CDW order [273, 274, 112, 275, 276, 277] followed by the onset of superconductivity at lower temperatures [112, 275, 278]. While there are multiple gaps identified with both evidence of s-wave pairing [279] and evidence of nodal quasiparticles [280], the interplay between superconductivity and the CDW state can in principle lead to unconventional behavior even in a fully gapped superconducting state [281].

The CDW instability in AV_3Sb_5 compounds seemingly competes with superconductivity [282, 283] and presages the formation of a potentially unconventional superconducting ground state [275, 283]. However, the microscopic origin of the CDW remains an open question. Concomitant to the onset of CDW order, an exceptionally large anomalous Hall effect (AHE) appears [284, 285], despite the absence of detectable local moments or magnetic correlations [286]. While the normal state electronic structure is a $\mathbb{Z}_2$ topological metal [275, 275] and topologically-protected surface states are predicted close to the Fermi level [275], below the CDW transition recent scanning tunneling microscopy (STM) data [273] and theoretical proposals [271] have suggested the formation of a chiral CDW order parameter. This chiral CDW, endemic to the kagome lattice, is proposed to break time reversal symmetry and generate a large Berry curvature, potentially accounting for the AHE. To date, however, data directly linking the onset of CDW order with reconstruction of vanadium orbitals associated with the kagome lattice in AV_3Sb_5 is lacking. Similarly, the applicability of minimal, single orbital tight binding kagome models in multiband AV_3Sb_5 compounds remains an open question.

Specifically, STM and diffraction experiments have observed charge order with an in-plane $\mathbf{q} = (0.5, 0.5)$ wave vector in KV_3Sb_5 [273] and CsV_3Sb_5 corresponding to 3**Q** CDW order. A kagome "breathing" mode can give rise to candidate distortions such as the "Star of David" (see Figure 5.1) and its inverse structure [287], and recent studies have shown strong electron-phonon coupling in KV_3Sb_5 promoting such a distortion [288]. Native electronic instabilities promoting CDW order along this wave vector have

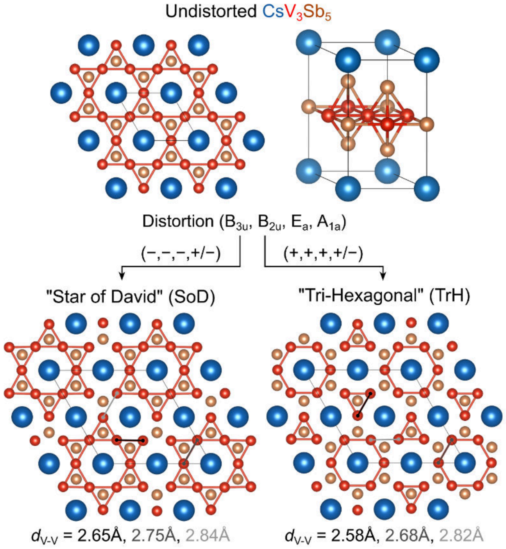

Figure 5.1: CsV_3Sb_5 crystal structure and breathing mode distortions. CsV_3Sb_5 is a layered, exfoliatable, kagome metal consisting of a structurally perfect lattice of vanadium at room temperature. Upon cooling below $T^* = 93\,\mathrm{K}$, CsV_3Sb_5 exhibits charge density wave order. A concurrent structural distortion emerges as well, which is suspected to be related to the kagome "breathing mode." Upon distortion and relaxation in both the positive and negative displacements, the "breathing mode" gives rise to the "Star of David (SoD)" and "Tri-Hexagonal (TrH)" candidate structures.

long been predicted in Kagome models at select fillings near Van Hove singularities [261, 268, 269, 270, 271], suggesting that a minimal model built around the kagome planes of these materials may capture the essential physics governing their unconventional electronic properties. Notably, additional features such as unidirectional charge stripe order [274] also seemingly coexist with the 3**Q** CDW state, further connecting the underlying interactions to stripe/nematic instabilities predicted within a kagome network [271].

Here we investigate the origins of the 3**Q** CDW order in AV_3Sb_5 kagome compounds via study of Shubnikov-De Haas (SdH) quantum oscillations in magnetotransport data of CsV_3Sb_5, which has the most pronounced CDW instability within the family. By correlating quantum oscillation data with DFT models of the breathing distortion of the kagome lattice, we are able to observe the effect of the CDW on the electronic structure. Specifically, we demonstrate that a series of low-frequency quantum oscillations originate from CDW-reconstructed vanadium orbitals and exhibit transport consistent with the Dirac-like features (high mobility, low cyclotron mass) of the kagome lattice. The multiplicity and frequencies associated with these vanadium orbits are shown to originate from a reconstructed Fermi surface with small pockets linked to folded, vanadium-dominated bands. We further demonstrate that the CDW instability is three-dimensional in nature with a resulting 2×2×4 superstructure. Synchrotron x-ray data are ananlyzed to provide a model for the average superstructure. Together, our results provide direct evidence that the in-plane CDW is derived from vanadium orbitals which comprise the kagome lattice in AV_3Sb_5 and validate recent efforts to map the core interactions in these materials to minimal tight-binding models built from a two-dimensional kagome network.

5.2 Methods

5.2.1 Synthesis

Single crystals of CsV_3Sb_5 were synthesized from Cs (liquid, Alfa 99.98%), V (powder, Sigma 99.9%) and Sb (shot, Alfa 99.999%). As-received vanadium powder was purified in-house to remove residual oxides. Due to extreme reactivity of elemental Cs, all further preparation of CsV_3Sb_5 was performed in an argon glovebox with oxygen and moisture levels <0.5 ppm. Single crystals of CsV_3Sb_5 were synthesized using the self-flux method. The flux is a eutectic mixture of CsSb and Cs_3Sb_7[289] mixed with VSb_2. Elemental reagents were milled in a pre-seasoned tungsten carbide vial to form a composition which is 50 at.% $Cs_{0.4}Sb_{0.6}$ eutectic and approximately 50 at.% VSb_2. Excess antimony can be added to the flux to improve volatility if needed. The fluxes were loaded into alumina crucibles and sealed within stainless steel jackets. The samples were heated to 1000 at 250/hr and soaked there for 24 h. The samples were subsequently cooled to 900 at 100/hr and then further to 500 at 2/hr. Once cooled, the crystals are recovered mechanically. Crystals are hexagonal flakes with brilliant metallic luster. Samples can range up to 1 cm in side length and up to 1 mm thick. Elemental composition of the crystals was assessed using energy dispersive x-ray spectroscopy (EDX) using a APREO C scanning electron microscope.

5.2.2 Electrical transport measurements

Electronic transport measurements were performed using a Quantum Design 14 T Dynacool Physical Property Measurement System (PPMS). A Quantum Design rotator option was used to collect angle-dependent and temperature-dependent data. Crystals are exfoliated to remove any surface contaminants, and electrical contacts were made in a standard 4-point geometry using gold wire and silver paint. Crystals were initially mounted such that the c-axis was parallel to the field (flat plates mounted flush on resistivity stage). An alternating current of 8 mA and 12.2 Hz was driven in the ab-plane.

5.2.3 Electronic structure calculations

DFT simulations of the electronic structure of CsV_3Sb_5 unit cell were performed in VASP *v*5.4.4 using identical parameters to several recently reported studies [275, 275, 290]. We employed the PBE functional [94] with D3 corrections [291], a 500 eV plane wave energy cutoff, a Γ-centered $11 \times 11 \times 5$ k-mesh, and the recommended PAW pseudopotentials for v5.2. Spin orbit coupling was activated for all calculation steps except for structural relaxation. All calculations were completed with an energy con-

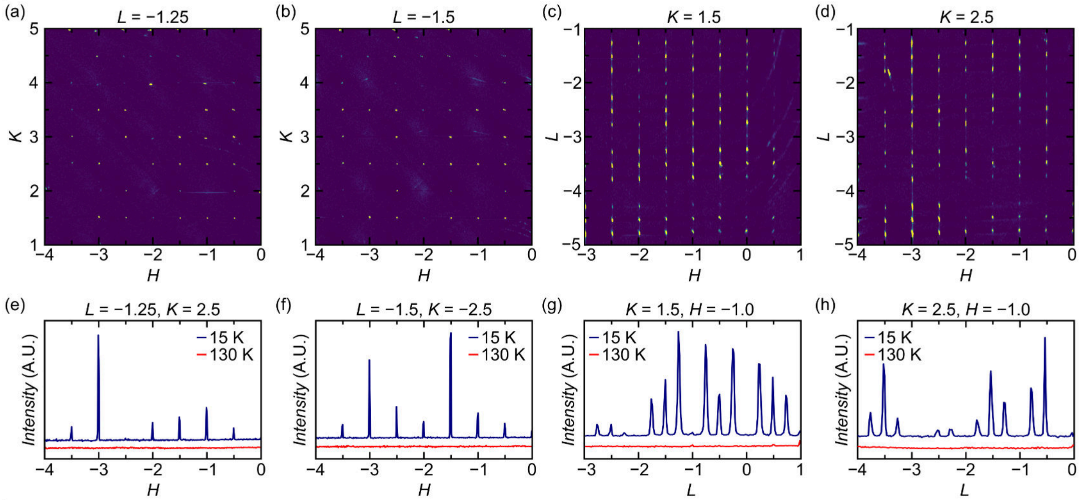

Figure 5.2: CsV_3Sb_5 low temperature XRD data. (a–d) 2-dimensional slices through reciprocal space on half-integer Bragg planes at 15 K, highlighting superlattice peaks in CsV_3Sb_5. (e–h) Line cuts through the 2D data, highlighting the periodicity of the superlattice peaks. Blue data are 1D traces showing data collected at base temperature (15 K). Red data shows the data collected at 130 K data, confirming that the superlattice peaks emerge alongside the charge density wave order emerges $T^* \sim 94$ K. Our data indicates that the superlattice in CsV_3Sb_5 is described by a wave vector of (0.5, 0.5, 0.25).

vergence cutoff of 10^{-6} eV or better. The unit cell was relaxed, as previously described [275], with final a and c lattice parameters of 5.45 Å and 9.35 Å; in good agreement with the room-temperature values determined by X-ray diffraction, 5.52 Å and 9.36 Å, respectively.

WANNIER90 [91] was used to fit Wannier functions (Cs s, p; V s, p, d; Sb s, p; with a frozen fitting window $E_F \pm 2$ eV) and interpolate unit cell Fermi surfaces on a $101 \times 101 \times 101$ grid. Extremal orbits were determined using SERENDIPITY,[2] a new code that builds on the algorithms developed by Rourke and Julian[245] with additional symmetry and interactive visualization tools enabled by the python packages SPGLIB,[246] TRIMESH,[247] and PLOTLY[248].

Supercell calculations were completed on a $2 \times 2 \times 1$ supercell simulated using

---

[2] SERENDIPITY is in development. Interested parties can contact Samuel Teicher: steicher@ucsb.edu

identical parameters and a $5 \times 5 \times 5$ k-mesh that was distorted along the M_1^+ P_3 irreducible representation in ISODISTORT.[292, 293] M_1^+ P_3 involves four distinct distortion modes, including B_{3u} and B_{2u} V sublattice modes and E_a and A_{1a} Sb_2 (antimonene layer) sublattice modes. Cs and Sb_1 (kagome layer) atomic positions are unaffected. Negative magnitudes of the B_{3u}, B_{2u}, and E_a modes recreate the "Star of David" (SoD) while positive magnitudes recreate the inverse "Tri-Hexagonal" (TrH) structure. We initialized super cell structural relaxations with four different sets of mode magnitudes, $(B_{3u},\ B_{2u},\ E_a,\ A_{1a}) = 0.3\,\text{Å}\cdot\{(+,+,+,+);\ (+,+,+,-);\ (-,-,-,+);\ (-,-,-,-)\}$, testing both the SoD and TrH structures, while additionally trialing both positive and negative magnitudes of the A_{1a} mode, which corresponds to c-axial buckling of the antimonene lattice.

Relaxation proceeded in three steps: volumetric optimization, followed by adjustment of the ionic positions, and finally a free relaxation of the super cell lattice parameters and ionic positions simultaneously. Ultimately, the two SoD configurations relaxed to a similar structure, and the same was true for the two TrH structures. In the final SoD structure we find a positive A_{1a} mode, corresponding to Sb_2 atoms moving further from the smaller triangles and closer to the larger triangles of the SoD structure. In the final TrH structure, we find that a negative A_{1a} mode is favored, in which the Sb_2 atoms similarly move away from the smaller V-V triangle units. In each case, c-axial buckling of the Sb_2 layer is minuscule, 0.005c and 0.002c for SoD and TrH, respectively.

The SoD and TrH distorted super cells are energetically favored over the undistorted unit cell by 4.7 meV and 13.5 meV per formula unit, respectively, consistent with recently reported simulations [287]. Super cell band unfolding employed a modified version of VASPBANDUNFOLDING [294]. Unfolded Fermi surface slices in Fig. 5.8 were calculated on a 51×51 BZ mesh. Cubic spline interpolation was used for smoothing/upsampling prior to projecting onto the larger display range.

Fermi levels for the electronic structure calculations in Fig. 5.4 and Fig. 5.8 were determined based on prior experiment. Additional discussion is provided in the supporting material [295]. Errors in extracting frequencies associated with extremal orbits of the unfolded supercells were determined by graphically selecting orbit paths clearly within a given orbit and those clearly outside and are a product of the pixel resolution of the calculations. The top of the error bar is the outer bounding area, the bottom the inner bounding area, and the average of these bounds was chosen as the nominal value. Errors in determining the extremal orbits of the parent structure are small and not shown (<10 T).

5.2.4 X-ray diffraction measurements

High dynamic range x-ray diffraction maps were collected at the QM2 beamline at CHESS. The incident x-ray wavelength was 0.42755Å, selected using a double-bounce diamond monochromator. Temperature was controlled by bathing the small single crystal samples inside a stream of cold flowing helium gas. Diffraction was recorded in transmission though the sample using a 6 megapixel photon-counting pixel-array detector with a silicon sensor layer. Full 360 degree sample rotations, sliced into 0.1 degree frames, were indexed to the high-temperature crystal structure and transformed to reciprocal space. Some elements of the data reduction employed the NeXpy software package. Crystal structures were visualized in VESTA.[167]. Diffraction data were analyzed within the APEX3 software package and data were corrected for absorption and extinction effects. Refinement of the structure was performed using the integrated SHELX software package.[296] Charge flipping simulations of diffraction data were performed using the TOPAZ software package.[297, 298, 299]

5.2.5 Second harmonic generation optical measurements

Second harmonic generation (SHG) measurements were performed using an ultrafast laser with a pulse duration of 40 fs and a repetition rate of 50 kHz. The laser was tuned to a center wavelength of 800 nm and a sample fluence of 3 mJ/cm^2. An oblique incidence reflection geometry was employed with both incoming and outgoing beams P-polarized. The reflected SHG at 400 nm was isolated with a spectral filter and detected using a back-illuminated CMOS image sensor. Overall SHG intensities were extracted by averaging over the scattering plane angle. A sample-in-vacuum optical cryostat was used to cool the sample below the CDW phase transition temperature.

5.3 Results

5.3.1 Crystal Structure

The AV_3Sb_5 (A: K, Rb Cs) family of kagome metals are layered, exfoliable materials consisting of V_3Sb_5 slabs intercalated by alkali metal cations. The vanadium sublattice forms a perfect kagome lattice under ambient conditions (Figure 5.1). CsV_3Sb_5 is the terminal endpoint of the alkali-metal series, shows the highest superconducting transition ($T_c = 2.5\,\mathrm{K}$), and an onset of CDW order below $T^* = 94\,\mathrm{K}$ [275]. The CDW is accompanied by a weak structural distortion manifest as a superlattice of Bragg scattering in synchrotron x-ray diffraction data.

Early measurements within the $L = 0$ scattering plane resolved only $\mathbf{q} = (0.5, 0, 0)$ and $(0, 0.5, 0)$-type superlattice reflections [275], which is seemingly at odds with recent STM reports of 2×2 supercells associated with 3Q charge order. To address this, an expanded exploration of superlattice peaks was conducted at finite L-values with the results shown in Fig. 5.2. In this higher resolution data, a more complex, three-dimensional superlattice structure is observed that is best indexed by a $\mathbf{q} = (0.5, 0.5, 0.25)$ wave vector. (0.5, 0.5)-type superlattice reflections are largely not resolvable in the $L = 0$ plane, accounting for the initial failure to index them. The in-plane component of the superlattice modulation agrees with the 3**Q** structure observed in local probes. The superlattice peaks at (0.5, 0.5, 0.25)-type positions vanish above the CDW ordering temperature and indicate a modulation of the in-plane distortion along the c-axis (interplane phasing).

Considering first the in-plane distortions allowed on an idealized kagome lattice, the kagome "breathing" mode often leads to lower energy structures, and this mode matches preliminary conclusions drawn from STM and DFT studies of KV_3Sb_5 [273, 287, 288]. As shown in Figure 5.1, the structure can distort between two potential candidates: (1) the SoD distortion and (2) the TrH distortion. The phasing along the c-axis, which governs the modulation of the distortion motifs along the out-of-plane direction are naively expected to be of a lower energy scale than the in-plane components. To determine the nature of the three-dimensional superstructure that forms below the CDW transition, the low-temperature (15 K) diffraction data was refined. Approximately 30000 reflections (∼4500 unique) were indexed within a hexagonal unit cell with lattice parameters $a = b = 11.05410(13)$Å, $c = 37.334(5)$Å, and $\alpha = \beta = 90°$ $\gamma = 120°$.

SHG data indicate that inversion symmetry is not broken below the ordering transition [295], and, as a result, data were initially analyzed via charge-flipping in the $P\bar{1}$ space group. This provided a baseline visualization for distortions below the transition, and, absent any further constraints, already suggests an average cell with modulation between TrH and SoD-type distortions along the c-axis. Further refinement was then pursued within the space group $P\bar{3}$, assuming a minimal three-fold symmetry that conformed with the diffraction data as well as inversion symmetry demonstrated from the

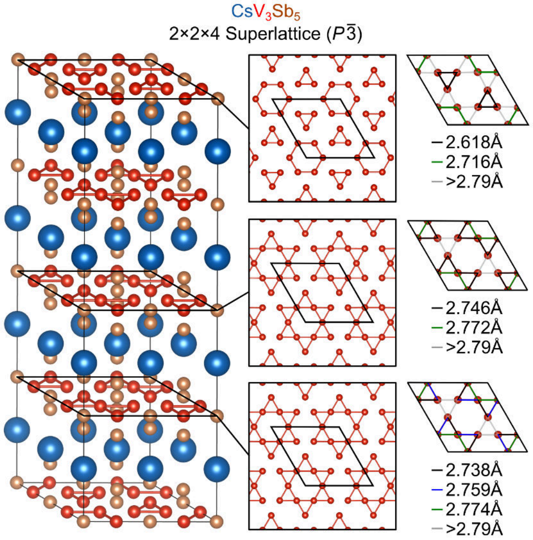

Figure 5.3: CsV_3Sb_5 low temperature XRD structure solution. Single-crystal diffraction data implies that CsV_3Sb_5 distorts into $2{\times}2{\times}4$ supercell, where the kagome layers exhibit both TrH- and SoD-like distortions. Our current model indexes the cell in the $P\bar{3}$ space group. The SoD-like distortions are substantially weaker than the TrH-like distortion, and two unique SoD layers are noted.

SHG data. While the data can potentially be indexed in a lower rotational symmetry (e.g. centered orthorhombic), we could not find sufficient evidence within the current data to perform the refinement lower than $P\bar{3}$. For the solution in $P\bar{3}$, a twinning model was used with twins realized via a two-fold rotation along the (0, 0, 1) axis. We qualitatively tested alternate hexagonal twinning models, and in all cases the refined structure remains nearly unchanged.

Atomic positions and displacement parameters were refined in $P\bar{3}$ (R1 = 0.089, GoF = 1.32) with the resulting refinement parameters provided in the supplemental information [295]. The resulting $P\bar{3}$ structure is shown in Fig. 5.3. To highlight the differences in bonding and V-V motifs, we have selected to draw V-V bond lengths ≤ 2.79Å. The middle panels demonstrate the different motifs with distortions in each kagome plane highlighted. The top and bottom layers of the lattice assume an in-plane TrH distortion while the intervening layers assume a weak SoD-like distortion. The right most panels of Figure 5.3 identify the distorted V-V bond distances. For graphical simplicity, bonds within 0.0025Å of their mean value were grouped and averaged. Full bonding information is available in the CIF file.[295] The TrH-like layers feature the most distinct distortion, which manifests the largest deviation in bond lengths from the parent structure. The two unique SoD-like layers are similar, though the central layer exhibits slightly weaker V-V bond distortions. We emphasize here that this is a depiction of the *average* structure produced by modeling the x-ray diffraction data. More complex twinning effects or stacking disorder within the 4 layer unit cell can influence the appearance of the average structure.

5.3.2 Electronic Structure

As the interlayer interactions are expected to be weak in CsV_3Sb_5, we neglect the impact of the c-axis component of the superlattice on the electronic structure and focus on the impact of the in-plane distortion modes. This was verified by comparing the calculated band structures of the nominal $2 \times 2 \times 1$ cell with the $2 \times 2 \times 4$ cell proposed by SCXRD [295]. Candidate structures (M_1^+ P_3 irrep.) matching the pure TrH and SoD distortions were selected for DFT relaxation and band structure calculations. Our DFT studies find that both the SoD and TrH distortions are slightly favored over the undistorted structure; by 4.7 meV/f.u and 13.5 meV/f.u, respectively. DFT-relaxed structures are shown alongside the experimental, undistorted crystal structure in Figure 5.1.

Despite the low stabilization energy of the distorted structures relative to the parent structure, the predicted vanadium lattice distortions are significant. The V-V bond lengths are all equally 2.72Å in the parent structure, and transform to 3 distinct lengths: 2.65Å 2.75Å and 2.84Å for the SoD distortion, and 2.58Å 2.68Å and 2.82Å for the TrH distortion. The experimentally refined structure shows slightly weaker

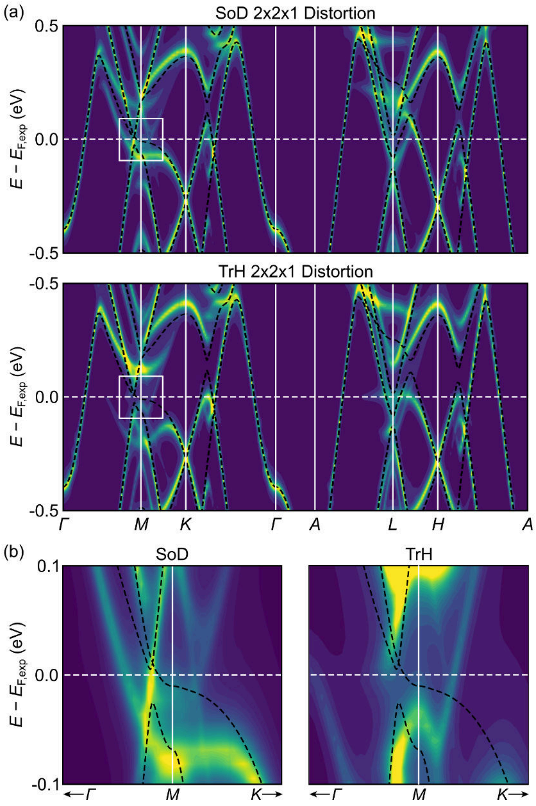

Figure 5.4: CsV_3Sb_5 band structure unfolding. (a) Unfolded electronic structure of the “Star of David (SoD)” and “Tri-Hexagonal (TrH)” distortions in CsV_3Sb_5 with the undistorted electronic structure superimposed for comparison (black). Largest perturbation to the structure appears near the Dirac-like bands near M. (b) Close-up of the changes near the M-point, highlighting the new bands that appear as a result of the CDW and the associated structural distortion.

distortions and corresponding lengths of 2.74Å 2.77Å and 2.79Å for SoD layers and 2.62Å 2.72Å and 2.86Å for the TrH layers. Concurrently, the Sb graphitic sublattice is fragmented into individual hexagons and also hosts a slight buckling in the c-direction for both distorted structure types.

Figure 5.4 shows the effect of the two superlattice types (SoD and TrH) on the *ab initio* electronic structure of CsV_3Sb_5. The resulting band diagrams were unfolded for comparison to the undistorted electronic structure shown in previous works [272, 275]. The heat map shows the relative projections of the electronic states after the unfolding, and the black bands are the undistorted structure of CsV_3Sb_5. In the low-temperature distorted state, the electronic structure is largely unperturbed, particularly the central band about Γ which derives from the Sb p-orbitals. However, the bands near the M-point, which are the relevant Dirac-like bands associated with the vanadium d-orbitals, are altered significantly.

Figure 5.4(b) shows expanded views of the SoD and TrH electronic structures in the vicinity of the M-points. An orbital decomposed band diagram (“orbital bands”) further identifies these states as originating primarily from vanadium orbitals [295]. The emergence of the CDW and the resulting superlattice therefore has a clear effect on the electronic structure near E_{F} for the vanadium orbitals comprising the Dirac-like crossings. This effect has a significant impact on the Fermi surface and is expected to impact transport sensitive to topographical changes at E_{F}. Experimental detection of these effects are discussed in the next section.

5.3.3 Quantum Oscillation Measurements

A effective bulk probe of the low energy band structure is the measurement of quantum oscillations in high-field electron transport measurements. Crystals of the AV_3Sb_5 kagome metals are high mobility metals with low residual resistivity ($\sim 0.1\ \mu\Omega$-cm) values [272, 275, 284], rendering quantum oscillation measurements an appealing probe for exploring the low temperature electronic structure.

Figure 5.5 presents a series of temperature-dependent quantum oscillation measurements on stoichiometric crystals of CsV_3Sb_5 with RRR ≈ 80. The crystals were mounted with the c-axis parallel to the magnetic field while current was driven within the ab-plane. The normal “background” magnetoresistance (MR) was modeled using a power function $\rho_0 \approx \alpha H^{\beta} + \gamma$ fit over the range from 4 T to 14 T. The oscillatory component of the MR was then isolated by subtracting the background MR

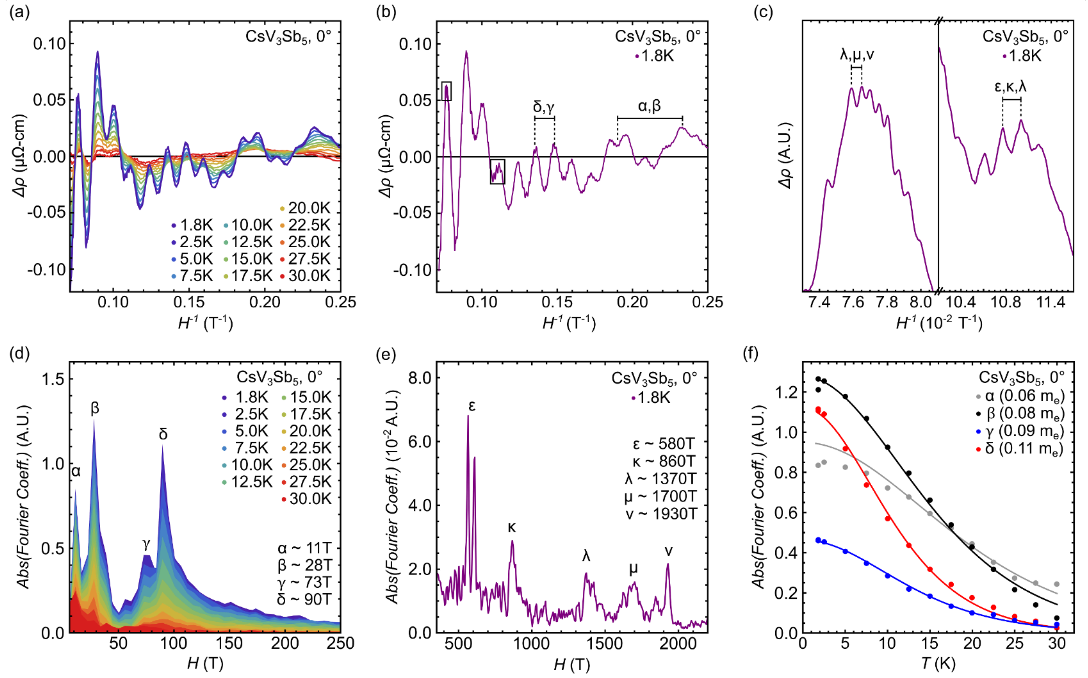

Figure 5.5: Overview of CsV_3Sb_5 quantum oscillations and temperature dependence. (a) Oscillatory component of the magnetoresistance extracted from the temperature-dependent SdH data collected on single crystals of CsV_3Sb_5 mounted with the c-axis parallel to the magnetic field (0. (b) A high-resolution scan at 1.8 K shows significant contributions from high-frequency modes, particularly at the peaks and troughs of the general oscillatory behavior. (c) Magnified view of the high-frequency features, providing visual confirmation for multiple high-frequency modes. (d,e) Fourier transformation of the quantum oscillation data, showing the low- and high-frequency components of the power spectrum. The 9 unique frequencies have been assigned greek letters. (f) The magnitude of the Fourier coefficients is used in conjunction with the Lifshitz-Kosevich (LK) formula to extract the cyclotron "effective mass." All low-frequency modes show very low effective masses, consistent with transport originating from the Dirac-like crossings at M.

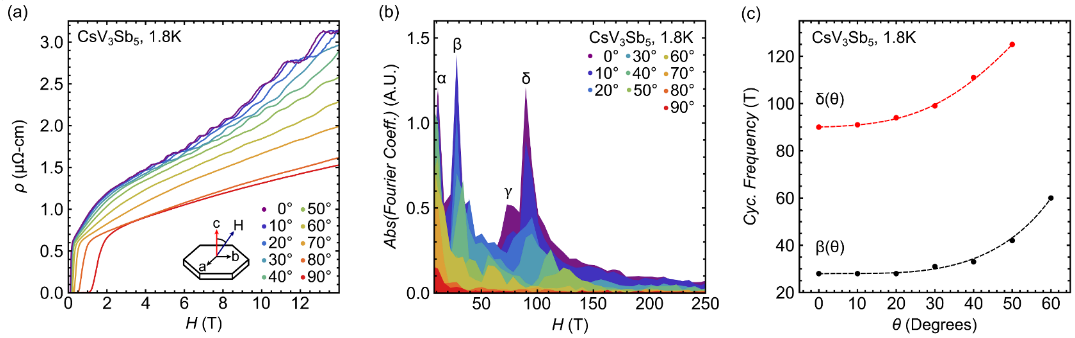

Figure 5.6: Angular dependence of CsV_3Sb_5 quantum oscillations. (a) Raw electronic resistivity as a function as field and angle, where the angle is defined as between the c-axis and the magnetic field. Oscillations are clearly visible $>2\,$T. The oscillations appear dampened with angle, vanishing for θ >60 (b) Fourier transform of angle-resolved SdH data, showing primary low-frequency contributions to the power spectrum. The high-frequency contributions are suppressed rapidly by rotation. (c) The most prominent frequencies (β, δ) are shown as a function of rotation angle – dashed lines serve as a guide to the eye. The frequencies were estimated from (b) using Gaussian functions to approximate both the broadening and shortening of peaks. These frequencies exhibit a delayed onset of the angular dependence, consistent with Dirac-like pockets.

$\Delta\rho(H) = \rho(H) - \rho_0(H)$. Figure 5.5(a) shows the oscillatory component of the magnetoresistance as a function of temperature and field, and oscillations are seen to persist up to $25\,$K. The oscillation pattern is relatively complex, with multiple harmonics visible by inspection.

Quantum oscillation data collected at $1.8\,$K is isolated in Figure 5.5(b), where multiple frequency components have been noted by Greek letters. At higher fields, we further highlight several regions that show contributions from additional, higher frequency oscillations in Figure 5.5(c). Due to the presence of multiple closely spaced frequencies (discussed in the next paragraph), we have grouped similar frequency components together in this initial inspection of the subtracted data. All frequencies persist between different measurements and different crystals.

Turning first to the low frequency spectrum, Figure 5.5(d) shows the Fourier transform of the data at multiple temperatures with $H \leq 250\,$T. Four well-defined frequencies appear ($\alpha, \beta, \gamma, \delta$). At higher frequencies with $400 < H < 2000\,\mathrm{T}$, the Fourier transform in Figure 5.5(e) shows an additional five well-defined frequencies ($\epsilon, \kappa, \lambda, \mu, \eta$). The peak designated ϵ technically appears as two sharp peaks; however, this effect is likely extrinsic, and we currently consider the ϵ peak as the average of these two peaks.

While the modes above 250 T vanish quickly with increasing temperature above 2 K, the low frequency modes remain well-defined up to 25 K. The temperature dependence of the Fourier coefficients of the α, β, γ and δ orbits are shown in Figure 5.5(f). The cyclotron "effective mass" (m^*_{eff}) can be extracted using the approximate Lifshitz-Kosevich (LK) form $a_i(T) \approx X/(B \sinh X/B)$, where $X = \alpha\, m^*_{\text{eff}} T$. Here, B is the magnetic flux density and is typically selected as the mean field within the FFT window. The parameter α is a constant defined as 14.69 T/K. The resulting m^*_{eff} values are low for these low frequency orbits—nearly $1/10$ of the free electron mass—consistent with transport originating from the Dirac modes expected near the M-point.

Whereas the temperature-dependence of the quantum oscillations provides information regarding the scattering, lifetime, and effective mass of the carriers, the angular-dependence can provide information regarding the topography of the Fermi surface. Figure 5.6(a) presents a series of angle-dependent quantum oscillation measurements collected at 1.8 K where $\theta = 0^\circ$ denotes the c-axis parallel to the H-field. The Fourier transforms of the data in Figure 5.6(a) are shown in Figure 5.6(b), and the frequencies of the δ and β orbits are plotted as a function of angle in Figure 5.6(c). The α and γ orbits shift and quickly convolve into neighboring frequencies with increasing angle, precluding their analysis at finite θ.

Conceptually, the orbits that generate the oscillations can be imagined as slices through the Fermi surface at different approach angles. 'Extremal' cross-sections with the largest and smallest cross-sectional area will generate distinct oscillation frequencies. For example, a perfectly spherical Fermi pocket exhibits no angular dependence and only one frequency from the circular cross-section. A strongly anisotropic pocket (e.g. those from 2D Dirac cones) would show a strong dependence with angle, as oblique slices through a cylinder become progressively larger as the angle increases. The sharp upturns seen above 40° in the δ and γ orbits are consistent with orbits derived from strongly anisotropic pockets, and—as we will demonstrate in the next section—are best ascribed to electrons within Dirac-like features associated with the vanadium kagome lattice.

5.3.4 Fermi Surface Topography and Frequency Correlation

The transport data shown in Figures 5.5 and 5.6 reveal a complex superposition of quantum oscillations originating from multiple portions of the Fermi surface. In order to identify how the CDW and the associated crystallographic distortions perturb the Fermi surface, the oscillation frequencies (i.e. enclosed Fermi surface pockets) seen experimentally must be correlated to the DFT-calculated Fermi surfaces. To do so, we first examine the undistorted Fermi surface in the context of the possible extremal orbits.

To determine the orbits accurately, the Fermi energy needs to be well-defined. It is worth taking a moment to review the spread of E_{F}'s reported in the current literature, as the Dirac-like nature of the bands near E_{F} renders rapid changes in the sizes of electron pockets with relatively minor shifts in Fermi energy. Initial DFT studies [272, 275, 275, 273, 284] found Fermi levels slightly below those determined experimentally by ARPES [265, 275] and STM measurements [273, 274]. For simplicity, we will refer to these earlier results as $E_{\mathrm{F,lit}}$ and $E_{\mathrm{F,exp}}$ respectively. Recent DFT studies have since provided self-consistent results closer to experimental values [287]; we refer to this value as $E_{\mathrm{F,DFT}}$, which agree with the self-consistent DFT calculations presented in this

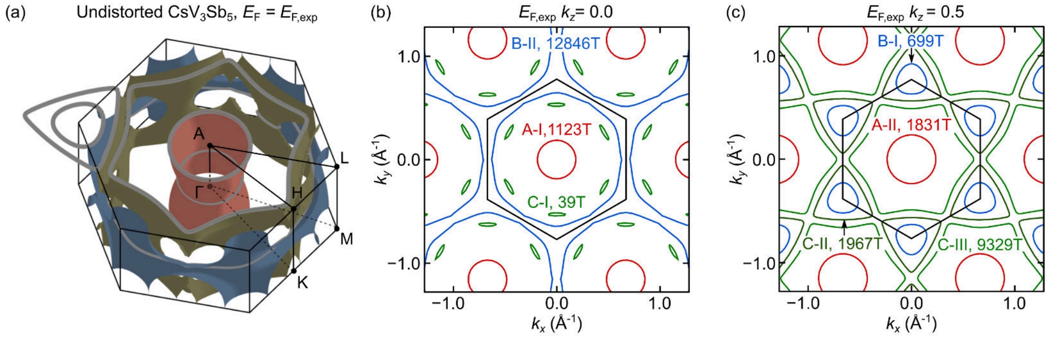

Figure 5.7: Fermi surface of undistorted CsV$_3$Sb$_5$. (a) The Fermi surface for undistorted CsV$_3$Sb$_5$ calculated with $E_\mathrm{F} = E_\mathrm{F,exp}$ shows a variety of potential orbits. Orbits calculated by the SERENDIPITY python package are shown highlighted in grey. (b,c) For clarity, isoenergy contours at $k_z = 0$ and $k_z = 0.5$ for the $E_\mathrm{F} = E_\mathrm{F,exp}$ surface are shown with all unique extremal orbits marked. Several high- and low-frequency orbits can be identified. The Fermi surface pocket of origin is indicated through the orbit color, which will be used for comparison throughout our discussion. While there are clearly multiple frequencies in the predicted spectrum, note that there is only 1 symmetry unique (39 T) low frequency-mode, which seems at odds with our experimental observations. Further, for frequencies $400 < f < 2000$ T, there are only 4 predicted modes, as opposed to the 5 experimentally observed components.

work.

Figure 5.7 shows the calculated Fermi surface using the *undistorted* CsV$_3$Sb$_5$ structure where $E_\mathrm{F} = E_\mathrm{F,exp}$. Despite already motivating that the underlying electronic structure is perturbed by the influence of the CDW, it is nevertheless instructive to first understand the undistorted Fermi surface. The orbits identified by SERENDIPITY are shown in Figure 5.7(a) in grey. 2D slices of the Fermi surface at $k_z = 0$ and $k_z = 0.5$ are provided for a more convenient comparison, since all of the extremal orbits at $E_\mathrm{F,exp}$ occur on these two high-symmetry planes. The Fermi surface maps reveal a variety of possible extremal orbits, confirming that the quantum oscillations in CsV$_3$Sb$_5$ should contain multiple frequencies, though the 9329 T and 12846 T frequencies are significantly above the experimental range of detection in 5.5(d,e) and Figure 5.6(b).

First considering the measurable high frequencies (250 T $< f <$ 2000 T), we find only four extremal orbits (B-I, 699 T; A-I, 1123 T; A-II, 1831 T; and C-II, 1967 T) to match to five measured values ($\eta \approx 580\,\mathrm{T}$, $\kappa \approx 860\,\mathrm{T}$, $\lambda \approx 1370\mathrm{T}$, $\mu \approx 1700\,\mathrm{T}$, $\nu \approx 1930\,\mathrm{T}$). At lower frequencies, the agreement is much worse: only one calculated low frequency orbit (C-I, 39 T) is found to compare with four low frequency oscillations observed in experiments ($\alpha \approx 11\,\mathrm{T}$, $\beta \approx 28\,\mathrm{T}$, $\gamma \approx 74\,\mathrm{T}$, and $\delta \approx 90\,\mathrm{T}$). A table of the calculated (DFT) frequencies at $E_{\mathrm{F}} = E_{\mathrm{F,exp}}$, along with the associated cyclotron masses m_{cyc} has been included in the supplementary supporting material (SFig. 3).[295]

Given the significant CDW band reconstruction presented in Fig. 5.4, a low-temperature Fermi surface modification in CsV$_3$Sb$_5$ is expected. Figure 5.8 displays unfolded Fermi surface slices for pure SoD and TrH $2 \times 2 \times 1$ supercells at $E_{\mathrm{F,exp}}$, demonstrating this reconstruction. While the central Sb p-orbits are largely unaffected by the CDW, V d-bands gap and change the Fermi surface. On the $k_z = 0.0$ plane, the single, large B-II orbit reconstructs into small orbits in both structures, generating triangular orbits around the K points at the corners of the Brillouin zone. On the $k_z = 0.5$ plane, the A-II central pocket and the smaller B-I orbit around K are largely unaffected by the CDW; however, the larger C-II orbit (dashed line) is strongly affected. In the SoD structure, this orbit is completely gapped out at $E_{\mathrm{F,exp}}$, while in the TrH structure, the C-II orbit persists.

Supporting these models, prior ARPES results show the A-I and A-II orbits as well as the B-I orbit in KV$_3$Sb$_5$ and CsV$_3$Sb$_5$ both above and below the CDW transition [275, 273]. STM results at lower temperature also show the preservation of the A-I and A-II orbits and are consistent with at least one triangular orbit at the K-points [274]. Therefore, with regard to the preservation of the A-I, A-II, and B-I orbits, CDW calculations in both SoD and TrH structures appear consistent with experimental results to-date. STM data also validate the reconstruction of the B-II orbit captured within the DFT models; however our models also predict numerous other changes in the low frequency (small orbit) regime.

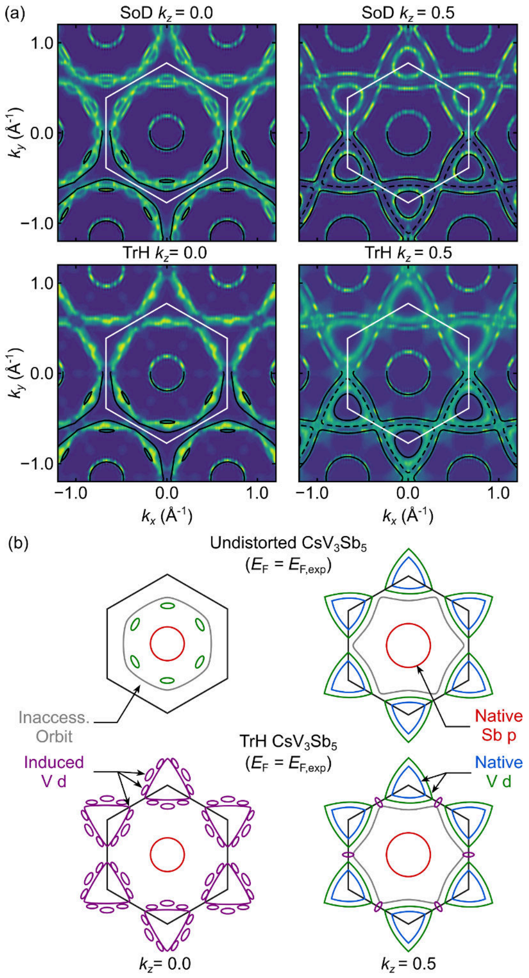

Figure 5.8: Unfolded Fermi surfaces of CsV_3Sb_5 in the breathing mode phases. (a) Fermi surfaces for the SoD and TrH distortions in CsV_3Sb_5 generated from the unfolded supercell band structures. Undistorted Fermi surface (black lines) contours are shown for comparison. A significant reconstruction of the V d states occurs. Most high-frequency modes are preserved, though the C-II orbit (dashed) is gapped in the SoD structure. (b) Schematic description of Fermi surface reconstruction. Grey orbits are well above measurable frequencies. Band reconstruction in the TrH supercell introduces one additional triangular orbit around the M-point while preserving higher frequency native V d and Sb p orbits. Notably, the distortion also introduces 3 smaller, Dirac-like orbits (purple) consistent with our measurements.

Investigating the band reconstruction in the distorted state further, the data shown in Figure 5.8(a) clearly show additional features. Figure 5.8(b) provides a simplified, pictorial representation of the Fermi surface and closed orbits in the undistorted and TrH structures to aide discussion. All possible orbits that exist in the undistorted structure 5.8(a) are depicted at $E_{\mathrm{F,exp}}$. Orbits which are too large to be experimentally observed with our current data are shown in grey. The remaining orbits are color-coded consistent with the pocket designations shown previously in Figure 5.7. For this qualitative comparison, we focus on the orbits within the TrH structure for two reasons; 1) the additional modes are less obvious in the 2D data for the TrH (but no less relevant), and 2) as we will show, the TrH structure produces one additional frequency in the "mid-frequency" regime which makes the presence of layers with this configuration distinguishable.

Focusing on comparison of the high-frequency orbits, we see that there are a total of 4 experimentally accessible orbits at $E_{\mathrm{F,exp}}$ in the undistorted structure. Upon introducing the TrH distortion, several key changes occur. In the $k_z = 0$ plane, the distortion generates 3 distinct vanadium d-orbits at $E_{\mathrm{F,exp}}$ by shifting and gapping bands around the M and K points near the corners and sides of the zone. Notably, band reconstruction about the M point forms a new medium-frequency triangular orbit at $E_{\mathrm{F,exp}}$. The $k_z = 0.5$ plane, in contrast, is largely preserved in the new configuration, with the exception of the addition of one Dirac-like orbit at the L point.

Thus, in this high frequency regime, the TrH distortion has several effects: 1) the generation of 3 additional Dirac-like modes, 2) the preservation of high frequency orbits primarily comprised of Sb-states, and 3) the introduction of a new triangular orbit from the band reconstruction. It is worth noting that other, smaller Dirac-like orbits are likely present, but the resolution of the present supercell calculation limits our search to orbits $>30\,\mathrm{T}$.

Figure 5.9 summarizes all the numerical data characterizing orbits in the undistorted and distorted SoD and TrH Fermi surfaces and overlays these with the experimentally observed quantum oscillations. An exhaustive search was performed for all extremal orbits within a range of E_{F} spanning from above and below the Fermi levels reported throughout the literature thus far ($E_{\mathrm{F,lit}}$–$E_{\mathrm{F,exp}}$–$E_{\mathrm{F,DFT}}$). Orbits are again colored to remain consistent with their pocket designations in previous figures. For completeness, we also show orbits up to 15000 T, though these orbits are not resolvable in the current experiments. The experimentally observed frequencies are overlaid as horizontal grey bars.

First examining comparisons of the models in the high-frequency regime ($200 < f < 3000\,\mathrm{T}$), there are a total of four possible (symmetry unique) orbits at $E_{\mathrm{F,exp}}$. These are the same four shown in the schematic representation. There is one orbit (B-III) which appears at slightly lower E_{F}, though it is gapped by $E_{\mathrm{F,exp}}$. Comparison at $E_{\mathrm{F}} = E_{\mathrm{F,exp}}$, shows that, while precise quantitative agreement between all the frequencies varies between orbits, TrH layers are the only *qualitative* match to 5 frequencies in this regime. In contrast, due to the loss of the C-II orbit, the SoD distortion only recovers 4 of the 5 modes. More detailed comparisons for E_{F} shifted away from $E_{\mathrm{F,exp}}$ will be discussed in the Discussion section.

Next, examining the low-frequency ($f < 200\,\mathrm{T}$) regime, the data show at least 4 well-defined frequencies about $E_{\mathrm{F,exp}}$. However, at $E_{\mathrm{F,exp}}$ there is only 1 orbit in the undistorted structure. This orbit (C-I) is predominantly comprised of vanadium d-orbitals associated with the Dirac-like crossings along the Γ-K line. However, as shown throughout this manuscript, *substantial* reconstruction is expected about the M point. Characterization of the well-defined, closed orbits in the supercell models is shown to the right of the low-frequency (undistorted) structure panel. There are 4 orbits in the SoD model, and 3 in the TrH model. However, it is important to note that our unfolded

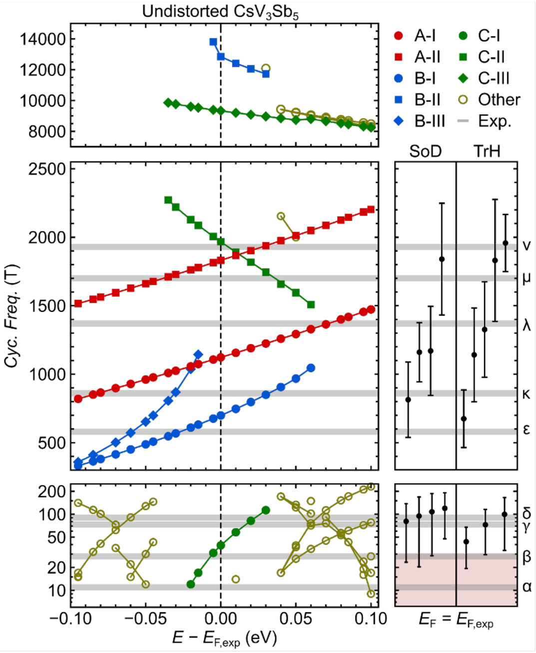

Figure 5.9: Numerical comparison of predicted and measured CsV_3Sb_5 quantum oscillation frequencies. Frequencies extracted as a function of Fermi level in undistorted CsV_3Sb_5 allow us to directly compare the experimental SdH data (grey bars) with the DFT models. The undistorted oscillation frequencies are shown as a function of Fermi level (left). Colored frequencies have been grouped by the pocket and orbit of origin. A conservative numerical estimate for the supercell orbits for the SoD and TrH structures are shown (left) at $E_\mathrm{F} = E_\mathrm{F,exp}$. While 5 mid-frequency orbits are indeed expected in the range $E_\mathrm{F} \pm 0.1\,\mathrm{eV}$, no singular choice of E_F produces complete agreement with experiment. However, the TrH distortion introduces a new high-frequency V d orbit, similar to B-III, which provides a consistent hypothesis. The DFT resolution limit (pink shaded) indicates the frequency range below which we cannot accurately resolve closed orbits.

supercell calculations are unable to resolve orbits with frequencies $< 30\,\mathrm{T}$.

5.4 Discussion

While precise numerical agreement between quantum oscillation frequencies and DFT-derived oscillation frequencies at $E_{\mathrm{F,exp}}$ is lacking in all single layer structures modeled, the presence of the TrH structure at $E_{\mathrm{F,exp}}$ within the unit cell is the only means of capturing the multiplicity of orbits within the experimentally-accessible frequency windows. This is confirmed within x-ray diffraction data which identify TrH distorted planes within the structure; however, the modulation between TrH and SoD distorted planes along the c-axis likely renders a more complex convolution of the orbits calculated within single layer models. Further work computationally modeling the much larger $2 \times 2 \times 4$ supercell with full spin-orbit coupling is required to definitely assess the impact of this modulated supercell and generate a more quantitative comparison to the experimentally observed orbital frequencies.

Irrespective of the out-of-plane modulation, when combined with DFT models, our quantum oscillation data demonstrate that the reconstructed electronic states near the Fermi level are intimately tied to the vanadium d-orbitals. This is particularly true for the M points, which are relevant for their contributions to the topologically protected surface states. Specifically, the observation of multiple low frequency orbits provides direct evidence of a CDW-derived reconstruction of vanadium bands endemic to the underlying Kagome lattice in CsV_3Sb_5. This finding agrees with recent ARPES results which identify gapping around the states at the M-points [300].

When matching ARPES or other Fermi-surface sensitive probes, it is worthwhile to consider the impact of choosing alternative Fermi levels in the single-layer DFT models (i.e. away from $E_{\mathrm{F,exp}}$), in the comparison between models and the data. In the low frequency regime for the undistorted structure, multiple orbits appear when moving both above and below $E_{\mathrm{F,exp}}$, mimicking the multiple modes found in the experiment; however, this scenario can be precluded with the following arguments: (1) For the case where E_{F} lies below $E_{\mathrm{F,exp}}$—in the regime where multiple low frequency orbits appear—the multiplicity of the high-frequency modes does not match the data, as the C-II mode is absent. (2) For the case where E_{F} lies above $E_{\mathrm{F,exp}}$, the C-II and B-I orbits are quickly gapped out in the distorted structures, leaving no explanation for the five mid-frequency oscillations.

Superlattice reflections with a propagation wave vector **q** $= (0.5, 0.5, 0.25)$ in x-ray scattering data indicating a 2×2×4 superstructure with a correlation length matching the native crystallinity of the sample. Primary Bragg reflections in the undistorted state are anisotropic due to c-axis broadening, and the superlattice reflections show the same degree of anisotropy. This indicates a minimum correlation length of ≈ 200Å for the out-of-plane superlattice modulation, which is born from the poorer interplane crystallinity. While the in-plane wave vector $(h, k) = (0.5, 0.5)$ matches the 3**Q** structure observed in STM, the out-of-plane component of **q** implies a four unit cell phasing along the c-axis. The average structure refined in $P\bar{3}$ suggests a modulation of distortion types along the c-axis. While there are a number of possible stacking sequences of SoD and TrH structures, the solution presented here almost falls naturally out of charge flipping in $P\bar{1}$ and is further sharpened by refining the structure within $P\bar{3}$. Future work resolving the presence of orthorhombic twins in the bulk is necessary to justify pursing lower symmetry structures, or more complex combinations of motifs (e.g. phased offsets between layers).

The $2 \times 2 \times 4$ unit cell resolved in CsV_3Sb_5 seemingly contrasts the $2 \times 2 \times 2$ cell identified in KV_3Sb_5 [273]. Future diffraction studies will be required to fully explore this apparent difference; however one potential reason is the poorer c-axis crystallinity of the KV_3Sb_5 crystal explored in the earlier study. This broadening along L can potentially mask $q_L = 0.25$-type reflections or the enhanced disorder can modify the structural ground state. While this paper was in review, another manuscript appeared by Li et al. [301] instead reporting a 2×2×2 superstructure in CsV_3Sb_5. We note here that our data are in agreement in the momentum space regions reported in that work. In these regions the $q_L = 0.25$-type superlattice peaks are weak and below our experimental resolution. Larger surveys of reciprocal space reveal are required to map the 1/4-type c-axis superlattice reflections. Disorder within a crystal can also disrupt the longer wavelength stacking, and random stacking faults are unable to create a smaller q periodicity.

5.5 Conclusion

Combined DFT modeling, high-resolution x-ray scattering, and quantum oscillation measurements demonstrate that the CDW state in CsV_3Sb_5 derives from the reconstruction of the kagome-plane vanadium orbitals with an accompanying out-of-plane modulation of the distorted structure. The in-plane component of the resulting $2 \times 2 \times 4$ superstructure is best modeled using the kagome "breathing mode", with the SoD and TrH patterns emerging as energetically favorable structures. X-ray diffraction data are best fit via a model of modulated SoD and TrH distortions along the c-axis of the average structure. Quantum oscillation measurements provide a bulk probe of the electronic structure that demonstrates the CDW's reconstruction of the Fermi surface. They show the dominant role of vanadium orbitals within the kagome planes in CsV_3Sb_5 in the CDW, and support theoretical approaches drawn from minimal models focused on the kagome substructure in AV_3Sb_5 superconductors.

Chapter 6

Electronic structure of topological kagome metals YV_6Sn_6 and GdV_6Sn_6

[1]The synthesis and electronic structure characterization of vanadium-based kagome metals YV_6Sn_6 and GdV_6Sn_6 are presented. X-ray diffraction reveals an ideal kagome network of V-ions coordinated by Sn and separated by triangular lattice planes of rare-earth ions. Density functional theory calculations are presented modeling the band structures of both nonmagnetic YV_6Sn_6 and magnetic GdV_6Sn_6, which can be classified as $\mathbb{Z}_2$ topological metals in the paramagnetic state. These compounds present an interesting platform for controlling the interplay between magnetic order associated with the R-site sublattice and nontrivial band topology associated with the V-based kagome network. Our results invite future exploration of other RV_6Sn_6 (R=rare earth) variants where this interplay can be tuned via R-site substitution.

---

[1] The contents of this chapter previously appeared in Ref. [127]: G. Pokharel, S. M. L. Teicher, B. R. Ortiz, P. M. Sarte, G. Wu, S. Peng, J. He, R. Seshadri, and S. D. Wilson, Electronic structure of topological kagome metals YV_6Sn_6 and GdV_6Sn_6, *Phys. Rev.* B **104**, 235139. ©APS publishing, 2021, reprinted with permission. The text has been abridged and lightly edited to emphasize the portion of the text—electronic structure calculations—contributed by the dissertation author. The full article includes additional experimental characterization, including transport and magnetization measurements, which are omitted here.

6.1 Introduction

The structural motif of a kagome net of metal ions gives rise to both Dirac points in the band structure as well as destructive interference-derived flat band effects. As a result, kagome metals have the potential to host topologically nontrivial band structures intertwined with electron-electron correlation effects. Electronic instabilities resulting from this interplay have been studied theoretically ranging from bond density wave order, to charge density waves (CDW) to superconductivity [269, 261, 262, 267, 302, 266, 303]. Recent experiments have begun to probe this rich phase space and have uncovered the emergence of an unusually large anomalous Hall effect [284, 304, 70], complex patterns of magnetism [305, 306], charge density waves [273, 274], and superconductivity [275, 112, 278], validating the promise of kagome metals to form a rich frontier of unconventional electronic phenomena.

One family of kagome metals are the so-called “166” compounds that crystallize in the $MgFe_6Ge_6$ structural prototype. This class of materials is chemically very diverse, and considering the structure as AB_6X_6, the A-site can host a variety of alkali, alkali earth, and rare earth metals (e.g. Li, Mg, Yb, Sm, Gd...). The B-site generally hosts a transition metal (e.g. Co, Cr, Mn, V, Ni...), and the X-site is generally restricted to the group IV elements (Si, Ge, Sn). Due to this chemical diversity, 166 materials host a wide variety of functionalities, particularly among those with magnetic host lattices. Examples include the existence of spin polarized Dirac cones in YMn_6Sn_6 [307]; large anomalous hall effects in $LiMn_6Sn_6$ [308], $GdMn_6Sn_6$ [309]; Chern topological magnetism in $TbMn_6Sn_6$ [310]; competing magnetic phases in YMn_6Sn_6 [311]; catalytic properties in $MgCo_6Ge_6$ [312]; negative magnetoreistance in $YMn_6Sn_{6-x}Ga_x$[313]; and a cycloidal spin structure in $HoMn_{6-x}Cr_xGe_6$ [314].

One appeal of the chemical versatility of the 166 class of compounds is the ability

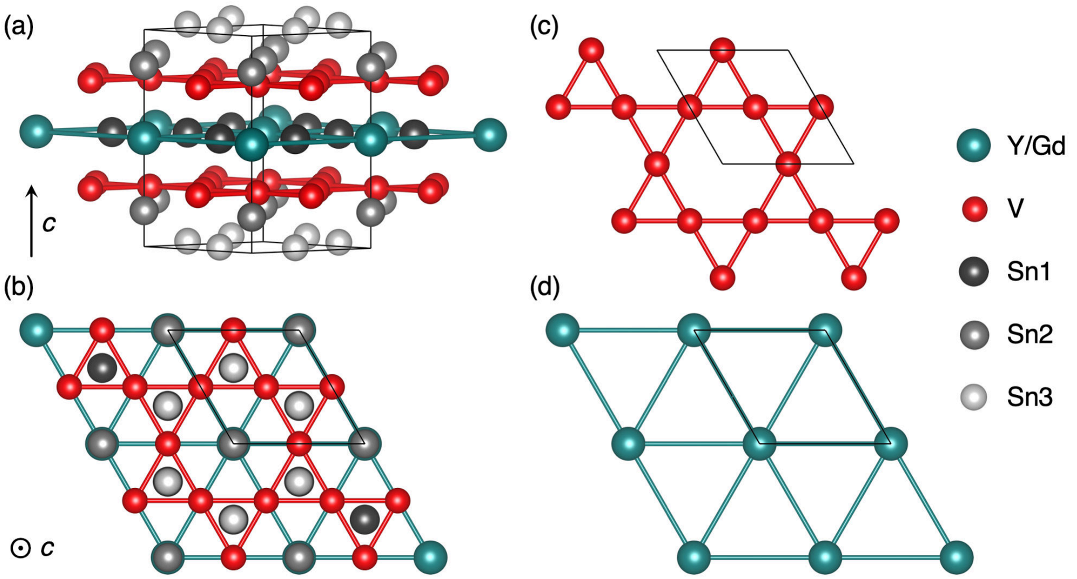

Figure 6.1: Crystal structure of RV_6Sn_6 (R = Gd, Y). (a) RV_6Sn_6 lattice structure comprised of different layers of V_3Sn2, RSn1 and Sn3 atoms. The three different types of Sn sites are represented by Sn1, Sn2 and Sn3. (b) Top view of crystal structure looking along the c-axis and showing the kagome plane of V-atoms and projected Sn1 and Sn3 sites. (c) 2D kagome net of V-atoms. (d) Triangular lattice of R-site (Gd, Y) ions interwoven between kagome planes as shown looking along the c-axis.

to design materials where magnetic interactions can be tuned independently from the kagome lattice. Nonmagnetic B-site variants, in principle, provide this flexibility and allow the interplay between magnetism and the kagome-derived band structures to be explored. This potentially allows access to new electronic phenomena derived from coupling the triangular-lattice planes of magnetic A-site ions and a nonmagnetic B-site kagome net. Nonmagnetic kagome metals are rather underexplored relative to their magnetic counterparts, and recent investigation of nonmagnetic AV_3Sb_5 compounds [272] have shown that unusual charge density wave instabilities and superconductivity may appear when local magnetic interactions are absent [112, 273]. Finding new, nonmagnetic kagome metal variants and tuning/proximitizing magnetic coupling allowed in the 166 structure via the neighboring layers is an appealing next step in this field.

In this work, we report the synthesis of single crystals of YV_6Sn_6 and GdV_6Sn_6 kagome metal compounds and study their physical properties. *Ab initio* modeling of the band structures of these compounds establishes the presence of topological surface states at the Fermi level and categorizes the paramagnetic state as a $\mathbb{Z}_2$ topological metal. The relative accuracy of the electronic structure calculations is confirmed via angle resolved photoemission spectroscopy (ARPES). Our results demonstrate that vanadium-based 166 kagome metals are interesting platforms for studying the interplay between nontrivial band topology and correlation effects endemic to a nonmagnetic kagome lattice proximitized to magnetic order in the neighboring rare-earth layers.

6.2 Experimental Details

Single crystals of YV_6Sn_6 and GdV_6Sn_6 were synthesized via a flux-based technique. Gd (pieces, 99.9%), Y (powder, 99.9%), V (pieces, 99.7%), Sn (shot, 99.99%) were loaded inside an alumina crucible with the molar ratio of 1:6:20 and then heated at 1125^{o}C for 12 hours. Then, the mixture was cooled at a rate of 2^{o}C/h. The single crystals were separated from the flux via centrifuging at 780 ^{o}C. Crystals grown via this method were generally a few millimeters in length and $<$ 1 mm in thickness. The separated single crystals were subsequently cleaned with dilute HCl to remove any flux contamination. Crystals were then transferred into a small jar of mercury to further remove additional tin contamination to the crystals.

Single-crystal x-ray diffraction measurement were carried out on a Kappa Apex II single-crystal diffractometer with a charge coupled device (CCD) detector and a Mo source. Structural solutions were obtained using the SHELX software package [315]. Powder x-ray diffraction (PXRD) measurements were performed on a Pana-

Table 6.1: Structural details of YV_6Sn_6. Obtained from the refinement of single crystal x-ray diffraction data at T = 300 K. Cell refinement in $P6/mmm$ yields R_f = 0.0175, WR_f = 0.0399, and
a = b = 5.520(2), c = 9.168(4) Å.

atom (site)	x	y	z	U_{ani}	occupancy
Y (*1a*)	1.0000	1.0000	0.5000	0.0085(3)	1
V (*6i*)	0.5000	0.5000	0.7481(1)	0.0053(3)	1
Sn1 (*2e*)	1.0000	1.0000	0.8335(1)	0.0066(2)	1
Sn2 (*2d*)	0.3333	0.6667	0.5000(1)	0.0063(2)	1
Sn3 (*2c*)	0.3333	0.6667	1.0000	0.0054(2)	1

Table 6.2: Structural details of GdV_6Sn_6. Obtained from the refinement of single crystal x-ray diffraction data at T = 300 K. Cell refinement in $P6/mmm$ yields R_f = 0.039, WR_f = 0.085, and a = 5.5348(7), c = 9.1797(11) Å.

atom (site)	x	y	z	U_{ani}	occupancy
Gd (*1b*)	1.0000	1.0000	0.5000	0.0063(4)	1
V (*6i*)	0.5000	0.5000	0.7487(2)	0.0055(4)	1
Sn1 (*2e*)	1.0000	1.0000	0.8344(1)	0.0072(4)	1
Sn2 (*2d*)	0.3333	0.6667	0.5000	0.0054(4)	1
Sn3 (*2c*)	0.3333	0.6667	1.0000	0.0064(4)	1

lytical Empyrean powder diffractometer using powdered single crystals. This was done to further verify the structure and phase purity over a larger volume.

ARPES results were obtained at Beamline 5-2 of the Stanford Synchrotron Radiation Lightsource (SSRL) of SLAC National Accelerator Laboratory using 100 eV photons with a total energy resolution better than 20 meV and a base pressure better than 3×10^{-11} torr. The measurements presented here were performed using linear horizontal (LH) polarized light on a Sn-terminated crystal plane.

6.3 Computational Methods

Ab initio simulations were completed in VASP [150, 151, 152] using the PBE functional [94] with projector-augmented waves, [90, 154]. PAW potentials for V and Sn were selected based on the VASP $v5.2$ recommendations. For the calculations presented in the chapter body, Gd potentials with a frozen f-orbital core were chosen in order to approximate the paramagnetic phase previously investigated in ARPES experiments [316]. In the supporting material, electronic structure calculations are completed for the low-temperature ferromagnetic phase using complete Gd potentials with a Hubbard potential $U = 6$ eV applied to the Gd f orbitals. This choice of U gives a magnetic moment $\mu \approx 7\,\mu$B, consistent with experiment (a Hubbard U correction near 6 eV is generally expected for Gd [317]). Calculations employed an $11\times11\times5$ Γ-centered k-mesh and a plane wave energy cutoff of 400 eV. Structures were relaxed in VASP *via* the conjugate gradient descent algorithm with a force-energy cutoff of 10^{-4} eV. All calculations after relaxation employed spin-orbit coupling corrections with an energy convergence cutoff of 10^{-6} eV. Tight-binding models were constructed by projecting onto valence orbitals (Gd d; V d; Sn p; inner window $E_F \pm 2$ eV; outer window $E > E_F - 5.3$ eV) using the disentanglement procedure in WANNIER90 [91]. Surface state Green's function calculations were completed in the WANNIER TOOLS package [166, 113]. Irreducible representations used to determine the $\mathbb{Z}_2$ invariant were determined with IRVSP [31]. COHP calculations and orbital projections employed LOBSTER; these calculations do not incorporate spin-orbit coupling, which is not implemented in LOBSTER [33, 34, 35, 36]. A Gaussian smoothing with standard deviation 0.1 eV was applied to the density of states and COHPs. Structures were visualized with VESTA [167].

We performed bulk electronic structure ARPES simulations using parameters similar to the experimental values (100 eV photon energy, T=30 K, σ_E=0.011 eV, polarization vector = [001]) in CHINOOK [318]. Due to computational constraints, tight-binding terms with magnitude less than 1 meV were omitted. This model employs the naïve assumption of perfect spherical harmonic d and p orbitals. Gd d orbitals were approximated as Y d. Due to the apparent lack of k_z resolution in the experiment, simulations were performed for 41 slices, sampling the full Brillouin zone for $k_z = -\pi/c, \cdots, \pi/c$ and then averaged.

Additional computational details, including a comparison of the relaxed vs. experimental lattice parameters and the full $\mathbb{Z}_2$ invariant calculations are available in the supporting material.[319]

6.4 Results

6.4.1 Crystal structure

The crystal structure of RV_6Sn_6 (R = Y, Gd) was obtained from the refinement of x-ray single crystal diffraction data and the structure is illustrated in Fig. 6.1. YV_6Sn_6 and GdV_6Sn_6 both exhibit the $MgFe_6Ge_6$-type structure with a stacking of the kagome layers of V-ions along the cryostallographic c-axis. The Y/Gd ions as well as the vanadium ions occupy unique crystallographic sites; whereas Sn ions occupy three different types of crystallographic sites denoted by Sn1, Sn2 and Sn3 in Fig. 6.1. A unit cell consists of the layers of V_3Sn2 separated by two inequivalent layers of Sn3 and RSn1, forming [V_3Sn2][RSn1][V_3Sn2][Sn3] layers along the c-axis. Fig. 6.1(b) reveals the topside view of the crystal structure where the V-atoms form a kagome layer within the ab-plane. Sn2 and Sn3 sites form stannene planes between the kagome layers of V atoms. The isolated kagome net of V atoms is shown in Fig. 6.1(c). The interstitial rare-earth atoms form a triangular lattice plane as shown in Fig. 6.1(d).

The refined structural parameters of YV_6Sn_6 and GdV_6Sn_6 are shown in Table 6.1. Nearest neighbor distances within the kagome plane are reasonably close with V-V distances being 2.76 Å in YV_6Sn_6 and 2.77 Å in GdV_6Sn_6. Sn2 atoms center laterally within the hexagons of the V-based kagome plane and are displaced slightly upward/downward along the c-axis. This is analogous to the CoSn-B35 type structure where the R sites are empty and the Sn atoms reside within the kagome planes of Co-atoms [320]. In RV_6Sn_6, steric effects introduced by the R atoms push the Sn2 atoms out of the kagome layer, and this arrangement is distinct from the structures of other well-known Sn-based kagome metals such as Fe_3Sn_2 [321, 322] and $Co_3Sn_2S_2$ [323] where the Sn atoms almost lie within the kagome layers of Fe and Co atoms respectively.

6.4.2 Calculated electronic structure

The electronic structure of (Y,Gd)V_6Sn_6 was modeled via density functional theory calculations. YV_6Sn_6 and GdV_6Sn_6 show qualitatively similar band structures in the paramagnetic state and for clarity, we focus on the electronic structure of GdV_6Sn_6 in the paramagnetic phase in the following paragraphs.

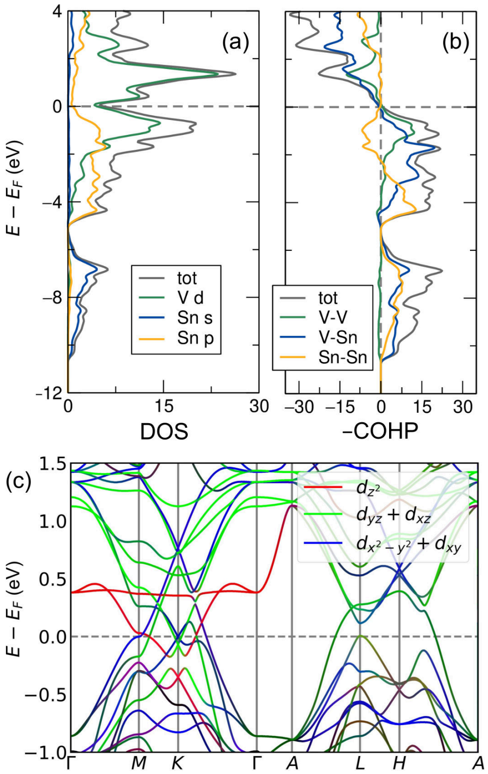

Figure 6.2: Orbital origins of GdV_6Sn_6 electronic structure. (a) orbital-projected density of states showing that the electronic structure near E_F derives primarily from the V d states. (b) crystal orbital Hamilton population curves for V-V, V-Sn, and Sn-Sn bonding. (c) V d orbital decomposed band structure.

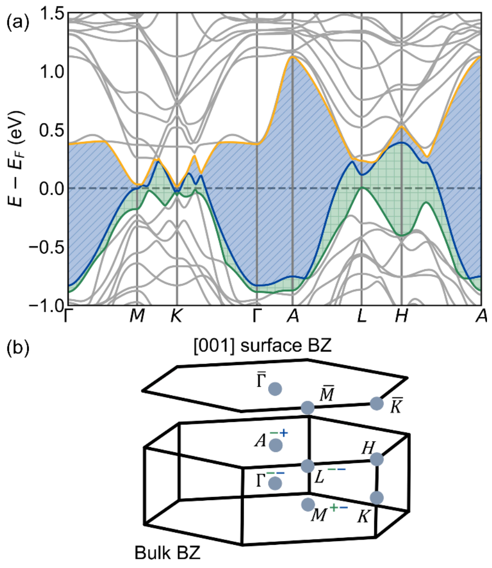

(c)

	parity prod.				invariant
band	δ_Γ	δ_M	δ_A	δ_L	$(\mathbb{Z}_2;\nu_1\nu_2\nu_3)$
173	+	+	+	+	(0;000)
171	−	−	+	−	(1;001)
169	−	+	−	−	(1;000)

Figure 6.3: Topological classification of GdV_6Sn_6. (a) band structure with bands 169 (green), 171 (blue), and 173 (orange). Shaded regions show (E, k) space where topologically nontrivial states are expected to appear (b) visualization of the hexagonal Brillouin zone and projected [001] surface Brillouin zone, identifying high symmetry points. (c) Parity products classifying the $\mathbb{Z}_2$ invariant for each band. Bands 169 and 171 are characterized by a strong topological invariant, $\mathbb{Z}_2 = 1$. Band 173 is trivial with no topological invariants. In addition to the strong invariant, band 171 also supports a weak invariant $\nu_3 = 1$.

Figure 6.2 shows the orbitally decomposed electronic structure of GdV_6Sn_6 with the orbital breakdown of the density of states shown in Fig. 6.2 (a). Fig. 6.2 (b) shows the crystal orbital Hamilton population curves projected for V-V, V-Sn, and Sn-Sn bonding interactions, where all are shown to contribute significantly near the Fermi-level. V-Sn and V-V bands are approximately half-filled, whereas states arising from the Sn p-Sn p interaction are fully filled. As a result, filled Sn p-Sn p antibonding states contribute near the Fermi level and likely play an important role in the structure. Fig. 6.2 (c) shows the V-based d-orbital band structure endemic to the kagome lattice. A prominent d_z^2 kagome flat-band can be seen above E_F, and Dirac cones and saddle points similar to those expected from minimal kagome tight-binding models lie at the Fermi level. Given the local kagome coordination in this structure, it is unsurprising that out-of-plane d_z^2 orbital states fill prior to d_{yz} + d_{xz} and in-plane $d_{x^2-y^2}$ + d_{xy} states.

Figure 6.3 shows the band structure of GdV_6Sn_6 in the paramagnetic phase alongside the topological classification of the metallic state based on the bands crossing E_F. Bands crossing E_F are highlighted in Fig. 6.3 (a) with high symmetry points labeled in Fig. 6.3 (b) for reference. Due to the presence of small, but continuous gaps between bands, the $\mathbb{Z}_2$ topological classification can be determined for each band using parity products, and a strong topological invariant $\mathbb{Z}_2 = 1$ can be assigned to bands 171 (blue) and 169 (green), while the topmost band 173 (yellow) is topologically trivial. As a result of these invariants, topological surface states are expected in the gaps between bands 169 and 171 (green, square-hatched) as well as between bands 171 and 173 (blue, diagonal-hatched) marked in Fig. 6.3 (a). Further classification is presented in the supplemental material[319].

Exploring the possibility of topologically nontrivial surface states further, Fig. 6.4 plots projections of predicted surface states along the [001] surface with bulk bands in Fig. 6.4 (a) and a Gd/Sn1-terminated surface spectrum in Fig. 6.4 (b). Comparing

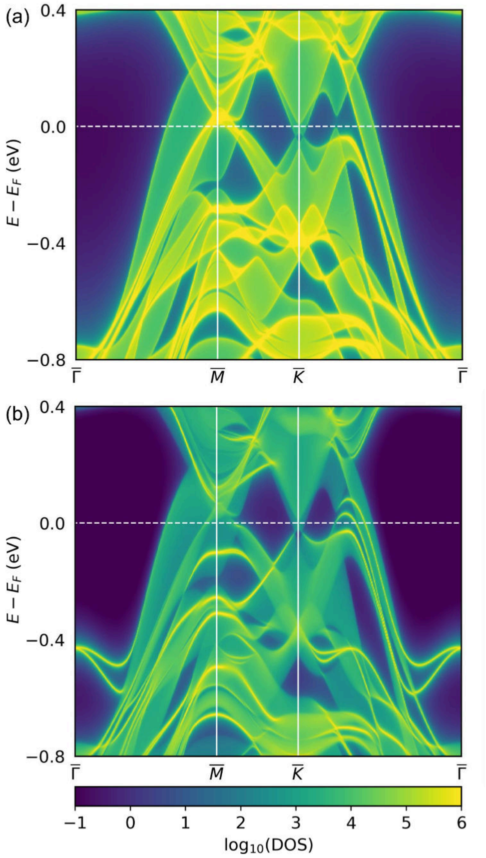

Figure 6.4: GdV_6Sn_6 [001] surface states. (a) and (b) display the surface Green's function projection of pure bulk states and the states on a Gd/Sn_1 terminated surface, respectively.

the two plots, many bright surface state bands can be identified in (b) which are not present in the bulk. Near-Fermi level surface bands can be seen emitting from the bulk Dirac cones on either side of $\overline{K}$. A pair of surface states bridge the large local band gap at $\overline{\Gamma}$, with a surface Weyl band crossing appearing at $E \approx -0.4$ eV. The presence of this rich surface state spectrum is expected from the topological invariant calculation described in Figure 6.3.

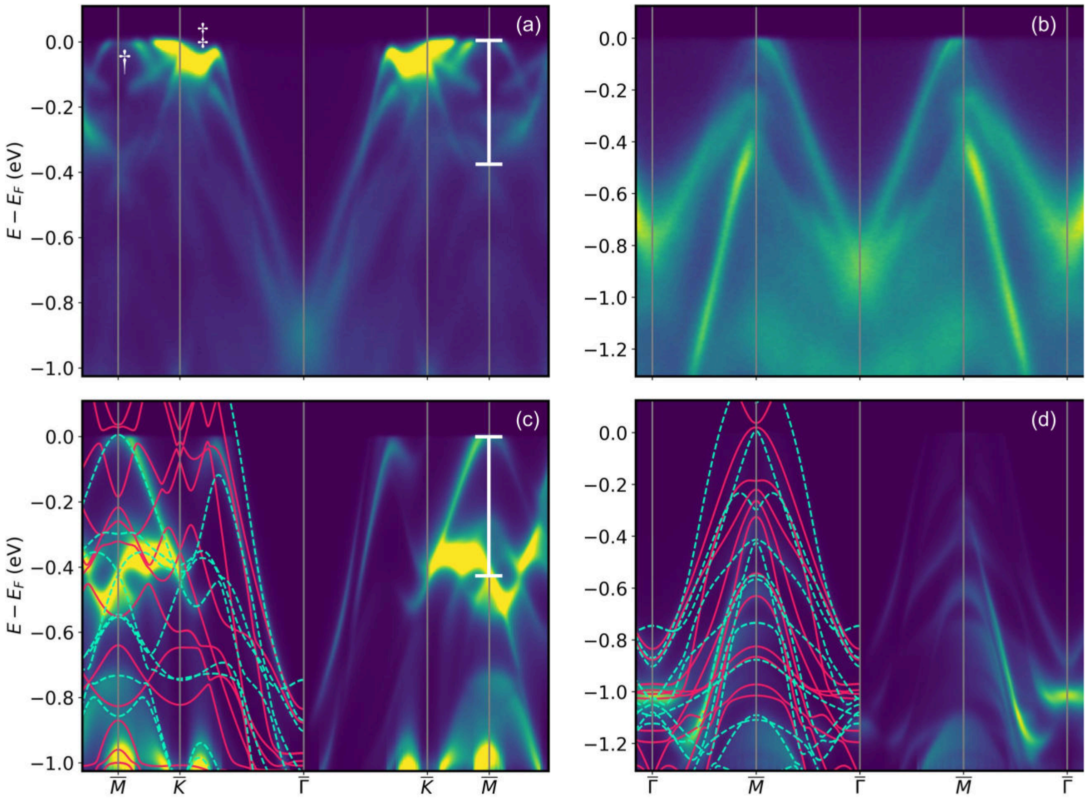

Figure 6.5: Comparison between experimental and simulated ARPES of GdV_6Sn_6. (a,b) measured ARPES intensity along the Γ-K-M and Γ-M-Γ high-symmetry lines. (c,d) simulated ARPES spectra using experimental measurement parameters along the same lines. Band structures for the $k_z = 0$ and $k_z = \pi/c$ planes are overlaid in pink and teal (dashed), respectively. Comparing the lengths of the white bars at the K point in (a,c), we can estimate an approximate renormalization factor of 1.12.

6.4.3 Comparison of simulated and observed ARPES spectra

In order to confirm the predicted band structure, we characterized single crystals of GdV_6Sn_6 using angle-resolved photoemission spectroscopy performed in the paramagnetic state. Our results, summarized in Fig. 6.5, show good agreement between prediction and experiment. In addition to allowing clear identification of some predicted bands, the simulation also provides explanation for some of bands that are not observed in the experiment, most notably the spectral weight suppression near the M point (†), strongly suggesting that much of the discrepancy between simulation and experiment derives from matrix element effects. The high intensity of the measured states near K (‡) may relate to the expected topological surface states. While experimental identification of the predicted surface states is still forthcoming, relatively accurate intensity in the simulation suggests that our *ab initio* modeling recreates the correct bands just below the Fermi level with qualitatively correct orbital symmetry, which is a very promising sign for the proposed topological classification.

Finally, our results indicate that while correlation and renormalization effects related to the V d kagome lattice that are not accounted for in the DFT are likely present, they are relatively minor in magnitude. Comparing using the white overlaid bar, we estimate an approximate renormalization factor of 1.12.

6.5 Discussion

Similar to the recently reported AV_3Sb_5 compounds [275, 112], the band structures of both YV_6Sn_6 and GdV_6Sn_6 in the paramagnetic phase can be categorized as $\mathbb{Z}_2$ topological metals with surface states predicted at E_F. Furthermore, a clear flat band appears in the band structure ≈ 400 meV above E_F, consistent with the interference effects expected from a kagome-derived band. Multiple Dirac points appear near E_F at the K points as well as a van Hove singularity (vHs) near the M-point—both arise from the vanadium d-orbitals comprising the kagome lattice. Given the potential for nesting effects along the M-points at fillings that reach these vHs, slight carrier-doping in these systems is an appealing next step in engineering correlation effects.

6.6 Conclusions

The synthesis of single crystals of two new kagome metals GdV_6Sn_6 and YV_6Sn_6, each with a nonmagnetic kagome V sublattice, is presented. The lattice structures and electronic ground states were studied via x-ray diffraction and ARPES. Both compounds possess an ideal $P6/mmm$ symmetry with perfect kagome nets of vanadium atoms coordinated by Sn ions and spaced into layers via interleaving triangular lattice nets of rare earth ions. In the paramagnetic state, DFT modeling categorizes these compounds as $\mathbb{Z}_2$ kagome metals with multiple Dirac crossings and vHs close to E_F. The presence of topological surface states, Dirac points, and vHs's near E_F in the bulk band structure combined with the ability to tune magnetic interactions in these compounds via control of the R-sites suggest they are promising platforms for unconventional electronic states born from a model kagome network proximitized with a tunable magnetic layer.

Part III

Conclusion and Endmatter

Chapter 7

Conclusion and Future Directions

In this dissertation, I have presented several studies examining the orbital and structural bonding origins of electronic structure in topological metals. Overall, these results support the view that band topology is common to a wide-variety of high-symmetry crystal bonding motifs. Despite the presence of a wide variety of promising candidates, understanding subtle structural and magnetic transitions, as well as low temperature electron correlations, is essential to realizing desired functionality, particularly in proposed quantum devices. These electronic transitions are not necessarily a problem, and in some cases enhance the promise of a material, but in all cases require close collaboration between experimentalists, simulation experts, and theorists.

Chapters 2 and 3 highlight new electronic structure discoveries in established materials systems with known applications. $Na(Pd,Pt)_3O_4$ compounds are known catalysts with doping-controlled metal insulator transitions. Mn_3ZnC has long been studied for its interesting magnetostructural transitions. Both materials highlight the problems and promise of electronic instability. While interest is growing in topological catalysts, catalytic activity is driven by reactivity. Many promising semimetal candidates predicted in idealized first-principles simulations are so reactive that they are hard to grow, maintain and study as single crystals. Our work on Mn_3ZnC similarly hints that many predicted Weyl semimetals may, in fact, be unstable to magnetostructurally-coupled transitions to more complex ground states. From another perspective, metal insulator transitions and magnetostructural transitions enable new functionality such as switching of topological transport properties through electron carrier population, temperature, and magnetic field. Switchable surface transport, a first step towards spintronic anomalous hall diodes, is of great current interest. Verification of the predicted electronic properties in Na(Pd,Pt)$_3$O$_4$ and Mn$_3$ZnC via the methods described in this dissertation—quantum oscillations and ARPES—will require the growth of large single crystals. I have not succeeded in adapting the flux growth technique of Ref. [170] with Na-doping. However, many other flux methods are available. It may be possible to grow large crystals of Mn$_3$ZnC as well as related antiperovskite carbides and nitrides via high temperature floating zone techniques.

Chapters 4 and 5 unravel subtle electronic structure details of two metals with low temperature superconducting transitions. Development of a simple p orbital tight-binding model in LaIn$_3$, combined with a careful 3D reconstruction of the Fermi surface, supports a naïve, yet informative, electronic structure adjustment that can be rationalized as a correction to the calculated La d correlation. Ultimately, our best fit suggests that LaIn$_3$ likely hosts Dirac nodes and surface states at the Fermi level. Due to the presence of a large variety of Dirac states just above E_F, transport studies involving doping by adding electrons and additional spin-orbit coupling through Sn, Tl, and Pb substitutions on the In site are an obvious next step. By comparing *ab initio* simulations to experimental X-ray diffraction and quantum oscillation measurements, our work has shown that the charge-density wave distortion in CsV$_3$Sb$_5$ derives from a breathing mode distortion of the vanadium d kagome bonding and has revealed the delicate energy scale of this transition and the additional c axial stacking distortion. Further simulation and experimental efforts are needed to unravel the full 3D nature of the charge-density wave, the relationship between the charge density wave, superconductivity, and other proposed correlated phenomena in this compound, and the subtle experimental differences observed between $\mathrm{CsV_3Sb_5}$ and sister compounds $\mathrm{KV_3Sb_5}$ and $\mathrm{RbV_3Sb_5}$, which are currently reported to have different c-axial charge density wave distortions. Ultimately, the proposed band reconstruction suggests that previously predicted topological surface states in $\mathrm{CsV_3Sb_5}$ may lower in energy during cooling, lying near the Fermi level at low temperatures. Both $\mathrm{LaIn_3}$ and $\mathrm{CsV_3Sb_5}$ appear to be very promising research platforms for examining the interplay of topology and superconductivity, an important first step towards the dream of topologically protected qubits.

In chapter 6, compounds $\mathrm{GdV_6Sn_6}$ and $\mathrm{YV_6Sn_6}$ were realized as single crystals and electronic structure calculations were performed and compared with experimental ARPES. Similar to the $A\mathrm{V_3Sb_5}$ family, these materials can be categorized as $\mathbb{Z}_2$ topological metals with predicted surface states. The discovery of this new family of vanadium kagome compounds, combined with the geometric intuition of section 1.11, hints that $\mathbb{Z}_2$ states may be common in kagome metals, making these metals ideal candidates for further exploratory synthesis and simulation. An important next step is verification of the proposed surface states via high-resolution ARPES. Unlike the surface states in $\mathrm{CsV_3Sb_5}$, the surface states in $\mathrm{GdV_6Sn_6}$ and $\mathrm{YV_6Sn_6}$ appear in a wide band gap with large band dispersion, meaning that experimental verification may prove relatively simple. Magnetic functionality enabled by substitution of rare-earth elements on the R site encourages further study of $R\mathrm{V_6Sn_6}$ compounds in order to examine new magnetic transitions and their interplay with the predicted band topology.

Appendix A

Computational parameters for introductory figures

Computational details for figures adapted from previously published results in section 1.11 and Fig. 1.19 are provided in Refs. [112] and [120], respectively. Computational details for additional introductory figures are detailed here.

All calculations employed the VASP code[150, 151, 152] using the recommended PAW[90, 154] pseudopotentials with convergence better than 1e^{-5} eV. Relevant parameters are detailed in Table A.1. k-space Fermi surface interpolation was performed in WANNIER90[91] and surface states were computed using WANNIERTOOLS[166].

Fig #	name	functional	k-mesh	plane-wave cutoff	additional details
1.7	C	PBE	15×15×1	500 eV	
1.9	Bi_2Se_3	PBE	12×12×12	300 eV	Bi p and Se p wannier projections with a frozen window -2 eV< E < 5.5 eV
1.10	PdO	PBE|MBJ|HSE	>=8×8×8	>=400 eV	Bands plotted with SUMO.[324]
1.13	Bi	LDA	14×14×13	300 eV	Bi p wannier projection with frozen window $E_F - 6$ eV< $E < E_F + 2$ eV
1.14	Cu	PBE	21×21×21	400 eV	automatic wannierization with 26 bands and 26 wannier functions
1.18	ZrSiS	PBE	8×8×4	400 eV	Bands plotted with SUMO.[324]
1.18	GdPS	PBE	6×6×2	400 eV	Bands plotted with SUMO[324] with E_F set to E_{VBM}.
1.20	Cr	PBE	17×17×17	400 eV	DOS and COHP curves were computed in LOBSTER[33, 34, 35, 36] with a 0.1 eV Gaussian smoothing applied.

Table A.1: Additional computational details for introductory figures.

Appendix B

Formal definition of COHP

This appendix expands on the definition of the crystal orbital Hamilton population, or COHP, providing further details for computational calculation following the notation in Refs. [33, 34]. We start by assuming that our wavefunction, ψ_n for band n can be decomposed into contributions from local basis functions corresponding to orbitals, L, on crystal sites, R:

$$|\psi_n\rangle = \sum_{RL} u_{RL,n} \, |\chi_{RL}\rangle$$

The total band energy is defined as the sum of the occupied energy eigenvalues:

$$E^{band} \equiv \int^{E_F} d\varepsilon \sum_n f_n \delta(\varepsilon_n - \varepsilon)$$

where f_n is the occupation of band n and ε_n is the corresponding eigenvalue. This sum can be rewritten as a sum over the Hamiltonian element corresponding to the interaction between each orbital pair multiplied by the joint density of states:

$$= \int^{E_F} d\varepsilon \sum_{RL} \sum_{R'L'} \langle \chi_{RL} | \hat{H} | \chi_{R'L'} \rangle \sum_n f_n u^*_{RL,n} u_{R'L',n} \delta(\varepsilon_n - \varepsilon)$$

which gives the formal definition of COHP, which is a DOS-weighted Hamiltonian population:

$$E^{band} = \sum_{RL} \sum_{R'L'} \text{COHP}_{RL,R'L'}(\varepsilon)$$

In order to evaluate the strength of a bonding interaction, it is common to evaluate the contribution of a particular pair of orbitals, μ, ν, to the COHP, which is called the partial COHP, or pCOHP[1]:

$$\text{pCOHP}_{\mu,\nu}(\varepsilon) = \sum_{k,n} \mathbb{R}[\langle \chi_\mu | \psi_n(k) \rangle \langle \psi_n(k) | \chi_\nu \rangle \cdot$$

$$\sum_{\ell} \varepsilon_\ell(k) \langle \chi_\mu | \psi_\ell(k) \rangle \langle \psi_\ell(k) | \chi_\nu \rangle] \times \delta(\varepsilon_n(k) - \varepsilon)$$

where ℓ is a second (dummy) band index and only the real part of the first bracketed term is taken. Here, it is also indicated that an additional summation needs to be made over each k-point, k, in the calculation. COHP is used as an estimate of the bonding strength in a system. As can be seen in the equations, what COHP functionally measures is the contribution of the overlap of a given pair of orbitals, χ_μ,χ_ν to the overall band energy in a material. The band energy alone does not provide a complete description of the energetic stabilization of a given crystal structure and COHP is therefore only a semi-quantitative estimate of the bond strength. One major assumption is the validity of a linear combination of atomic orbitals (LCAO) description of the wavefunction. Practically speaking, careful choice of local atomic wavefunctions is necessary to develop a basis set that both reasonably approximates expected spherical harmonic orbitals and can be projected onto the results of plane-wave DFT calculations with proper accounting for the interstitial charge far from the local atomic sites (low

---

[1] Here we are condensing the labels R, L and R', L' into a single pair of labels since we only care about a single pair of orbitals and the atomic labeling no longer matters

‘charge-spilling’). Basis set considerations are detailed in the documentation for the LOBSTER code.[36]

Appendix C

Landau Quantization

This appendix briefly motivates the origin of magnetic field driven splitting in electronic structure (*Landau levels*) and discusses the origin of the Onsager relation with greater rigor.

C.1 Landau levels in a confined system

In a system with confinement under a uniform magnetic field, the charged particles occupy orbits with quantized energies. This section summarizes a simple example using notation similar to original work by Lev Landau.[325]

Let our system contain a charged particle with charge q, confined within a region of dimensions a_x, a_y in the x-y plane, in a uniform magnetic field, $\mathbf{B} = B\hat{z}$, directed along the z axis. The particle will have kinetic energy and an energy $q\hat{\mathbf{A}}$ associated with the magnetic field where $\hat{\mathbf{A}}$ is the vector potential and $\mathbf{B} \equiv \nabla \times \hat{\mathbf{A}}$. There are multiple possible choices of $\hat{\mathbf{A}}$ (gauge freedom), but we will choose the simple case in A is directed along the y axis, $\hat{\mathbf{A}} = Bx\hat{y}$. The Hamiltonian of the system is:

$$\hat{H} = \frac{1}{2m}[\hat{\mathbf{p}} - q\hat{\mathbf{A}}]^2 = \frac{1}{2m}[\hat{p}_y^2 - Bx\hat{x}]^2 + \frac{1}{2m}[\hat{p}_x^2 + \hat{p}_z^2]$$

$$= \frac{1}{2m}[\hbar k_y^2 - Bx\hat{x}]^2 + \frac{1}{2m}[\hat{p}_x^2 + \hat{p}_z^2]$$

In analog to the classical case of cyclotron motion a magnetic field,

$$\frac{mv^2}{r} = qBv; \omega_c \equiv \frac{v}{r} = \frac{qB}{m}$$

we can substitute in the cyclotron frequency to rewrite:

$$= \frac{\hat{p}_x^2}{2m} + \frac{1}{2}m\omega_c^2\left[\frac{\hbar k_y^2}{m\omega_c} - \hat{x}\right]^2 + \frac{\hat{p}_z^2}{2m}$$

This final expression takes the form of a quantum harmonic oscillator ($\hat{H} = \frac{\hat{p}^2}{2m}) + \frac{1}{2}m\omega^2\hat{x}^2$) with the minimum of the potential along x slightly shifted (by $\frac{\hbar k_y^2}{m\omega_c}$). The solution to this Hamiltonian is then:

$$E_n = \hbar\omega_c\left(n + \frac{1}{2}\right) + \frac{p_z^2}{2m}$$

These discretized energy levels for different values of n are known as *Landau levels*. Due to the fact that p_z is not necessarily quantized, the allowed Landau states can take the form of cylinders or *Landau tubes* as visualized in Fig. 1.12.

C.2 Cyclotron frequency and cyclotron effective mass

We now derive an expression for the cyclotron frequency and effective mass in a solid state system in terms of the area of orbits on the Fermi surface. Consider an electron under the influence of a magnetic field with Lorentz force:

$$F = m\dot{p} = e(v \times B)$$

where F is the force, p is the momentum, v is the electron velocity, and B is the magnetic field. Using $p = \hbar k$, and $E = \hbar\omega \rightarrow \frac{1}{\hbar}\nabla E = \frac{\partial\omega}{\partial k} = v$ we can substitute:

$$\hbar\dot{k} = \frac{e}{\hbar}(\nabla E \times B)$$

Splitting up $\dot{k} = dk/dt$:

$$dt = dk\frac{\hbar^2}{e}(\nabla E \times B)^{-1}$$

In a metal in which there is no electron current on average, the electron orbit will be perpendicular to the applied magnetic field. We can therefore separate the k momentum into components along the orbit ($k_\parallel$) and perpendicular to it ($k_\perp$):

$$dt = dk_\parallel\frac{\hbar^2}{eB}\frac{\Delta k_n}{\Delta E}$$

$$dt = \frac{\hbar^2}{eB}\frac{\Delta(dA)}{\Delta E} = \frac{\hbar^2}{eB}\left(\frac{\partial(dA)}{\partial E}\right)\Bigg|_{k_\perp}$$

where Δk_n is the change of the k in the in-plane direction normal to $k_\parallel$ and dA is the infinitesimal area spacing between neighboring orbits with energies separated by ΔE. Integrating around the orbit, we find the orbit period, T_c and the cyclotron frequency, ω_c where $\omega_c \equiv \frac{2\pi}{T_c}$:

$$T_c = \frac{\hbar^2}{eB}\left(\frac{\partial A}{\partial E}\right)\Bigg|_{k_\perp}$$

$$\omega_c = \frac{2\pi eB}{\hbar^2}\left[\left(\frac{\partial A}{\partial E}\right)\Bigg|_{k_\perp}\right]^{-1}$$

we can also use these quantities to define a local effective mass for the electron on a given orbit, called the cyclotron mass, m_c. In analog to the classical case of cyclotron motion a magnetic field:

$$m = \frac{eB}{\omega}$$

we define:

$$m_c = \frac{eB}{\omega_c} = \frac{\hbar^2}{2\pi}\left(\frac{\partial A}{\partial E}\right)\Bigg|_{k_\perp}$$

The cyclotron mass can be therefore be determined directly from calculated orbits on the Fermi surface and compared directly to experimental measurements as in Chapter 5. A more detailed derivation is provided by Shoenberg [109].

C.3 Onsager relation

Combining the two previous results, we can consider the origin of the Onsager relation in a larger system with distinct Landau levels. Assuming a reasonably large quantum number, n, the energy separation between adjacent Landau levels is well approximated by the frequency of the associated classical motion of the electron in an orbit (Bohr utilized a similar 'correspondence principle' when building semiclassical models of electron orbits in atoms):

$$E_{n+1} - E_n = hf = \frac{h}{T_c}$$

where T_c is the cyclotron period of electron motion. Substituting the equation for T_c from the previous section (C.2), we find that:

$$E_{n+1} - E_n = h\left(\frac{\hbar^2}{eB}\frac{\partial A}{\partial E}\right)^{-1}$$

$$(E_{n+1} - E_n)\frac{\partial A}{\partial E} = \frac{2\pi eB}{\hbar}$$

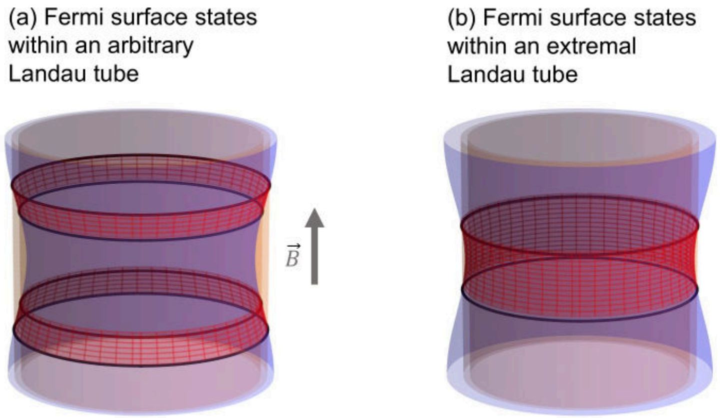

Figure C.1: Geometric argument for the Onsager relation. The number of occupied states associated with a Landau tube is proportional to the region of the Fermi surface enclosed. On this hourglass Fermi surface, an arbitrary orange Landau tube with small thickness dA is shown in (a). The enclosed region of the Fermi surface is indicated with the red, checked pattern. In (b), the surface enclosed by a Landau tube of similar thickness is shown enclosing the innermost extremal orbit (the thinnest part of the hourglass, see Fig. 1.12). The enclosed region of the Fermi surface is larger, meaning that there will be a maximum in the density of states. This is a general property of Landau tubes enclosing extremal orbits, since extremal orbits occur in regions where the Fermi surface normal is perpendicular to the applied field axis.

Here, under the assumption of a small Landau splitting relative to the total energy scale ($E \approx E_F$), we can make the approximation:

$$\frac{\partial A}{\partial E} \approx \frac{A_{n+1} - A_n}{E_{n+1} - E_n}$$

which yields:

$$A_{n+1} - A_n = \frac{2\pi e B}{\hbar}$$

meaning that the difference in areas between neighboring Landau tubes is given by:

$$\Delta A = \frac{2\pi e}{\hbar} B$$

The density of states in a metal reaches a local maximum whenever electron orbits are extremal, which can be rationalized from a simple visual argument as in Fig. C.1. The density of states will therefore fluctuate, reaching maxima whenever one of the Landau tubes has cross-section equal to an extremal orbit, A_e, matching the quantization condition:

$$A_e = (n + \lambda)\Delta A$$

where λ is an integer. We can therefore write:

$$\frac{2\pi e}{\hbar} B(n + \lambda) = A_e$$

$$B = \left(\frac{1}{n + \lambda}\right)\left(\frac{\hbar}{2\pi e}\right) A_e$$

and then, inverting:

$$\frac{1}{B} = (n + \lambda)\left(\frac{2\pi e}{\hbar}\right)\left(\frac{1}{A_e}\right)$$

meaning that that the density of states will be maximized at regularly spaced intervals in $1/B$ with frequency given by:

$$F = \frac{\hbar}{2\pi e} A_e$$

which is precisely the Onsager relation. Since measureable properties of metals such as magnetization and resistivity depend on the density of states at the Fermi level, these properties are expected to exhibit similar periodic fluctuations. Further discussion can be found in Onsager's original work[326] and Ref. [327].

Bibliography

[1] M. G. Vergniory, L. Elcoro, C. Felser, N. Regnault, B. A. Bernevig, and Z. Wang, A complete catalogue of high-quality topological materials, *Nature* **566**, 480–485 (2019), doi:10.1038/s41586-019-0954-4.

[2] F. Tang, H. C. Po, A. Vishwanath, and X. Wan, Comprehensive search for topological materials using symmetry indicators, *Nature* **566**, 486–489 (2019), doi:10.1038/s41586-019-0937-5.

[3] T. Zhang, Y. Jiang, Z. Song, H. Huang, Y. He, Z. Fang, H. Weng, and C. Fang, Catalogue of topological electronic materials, *Nature* **566**, 475–479 (2019), doi:10.1038/s41586-019-0944-6.

[4] E. W. Weisstein, Gauss-bonnet formula, Accessed at `https://mathworld.wolfram.com/Gauss-BonnetFormula.html` in February 2022.

[5] E. W. Weisstein, Euler characteristic, Accessed at `https://mathworld.wolfram.com/Gauss-BonnetFormula.html` in February 2022.

[6] Y. Ando, Topological insulator materials, *J. Phys. Soc. Jpn.* **82**, 102001 (2013), doi:10.7566/JPSJ.82.102001.

[7] M. Z. Hasan and J. E. Moore, Three-dimensional topological insulators, *Annu. Rev. Condens. Mat. Phys.* **2**, 55–78 (2011), doi:10.1146/annurev-conmatphys-062910-140432.

[8] L. Müchler, F. Casper, B. Yan, S. Chadov, and C. Felser, Topological insulators and thermoelectric materials, *Phys. Status Solidi Rapid Res. Lett.* **7**, 91–100 (2013), doi:https://doi.org/10.1002/pssr.201206411.

[9] C. Fu, Y. Sun, and C. Felser, Topological thermoelectrics, *APL Mater.* **8**, 040913 (2020), doi:10.1063/5.0005481.

[10] C. R. Rajamathi, U. Gupta, N. Kumar, H. Yang, Y. Sun, V. Süß, C. Shekhar, M. Schmidt, H. Blumtritt, P. Werner, B. Yan, S. Parkin, C. Felser, and C. N. R. Rao, Weyl semimetals as hydrogen evolution catalysts, *Adv. Mater.* **29**, 1606202 (2017), doi:10.1002/adma.201606202.

[11] B. Yan, B. Stadtmüller, N. Haag, S. Jakobs, J. Seidel, D. Jungkenn, S. Mathias, M. Cinchetti, M. Aeschlimann, and C. Felser, Topological states on the gold surface, *Nat. Commun.* **6**, 10167 (2015), doi:10.1038/ncomms10167.

[12] G. Li, C. Fu, W. Shi, L. Jiao, J. Wu, Q. Yang, R. Saha, M. E. Kamminga, A. K. Srivastava, E. Liu, A. N. Yazdani, N. Kumar, J. Zhang, G. R. Blake, X. Liu, M. Fahlman, S. Wirth, G. Auffermann, J. Gooth, S. Parkin, V. Madhavan, X. Feng, Y. Sun, and C. Felser, Dirac nodal arc semimetal $PtSn_4$: An ideal platform for understanding surface properties and catalysis for hydrogen evolution, *Angew. Chem. Int. Ed.* **58**, 13107–13112 (2019), doi:doi.org/10.1002/anie.201906109.

[13] U. Gupta, C. R. Rajamathi, N. Kumar, G. Li, Y. Sun, C. Shekhar, C. Felser, and C. Rao, Effect of magnetic field on the hydrogen evolution activity using non-magnetic Weyl semimetal catalysts, *Dalton Trans.* **49**, 3398–3402 (2020), doi:10.1039/D0DT00050G.

[14] J. Gujt, P. Zimmer, F. Zysk, V. Süß, C. Felser, M. Bauer, and T. D. Kühne, Water structure near the surface of Weyl semimetals as catalysts in photocatalytic proton reduction, *Struct. Dyn.* **7**, 034101 (2020), doi:10.1063/4.0000008.

[15] D. W. Boukhvalov, C.-N. Kuo, S. Nappini, A. Marchionni, G. D'Olimpio, J. Filippi, S. Mauri, P. Torelli, C. S. Lue, F. Vizza, and A. Politano, Efficient electrochemical water splitting with $PdSn_4$ Dirac nodal arc semimetal, *ACS Catal.* **11**, 7311–7318 (2021), doi:10.1021/acscatal.1c01653.

[16] G. Li, Q. Xu, W. Shi, C. Fu, L. Jiao, M. E. Kamminga, M. Yu, H. Tüysüz, N. Kumar, V. Süß, R. Saha, A. K. Srivastava, S. Wirth, G. Auffermann, J. Gooth, S. Parkin, Y. Sun, E. Liu, and C. Felser, Surface states in bulk single crystal of topological semimetal $Co_3Sn_2S_2$ toward water oxidation, *Sci. Adv.* **5** (2019), doi:10.1126/sciadv.aaw9867.

[17] S. A. Yang, Dirac and Weyl materials: Fundamental aspects and some spintronics applications, *SPIN* **06**, 1640003 (2016), doi:10.1142/S2010324716400038.

[18] K. Manna, Y. Sun, L. Muechler, J. Kübler, and C. Felser, Heusler, Weyl and Berry, *Nat. Rev. Mater.* **3**, 244–256 (2018), doi:10.1038/s41578-018-0036-5.

[19] P. Narang, C. A. C. Garcia, and C. Felser, The topology of electronic band structures, *Nat. Mater.* **20**, 293–300 (2021), doi:10.1038/s41563-020-00820-4.

[20] M. Sato and Y. Ando, Topological superconductors: a review, *Rep. Prog. Phys.* **80**, 076501 (2017), doi:10.1088/1361-6633/aa6ac7.

[21] G. Popkin, Quest for qubits, *Science* **354**, 1090–1093 (2016), doi:10.1126/science.354.6316.1090.

[22] S. M. Frolov, M. J. Manfra, and J. D. Sau, Topological superconductivity in hybrid devices, *Nat. Phys.* **16**, 718–724 (2020), doi:10.1038/s41567-020-0925-6.

[23] G. Xu, B. Lian, P. Tang, X.-L. Qi, and S.-C. Zhang, Topological superconductivity on the surface of Fe-based superconductors, *Phys. Rev. Lett.* **117**, 047001 (2016), doi:10.1103/PhysRevLett.117.047001.

[24] L. Fu and E. Berg, Odd-parity topological superconductors: theory and application to $Cu_xBi_2Se_3$, *Phys. Rev. Lett.* **105**, 097001 (2010), doi:10.1103/PhysRevLett.105.097001.

[25] Y. Ando and L. Fu, Topological crystalline insulators and topological superconductors: From concepts to materials, *Annu. Rev. Condens. Matter Phys.* **6**, 361–381 (2015), doi:10.1146/annurev-conmatphys-031214-014501.

[26] M. V. Berry, Quantal phase factors accompanying adiabatic changes, *Proc. R. Soc. Lond. A.* **392**, 45–57 (1984), doi:10.1098/rspa.1984.0023.

[27] D. Vanderbilt, *Berry Phases in Electronic Structure Theory*, Cambridge University Press (2018).

[28] E. Cohen, H. Larocque, F. Bouchard, F. Nejadsattari, Y. Gefen, and E. Karimi, Geometric phase from Aharonov–Bohm to Pancharatnam–Berry and beyond, *Nat. Rev. Phys.* **1**, 437–449 (2019), doi:10.1038/s42254-019-0071-1.

[29] R. Hoffmann, How chemistry and physics meet in the solid state, *Angew. Chem. Int. Ed.* **26**, 846–878 (1987), doi:10.1002/anie.198708461.

[30] L. M. Schoop, F. Pielnhofer, and B. V. Lotsch, Chemical principles of topological semimetals, *Chem. Mater.* **30**, 3155–3176 (2018), doi:10.1021/acs.chemmater.7b05133.

[31] J. Gao, Q. Wu, C. Persson, and Z. Wang, Irvsp: To obtain irreducible representations of electronic states in the vasp, *Comp. Phys. Commun.* **261**, 107760 (2021), doi:10.1016/j.cpc.2020.107760.

[32] R. Peierls, *More Surprises in Theoretical Physics*, Princeton University Press (1991), Original publication date: 1930.

[33] R. Dronskowski and P. E. Bloechl, Crystal orbital Hamilton populations (COHP): energy-resolved visualization of chemical bonding in solids based on density-functional calculations, *J. Phys. Chem.* **97**, 8617 (1993), doi:10.1021/j100135a014.

[34] V. L. Deringer, A. L. Tchougréeff, and R. Dronskowski, Crystal orbital Hamilton population (COHP) analysis as projected from plane-wave basis sets, *J. Phys. Chem. A* **115**, 5461 (2011), doi:10.1021/jp202489s.

[35] S. Maintz, V. L. Deringer, A. L. Tchougréeff, and R. Dronskowski, Analytic projection from plane-wave and PAW wavefunctions and application to chemical-bonding analysis in solids, *J. Comput. Chem.* **34**, 2557 (2013), doi:10.1002/jcc.23424.

[36] S. Maintz, V. L. Deringer, A. L. Tchougréeff, and R. Dronskowski, LOBSTER: A tool to extract chemical bonding from plane-wave based DFT, *J. Comput. Chem.* **37**, 1030 (2016), doi:10.1002/jcc.24300.

[37] A. H. Castro Neto, F. Guinea, N. M. R. Peres, K. S. Novoselov, and A. K. Geim, The electronic properties of graphene, *Rev. Mod. Phys.* **81**, 109–162 (2009), doi:10.1103/RevModPhys.81.109.

[38] A. K. Geim, Nobel lecture: Random walk to graphene, *Rev. Mod. Phys.* **83**, 851–862 (2011), doi:10.1103/RevModPhys.83.851.

[39] K. S. Novoselov, Graphene: Materials in the Flatland (Nobel lecture), *Angew. Chem. Int. Ed.* **50**, 6986–7002 (2011), doi:10.1002/anie.201101502.

[40] F. D. M. Haldane, Nobel lecture: Topological quantum matter, *Rev. Mod. Phys.* **89**, 040502 (2017), doi:10.1103/RevModPhys.89.040502.

[41] J. M. Kosterlitz, Nobel lecture: Topological defects and phase transitions, *Rev. Mod. Phys.* **89**, 040501 (2017), doi:10.1103/RevModPhys.89.040501.

[42] G. F. Koster, *Properties of the thirty-two point groups* volume 24, The MIT Press (1963).

[43] F. D. M. Haldane, Model for a quantum Hall effect without Landau levels: Condensed-matter realization of the "parity anomaly", *Phys. Rev. Lett.* **61**, 2015–2018 (1988), doi:10.1103/PhysRevLett.61.2015.

[44] C. L. Kane and E. J. Mele, $\mathbb{Z}_2$ topological order and the quantum spin hall effect, *Phys. Rev. Lett.* **95**, 146802 (2005), doi:10.1103/PhysRevLett.95.146802.

[45] B. A. Bernevig, T. L. Hughes, and S.-C. Zhang, Quantum spin Hall effect and topological phase transition in HgTe quantum wells, *Science* **314**, 1757–1761 (2006), doi:10.1126/science.1133734.

[46] M. König, S. Wiedmann, C. Brüne, A. Roth, H. Buhmann, L. W. Molenkamp, X.-L. Qi, and S.-C. Zhang, Quantum spin hall insulator state in HgTe quantum wells, *Science* **318**, 766–770 (2007), doi:10.1126/science.1148047.

[47] J. E. Moore and L. Balents, Topological invariants of time-reversal-invariant band structures, *Phys. Rev. B* **75**, 121306 (2007), doi:10.1103/PhysRevB.75.121306.

[48] L. Fu and C. L. Kane, Topological insulators with inversion symmetry, *Phys. Rev. B* **76**, 045302 (2007), doi:10.1103/PhysRevB.76.045302.

[49] D. Hsieh, D. Qian, L. Wray, Y. Xia, Y. S. Hor, R. J. Cava, and M. Z. Hasan, A topological Dirac insulator in a quantum spin Hall phase, *Nature* **452**, 970–974 (2008), doi:10.1038/nature06843.

[50] H. Zhang, C.-X. Liu, X.-L. Qi, X. Dai, Z. Fang, and S.-C. Zhang, Topological insulators in Bi_2Se_3, Bi_2Te_3 and Sb_2Te_3 with a single Dirac cone on the surface, *Nat. Phys.* **5**, 438–442 (2009), doi:10.1038/nphys1270.

[51] Y. Xia, D. Qian, D. Hsieh, L. Wray, A. Pal, H. Lin, A. Bansil, D. Grauer, Y. S. Hor, R. J. Cava, and M. Z. Hasan, Observation of a large-gap topological-insulator class with a single Dirac cone on the surface, *Nat. Phys.* **5**, 398–402 (2009), doi:10.1038/nphys1274.

[52] Y. L. Chen, J. G. Analytis, J.-H. Chu, Z. K. Liu, S.-K. Mo, X. L. Qi, H. J. Zhang, D. H. Lu, X. Dai, Z. Fang, S. C. Zhang, I. R. Fisher, Z. Hussain, and Z.-X. Shen, Experimental realization of a three-dimensional topological insulator, Bi_2Te_3, *Science* **325**, 178–181 (2009), doi:10.1126/science.1173034.

[53] P. A. M. Dirac and R. H. Fowler, The quantum theory of the electron, *Proc. R. Soc. Lond.* **117**, 610–624 (1928), doi:10.1098/rspa.1928.0023.

[54] Z. Wang, H. Weng, Q. Wu, X. Dai, and Z. Fang, Three-dimensional Dirac semimetal and quantum transport in Cd_3As_2, *Phys. Rev. B* **88**, 125427 (2013), doi:10.1103/PhysRevB.88.125427.

[55] M. Neupane, S.-Y. Xu, R. Sankar, N. Alidoust, G. Bian, C. Liu, I. Belopolski, T.-R. Chang, H.-T. Jeng, H. Lin, A. Bansil, F. Chou, and M. Z. Hasan, Observation of a three-dimensional topological Dirac semimetal phase in high-mobility Cd_3As_2, *Nat. Comms.* **5**, 3786 (2014), doi:10.1038/ncomms4786.

[56] Z. K. Liu, J. Jiang, B. Zhou, Z. J. Wang, Y. Zhang, H. M. Weng, D. Prabhakaran, S.-K. Mo, H. Peng, P. Dudin, T. Kim, M. Hoesch, Z. Fang, X. Dai, Z. X. Shen, D. L. Feng, Z. Hussain, and Y. L. Chen, A stable three-dimensional topological Dirac semimetal Cd_3As_2, *Nat. Mater.* **13**, 677 (2014).

[57] Z. Wang, Y. Sun, X.-Q. Chen, C. Franchini, G. Xu, H. Weng, X. Dai, and Z. Fang, Dirac semimetal and topological phase transitions in A_3Bi ($A =$Na, K, Rb), *Phys. Rev. B* **85**, 195320 (2012), doi:10.1103/PhysRevB.85.195320.

[58] Z. K. Liu, B. Zhou, Y. Zhang, Z. J. Wang, H. M. Weng, D. Prabhakaran, S.-K. Mo, Z. X. Shen, Z. Fang, X. Dai, Z. Hussain, and Y. L. Chen, Discovery of a three-dimensional topological Dirac semimetal, Na_3Bi, *Science* **343**, 864–867 (2014), doi:10.1126/science.1245085.

[59] H. Nielsen and M. Ninomiya, The Adler-Bell-Jackiw anomaly and Weyl fermions in a crystal, *Phys. Lett. B* **130**, 389–396 (1983), doi:/10.1016/0370-2693(83)91529-0.

[60] H. Weyl, Gravitation and the electron, *Proc. Natl. Acad. Sci. U.S.A.* **15**, 323–334 (1929), doi:10.1073/pnas.15.4.323.

[61] S.-M. Huang, S.-Y. Xu, I. Belopolski, C.-C. Lee, G. Chang, B. Wang, N. Alidoust, G. Bian, M. Neupane, C. Zhang, S. Jia, A. Bansil, H. Lin, and M. Z. Hasan, A Weyl fermion semimetal with surface Fermi arcs in the transition metal monopnictide TaAs class, *Nat. Commun.* **6**, 7373 (2015), doi:10.1038/ncomms8373.

[62] H. Weng, C. Fang, Z. Fang, B. A. Bernevig, and X. Dai, Weyl semimetal phase in noncentrosymmetric transition-metal monophosphides, *Phys. Rev. X* **5**, 011029 (2015), doi:10.1103/PhysRevX.5.011029.

[63] B. Q. Lv, N. Xu, H. M. Weng, J. Z. Ma, P. Richard, X. C. Huang, L. X. Zhao, G. F. Chen, C. E. Matt, F. Bisti, V. N. Strocov, J. Mesot, Z. Fang, X. Dai, T. Qian, M. Shi, and H. Ding, Observation of Weyl nodes in TaAs, *Nat. Phys.* **11**, 724–727 (2015), doi:10.1038/nphys3426.

[64] B. Q. Lv, H. M. Weng, B. B. Fu, X. P. Wang, H. Miao, J. Ma, P. Richard, X. C. Huang, L. X. Zhao, G. F. Chen, Z. Fang, X. Dai, T. Qian, and H. Ding, Experimental discovery of Weyl semimetal TaAs, *Phys. Rev. X* **5**, 031013 (2015), doi:10.1103/PhysRevX.5.031013.

[65] B. Feng, Y.-H. Chan, Y. Feng, R.-Y. Liu, M.-Y. Chou, K. Kuroda, K. Yaji, A. Harasawa, P. Moras, A. Barinov, W. Malaeb, C. Bareille, T. Kondo, S. Shin, F. Komori, T.-C. Chiang, Y. Shi, and I. Matsuda, Spin texture in type-II Weyl semimetal WTe_2, *Phys. Rev. B* **94**, 195134 (2016), doi:10.1103/PhysRevB.94.195134.

[66] L. Huang, T. M. McCormick, M. Ochi, Z. Zhao, M.-T. Suzuki, R. Arita, Y. Wu, D. Mou, H. Cao, J. Yan, N. Trivedi, and A. Kaminski, Spectroscopic evidence for a type II Weyl semimetallic state in $MoTe_2$, *Nat. Mater.* **15**, 1155–1160 (2016), doi:10.1038/nmat4685.

[67] C. Wang, Y. Zhang, J. Huang, S. Nie, G. Liu, A. Liang, Y. Zhang, B. Shen, J. Liu, C. Hu, Y. Ding, D. Liu, Y. Hu, S. He, L. Zhao, L. Yu, J. Hu, J. Wei, Z. Mao, Y. Shi, X. Jia, F. Zhang, S. Zhang, F. Yang, Z. Wang, Q. Peng, H. Weng, X. Dai, Z. Fang, Z. Xu, C. Chen, and X. J. Zhou, Observation of Fermi arc and its connection

with bulk states in the candidate type-II Weyl semimetal WTe_2, *Phys. Rev. B* **94**, 241119 (2016), doi:10.1103/PhysRevB.94.241119.

[68] C. Shekhar, A. K. Nayak, Y. Sun, M. Schmidt, M. Nicklas, I. Leermakers, U. Zeitler, Y. Skourski, J. Wosnitza, Z. Liu, Y. Chen, W. Schnelle, H. Borrmann, Y. Grin, C. Felser, and B. Yan, Extremely large magnetoresistance and ultrahigh mobility in the topological Weyl semimetal candidate NbP, *Nat. Phys.* **11**, 645–649 (2015), doi:10.1038/nphys3372.

[69] Y.-Y. Lv, B.-B. Zhang, X. Li, S.-H. Yao, Y. B. Chen, J. Zhou, S.-T. Zhang, M.-H. Lu, and Y.-F. Chen, Extremely large and significantly anisotropic magnetoresistance in ZrSiS single crystals, *Appl. Phys. Lett.* **108**, 244101 (2016), doi:10.1063/1.4953772.

[70] E. Liu, Y. Sun, N. Kumar, L. Muechler, A. Sun, L. Jiao, S.-Y. Yang, D. Liu, A. Liang, Q. Xu, J. Kroder, V. Süß, H. Borrmann, C. Shekhar, Z. Wang, C. Xi, W. Wang, W. Schnelle, S. Wirth, Y. Chen, S. T. B. Goennenwein, and C. Felser, Giant anomalous hall effect in a ferromagnetic kagome-lattice semimetal, *Nat. Phys.* **14**, 1125–1131 (2018), doi:10.1038/s41567-018-0234-5.

[71] F. de Juan, A. G. Grushin, T. Morimoto, and J. E. Moore, Quantized circular photogalvanic effect in Weyl semimetals, *Nat. Comms.* **8**, 15995 (2017), doi:10.1038/ncomms15995.

[72] C. Le, Y. Zhang, C. Felser, and Y. Sun, Ab initio study of quantized circular photogalvanic effect in chiral multifold semimetals, *Phys. Rev. B* **102**, 121111 (2020), doi:10.1103/PhysRevB.102.121111.

[73] C. Le and Y. Sun, Topology and symmetry of circular photogalvanic effect in the chiral multifold semimetals: a review, *J. Phys.: Condens. Matter* **33**, 503003 (2021), doi:10.1088/1361-648X/ac2928.

[74] A. C. Potter, I. Kimchi, and A. Vishwanath, Quantum oscillations from surface Fermi arcs in Weyl and Dirac semimetals, *Nat. Commun.* **5**, 5161 (2014), doi:10.1038/ncomms6161.

[75] P. J. W. Moll, N. L. Nair, T. Helm, A. C. Potter, I. Kimchi, A. Vishwanath, and J. G. Analytis, Transport evidence for Fermi-arc-mediated chirality transfer in the Dirac semimetal Cd_3As_2, *Nature* **535**, 266–270 (2016), doi:10.1038/nature18276.

[76] L. S. Xie, L. M. Schoop, E. M. Seibel, Q. D. Gibson, W. Xie, and R. J. Cava, A new form of Ca_3P_2 with a ring of Dirac nodes, *APL Mater.* **3**, 083602 (2015), doi:10.1063/1.4926545.

[77] L. M. Schoop, M. N. Ali, C. Straßer, A. Topp, A. Varykhalov, D. Marchenko, V. Duppel, S. S. P. Parkin, B. V. Lotsch, and C. R. Ast, Dirac cone protected by non-symmorphic symmetry and three-dimensional Dirac line node in ZrSiS, *Nat. Commun.* **7**, 11696 (2016), doi:10.1038/ncomms11696.

[78] M. Neupane, I. Belopolski, M. M. Hosen, D. S. Sanchez, R. Sankar, M. Szlawska, S.-Y. Xu, K. Dimitri, N. Dhakal, P. Maldonado, P. M. Oppeneer, D. Kaczorowski, F. Chou, M. Z. Hasan, and T. Durakiewicz, Observation of topological nodal fermion semimetal phase in ZrSiS, *Phys. Rev. B* **93**, 201104 (2016), doi:10.1103/PhysRevB.93.201104.

[79] A. Topp, J. M. Lippmann, A. Varykhalov, V. Duppel, B. V. Lotsch, C. R. Ast, and L. M. Schoop, Non-symmorphic band degeneracy at the Fermi level in ZrSiTe, *New J. Phys.* **18**, 125014 (2016), doi:10.1088/1367-2630/aa4f65.

[80] B. Bradlyn, J. Cano, Z. Wang, M. G. Vergniory, C. Felser, R. J. Cava, and B. A. Bernevig, Beyond Dirac and Weyl fermions: Unconventional quasiparticles in conventional crystals, *Science* **353**, 6299 (2016), doi:10.1126/science.aaf5037.

[81] J. Cano, B. Bradlyn, and M. G. Vergniory, Multifold nodal points in magnetic materials, *APL Mater.* **7**, 101125 (2019), doi:10.1063/1.5124314.

[82] L. Z. Maulana, K. Manna, E. Uykur, C. Felser, M. Dressel, and A. V. Pronin, Optical conductivity of multifold fermions: The case of RhSi, *Phys. Rev. Res.* **2**, 023018 (2020), doi:10.1103/PhysRevResearch.2.023018.

[83] M. Born, Statistical interpretation of quantum mechanics, *Science* **122**, 675–679 (1955), doi:10.1126/science.122.3172.675.

[84] D. S. Sholl and J. A. Steckel, *Density functional theory: a practical introduction*, Wiley (2009).

[85] M. Born and R. Oppenheimer, Zur quantentheorie der molekeln, *Ann. Phys.* **389**, 457–484 (1927), doi:10.1002/andp.19273892002.

[86] P. Hohenberg and W. Kohn, Inhomogeneous electron gas, *Phys. Rev.* **136**, B864–B871 (1964), doi:10.1103/PhysRev.136.B864.

[87] R. M. Martin, *Electronic Structure: Basic Theory and Practical Methods*, Cambridge University Press (2004).

[88] W. Kohn and L. J. Sham, Self-consistent equations including exchange and correlation effects, *Phys. Rev.* **140**, A1133–A1138 (1965), doi:10.1103/PhysRev.140.A1133.

[89] D. Vanderbilt, Soft self-consistent pseudopotentials in a generalized eigenvalue formalism, *Phys. Rev. B* **41**, 7892–7895 (1990), doi:10.1103/PhysRevB.41.7892.

[90] P. E. Blöchl, Projector augmented-wave method, *Phys. Rev. B* **50**, 17953 (1994), doi:10.1103/PhysRevB.50.17953.

[91] A. A. Mostofi, J. R. Yates, G. Pizzi, Y.-S. Lee, I. Souza, D. Vanderbilt, and N. Marzari, An updated version of wannier90: A tool for obtaining maximally-localised Wannier functions, *Comput. Phys. Commun.* **185**, 2309 (2014), doi:10.1016/j.cpc.2014.05.003.

[92] D. M. Ceperley and B. J. Alder, Ground state of the electron gas by a stochastic method, *Phys. Rev. Lett.* **45**, 566–569 (1980), doi:10.1103/PhysRevLett.45.566.

[93] J. P. Perdew and A. Zunger, Self-interaction correction to density-functional approximations for many-electron systems, *Phys. Rev. B* **23**, 5048–5079 (1981), doi:10.1103/PhysRevB.23.5048.

[94] J. P. Perdew, K. Burke, and M. Ernzerhof, Generalized gradient approximation made simple, *Phys. Rev. Lett.* **77**, 3865 (1996), doi:10.1103/PhysRevLett.77.3865.

[95] E. Runge and E. K. U. Gross, Density-functional theory for time-dependent systems, *Phys. Rev. Lett.* **52**, 997–1000 (1984), doi:10.1103/PhysRevLett.52.997.

[96] J. P. Perdew, Density functional theory and the band gap problem, *Int. J. Quant. Chem.* **28**, 497–523 (1985), doi:10.1002/qua.560280846.

[97] N. F. Mott, The basis of the electron theory of metals, with special reference to the transition metals, *Proc. Phys. Soc. A* **62**, 416–422 (1949), doi:10.1088/0370-1298/62/7/303.

[98] B. Bradlyn, L. Elcoro, J. Cano, M. G. Vergniory, Z. Wang, C. Felser, M. I. Aroyo, and B. A. Bernevig, Topological quantum chemistry, *Nature* **547**, 298–305 (2017), doi:10.1038/nature23268.

[99] M. G. Vergniory, B. J. Wieder, L. Elcoro, S. S. P. Parkin, C. Felser, B. A. Bernevig, and N. Regnault, All topological bands of all stoichiometric materials, *arXiv preprint arXiv:2105.09954* (2021).

[100] Topological material database: O1 Pd1 (2021), Data retrieved from `https://www.topologicalquantumchemistry.com/#/detail/28834`.

[101] F. Tran and P. Blaha, Accurate band gaps of semiconductors and insulators with a semilocal exchange-correlation potential, *Phys. Rev. Lett.* **102**, 226401 (2009), doi:10.1103/PhysRevLett.102.226401.

[102] J. Heyd, G. E. Scuseria, and M. Ernzerhof, Erratum: “Hybrid functionals based on a screened coulomb potential” [J. Chem. Phys. 118, 8207 (2003)], *J. Chem. Phys.* **124**, 219906 (2006), doi:10.1063/1.2204597.

[103] J. A. Kurzman, M.-S. Miao, and R. Seshadri, Hybrid functional electronic structure of $PbPdO_2$, a small-gap semiconductor, *J. Phys. Condens. Matter* **23**, 465501 (2011), doi:10.1088/0953-8984/23/46/465501.

[104] D. B. Rogers, R. D. Shannon, and J. L. Gillson, Crystal growth and semiconductivity of palladium oxide, *J. Solid State Chem.* **3**, 314–316 (1971), doi:10.1016/0022-4596(71)90045-4.

[105] Topological material database: Ni1 O1 (2021), Data retrieved from `https://www.topologicalquantumchemistry.com/#/detail/29281`.

[106] A. Damascelli, Probing the electronic structure of complex systems by ARPES, *Phys. Scr.* **T109**, 61 (2004), doi:10.1238/physica.topical.109a00061.

[107] V. Strocov, Intrinsic accuracy in 3-dimensional photoemission band mapping, *J. Electron Spectrosc. Relat. Phenom.* **130**, 65–78 (2003), doi:10.1016/S0368-2048(03)00054-9.

[108] L. D. Landau, Diamagnetismus der metalle, *Zeitschrift für Physik* **64**, 629–637 (1930), doi:10.1007/BF01397213.

[109] D. Shoenberg, *Magnetic oscillations in metals*, Cambridge University Press (1984).

[110] W. J. de Haas and P. M. van Alphen, The dependence of the susceptibility of diamagnetic metals upon the field, *Proc. Acad. Sci. Amst.* **33**, 1106 (1930).

[111] A. S. Joseph, A. C. Thorsen, E. Gertner, and L. E. Valby, Low-field de Haas-van Alphen effect in copper, *Phys. Rev.* **148**, 569–575 (1966), doi:10.1103/PhysRev.148.569.

[112] B. R. Ortiz, S. M. L. Teicher, Y. Hu, J. L. Zuo, P. M. Sarte, E. C. Schueller, A. M. M. Abeykoon, M. J. Krogstad, S. Rosenkranz, R. Osborn, R. Seshadri, L. Balents, J. He, and S. D. Wilson, CsV_3Sb_5: a $\mathbb{Z}_2$ topological kagome metal with a superconducting ground state, *Phys. Rev. Lett.* **125**, 247002 (2020), doi:10.1103/PhysRevLett.125.247002.

[113] M. P. L. Sancho, J. M. L. Sancho, J. M. L. Sancho, and J. Rubio, Highly convergent schemes for the calculation of bulk and surface Green functions, *J. Phys. F* **15**, 851 (1985), doi:10.1088/0305-4608/15/4/009.

[114] Y. Hu, X. Wu, B. R. Ortiz, S. Ju, X. Han, J. Z. Ma, N. C. Plumb, M. Radovic, R. Thomale, S. D. Wilson, A. P. Schnyder, and M. Shi, Rich nature of van hove singularities in kagome superconductor CsV_3Sb_5, *arXiv preprint arXiv:2106.05922* (2021).

[115] Y. Hu, S. M. L. Teicher, B. R. Ortiz, Y. Luo, S. Peng, L. Huai, J. Ma, N. C. Plumb, S. D. Wilson, J. He, and M. Shi, Topological surface states and flat bands in the kagome superconductor CsV_3Sb_5, *Sci. Bull.* **XX**, XXX (2021), doi:10.1016/j.scib.2021.11.026.

[116] T. Park, M. Ye, and L. Balents, Electronic instabilities of kagome metals: Saddle points and Landau theory, *Phys. Rev. B* **104**, 035142 (2021), doi:10.1103/PhysRevB.104.035142.

[117] M. D. Johannes and I. I. Mazin, Fermi surface nesting and the origin of charge density waves in metals, *Phys. Rev. B* **77**, 165135 (2008), doi:10.1103/PhysRevB.77.165135.

[118] S. Klemenz, S. Lei, and L. M. Schoop, Topological semimetals in square-net materials, *Annu. Rev. Mater. Res.* **49**, 185–206 (2019), doi:10.1146/annurev-matsci-070218-010114.

[119] W. Tremel and R. Hoffmann, Square nets of main-group elements in solid-state materials, *J. Am. Chem. Soc.* **109**, 124–140 (1987), doi:10.1021/ja00235a021.

[120] S. Lei, S. M. L. Teicher, A. Topp, K. Cai, J. Lin, G. Cheng, T. H. Salters, F. Rodolakis, J. L. McChesney, S. Lapidus, N. Yao, M. Krivenkov, D. Marchenko, A. Varykhalov, C. R. Ast, R. Car, J. Cano, M. G. Vergniory, N. P. Ong, and L. M. Schoop, Band engineering of Dirac semimetals using charge density waves, *Adv. Mater.* **33**, 2101591 (2021), doi:10.1002/adma.202101591.

[121] S. Klemenz, A. K. Hay, S. M. L. Teicher, A. Topp, J. Cano, and L. M. Schoop, The role of delocalized chemical bonding in square-net-based topological semimetals, *J. Am. Chem. Soc.* **142**, 6350–6359 (2020), doi:10.1021/jacs.0c01227.

[122] R. Singha, T. H. Salters, S. M. L. Teicher, S. Lei, J. F. Khoury, N. P. Ong, and L. M. Schoop, Evolving devil's staircase magnetization from tunable charge density waves in nonsymmorphic Dirac semimetals, *Adv. Mater.* **33**, 2103476 (2021), doi:10.1002/adma.202103476.

[123] A. Decker, G. A. Landrum, and R. Dronskowski, Structural and electronic Peierls distortions in the elements (B): The antiferromagnetism of chromium, *Z. Anorg. Allg. Chem.* **628**, 303 (2002), doi:10.1002/1521-3749(200201)628:1<303::AID-ZAAC303>3.0.CO;2-W.

[124] S. M. L. Teicher, L. K. Lamontagne, L. M. Schoop, and R. Seshadri, Fermi-level Dirac crossings in $4d$ and $5d$ cubic metal oxides: $NaPd_3O_4$ and $NaPt_3O_4$, *Phys. Rev. B* **99**, 195148 (2019), doi:10.1103/PhysRevB.99.195148.

[125] S. M. L. Teicher, I. K. Svenningsson, L. M. Schoop, and R. Seshadri, Weyl nodes and magnetostructural instability in antiperovskite Mn_3ZnC, *APL Mater.* **7**, 121104 (2019), doi:10.1063/1.5129689.

[126] B. R. Ortiz, S. M. L. Teicher, L. Kautzsch, P. M. Sarte, N. Ratcliff, J. Harter, J. P. C. Ruff, R. Seshadri, and S. D. Wilson, Fermi surface mapping and the nature of charge-density-wave order in the kagome superconductor CsV_3Sb_5, *Phys. Rev. X* **11**, 041030 (2021), doi:10.1103/PhysRevX.11.041030.

[127] G. Pokharel, S. M. L. Teicher, B. R. Ortiz, P. M. Sarte, G. Wu, S. Peng, J. He, R. Seshadri, and S. D. Wilson, Study of the electronic properties of topological kagome metals YV_6Sn_6 and GdV_6Sn_6, *Phys. Rev. B* **104**, 235139 (2021), doi:10.1103/PhysRevB.104.235139.

[128] N. P. Armitage, E. J. Mele, and A. Vishwanath, Weyl and Dirac semimetals in three-dimensional solids, *Rev. Mod. Phys.* **90**, 015001 (2018), doi:10.1103/RevModPhys.90.015001.

[129] Q. D. Gibson, L. M. Schoop, L. Muechler, L. S. Xie, M. Hirschberger, N. P. Ong, R. Car, and R. J. Cava, Three-dimensional Dirac semimetals: Design principles and predictions of new materials, *Phys. Rev. B* **91**, 205128 (2015), doi:10.1103/PhysRevB.91.205128.

[130] B.-J. Yang and N. Nagaosa, Classification of stable three-dimensional Dirac semimetals with nontrivial topology, *Nat. Commun.* **5**, 4898 (2014), doi:10.1038/ncomms5898.

[131] C. Fang, Y. Chen, H.-Y. Kee, and L. Fu, Topological nodal line semimetals with and without spin-orbital coupling, *Phys. Rev. B* **92**, 081201 (2015), doi:10.1103/PhysRevB.92.081201.

[132] Y.-H. Chan, C.-K. Chiu, M. Y. Chou, and A. P. Schnyder, Ca_3P_2 and other topological semimetals with line nodes and drumhead surface states, *Phys. Rev. B* **93**, 205132 (2016), doi:10.1103/PhysRevB.93.205132.

[133] J. Wang, Y. Liu, K.-H. Jin, X. Sui, L. Zhang, W. Duan, F. Liu, and B. Huang, Pseudo Dirac nodal sphere semimetal, *Phys. Rev. B* **98**, 201112 (2018), doi:10.1103/PhysRevB.98.201112.

[134] G. Hautier, A. Miglio, G. Ceder, G.-M. Rignanese, and X. Gonze, Identification and design principles of low hole effective mass p-type transparent conducting oxides, *Nat. Commun.* **4**, 2292 (2013), doi:10.1038/ncomms3292.

[135] S. Sheng, G. Fang, C. Li, S. Xu, and X. Zhao, p-type transparent conducting oxides, *Phys. Status Solidi A* **203**, 1891–1900 (2006), doi:10.1002/pssa.200521479.

[136] S. Ichikawa and I. Terasaki, Metal-insulator transition in $Ca_{1-x}Li_xPd_3O_4$, *Phys. Rev. B* **68**, 233101 (2003), doi:10.1103/PhysRevB.68.233101.

[137] K. Itoh and N. Tsuda, Metal to semiconductor like transition for sintered $Ca_{1-x}Na_xPd_3O_4$, *Solid State Commun.* **109**, 715 – 719 (1999), doi:10.1016/S0038-1098(98)00549-3.

[138] T. Taniguchi, Y. Nagata, T. Ozawa, M. Sato, Y. Noro, T. Uchida, and H. Samata, Insulator–metal transition induced in $Sr_{1-x}Na_xPd_3O_4$ for small Na-substitutions, *J. Alloys Compd.* **373**, 67 – 72 (2004), doi:10.1016/j.jallcom.2003.11.004.

[139] K. Itoh, Y. Yano, and N. Tsuda, Metal to insulator transition for $Ca_{1-x}Na_xPd_3O_4$, *J. Phys. Soc. Jpn.* **68**, 3022–3026 (1999), doi:10.1143/JPSJ.68.3022.

[140] L. K. Lamontagne, G. Laurita, M. Knight, H. Yusuf, J. Hu, R. Seshadri, and K. Page, The role of structural and compositional heterogeneities in the insulator-to-metal transition in hole-doped $A\mathrm{Pd_3O_4}$ (A = Ca, Sr), *Inorg. Chem.* **56**, 5158–5164 (2017), doi:10.1021/acs.inorgchem.7b00307.

[141] V. Voorhees and R. Adams, The use of the oxides of platinum for the catalytic reduction of organic compounds. I, *J. Am. Chem. Soc.* **44**, 1397–1405 (1922), doi:10.1021/ja01427a021.

[142] D. Cahen and J. A. Ibers, Platinum bronzes: III. a reinvestigation of the composition of Adams' catalyst, *J. Catal.* **31**, 369 – 371 (1973), doi:10.1016/0021-9517(73)90306-0.

[143] M. S. Hegde, G. Madras, and K. C. Patil, Noble metal ionic catalysts, *Acc. Chem. Res.* **42**, 704–712 (2009), doi:10.1021/ar800209s.

[144] J. A. Kurzman, L. M. Misch, and R. Seshadri, Chemistry of precious metal oxides relevant to heterogeneous catalysis, *Dalton Trans.* **42**, 14653–14667 (2013), doi:10.1039/C3DT51818C.

[145] Y. Nishihata, J. Mizuki, T. Akao, H. Tanaka, M. Uenishi, M. Kimura, T. Okamoto, and N. Hamada, Self-regeneration of a Pd-perovskite catalyst for automotive emissions control, *Nature* **418**, 164 (2002), doi:10.1038/nature00893.

[146] J. Li, U. G. Singh, T. D. Schladt, J. K. Stalick, S. L. Scott, and R. Seshadri, Hexagonal $YFe_{1-x}Pd_xO_{3-\delta}$: Nonperovskite host compounds for Pd^{2+} and their catalytic activity for CO oxidation, *Chem. Mater.* **20**, 6567–6576 (2008), doi:10.1021/cm801534a.

[147] B. J. Wieder, Y. Kim, A. M. Rappe, and C. L. Kane, Double Dirac semimetals in three dimensions, *Phys. Rev. Lett.* **116**, 186402 (2016), doi:10.1103/PhysRevLett.116.186402.

[148] M. L. Doublet, E. Canadell, and M. H. Whangbo, Structure-property correlations in the platinum oxide and palladium sulfide bronzes with columnar chains of square-planar TX_4 units (T = Pt, X = O; T = Pd, X = S), *J. Am. Chem. Soc.* **116**, 2115–2120 (1994), doi:10.1021/ja00084a057.

[149] G. Li, B. Yan, Z. Wang, and K. Held, Topological Dirac semimetal phase in Pd and Pt oxides, *Phys. Rev. B* **95**, 035102 (2017), doi:10.1103/PhysRevB.95.035102.

[150] G. Kresse and J. Hafner, Ab initio molecular-dynamics simulation of the liquid-metal–amorphous-semiconductor transition in germanium, *Phys. Rev. B* **49**, 14251 (1994), doi:10.1103/PhysRevB.49.14251.

[151] G. Kresse and J. Furthmüller, Efficient iterative schemes for ab initio total-energy calculations using a plane-wave basis set, *Phys. Rev. B* **54**, 11169 (1996), doi:10.1103/PhysRevB.54.11169.

[152] G. Kresse and J. Furthmüller, Efficiency of ab-initio total energy calculations for metals and semiconductors using a plane-wave basis set, *Comput. Mater. Sci.* **6**, 15 (1996), doi:10.1016/0927-0256(96)00008-0.

[153] P. Blaha, K. Schwarz, G. Madsen, D. Kvasnicka, and J. Luitz, *WIEN2K: An Augmented Plane Wave and Local Orbitals Program for Calculating Crystal Properties*, Karlheinz Schwarz (2001).

[154] G. Kresse and D. Joubert, From ultrasoft pseudopotentials to the projector augmented-wave method, *Phys. Rev. B* **59**, 1758 (1999), doi:10.1103/PhysRevB.59.1758.

[155] K. Schwarz, P. Blaha, and G. Madsen, Electronic structure calculations of solids using the WIEN2k package for material sciences, *Comput. Phys. Commun.* **147**, 71 – 76 (2002), doi:10.1016/S0010-4655(02)00206-0.

[156] S. H. Vosko, L. Wilk, and M. Nusair, Accurate spin-dependent electron liquid correlation energies for local spin density calculations: a critical analysis, *Can. J. Phys.* **58**, 1200–1211 (1980), doi:10.1139/p80-159.

[157] A. V. Krukau, O. A. Vydrov, A. F. Izmaylov, and G. E. Scuseria, Influence of the exchange screening parameter on the performance of screened hybrid functionals, *J. Chem. Phys.* **125**, 224106 (2006), doi:10.1063/1.2404663.

[158] P. Janthon, S. Luo, S. M. Kozlov, F. Viñes, J. Limtrakul, D. G. Truhlar, and F. Illas, Bulk properties of transition metals: A challenge for the design of universal density functionals, *J. Chem. Theory Comput.* **10**, 3832–3839 (2014), doi:10.1021/ct500532v.

[159] F. Tran, D. Koller, and P. Blaha, Application of screened hybrid functionals to the bulk transition metals Rh, Pd, and Pt, *Phys. Rev. B* **86**, 134406 (2012), doi:10.1103/PhysRevB.86.134406.

[160] H. J. Monkhorst and J. D. Pack, Special points for Brillouin-zone integrations, *Phys. Rev. B* **13**, 5188–5192 (1976), doi:10.1103/PhysRevB.13.5188.

[161] M. Methfessel and A. T. Paxton, High-precision sampling for Brillouin-zone integration in metals, *Phys. Rev. B* **40**, 3616–3621 (1989), doi:10.1103/PhysRevB.40.3616.

[162] P. E. Blöchl, O. Jepsen, and O. K. Andersen, Improved tetrahedron method for Brillouin-zone integrations, *Phys. Rev. B* **49**, 16223–16233 (1994), doi:10.1103/PhysRevB.49.16223.

[163] See Supplemental Material at http://link.aps.org/supplemental/ 10.1103/PhysRevB.99.195148 for comparisons between electronic structure in VASP, WIEN2k, and our tight-binding model, density of states calculations, and additional comparisons between the B_+ and B_- bands described in the text for both the platinum and palladium compound, with and without SOC.

[164] R. V. Panin, N. R. Khasanova, A. M. Abakumov, E. V. Antipov, G. V. Tendeloo, and W. Schnelle, Synthesis and crystal structure of the palladium oxides $NaPd_3O_4$, Na_2PdO_3 and $K_3Pd_2O_4$, *J. Solid State Chem.* **180**, 1566 – 1574 (2007), doi:10.1016/j.jssc.2007.03.005.

[165] J. Waser and E. D. McClanahan, The structure of $NaPt_3O_4$, *Experientia* **6**, 379–380 (1950), doi:10.1007/BF02178934.

[166] Q.-S. Wu, S.-N. Zhang, H.-F. Song, M. Troyer, and A. A. Soluyanov, WannierTools: An open-source software package for novel topological materials, *Comput. Phys. Commun.* **224**, 405 (2018), doi:10.1016/j.cpc.2017.09.033.

[167] K. Momma and F. Izumi, *VESTA3* for three-dimensional visualization of crystal, volumetric and morphology data, *J. Appl. Crystallogr.* **44**, 1272 (2011), doi:10.1107/S0021889811038970.

[168] D. Cahen, J. A. Ibers, and J. B. Wagner, Platinum bronzes. IV. preparation, crystal chemistry, and physical properties, *Inorg. Chem.* **13**, 1377–1388 (1974), doi:10.1021/ic50136a026.

[169] W. Weber, G. Graham, A. Chen, K. Hass, and B. Chamberland, Micro-raman study of $Na_xPt_3O_4$ crystals, *Solid State Commun.* **106**, 95 – 100 (1998), doi:10.1016/S0038-1098(97)10247-2.

[170] P. L. Smallwood, M. D. Smith, and H.-C. zur Loye, Flux synthesis of alkaline earth palladates, *J. Cryst. Growth* **216**, 299 – 303 (2000), doi:10.1016/S0022-0248(00)00432-2.

[171] H. Samata, S. Tanaka, S. Mizusaki, Y. Nagata, T. C. Ozawa, A. Sato, and K. Kosuda, Synthesis and characterization of $CaPd_3O_4$ crystals, *J. Cryst. Process Technol.* **2**, 16 (2012), doi:10.4236/jcpt.2012.21003.

[172] S. Pezzini, M. R. van Delft, L. M. Schoop, B. V. Lotsch, A. Carrington, M. I. Katsnelson, N. E. Hussey, and S. Wiedmann, Unconventional mass enhancement around the Dirac nodal loop in ZrSiS, *Nat. Phys.* **14**, 178 (2017), doi:10.1038/nphys4306.

[173] J. Hu, Z. Tang, J. Liu, X. Liu, Y. Zhu, D. Graf, K. Myhro, S. Tran, C. N. Lau, J. Wei, and Z. Mao, Evidence of topological nodal-line fermions in ZrSiSe and ZrSiTe, *Phys. Rev. Lett.* **117**, 016602 (2016), doi:10.1103/PhysRevLett.117.016602.

[174] M. W. Barsoum, The $M_{N+1}AX_N$ phases: A new class of solids: Thermodynamically stable nanolaminates, *Prog. Solid State Ch.* **28**, 201 (2000), doi:10.1016/S0079-6786(00)00006-6.

[175] Y. Kimura, Y. Mishima, and C. Liu, Microstructure control and tensile properties of three-phase alloys based on the $E2_1$ Co_3AlC and B2 CoAl, *Intermetallics* **9**, 1069 (2001), doi:10.1016/S0966-9795(01)00113-3.

[176] Y. Wen, C. Wang, Y. Sun, M. Nie, L. Fang, and Y. Tian, Lattice, magnetic and transport properties in antiperovskite $Mn_3Sn_{1-x}Ge_xC$ compounds, *Solid State Commun.* **149**, 1519 – 1522 (2009), doi:10.1016/j.ssc.2009.06.009.

[177] T. Hamada and K. Takenaka, Giant negative thermal expansion in antiperovskite manganese nitrides, *J. Appl. Phys.* **109**, 07E309 (2011), doi:10.1063/1.3540604.

[178] K. Kamishima, T. Goto, H. Nakagawa, N. Miura, M. Ohashi, N. Mori, T. Sasaki, and T. Kanomata, Giant magnetoresistance in the intermetallic compound Mn_3GaC, *Phys. Rev. B* **63**, 024426 (2000), doi:10.1103/PhysRevB.63.024426.

[179] T. He, Q. Huang, A. P. Ramirez, Y. Wang, K. A. Regan, N. Rogado, M. A. Hayward, M. K. Haas, J. S. Slusky, K. Inumara, H. W. Zandbergen, N. P. Ong, and R. J. Cava, Superconductivity in the non-oxide perovskite $MgCNi_3$, *Nature* **411**, 54 (2001), doi:10.1038/35075014.

[180] S. Mollah, The physics of the non-oxide perovskite superconductor $MgCNi_3$, *J. Phys.: Condens. Matter* **16**, R1237 (2004), doi:10.1088/0953-8984/16/43/r01.

[181] T. Kariyado and M. Ogata, Three-dimensional Dirac electrons at the Fermi energy in cubic inverse perovskites: Ca_3PbO and its family, *J. Phys. Soc. Jpn.* **80**, 083704 (2011), doi:10.1143/JPSJ.80.083704.

[182] T. Kariyado and M. Ogata, Low-energy effective Hamiltonian and the surface states of Ca_3PbO, *J. Phys. Soc. Jpn.* **81**, 064701 (2012), doi:10.1143/JPSJ.81.064701.

[183] W. F. Goh and W. E. Pickett, Survey of the class of isovalent antiperovskite alkaline-earth pnictide compounds, *Phys. Rev. B* **97**, 035202 (2018), doi:10.1103/PhysRevB.97.035202.

[184] T. H. Hsieh, J. Liu, and L. Fu, Topological crystalline insulators and Dirac octets in antiperovskites, *Phys. Rev. B* **90**, 081112 (2014), doi:10.1103/PhysRevB.90.081112.

[185] S. Suetsugu, K. Hayama, A. W. Rost, J. Nuss, C. Mühle, J. Kim, K. Kitagawa, and H. Takagi, Magnetotransport in Sr_3PbO antiperovskite, *Phys. Rev. B* **98**, 115203 (2018), doi:10.1103/PhysRevB.98.115203.

[186] M. Oudah, A. Ikeda, J. N. Hausmann, S. Yonezawa, T. Fukumoto, S. Kobayashi, M. Sato, and Y. Maeno, Superconductivity in the antiperovskite Dirac-metal oxide $Sr_{3-x}SnO$, *Nat. Commun.* **7**, 13617 (2016), doi:10.1038/ncomms13617.

[187] R. Yu, H. Weng, Z. Fang, X. Dai, and X. Hu, Topological node-line semimetal and Dirac semimetal state in antiperovskite Cu_3PdN, *Phys. Rev. Lett.* **115**, 036807 (2015), doi:10.1103/PhysRevLett.115.036807.

[188] R. G. Butters and H. P. Myers, XVII. the structure and properties of some ternary alloys of manganese, zinc and carbon, *Philos. Mag.* **46**, 132 (1955), doi:10.1080/14786440208520557.

[189] B. N. Brockhouse and H. P. Myers, New type of magnetic transition in Mn_3ZnC, *Can. J. Phys.* **35**, 313 (1957), doi:10.1139/p57-035.

[190] M. L. Swanson and S. A. Friedberg, The electrical resistivity of Mn_3ZnC between 4.2° and 630° K, *Can. J. Phys.* **39**, 1429 (1961), doi:10.1139/p61-171.

[191] D. Fruchart and F. Bertaut, Magnetic studies of the metallic perovskite-type compounds of manganese, *J. Phys. Soc. Jpn.* **44**, 781 (1978), doi:10.1143/JPSJ.44.781.

[192] T. Kaneko, T. Kanomata, and K. Shirakawa, Pressure effect on the magnetic transition temperatures in the intermetallic compounds $\mathrm{Mn}_3M\mathrm{C}$ (M=Ga, Zn and Sn), *J. Phys. Soc. Jpn.* **56**, 4047 (1987), doi:10.1143/JPSJ.56.4047.

[193] D. Fruchart, E. Bertaut, B. L. Clerc, L. D. Khöi, P. Veillet, G. Lorthioir, E. Fruchart, and R. Fruchart, Études par diffraction neutronique et RMN de $\mathrm{ZnMn}_3\mathrm{C}$ et $\mathrm{GaMn}_3\mathrm{C}_{0.935}$, *J. Solid State Chem.* **8**, 182 (1973), doi:10.1016/0022-4596(73)90012-1.

[194] T. Kaneko, T. Kanomata, S. Miura, G. Kido, and Y. Nakagawa, Field-induced transitions in intermetallic compounds $\mathrm{Mn}_3\mathrm{GaC}$ and $\mathrm{Mn}_3\mathrm{ZnC}$, *J. Magn. Magn. Mater.* **70**, 261 (1987), doi:10.1016/0304-8853(87)90431-8.

[195] J. P. Jardin and J. Labbé, Modèle pour la structure électronique des composés perovskites du manganèse, *J. Phys. (France)* **36**, 1317 (1975), doi:10.1051/jphys:0197500360120131700.

[196] K. Motizuki and H. Nagai, Electronic band structures and magnetism of the cubic perovskite-type manganese compounds $\mathrm{Mn}_3\mathrm{MC}$ (M=Zn,Ga,In,Sn), *J. Phys. C* **21**, 5251 (1988), doi:10.1088/0022-3719/21/30/011.

[197] V. N. Antonov, B. N. Harmon, A. N. Yaresko, and A. P. Shpak, Electronic structure, noncollinear magnetism, and x-ray magnetic circular dichroism in the $\mathrm{Mn}_3\mathrm{ZnC}$ perovskite, *Phys. Rev. B* **75**, 165114 (2007), doi:10.1103/PhysRevB.75.165114.

[198] D. Gosálbez-Martínez, I. Souza, and D. Vanderbilt, Chiral degeneracies and Fermi-surface chern numbers in bcc Fe, *Phys. Rev. B* **92**, 085138 (2015), doi:10.1103/PhysRevB.92.085138.

[199] I. Belopolski, K. Manna, D. S. Sanchez, G. Chang, B. Ernst, J. Yin, S. S. Zhang, T. Cochran, N. Shumiya, H. Zheng, B. Singh, G. Bian, D. Multer, M. Litskevich, X. Zhou, S.-M. Huang, B. Wang, T.-R. Chang, S.-Y. Xu, A. Bansil, C. Felser, H. Lin, and M. Z. Hasan, Discovery of topological Weyl fermion lines and drumhead surface states in a room temperature magnet, *Science* **365**, 1278 (2019), doi:10.1126/science.aav2327.

[200] P. V. C. Medeiros, S. Stafström, and J. Björk, Effects of extrinsic and intrinsic perturbations on the electronic structure of graphene: Retaining an effective primitive cell band structure by band unfolding, *Phys. Rev. B* **89**, 041407 (2014), doi:10.1103/PhysRevB.89.041407.

[201] P. V. C. Medeiros, S. S. Tsirkin, S. Stafström, and J. Björk, Unfolding spinor wave functions and expectation values of general operators: Introducing the unfolding-density operator, *Phys. Rev. B* **91**, 041116 (2015), doi:10.1103/PhysRevB.91.041116.

[202] J. D. Bocarsly, R. F. Need, R. Seshadri, and S. D. Wilson, Magnetoentropic signatures of skyrmionic phase behavior in FeGe, *Phys. Rev. B* **97**, 100404 (2018), doi:10.1103/PhysRevB.97.100404.

[203] See Supplemental Material at https://dx.doi.org/10.1063/1.5129689.

[204] R. Dronskowski, K. Korczak, H. Lueken, and W. Jung, Chemically tuning between ferromagnetism and antiferromagnetism by combining theory and synthesis in iron/manganese rhodium borides, *Angew. Chem. Int. Ed.* **41**, 2528 (2002), doi:10.1002/1521-3773(20020715)41:14<2528::AID-ANIE2528>3.0.CO;2-6.

[205] Z. Wang, M. G. Vergniory, S. Kushwaha, M. Hirschberger, E. V. Chulkov, A. Ernst, N. P. Ong, R. J. Cava, and B. A. Bernevig, Time-reversal-breaking Weyl fermions in magnetic Heusler alloys, *Phys. Rev. Lett.* **117**, 236401 (2016), doi:10.1103/PhysRevLett.117.236401.

[206] P. Karen, H. Fjellvåg, A. Kjekshus, and A. F. Andresen, On the phase relations and structural and magnetic properties of the stable manganese carbides $Mn_{23}C_6$,Mn_5C_2 and Mn_7C_3, *Acta Chem. Scand.* **45**, 549 (1991), doi:10.3891/acta.chem.scand.45-0549.

[207] V. Franco, J. Blázquez, B. Ingale, and A. Conde, The magnetocaloric effect and magnetic refrigeration near room temperature: Materials and models, *Annu. Rev. Mater. Res.* **42**, 305 (2012), doi:10.1146/annurev-matsci-062910-100356.

[208] J.-H. Park, S. H. Lee, C. H. Kim, H. Jin, and B.-J. Yang, Two-dimensional Peierls instability via zone-boundary Dirac line nodes in layered perovskite oxides, *Phys. Rev. B* **99**, 195107 (2019), doi:10.1103/PhysRevB.99.195107.

[209] W. Shi, B. J. Wieder, H. L. Meyerheim, Y. Sun, Y. Zhang, Y. Li, L. Shen, Y. Qi, L. Yang, J. Jena, P. Werner, K. Koepernik, S. Parkin, Y. Chen, C. Felser, B. A. Bernevig, and Z. Wang, A Charge-Density-Wave Weyl Semimetal, *arXiv preprint arXiv:1909.04037* (2019).

[210] R. Singha, A. K. Pariari, B. Satpati, and P. Mandal, Large nonsaturating magnetoresistance and signature of nondegenerate Dirac nodes in ZrSiS, *Proc. Natl. Acad. Sci. U.S.A.* **114**, 2468–2473 (2017), doi:10.1073/pnas.1618004114.

[211] A. Y. Kitaev, Unpaired majorana fermions in quantum wires, *Phys. Usp.* **44**, 131–136 (2001), doi:10.1070/1063-7869/44/10s/s29.

[212] J. F. Khoury and L. M. Schoop, Chemical bonds in topological materials, *Trends Chem.* **3**, 700–715 (2021), doi:10.1016/j.trechm.2021.04.011.

[213] A. Thamizhavel, A. Galatanu, E. Yamamoto, T. Okubo, M. Yamada, K. Tabata, T. C Kobayashi, N. Nakamura, K. Sugiyama, K. Kindo, T. Takeuchi, R. Settai, and Y. Ōnuki, Low temperature magnetic properties of CeTBi$_2$ (T: Ni, Cu and Ag) single crystals, *J. Phys. Soc. Jpn.* **72**, 2632–2639 (2003), doi:10.1143/JPSJ.72.2632.

[214] M. M. Hosen, G. Dhakal, K. Dimitri, P. Maldonado, A. Aperis, F. Kabir, C. Sims, P. Riseborough, P. M. Oppeneer, D. Kaczorowski, T. Durakiewicz, and M. Neupane, Discovery of topological nodal-line fermionic phase in a magnetic material GdSbTe, *Sci. Rep.* **8**, 13283 (2018), doi:10.1038/s41598-018-31296-7.

[215] S. Lei, V. Duppel, J. M. Lippmann, J. Nuss, B. V. Lotsch, and L. M. Schoop, Charge density waves and magnetism in topological semimetal candidates GdSb$_x$Te$_{2-x-\delta}$, *Adv. Quantum Technol.* **2**, 1900045 (2019), doi:10.1002/qute.201900045.

[216] E. Jobiliong, J. S. Brooks, E. S. Choi, H. Lee, and Z. Fisk, Magnetization and electrical-transport investigation of the dense Kondo system CeAgSb$_2$, *Phys. Rev. B* **72**, 104428 (2005), doi:10.1103/PhysRevB.72.104428.

[217] S. Ran, C. Eckberg, Q.-P. Ding, Y. Furukawa, T. Metz, S. R. Saha, I.-L. Liu, M. Zic, H. Kim, J. Paglione, and N. P. Butch, Nearly ferromagnetic spin-triplet superconductivity, *Science* **365**, 684–687 (2019), doi:10.1126/science.aav8645.

[218] D. Aoki, A. Nakamura, F. Honda, D. Li, Y. Homma, Y. Shimizu, Y. J. Sato, G. Knebel, J.-P. Brison, A. Pourret, D. Braithwaite, G. Lapertot, Q. Niu, M. Vališka, H. Harima, and J. Flouquet, Unconventional superconductivity in heavy fermion UTe$_2$, *J. Phys. Soc. Jpn.* **88**, 043702 (2019), doi:10.7566/JPSJ.88.043702.

[219] A. Rossi, *Atti Accad. naz. Lincei Rc.* **17**, 955 (1934).

[220] R. Gambino, N. Stemple, and A. Toxen, Superconductivity of lanthanum intermetallic compounds with the Cu$_3$Au structure, *J. Phys. Chem. Solids* **29**, 295–302 (1968), doi:doi.org/10.1016/0022-3697(68)90074-7.

[221] W. D. Grobman, Transport properties and the electronic structure of LaSn$_{3-x}$In$_x$, *Phys. Rev. B* **5**, 2924–2931 (1972), doi:10.1103/PhysRevB.5.2924.

[222] Z. Fisk and A. C. Lawson, Normal state resistance behavior and superconductivity, *Solid. State. Commun* **13**, 277–279 (1973), doi:10.1016/0038-1098(73)90590-5.

[223] L. B. Welsh, A. M. Toxen, and R. J. Gambino, Contributions at the La and Sn-In sites to superconductivity and magnetism in LaSn$_x$In$_{3-x}$ alloys, In K. D. Timmerhaus, W. J. O'Sullivan, and E. F. Hammel, editors, *Low Temperature Physics-LT 13* , 387–391. Springer (1974).

[224] R. Elenbaas, C. Schinkel, and C. van Deudekom, Heat capacity and electrical resistivity of (Ce,La)In_3 and Ce(In,Sn)$_3$, *J. Magn. Magn. Mater.* **15-18**, 979–981 (1980), doi:10.1016/0304-8853(80)90851-3.

[225] I. Umehara, N. Nagai, and Y. Ōnuki, High field magnetoresistance and de haas-van alphen effect in $LaIn_3$, *J. Phys. Soc. Jpn.* **60**, 591–594 (1991), doi:10.1143/JPSJ.60.591.

[226] Z. Kletowski, M. Glinski, and A. Hasegawa, Magnetoresistance and the Fermi surface of the intermetallic compound $LaIn_3$, *J. Phys. F: Met. Phys* **17**, 993–998 (1987), doi:10.1088/0305-4608/17/4/024.

[227] I. Umehara, N. Nagai, and Y. Ōnuki, High field magnetoresistance and de Haas-van Alphen effect in $LaSn_3$, *J. Phys. Soc. Jpn.* **60**, 1294–1299 (1991), doi:10.1143/JPSJ.60.1294.

[228] A. Hasegawa and H. Yamagami, Band theory of itinerant f-electron compounds, *Prog. Theor. Phys. Suppl.* **108**, 27–54 (1992), doi:10.1143/PTPS.108.27.

[229] H. Kitazawa, Q. Gao, H. Shida, T. Suzuki, A. Hasegawa, and T. Kasuya, De Haas-van Alphen effects of $PrIn_3$ and $LaIn_3$, *J. Magn. and Magn. Mater.* **52**, 286–288 (1985), doi:10.1016/0304-8853(85)90281-1.

[230] D. Aoki, Y. Homma, H. Sakai, S. Ikeda, Y. Shiokawa, E. Yamamoto, A. Nakamura, Y. Haga, R. Settai, and Y. Ōnuki, Magnetic and Fermi surface properties in $NpIn_3$, *J. Phys. Soc. Jpn.* **75**, 084710 (2006), doi:10.1143/JPSJ.75.084710.

[231] Y. Ōnuki and R. Settai, de Haas–van Alphen effect and Fermi surface properties in rare earth and actinide compounds (review article), *Low Temp. Phys.* **38**, 89–153 (2012), doi:10.1063/1.3683408.

[232] A. Benoit, J. Boucherle, P. Convert, J. Flouquet, J. Palleau, and J. Schweizer, Magnetic structure of the compound $CeIn_3$, *Solid State Commun.* **34**, 293–295 (1980), doi:10.1016/0038-1098(80)90560-8.

[233] Y. Kurosawa, I. Umehara, M. Kikuchi, N. Nagai, K. Satoh, and Y. Ōnuki, Magnetoresistance and de Haas-van Alphen effect in $CeIn_3$, *J. Phys. Soc. Jpn.* **59**, 1545–1548 (1990), doi:10.1143/JPSJ.59.1545.

[234] I. Walker, F. Grosche, D. Freye, and G. Lonzarich, The normal and superconducting states of $CeIn_3$ near the border of antiferromagnetic order, *Phys. C: Supercond.* **282-287**, 303–306 (1997), doi:10.1016/S0921-4534(97)00267-0.

[235] M. Biasini, G. Ferro, and A. Czopnik, Fermi-surface topology of the heavy-fermion antiferromagnetic superconductor $CeIn_3$, *Phys. Rev. B* **68**, 094513 (2003), doi:10.1103/PhysRevB.68.094513.

[236] R. Settai, T. Kubo, T. Shiromoto, D. Honda, H. Shishido, K. Sugiyama, Y. Haga, T. D. Matsuda, K. Betsuyaku, H. Harima, T. C. Kobayashi, and Y. Ōnuki, Change of the Fermi surface across the critical pressure in $\mathrm{CeIn_3}$: The de Haas–van Alphen study under pressure, *J. Phys. Soc. Jpn.* **74**, 3016–3026 (2005), doi:10.1143/JPSJ.74.3016.

[237] N. Harrison, S. E. Sebastian, C. H. Mielke, A. Paris, M. J. Gordon, C. A. Swenson, D. G. Rickel, M. D. Pacheco, P. F. Ruminer, J. B. Schillig, J. R. Sims, A. H. Lacerda, M.-T. Suzuki, H. Harima, and T. Ebihara, Fermi surface of $\mathrm{CeIn_3}$ above the Néel critical field, *Phys. Rev. Lett.* **99**, 056401 (2007), doi:10.1103/PhysRevLett.99.056401.

[238] M.-T. Suzuki and H. Harima, Fermi surface of $\mathrm{CeIn_3}$ under pressure studied by the LDA+U method, *Phys. B: Condens. Matter* **403**, 1318–1320 (2008), doi:10.1016/j.physb.2007.10.359.

[239] I. M. Lifshitz and A. M. Kosevich, Theory of magnetic susceptibility in metals at low temperatures, *Zh. Eksp. Teor. Fiz.* **29**, 730–742 (1955).

[240] S. L. Dudarev, G. A. Botton, S. Y. Savrasov, C. J. Humphreys, and A. P. Sutton, Electron-energy-loss spectra and the structural stability of nickel oxide: An LSDA+U study, *Phys. Rev. B* **57**, 1505 (1998), doi:10.1103/PhysRevB.57.1505.

[241] J. Sun, A. Ruzsinszky, and J. P. Perdew, Strongly constrained and appropriately normed semilocal density functional, *Phys. Rev. Lett.* **115**, 036402 (2015), doi:10.1103/PhysRevLett.115.036402.

[242] I. Harris and G. Raynor, Rare earth intermediate phases: I. phases formed with tin and indium, *J. Less Common Met.* **9**, 7–19 (1965), doi:10.1016/0022-5088(65)90029-9.

[243] T. Yusufaly, D. Vanderbilt, and S. Coh, Tight-binding formalism in the context of the PythTB package (2018), `http://www.physics.rutgers.edu/pythtb`.

[244] C. Yue, wannhr_symm (2021), Retrieved from `http://www.github.com/quanshengwu/wannier_tools`.

[245] P. Rourke and S. Julian, Numerical extraction of de Haas–van Alphen frequencies from calculated band energies, *Comput. Phys. Commun* **183**, 324–332 (2012), doi:10.1016/j.cpc.2011.10.015.

[246] A. Togo and I. Tanaka, Spglib: a software library for crystal symmetry search, *arXiv preprint arXiv:1808.01590* (2018).

[247] M. Dawson-Haggerty, trimesh (2019), Retrieved from `https://trimsh.org/`.

[248] Plotly Technologies Inc., plotly (2015), Retrieved from `https://plot.ly`.

[249] A. Rohatgi, Webplotdigitizer: Version 4.5 (2021), Retrieved from `https://automeris.io/WebPlotDigitizer`.

[250] T. Shao-ping, Z. Kai-ming, and X. Xi-de, The electronic structures of $LaSn_3$ and $LaIn_3$, *J. Phys.: Condens. Matter* **1**, 2677–2682 (1989), doi:10.1088/0953-8984/1/16/003.

[251] U. V. Waghmare, N. A. Spaldin, H. C. Kandpal, and R. Seshadri, First-principles indicators of metallicity and cation off-centricity in the IV-VI rocksalt chalcogenides of divalent Ge, Sn, and Pb, *Phys. Rev. B* **67**, 125111 (2003), doi:10.1103/PhysRevB.67.125111.

[252] A. Walsh, D. J. Payne, R. G. Egdell, and G. W. Watson, Stereochemistry of post-transition metal oxides: revision of the classical lone pair model, *Chem. Soc. Rev.* **40**, 4455–4463 (2011), doi:10.1039/C1CS15098G.

[253] L. Muechler, A. Topp, R. Queiroz, M. Krivenkov, A. Varykhalov, J. Cano, C. R. Ast, and L. M. Schoop, Modular arithmetic with nodal lines: Drumhead surface states in ZrSiTe, *Phys. Rev. X* **10**, 011026 (2020), doi:10.1103/PhysRevX.10.011026.

[254] N. B. Kopnin, T. T. Heikkilä, and G. E. Volovik, High-temperature surface superconductivity in topological flat-band systems, *Phys. Rev. B* **83**, 220503 (2011), doi:10.1103/PhysRevB.83.220503.

[255] B. Roy, Interacting nodal-line semimetal: Proximity effect and spontaneous symmetry breaking, *Phys. Rev. B* **96**, 041113 (2017), doi:10.1103/PhysRevB.96.041113.

[256] D. E. Freedman, T. H. Han, A. Prodi, P. Müller, Q.-Z. Huang, Y.-S. Chen, S. M. Webb, Y. S. Lee, T. M. McQueen, and D. G. Nocera, Site specific X-ray anomalous dispersion of the geometrically frustrated kagome magnet, herbertsmithite, $ZnCu_3(OH)_6Cl_2$, *J. Am. Chem. Soc.* **132**, 16185–16190 (2010), doi:10.1021/ja1070398.

[257] D. Wulferding, P. Lemmens, P. Scheib, J. Röder, P. Mendels, S. Chu, T. Han, and Y. S. Lee, Interplay of thermal and quantum spin fluctuations in the kagome lattice compound herbertsmithite, *Phys. Rev. B* **82**, 144412 (2010), doi:10.1103/PhysRevB.82.144412.

[258] T. Han, S. Chu, and Y. S. Lee, Refining the spin hamiltonian in the spin-1/2 kagome lattice antiferromagnet $ZnCu_3(OH)_6Cl_2$ using single crystals, *Phys. Rev. Lett.* **108**, 157202 (2012), doi:10.1103/PhysRevLett.108.157202.

[259] M. Fu, T. Imai, T.-H. Han, and Y. S. Lee, Evidence for a gapped spin-liquid ground state in a kagome Heisenberg antiferromagnet, *Science* **350**, 655–658 (2015), doi:10.1126/science.aab2120.

[260] T.-H. Han, J. S. Helton, S. Chu, D. G. Nocera, J. A. Rodriguez-Rivera, C. Broholm, and Y. S. Lee, Fractionalized excitations in the spin-liquid state of a kagome-lattice antiferromagnet, *Nature* **492**, 406–410 (2012), doi:10.1038/nature11659.

[261] W.-S. Wang, Z.-Z. Li, Y.-Y. Xiang, and Q.-H. Wang, Competing electronic orders on kagome lattices at van Hove filling, *Phys. Rev. B* **87**, 115135 (2013), doi:10.1103/PhysRevB.87.115135.

[262] S. V. Isakov, S. Wessel, R. G. Melko, K. Sengupta, and Y. B. Kim, Hard-core bosons on the kagome lattice: Valence-bond solids and their quantum melting, *Phys. Rev. Lett.* **97**, 147202 (2006), doi:10.1103/PhysRevLett.97.147202.

[263] A. O'Brien, F. Pollmann, and P. Fulde, Strongly correlated fermions on a kagome lattice, *Phys. Rev. B* **81**, 235115 (2010), doi:10.1103/PhysRevB.81.235115.

[264] A. Rüegg and G. A. Fiete, Fractionally charged topological point defects on the kagome lattice, *Phys. Rev. B* **83**, 165118 (2011), doi:10.1103/PhysRevB.83.165118.

[265] S. Yan, D. A. Huse, and S. R. White, Spin-liquid ground state of the S= 1/2 kagome Heisenberg antiferromagnet, *Science* **332**, 1173–1176 (2011), doi:10.1126/science.1201080.

[266] H.-M. Guo and M. Franz, Topological insulator on the kagome lattice, *Phys. Rev. B* **80**, 113102 (2009), doi:10.1103/PhysRevB.80.113102.

[267] W.-H. Ko, P. A. Lee, and X.-G. Wen, Doped kagome system as exotic superconductor, *Phys. Rev. B* **79**, 214502 (2009), doi:10.1103/PhysRevB.79.214502.

[268] S.-L. Yu and J.-X. Li, Chiral superconducting phase and chiral spin-density-wave phase in a Hubbard model on the kagome lattice, *Phys. Rev. B* **85**, 144402 (2012), doi:10.1103/PhysRevB.85.144402.

[269] M. L. Kiesel, C. Platt, and R. Thomale, Unconventional Fermi surface instabilities in the kagome Hubbard model, *Phys. Rev. Lett.* **110**, 126405 (2013), doi:10.1103/PhysRevLett.110.126405.

[270] K. Barros, J. W. Venderbos, G.-W. Chern, and C. Batista, Exotic magnetic orderings in the kagome Kondo-lattice model, *Phys. Rev. B* **90**, 245119 (2014), doi:10.1103/PhysRevB.90.245119.

[271] X. Feng, K. Jiang, Z. Wang, and J. Hu, Chiral flux phase in the kagome superconductor AV_3Sb_5, *Sci. Bull* **66**, 1384–1388 (2021), doi:10.1016/j.scib.2021.04.043.

[272] B. R. Ortiz, L. C. Gomes, J. R. Morey, M. Winiarski, M. Bordelon, J. S. Mangum, I. W. H. Oswald, J. A. Rodriguez-Rivera, J. R. Neilson, S. D. Wilson, E. Ertekin, T. M. McQueen, and E. S. Toberer, New kagome prototype materials: discovery of KV_3Sb_5, RbV_3Sb_5, and CsV_3Sb_5, *Phys. Rev. Materials* **3**, 094407 (2019), doi:10.1103/PhysRevMaterials.3.094407.

[273] Y.-X. Jiang, J.-X. Yin, M. M. Denner, N. Shumiya, B. R. Ortiz, G. Xu, Z. Guguchia, J. He, M. S. Hossain, X. Liu, J. Ruff, L. Kautzsch, S. S. Zhang, G. Chang, I. Belopolski, Q. Zhang, T. A. Cochran, D. Multer, M. Litskevich, Z.-J. Cheng, X. P. Yang, Z. Wang, R. Thomale, T. Neupert, S. D. Wilson, and M. Z. Hasan, Unconventional chiral charge order in kagome superconductor KV_3Sb_5, *Nat. Mater.* **20**, 1353–1357 (2021), doi:10.1038/s41563-021-01034-y.

[274] H. Zhao, H. Li, B. R. Ortiz, S. M. L. Teicher, T. Park, M. Ye, Z. Wang, L. Balents, S. D. Wilson, and I. Zeljkovic, Cascade of correlated electron states in a kagome superconductor CsV_3Sb_5, *Nature* **599**, 216 (2021), doi:10.1038/s41586-021-03946-w.

[275] B. R. Ortiz, P. M. Sarte, E. M. Kenney, M. J. Graf, S. M. L. Teicher, R. Seshadri, and S. D. Wilson, Superconductivity in the $\mathbb{Z}_2$ kagome metal KV_3Sb_5, *Phys. Rev. Materials* **5**, 034801 (2021), doi:10.1103/PhysRevMaterials.5.034801.

[276] Z. Liang, X. Hou, W. Ma, F. Zhang, P. Wu, Z. Zhang, F. Yu, J.-J. Ying, K. Jiang, L. Shan, Z. Wang, and X.-H. Chen, Three-dimensional charge density wave and robust zero-bias conductance peak inside the superconducting vortex core of a kagome superconductor CsV_3Sb_5, *arXiv preprint arXiv:2103.04760* (2021).

[277] H. Chen, H. Yang, B. Hu, Z. Zhao, J. Yuan, Y. Xing, G. Qian, Z. Huang, G. Li, Y. Ye, S. Ma, S. Ni, H. Zhang, Q. Yin, C. Gong, Z. Tu, H. Lei, H. Tan, S. Zhou, C. Shen, X. Dong, B. Yan, Z. Wang, and H.-J. Gao, Roton pair density wave and unconventional strong-coupling superconductivity in a topological kagome metal, *arXiv preprint arXiv:2103.09188* (2021).

[278] Q. Yin, Z. Tu, C. Gong, Y. Fu, S. Yan, and H. Lei, Superconductivity and normal-state properties of kagome metal RbV_3Sb_5 single crystals, *Chin. Phys. Lett.* **38**, 037403 (2021), doi:10.1088/0256-307x/38/3/037403.

[279] C. Mu, Q. Yin, Z. Tu, C. Gong, H. Lei, Z. Li, and J. Luo, S-wave superconductivity in kagome metal CsV_3Sb_5 revealed by $^{121/123}$Sb NQR and ^{51}V NMR measurements, *Chin. Phys. Lett.* **38**, 077402 (2021), doi:10.1088/0256-307x/38/7/077402.

[280] C. C. Zhao, L. S. Wang, W. Xia, Q. W. Yin, J. M. Ni, Y. Y. Huang, C. P. Tu, Z. C. Tao, Z. J. Tu, C. S. Gong, H. C. Lei, Y. F. Guo, X. F. Yang, and S. Y. Li, Nodal superconductivity and superconducting domes in the topological kagome metal CsV_3Sb_5, *arXiv preprint arXiv:2102.083560* (2021).

[281] Y. Gu, Y. Zhang, X. Feng, K. Jiang, and J. Hu, Gapless excitations inside the fully gapped kagome superconductors AV_3Sb_5, *arXiv preprint arXiv:2108.04703* (2021).

[282] F. Du, S. Luo, B. R. Ortiz, Y. Chen, W. Duan, D. Zhang, X. Lu, S. D. Wilson, Y. Song, and H. Yuan, Pressure-tuned interplay between charge order and superconductivity in the kagome metal KV_3Sb_5, *arXiv preprint arXiv:2102.10959* (2021).

[283] K. Chen, N. Wang, Q. Yin, Z. Tu, C. Gong, J. Sun, H. Lei, Y. Uwatoko, and J.-G. Cheng, Double superconducting dome and triple enhancement of T_c in the kagome superconductor CsV_3Sb_5 under high pressure, *arXiv preprint arXiv:2102.09328* (2021).

[284] S.-Y. Yang, Y. Wang, B. R. Ortiz, D. Liu, J. Gayles, E. Derunova, R. Gonzalez-Hernandez, L. Šmejkal, Y. Chen, S. S. P. Parkin, S. D. Wilson, E. S. Toberer, T. McQueen, and M. N. Ali, Giant, unconventional anomalous hall effect in the metallic frustrated magnet candidate, KV_3Sb_5, *Sci. Adv.* **6**, 31 (2020), doi:10.1126/sciadv.abb6003.

[285] F. Yu, T. Wu, Z. Wang, B. Lei, W. Zhuo, J. Ying, and X. Chen, Concurrence of anomalous hall effect and charge density wave in a superconducting topological kagome metal, *arXiv preprint arXiv:2102.10987* (2021).

[286] E. M. Kenney, B. R. Ortiz, C. Wang, S. D. Wilson, and M. J. Graf, Absence of local moments in the kagome metal KV_3Sb_5 as determined my muon spin spectroscopy, *J. Phys. Condens. Matter* **33**, 235801 (2021), doi:10.1088/1361-648X/abe8f9.

[287] H. Tan, Y. Liu, Z. Wang, and B. Yan, Charge density waves and electronic properties of superconducting kagome metals, *Phys. Rev. Lett.* **127**, 046401 (2021), doi:10.1103/PhysRevLett.127.046401.

[288] E. Uykur, B. Ortiz, S. Wilson, M. Dressel, and A. Tsirlin, Optical detection of charge-density-wave instability in the non-magnetic kagome metal KV_3Sb_5, *arXiv preprint arXiv:2103.07912* (2021).

[289] J. Sangster and A. Pelton, The Cs-Sb (cesium-antimony) system, *J. Phase Equilibria* **18**, 382–386 (1997), doi:10.1007/s11669-997-0065-z.

[290] Y. Wang, S. Yang, P. K. Sivakumar, B. R. Ortiz, S. M. L. Teicher, H. Wu, A. K. Sirvastava, C. Garg, D. Liu, S. S. Parkin, E. Toberer, T. McQueen, S. D. Wilson, and M. N. Ali, Proximity-induced spin-triplet superconductivity and edge supercurrent in the topological kagome metal, $\mathrm{K}_{1-x}\mathrm{V}_3\mathrm{Sb}_5$, *arXiv preprint arXiv:2012.05898* (2020).

[291] S. Grimme, S. Ehrlich, and L. Goerigk, Effect of the damping function in dispersion corrected density functional theory, *J. Comput. Chem.* **32**, 1456–1465 (2011), doi:10.1002/jcc.21759.

[292] H. T. Stokes, D. M. Hatch, and B. J. Campbell, Isodistort, `iso.byu.edu`.

[293] B. J. Campbell, H. T. Stokes, D. E. Tanner, and D. M. Hatch, ISODISPLACE: a web-based tool for exploring structural distortions, *J. Appl. Crystallogr.* **39**, 607–614 (2006), doi:10.1107/S0021889806014075.

[294] Q. Zheng, Vasp Band Unfolding, `https://github.com/QijingZheng/VaspBandUnfolding`.

[295] See Supplemental Information, http://link.aps.org/supplemental/10.1103/PhysRevX.11.041030, for further details.

[296] G. M. Sheldrick, Crystal structure refinement with SHELXL, *Acta Cryst. C* **71**, 3–8 (2015), doi:10.1107/S2053229614024218.

[297] G. Oszlányi and A. Sütő, Ab initio structure solution by charge flipping, *Acta Crystallogr. A* **60**, 134–141 (2004), doi:10.1107/S0108767303027569.

[298] G. Oszlányi and A. Sütő, Ab initio structure solution by charge flipping. ii. use of weak reflections, *Acta Crystallogr. A* **61**, 147–152 (2005), doi:10.1107/S0108767304027746.

[299] A. Coelho, A charge-flipping algorithm incorporating the tangent formula for solving difficult structures, *Acta Crystallogr. A* **63**, 400–406 (2007), doi:10.1107/S0108767307036112.

[300] Z. Wang, S. Ma, Y. Zhang, H. Yang, Z. Zhao, Y. Ou, Y. Zhu, S. Ni, Z. Lu, H. Chen, K. Jiang, L. Yu, Y. Zhang, X. Dong, J. Hu, H.-J. Gao, and Z. Zhao, Distinctive momentum dependent charge-density-wave gap observed in $\mathrm{CsV}_3\mathrm{Sb}_5$ superconductor with topological kagome lattice, *arXiv preprint arXiv:2104.05556* (2021).

[301] H. Li, T. T. Zhang, T. Yilmaz, Y. Y. Pai, C. E. Marvinney, A. Said, Q. W. Yin, C. S. Gong, Z. J. Tu, E. Vescovo, C. S. Nelson, R. G. Moore, S. Murakami, H. C. Lei, H. N. Lee, B. J. Lawrie, and H. Miao, Observation of unconventional charge density wave without acoustic phonon anomaly in kagome superconductors $A\mathrm{V}_3\mathrm{Sb}_5$ (A= Rb, Cs), *arXiv preprint arXiv:2103.09769* (2021).

[302] M. L. Kiesel and R. Thomale, Sublattice interference in the kagome Hubbard model, *Phys. Rev. B* **86**, 121105 (2012), doi:10.1103/PhysRevB.86.121105.

[303] Y.-P. Lin and R. M. Nandkishore, Complex charge density waves at van Hove singularity on hexagonal lattices: Haldane-model phase diagram and potential realization in the kagome metals AV_3Sb_5 (A = K, Rb, Cs), *Phys. Rev. B* **104**, 045122 (2021), doi:10.1103/PhysRevB.104.045122.

[304] T. Kida, L. A. Fenner, A. A. Dee, I. Terasaki, M. Hagiwara, and A. S. Wills, The giant anomalous hall effect in the ferromagnet Fe_3Sn_2 a frustrated kagome metal, *J. Phys.: Condens. Matter* **23**, 112205 (2011), doi:10.1088/0953-8984/23/11/112205.

[305] L. A. Fenner, A. A. Dee, and A. S. Wills, Non-collinearity and spin frustration in the itinerant kagome ferromagnet Fe_3Sn_2, *J. Phys.: Condens. Matter* **21**, 452202 (2009), doi:10.1088/0953-8984/21/45/452202.

[306] R. L. Dally, J. W. Lynn, N. J. Ghimire, D. Michel, P. Siegfried, and I. I. Mazin, Chiral properties of the zero-field spiral state and field-induced magnetic phases of the itinerant kagome metal YMn_6Sn_6, *Phys. Rev. B* **103**, 094413 (2021), doi:10.1103/PhysRevB.103.094413.

[307] M. Li, Q. Wang, G. Wang, Z. Yuan, W. Song, R. Lou, Z. Liu, Y. Huang, Z. Liu, H. Lei, Z. Yin, and S. Wang, Spin-polarized Dirac cone, flat band and saddle point in kagome magnet YMn_6Sn_6, *Nat. Commun.* **12**, 3129 (2021), doi:10.1038/s41467-021-23536-8.

[308] D. Chen, C. Le, C. Fu, H. Lin, W. Schnelle, Y. Sun, and C. Felser, Large anomalous hall effect in the kagome ferromagnet $LiMn_6Sn_6$, *Phys. Rev. B* **103**, 144410 (2021), doi:10.1103/PhysRevB.103.144410.

[309] T. Asaba, S. M. Thomas, M. Curtis, J. D. Thompson, E. D. Bauer, and F. Ronning, Anomalous hall effect in the kagome ferrimagnet $GdMn_6Sn_6$, *Phys. Rev. B* **101**, 174415 (2020), doi:10.1103/PhysRevB.101.174415.

[310] J.-X. Yin, W. Ma, T. A. Cochran, X. Xu, S. S. Zhang, H.-J. Tien, N. Shumiya, G. Cheng, K. Jiang, B. Lian, Z. Song, G. Chang, I. Belopolski, D. Multer, M. Litskevich, Z.-J. Cheng, X. P. Yang, B. Swidler, H. Zhou, H. Lin, T. Neupert, Z. Wang, N. Yao, T.-R. Chang, S. Jia, and M. Zahid Hasan, Quantum-limit chern topological magnetism in $TbMn_6Sn_6$, *Nature* **583**, 533–536 (2020), doi:10.1038/s41586-020-2482-7.

[311] N. J. Ghimire, R. L. Dally, L. Poudel, D. C. Jones, D. Michel, N. T. Magar, M. Bleuel, M. A. McGuire, J. S. Jiang, J. F. Mitchell, J. W. Lynn, and I. I. Mazin, Competing magnetic phases and fluctuation-driven scalar spin chirality in the kagome metal YMn_6Sn_6, *Sci. Adv.* **6**, 51 (2020), doi:10.1126/sciadv.abe2680.

[312] C. Gieck, M. Schreyer, T. F. Fässler, S. Cavet, and P. Claus, Synthesis, crystal structure, and catalytic properties of $MgCo_6Ge_6$, *Chem. Eur. J* **12**, 1924–1930 (2006), doi:https://doi.org/10.1002/chem.200500411.

[313] S.-Y. Zhang, P. Zhao, Z.-H. Cheng, R.-w. Li, J.-r. Sun, H.-W. Zhang, and B.-G. Shen, Magnetism and giant magnetoresistance of $YMn_6Sn_{6-x}Ga_x$ (x = 0-1.8) compounds, *Phys. Rev. B* **64**, 212404 (2001), doi:10.1103/PhysRevB.64.212404.

[314] P. Schobinger-Papamantellos, J. Rodríguez-Carvajal, and K. Buschow, Cycloid spirals and cycloid cone transition in the $HoMn_{6-x}Cr_xGe_6$ (T, x) magnetic phase diagramm by neutron diffraction, *J. Magn. Magn. Mater.* **408**, 233–243 (2016), doi:10.1016/j.jmmm.2016.02.018.

[315] G. M. Sheldrick, SHELXT–integrated space-group and crystal-structure determination, *Acta Cryst. A* **71**, 3–8 (2015), doi:10.1107/S2053273314026370.

[316] S. Peng, Y. Han, G. Pokharel, Z. Li, M. Hashimoto, D.-H. Lu, Y. Luo, M. Guo, B. Wang, S. Cui, Z. Sun, Z.-H. Qiao, S. D. Wilson, and J.-F. He, Realizing kagome band structure in two-dimensional kagome surface states of RV_6Sn_6 (R =Gd,Ho), *arXiv preprint arXiv:2112.15007* (2021).

[317] V. I. Anisimov, F. Aryasetiawan, and A. I. Lichtenstein, First-principles calculations of the electronic structure and spectra of strongly correlated systems: the LDA + U method, *J. Phys.: Condens. Matter* **9**, 767–808 (1997), doi:10.1088/0953-8984/9/4/002.

[318] R. P. Day, B. Zwartsenberg, I. S. Elfimov, and A. Damascelli, Computational framework chinook for angle-resolved photoemission spectroscopy, *npj Quantum Mater.* **4**, 54 (2019), doi:10.1038/s41535-019-0194-8.

[319] See Supplemental Material at http://link.aps.org/supplemental/ 10.1103/PhysRevB.104.235139 for further details.

[320] A. Larsson, M. Haeberlein, S. Lidin, and U. Schwarz, Single crystal structure refinement and high-pressure properties of CoSn, *J. Alloys Compd.* **240**, 79–84 (1996), doi:https://doi.org/10.1016/0925-8388(95)02189-2.

[321] B. Malaman, B. Roques, A. Courtois, and J. Protas, Structure cristalline du stannure de fer Fe_3Sn_2, *Acta Cryst. B* **32**, 1348–1351 (1976), doi:10.1107/S0567740876005323.

[322] Z.-Z. Lin and X. Chen, Tunable massive Dirac fermions in ferromagnetic Fe_3Sn_2 kagome lattice, *Phys. Status Solidi Rapid Res. Lett.* **14**, 1900705 (2020), doi:https://doi.org/10.1002/pssr.201900705.

[323] S. N. Guin, P. Vir, Y. Zhang, N. Kumar, S. J. Watzman, C. Fu, E. Liu, K. Manna, W. Schnelle, J. Gooth, C. Shekhar, Y. Sun, and C. Felser, Zero-field Nernst effect in a ferromagnetic kagome-lattice Weyl-semimetal $Co_3Sn_2S_2$, *Adv. Mater.* **31**, 1806622 (2019), doi:https://doi.org/10.1002/adma.201806622.

[324] A. Ganose, SUMO: Heavyweight plotting tools for *ab initio* calculations (2018), Retrieved from `https://github.com/SMTG-UCL/sumo`.

[325] L. D. Landau and E. M. Lifshitz, *Quantum mechanics: non-relativistic theory*, Pergamon (1965).

[326] L. Onsager, Interpretation of the de haas-van alphen effect, *Philos. Mag.* **43**, 1006–1008 (1952), doi:10.1080/14786440908521019.

[327] N. W. Ashcroft and N. D. Mermin, *Solid State Physics*, Harcourt (1976).